Measurement of the Inclusive Semileptonic Branching Fraction of B Mesons using Fully Reconstructed B-mesons as Tags in the B_AB_{AR} Experiment

Valery Miftakhov
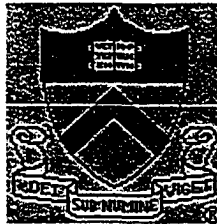
Princeton University

Department of Physics

UMI Number: 3103016

UMI®

Abstract

The *BABAR* experiment at SLAC provides an opportunity for measurement of the Standard Model parameters describing CP violation. A method of measuring the CKM matrix element $|V_{cb}|$ using Inclusive Semileptonic B decays in events tagged by a fully reconstructed decay of one of the B mesons is presented here. This mode is considered to be one of the most powerful approaches due to its large branching fraction, simplicity of the theoretical description and very clean experimental signatures. Using fully reconstructed B mesons to flag $B\overline{B}$ event we were able to produce the spectrum and branching fraction for electron momenta $P_{C.M.S.} > 0.5$ GeV/c. Extrapolation to the lower momenta has been carried out with Heavy Quark Effective Theory. The branching fractions are measured separately for charged and neutral B mesons. For 82 fb^{-1} of data collected at *BABAR* we obtain: $BR(B^{\pm} \rightarrow Xe\overline{\nu}) = 10.63 \pm 0.24 \pm 0.29$ %, $BR(B^{0} \rightarrow Xe\overline{\nu}) = 10.68 \pm 0.34 \pm 0.31$ %, averaged $BR(B \rightarrow Xe\overline{\nu}) = 10.65 \pm 0.19 \pm 0.27$ %, ratio of Branching fractions $BR(B^{\pm})/BR(B^{0}) = 0.996 \pm 0.039 \pm 0.015$ (errors are statistical and systematic, respectively). We also obtain $V_{cb} = 0.0409 \pm 0.00074 \pm 0.0010 \pm 0.000858$ (errors are: statistical, systematic and theoretical).

Contents

v

Acknowledgements

This work would not be possible without continuous support from many people who provided their expertise and gave their advice to me over the last years.

First, I want to mention that the *BABAR* collaboration itself was a great place to be in. I thank many dedicated people for their work in making the collaboration an excellent place to work and acquire knowledge and experience.

I would like to thank my advisor Professor Stewart Smith for making my experience at *BABAR* intellectually stimulating. I also thank Stew Smith and Peter Meyers for devoting their time to help me with the thesis document.

I would also like to thank many members of the "Inclusive Semileptonic Decays" physics analysis group I have had a chance to work in. I would like to especially acknowledge Vera Luth and Urs Langenegger who dedicated their time and patience to help me with their advice and insight.

Thanks to the following friends and colleagues for their help and encouragement: Vera Belenky, Alexander Tumanov, Ajit Mohapatra.

And last, but not least, I would like to thank my family members for their continuous support and worries. I will try to live up to your expectations.

Chapter 1

Introduction

1.1 Overview of CP Violation

In 1964 [1], physicists from Princeton University - V. L. Fitch, J. H. Christenson, J. W. Cronin, and R. Turlay observed one of the most interesting phenomena in particle physics, namely the violation of CP symmetry in decays of neutral Kaons. Until very recently, Kaons were still the only system in which CP violation had been seen for the last 30 years. Neutral B mesons provide another ideal system where large CP asymmetries can be measured [2]. This task is being successfully carried out on the currently operating B-physics experiments in Japan and USA. The first results confirming CP violation in the B-meson system were obtained in 2001 by BABAR .

The abbreviation CP stands for simultaneous charge conjugation C and parity reversal P operations. Charge conjugation interchanges particles with antiparticles. Parity, P, reverses space coordinates $(t, \overline{x}) \rightarrow (t, -\overline{x})$. The operation of time reversal, T, reverses the sign of time $(t, \overline{x}) \rightarrow (-t, \overline{x})$. The combination of these three operations, CPT, is an exact symmetry in any Lorentz invariant Lagrangian field theory. However, separately Parity, Time and Charge symmetry violations

7

are possible and have been observed in numerous experiments.

Within the frame of the Standard Model CP violation can be explained by the theory of weak interactions. In this model B meson decays are predicted to exhibit very clean CP asymmetries enabling us to make stringent tests of the Standard Model. In order to get an opportunity to confirm or(much more exciting) break the Standard Model description of CP violation, several HEP collaborations emerged all over the world. These tests have foremost importance for a number of reasons:

- 1. Cosmology. It was first noted by A. D. Sakharov that the observed dominance of matter over antimatter requires CP symmetry to be violated in fundamental processes in the early universe[3]. And as it's speculated recently, in order to see current levels of the baryon asymmetry the extent of the CP violation in the early universe should even have been larger than predicted by the Standard Model.

- 2. New Physics beyond the Standard Model. A great variety of models, fields and exotic particles are proposed in modern theoretical particle physics. Many of them predict, or depend on the values of CP violating effects, so the theorists can get very valuable insights from these experiments.

Many major laboratories and institutions are or have been engaged in B physics projects and especially are searching for CP violation. Among them are such as CERN, DESY, FNAL, KEK, SLAC etc. Princeton University takes part in *BABAR* (SLAC) and Belle(KEK). Most of the above experiments have already been commissioned and have started producing valuable data for very many interesting physics analyses. Further in this paper we will discuss in more detail the *BABAR* experiment with regard to semileptonic B decays.

8

1.2 CKM Matrix and CP Violation

In the Standard Model the electroweak Hamiltonian, more precisely the part of it which describes W boson coupling to quarks, has a form:

$$H_W = \frac{g}{\sqrt{2}} W^\mu \sum_{\substack{U=u,c,t \\ D=d,s,b}} V_{UD} \overline{U}_L \gamma_\mu D_L + \frac{g}{\sqrt{2}} W^{\mu^+} \sum_{U,D} V^*_{UD} \overline{D}_L \gamma_\mu U_L \quad (1)$$

Here V_{UD} are the coefficients of 3×3 matrix called Cabibbo-Kobayashi-Maskawa (CKM) matrix:

$$V_{CKM} = \begin{pmatrix} V_{ud} & V_{us} & V_{ub} \\ V_{cd} & V_{cs} & V_{cb} \\ V_{td} & V_{ts} & V_{tb} \end{pmatrix}$$

The off-diagonal elements of this matrix relate to the transitions between quarks of one family into another and that is why V_{CKM} is sometimes called the quark mixing matrix.

Under CP transformation H_W becomes[1]:

$$(CP)H_W(CP)^{-1} = (H_W)_{CP} =$$

$$= \frac{g}{\sqrt{2}} W^{\mu^+} \sum_{U,D} V_{UD} \overline{D}_L \gamma_\mu U_L + \frac{g}{\sqrt{2}} W^\mu \sum_{U,D} V^*_{UD} \overline{U}_L \gamma_\mu D_L \quad (2)$$

We see that if $V_{UD} = V^*_{UD}$ for any U, D then $(H_W)_{CP} = H_W$ and CP symmetry is not violated (at least not in this model), but the CKM matrix elements most generally are complex. So most generally this matrix contains 18 real parameters. However the unitarity of V_{CKM} imposes the following conditions:

$$|V_{ud}|^2 + |V_{cd}|^2 + |V_{td}|^2 = 1$$

$$|V_{us}|^2 + |V_{cs}|^2 + |V_{ts}|^2 = 1$$

---

[1]for more details see [4]

9

$$|V_{ub}|^2 + |V_{cb}|^2 + |V_{tb}|^2 = 1$$

$$V_{ud}V_{us}^* + V_{cd}V_{cs}^* + V_{td}V_{ts}^* = 0$$

$$V_{ud}V_{ub}^* + V_{cd}V_{cb}^* + V_{td}V_{tb}^* = 0$$

$$V_{us}V_{ub}^* + V_{cs}V_{cb}^* + V_{ts}V_{tb}^* = 0,$$

which reduce the number of independent real parameters to 9. Also, since the absolute phases of the quarks are not important, the phases of 5 elements of V_{CKM} (one row and one column) could be canceled. Thus, we are left with only four independent coefficients. There are several parametrizations of the CKM matrix that utilize this fact. The most popular parametrization currently is the so-called Wolfenstein's parameterization. It introduces four parameters: $\lambda, A, \rho,$ and η (last 3 being of order unity) and takes advantage of the knowledge of the relative sizes of the angles of the unitarity triangle:

$$\begin{pmatrix} 1 - \lambda^2/2 & \lambda & \lambda^3 A(\rho - i\eta) \\ -\lambda & 1 - \lambda^2/2 & \lambda^2 A \\ \lambda^3 A(1 - \rho - i\eta) & -\lambda^2 A & 1 \end{pmatrix}$$

One of the unitarity conditions for the CKM matrix, which contains the two smallest coupling constants, V_{ub} and V_{td} reads:

$$V_{ud}V_{ub}^* + V_{cd}V_{cb}^* + V_{td}V_{tb}^* = 0,$$

or

$$\frac{V_{ub}^*}{|\lambda V_{cb}|} + \frac{V_{td}}{|\lambda V_{cb}|} = 1$$

10
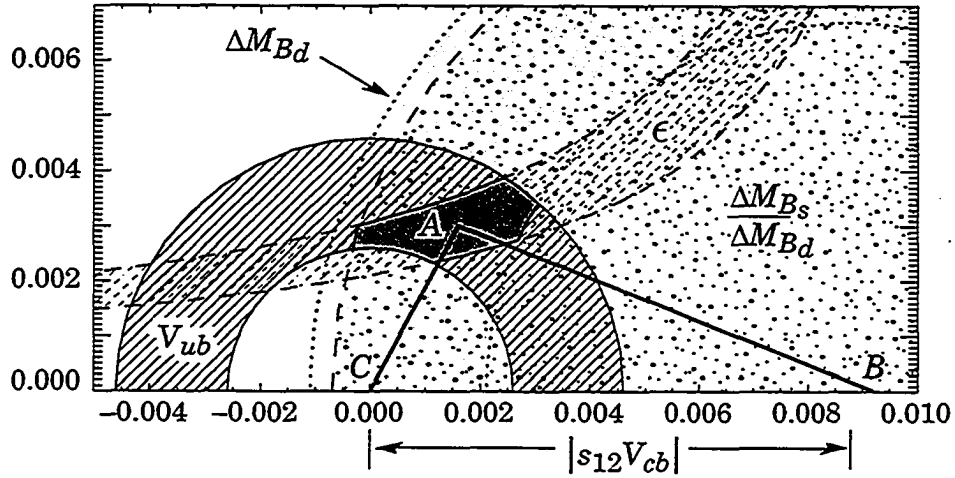
Figure 1.1: Unitarity Triangle. The filled area shows the constraints in effect in 2000, before the major results from *BABAR* were available. If CP had not been violated then the tip of the triangle (point A) would have been on horizontal axis.

The last relation is expressed as a triangle in a (ρ, η) plane(see Figures 1.1 and 1.2), referred to as the Unitarity Triangle, which plays a very important role in Standard Model.

Thus, since the CKM matrix elements can in general have phases between them, CP symmetry may be violated in certain weak processes.

1.3 *CP* Violation in the B Meson System

Let's consider B mesons. As we can infer from the form of (1) the mass eigenstates $|B_L\rangle$ and $|B_H\rangle$ are mixtures of the flavor eigenstates $|B^0\rangle$ and $|\overline{B}^0\rangle$:

$$|B_L\rangle = p|B^0\rangle + q|\overline{B}^0\rangle$$

$$|B_H\rangle = p|B^0\rangle - q|\overline{B}^0\rangle$$

11
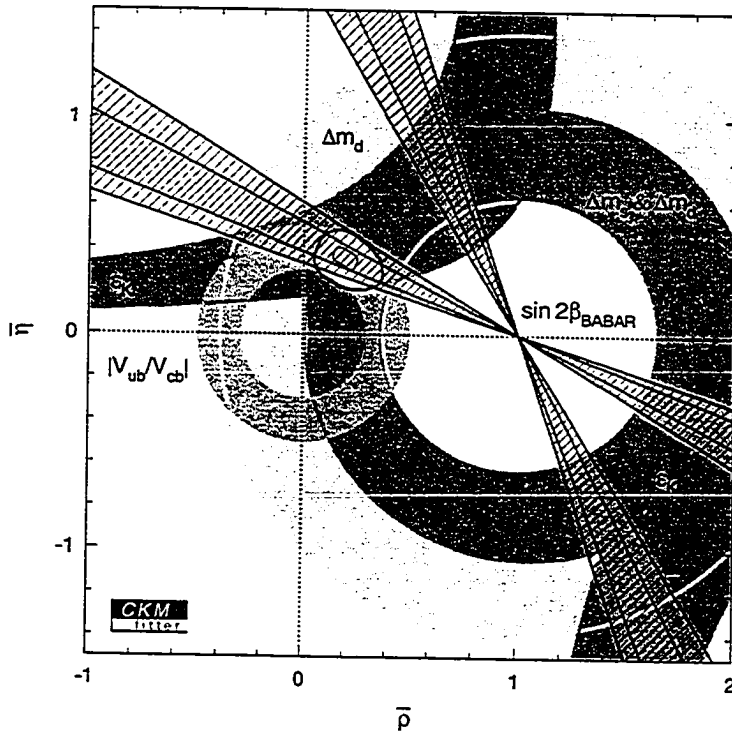
Figure 1.2: Unitarity Triangle in (η, ρ) plane with the current constraints on the position of the tip of the triangle.

12

and vice versa,

$$|B^0\rangle = \frac{1}{2p}(|B_H\rangle + |B_L\rangle)$$

$$|\overline{B}^0\rangle = \frac{1}{2q}(|B_L\rangle - |B_H\rangle)$$

There are two classes of the CP violation:

- 1. direct

  The difference in decay amplitudes

  $$A_f \neq \overline{A}_{\overline{f}}; \ A_f = \langle f|H|B^0\rangle, \ \overline{A}_{\overline{f}} = \langle \overline{f}|H|\overline{B}^0\rangle$$

  is called *direct* CP violation.

- 2. indirect

  There are two types of indirect CP violation:

  - * $|p| \neq |q|$ would result in difference between the probability of B^0 to oscillate into $\overline{B}^0$ and the probability of $\overline{B}^0$ to oscillate into B^0. This is called *CP violation in mixing* and this was what first has been discovered in K system.

  - * There is also another type of CP violation to be observed in neutral B system: *CP violation in the interference between decays with and without mixing*, sometimes abbreviated as "interference between decay and mixing". This happens when $|q/p| = 1$, $|\overline{A}_{\overline{f}_{CP}}/A_{f_{CP}}| = 1$, but $Im(q\overline{A}_{\overline{f}_{CP}}/pA_{f_{CP}}) \neq 0$.

For example, indirect CP violation implies different rates for $B_H \to f_{CP}$ and $B_L \to f_{CP}$, where f_{CP} is some CP even or odd final state. Direct CP violation states that the ratio of the rates $B_H \to f_{CP}$ and $B_L \to f_{CP}$ is different for

13
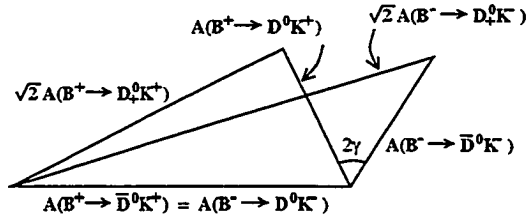
Figure 1.3: Example of extraction of one angle of the unitarity triangle. γ can be extracted using relations among $B^{\pm} \to DK^{\pm}$ decay amplitudes.

different f_{CP} [4], [5]. Direct CP violation is the only type which can occur in charged decays, and the final state doesn't have to be a CP eigenstate. It is very interesting to measure direct CP in the B system and *BABAR* provides us with unique opportunity to do that.

To test Standard Model predictions for the CP violation mechanism, one needs to make enough measurements to overconstrain the Unitarity Triangle. Consequently, one of the major physical tasks of the *BABAR* experiment is to measure as many parameters of the Unitarity Triangle as possible. This task can be broken down into two parts:

- 1. Measurement of all three angles of the unitarity triangle (fig.1.1) (with stress on α, β measurement) to find out whether they form a triangle in terms of the Standard Model. Several methods have been proposed to perform this challenging task ([6]):

  - (1) α - any mode with a contribution from $b \to du\bar{u}$ is a possible source of measurement of α. Examples: $B \to \pi\pi$, $B \to \pi\rho$.

  - (2) β:

    * (a) Color-suppressed modes $b \to c\bar{c}s$, for example one of the *BABAR* benchmarks - $B \to J/\psi K_S^0$.

    * (b) Cabibbo-suppressed modes $b \to c\bar{c}d$ ($B_s^0 \to D\overline{D}$ etc.)

14

* (c) Penguin-dominated modes $b \rightarrow s\bar{s}s$ or $b \rightarrow d\bar{d}s$ - $B_d^0 \rightarrow \pi^0 K^0$ etc.

- (3) γ: this is the least known angle in the unitarity triangle to date. Several methods have been suggested for its extraction, though it will be rather hard to employ these methods in *BABAR* (extremely low branching fractions):

    * (a) Triangle relations among B-decay amplitudes.

    * (b) $B^{\pm} \rightarrow DK^{\pm}$ and related decays - see Figure 1.3.

    * (c) Amplitude relations among $B_{u,d} \rightarrow \pi K$ decays.

- 2.Measurement of all three **sides** of the unitarity triangle to further constrain the triangle parameters and to provide a critical cross-checks on the other parameters. The following methods have been proposed to measure the sides of the triangle:

    - (1) determination of $|V_{cb}|$ and $|V_{ub}|$ by analizing the leptonic and semileptonic decays of B mesons. The ratio of these CKM matrix elements determines the length of the side of the triangle between angles α and γ (refer to fig.1.1). $|V_{cb}|$ CKM matrix element also enters the calculation of another side of the triangle between angles β and γ.

This thesis describes the study of semileptonic B decays and application of its results to help constrain two of the sides of the Unitarity Triangle.

1.4 Semileptonic Decays

One of the most powerful approaches for V_{cb} and V_{ub} extraction is to study the leptonic and semileptonic decays of B mesons. The experimental data used in this paper were collected within the *BABAR* detector in an experiment dedicated

15

mainly to studying CP symmetry violation phenomena in B physics. The resulting measurements of the sides of unitarity triangle are very important in understanding of the Standard Model in general and CP violation in particular.

1.4.1 $|V_{cb}|$ and $|V_{ub}|$ extraction

In the phenomenology of weak interactions, leptonic and semileptonic decays of bottom hadrons have a special standing. In both types of decays, the final state particles include a single charged lepton, which provides a very clear experimental signature. In addition these decays are relatively simple from the theoretical point of view, which makes them a good source to measure fundamental standard-model parameters and to perform detailed studies of decay dynamics. For a good overview of the leptonic and semileptonic decays of charm and bottom hadrons see [8]. Our discussion will deal only with semileptonic decays as they are much more accessible experimentally due to their larger branching fractions.

Particles containing heavy quarks can decay semileptonically in a manner similar to that of nuclear β decay. Figure 1.4 shows the underlying quark-level transitions for the semileptonic decays of the B mesons.
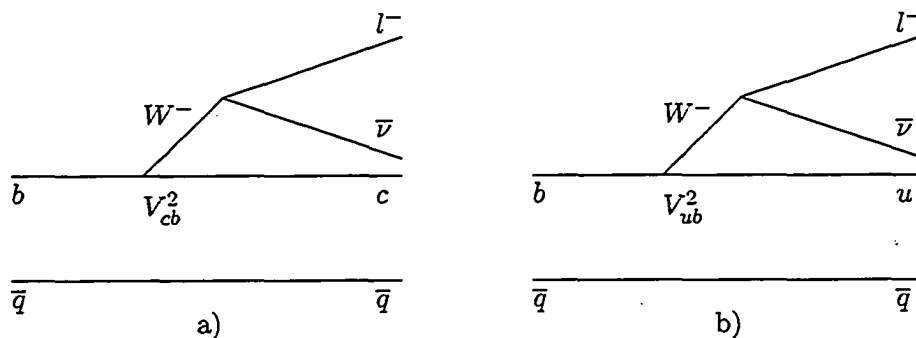
Figure 1.4: Diagrams for semileptonic decays of B_q^o meson: a) $B_d^q \rightarrow X_c l^- \overline{\nu}$, b) $B_d^q \rightarrow X_u l^- \overline{\nu}$.

A key feature of semileptonic decays is their relative simplicity, a consequence of the fact that the effect of the strong interactions can be isolated. The decay amplitude can be written as a product of a well-understood leptonic current for the $l^-\bar{\nu}$ system and a more complicated hadronic current for the quark transition. For example, semileptonic b decay $b \rightarrow c l\bar{\nu}$ is mediated by a four-fermion operator,

$$O_{bc} = \frac{G_F V_{cb}}{\sqrt{2}} \bar{c}\gamma^\mu(1-\gamma^5)b\bar{\nu}\gamma_\mu(1-\gamma^5)l.$$

The quark matrix element is easy to calculate at the quark level,

$$V_{quark} = \langle c l\bar{\nu}|O_{cb}|b\rangle = \frac{G_F V_{cb}}{\sqrt{2}}\bar{u}_c(p_c)\gamma^\mu(1-\gamma^5)u_b(p_b)\bar{u}_l(p_l)\gamma^\mu(1-\gamma^5)v_\nu(p_\nu).$$

However, V_{quark} is relevant at very short distances, otherwise QCD confinement implies that free b and c quarks are not asymptotic states. Instead, nonperturbative QCD effects dress the quark-level transition $b \rightarrow c l\bar{\nu}$ to a hadronic transition, such as

$$\overline{B} \rightarrow D l\bar{\nu}, \overline{B} \rightarrow D^* l\bar{\nu}, \dots$$

The hadronic matrix element depends on nonperturbative QCD and is difficult to calculate from first principles.

Nevertheless, because strong interactions affect only one of the two currents, semileptonic decays are much easier to describe theoretically than hadronic decays, in which the decay products of the W^- are also hadrons. To describe an hadronic part of the decay, several new theoretical approaches have emerged in the last few years. The one which is the most appropriate in our case is a Heavy Quark Effective Theory (HQET) [9], [10], a new theoretical approach for analizing decays of the mesons containing one heavy and one light quark. We now present some of the basic ideas of HQET.

1.4.2 HQET

Let us first consider the heavy quark limit, $m_Q \rightarrow \infty$. Consider a meson M_Q composed of a heavy quark Q and "light degrees of freedom", consisting of light quark/antiquark and gluons. The Compton wavelength of the heavy quark scales as the inverse of its mass, $\lambda_Q \sim 1/m_Q$. The light degrees of freedom, by contrast, are characterized by momenta of order Λ_{QCD}, corresponding to wavelengths $\lambda_l \sim 1/\Lambda_{QCD}$. Since $\lambda_l \gg \lambda_Q$, the light degrees of freedom cannot resolve features of the heavy quark other than its conserved gauge quantum numbers. In particular, they cannot probe the actual value of λ_Q, hence the value of m_Q. Let's move to momentum space. The asymptotic freedom of QCD implies that when quarks and gluons exchange momenta much larger then Λ_{QCD}, the process is perturbative in the strong coupling constant $\alpha_s(p)$. On the other hand, the typical momenta exchanged by the light degrees and the heavy quark are of order Λ_{QCD}, for which a perturbative expansion is of no use. For these exchanges, however, $p \ll m_Q$, and the heavy quark Q doesn't recoil ($|v_Q| = \Lambda_{QCD}/m_Q \rightarrow 0$ when $m_Q \rightarrow \infty$), remaining at rest in the rest frame of the meson. In this limit, Q acts as a static source of the chromoelectric gauge field, which holds M_Q together and is independent of m_Q. The result is that the properties of the light degrees of freedom depend only on the presence of the static gauge field, independent of flavor and mass of the heavy quark. Furthermore, the heavy quark's spin, which interacts with the system through a color magnetic moment proportional to $1/m_Q$, also decouples from the dynamics in this limit. Clearly, these factors enormously simplify the decay kinematics. This result is, of course, an approximation, since the mass of the bottom quark is not infinite. The appropriate corrections can be organized in a systematic expansion in powers of $\alpha_s(m_Q)$ and $1/m_Q$, using the HQET formalism.

Another advantage of having a heavy b-quark in the initial state is that we

can use the hypothesis of quark-hadron duality, an important concept in QCD. The assumption of duality is that cross-sections and decay rates, defined in the physical region, are calculable in QCD after "smearing" or "averaging" procedure has been applied. For semileptonic processes it is the integration over the lepton and neutrino phase space that provides a smearing over the invariant hadronic mass in the final state (so-called global duality).

These two principles combined give us an expression for the rates of decays $B \to X_c l\bar{\nu}$ and $B \to X_u l\bar{\nu}$ [6]:

$$\Gamma(\overline{B^0} \to X_q l^- \bar{\nu}) = \frac{G_f^2 m_b^5}{192\pi^3}\{c_3^{SLq}(1 + \frac{\lambda_1 + 3\lambda_2}{2m_b^2}) - c_5^{SLq}\frac{6\lambda_2}{m_b^2} + \ldots\}, \qquad (1.1)$$

where

$$c_3^{SLq} = |V_{qb}|^2(1 - 8x + 8x^3 - x^4 - 12x^2\log x + O(\alpha_s))$$
$$c_5^{SLq} = |V_{qb}|^2(1 - x)^4$$
$$x = (m_q/m_b)^2$$
$$\lambda_2 \simeq 0.12 GeV^2$$
$$0.1 GeV^2 < -\lambda_1 < 0.6 GeV^2$$

The main uncertainty here arises from the short-distance correction term c_3^{SLq}, known exactly to the order of α_s. In addition, there are uncertainties related to the explicit appearance of the heavy-quark mass, m_b in a large power. The latter uncertainty is not so large as it may appear from the form of (1.1). For charm decay, for example, it can be shown, that the actual mass dependence of the total semileptonic rate can be written as $\Gamma_{SL} \propto m_b^{2.3}(m_b - m_c)^{2.7}$. This splits the mass uncertainty into two uncorrelated parts, thereby reducing the resulting error in the decay rate. Adding all these errors in quadrature gives

$$|V_{cb}| = (0.0419)\sqrt{\frac{B(B \to X_c e\bar{\nu})}{10.5\%} \times \frac{1.55 ps}{\tau_B}} \qquad (1.2)$$
$$\times(1 - 0.012\frac{\mu_\pi^2 - 0.5 GeV/c^2}{0.1 GeV/c^2}) \qquad (1.3)$$
$$\times(1 \pm 0.015_{perturb} \pm 0.010_{m_b} \pm 0.012_{1/m_Q^3}) \qquad (1.4)$$

19

where

$\tau_B = (\tau_{B^\pm} + \tau_{B^0})/2 = 1.61 \pm 0.012 ps, \tau_{B^\pm} = 1.674 \pm 0.018 ps, \tau_{B^0} = 1.546 \pm 0.016 ps$ - mean lifetimes of corresponding B-mesons , [46],

$\mu_\pi^2 = 0.5\ GeV/c^2$ is related to the average kinetic energy of the b quark moving inside the B-meson .

Experimentally, the branching fraction B is determined by integrating dB/dp over a momentum range as wide as possible and by then extrapolating to all momenta in B decays. This process brings in another uncertainty, which depends on what model is using for extrapolation. Current state of theoretical knowledge of semileptonic decays of B mesons transfers into an error on V_{cb} of the order of 3%.

20

Chapter 2

The PEP-II Asymmetric Collider and The B_AB_{AR} Detector

One of the major experiments currently active in B physics studies, *BABAR* , is located at the Stanford Linear Accelerator Center (SLAC), in California. Using asymmetric beams of the accelerator to produce $\simeq 10^8$ $b\bar{b}$ pairs a year and a state-of-the-art detector, this experiment allows us to perform extensive tests of the Standard Model and to study CP violation phenomena in detail. In Table 2.1 we compare *BABAR* to the previous major B-physics experiment of this kind, CLEO []. The major advantages of *BABAR* over CLEO are asymmetric design, much higher luminosity and better particle ID. The impact of these improvements on our subject, semileptonic B decays, will be discussed later in this section.

	BaBar	CLEO, as of 2001 [7]
Accelerator Type	e^+e^- asymmetric collider	e^+e^- symmetric collider
Luminosity, 10^{33} $cm^{-2}sec^{-1}$	3	0.6
Beams, GeV	3.1 e^+ 9.0 e^-	4.7-5.6 e^+ and e^-
$\sigma_{b\bar{b}}$, nb	1.05	1.05
$b\bar{b}$ production rates, Hz	~ 1	~ 0.2
Mean B meson path, μm	250	25
Spatial hit resolution, μm	$\sigma_{xy} = 50$ $\sigma_z = 50$	$\sigma_{xy} = 50$ $\sigma_z = 50$

Table 2.1: Comparison of the *BABAR* and CLEO Experiments.

2.1 The PEP-II Asymmetric Collider

PEP-II is a storage ring system for asymmetric e^+e^- beams, produced by and injected from the existing linear accelerator at SLAC. It is designed to operate at a center of mass (c.m.) energy of 10.58 GeV, corresponding to the mass of the $\Upsilon(4S)$ resonance. The parameters of these storage rings are presented in Table 2.2. PEP-II was designed to produce about 30 million $b\bar{b}$ pairs per year at a design luminosity of 3×10^{33} cm^{-2} sec^{-1}. PEP-II has surpassed its design goals, both in terms of instantaneous and integrated daily luminosity as well as $b\bar{b}$ production rates, with significantly fewer bunches than anticipated. Figure 2.1 represents a schematic view of the PEP-II storage ring system.

The machine operates at the $\Upsilon(4S)$ resonance, which allows placing several kinematic constraints using knowledge of the exact 4-momentum of the $b\bar{b}$ pair and also knowledge of the momentum magnitudes of the two B mesons individually in the center-of-mass frame. These constraints help considerably in sup-
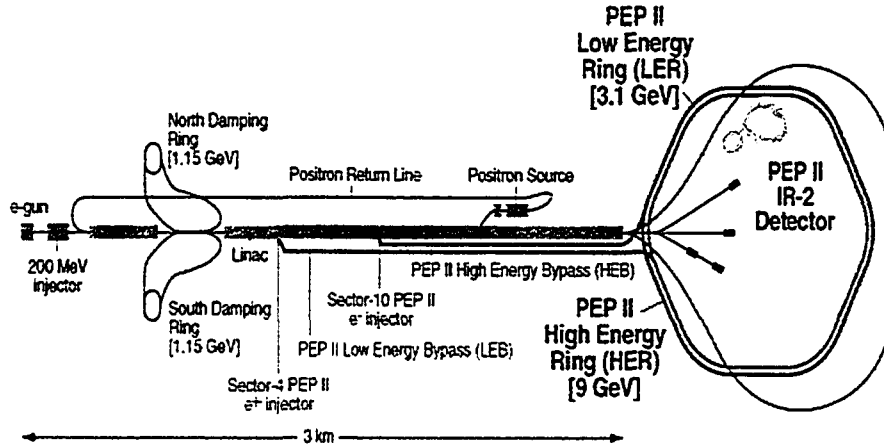
Figure 2.1: PEP-II storage ring system

pressing background. While $\Upsilon(4S)$ is the main mode of the machine, significant amount of data (approx. 1/8th) is being taken in continuum mode (60 MeV below $\Upsilon(4S)$ mass) for background studies.

During the operation, the mean energies of the beams are constantly monitored so that the combined c.m. energy is always close to the peak of the $\Upsilon(4S)$ resonance. Typical precision of the control methods varies from 1.1 MeV per fb^{-1} for statistical measurement to 2 MeV for instantaneous measurement. The beam energies are necessary input for the calculation of the two kinematic variables, ΔE and M_{ES}, that are commonly used to separate signal from background in the analysis of exclusive B-meson decays and any other analyses depending on exclusive or semi-exclusive B-meson decay reconstruction (such as the analysis described in this document). These kinematic variables, which make optimum use of the measured quantities and are largely uncorrelated, are Lorentz-invariants which can be evaluated both in the laboratory and c.m. frames. The first variable, ΔE, can be expressed in Lorentz-invariant form as

$$\Delta E = (2q_B q_0 - s)/2\sqrt{s},$$

where $\sqrt{s} = 2E_{beam}^*$ is the total energy of the e^+e^- system in the c.m. frame,

23

Parameters	Design	Achieved (typical)
Energy HER/LER (GeV)	9.0/3.1	9.0/3.1
Current HER/LER (A)	0.75/2.15	0.8/1.6
number of bunches	1658	553-829
bunch spacing (ns)	4.2	6.3-10.5
σ_{L_x} (μm)	110	120
σ_{L_y} (μm)	3.3	5.6
σ_{L_z} (mm)	9	9
Luminosity ($10^{33} cm^{-2} s^{-1}$)	3	3.5
Luminosity (pb^{-1}/day)	135	250

Table 2.2: PEP-II beam parameters. HER stands for "high-energy ring", LER - for "low energy ring". σ_{L_x}, σ_{L_y} and σ_{L_z} refer to the horizontal, vertical and longitudinal RMS size of the luminous region.

24

and q_B and $q_0 = (E_0, p_0)$ are the Lorentz vectors representing the momentum of the B candidate and of the e^+e^- system, $q_0 = q_{e^+} + q_{e^-}$. In the c.m. frame, ΔE takes the following form:

$$\Delta E = E_B^* - E_{beam}^*,$$

where E_B^* is the reconstructed energy of the B meson. The ΔE distribution receives a sizeable contribution from the beam energy spread, but is generally dominated by the detector resolution. The second variable is the energy-substituted mass, M_{ES}, defined as $m_{ES}^2 = q_B^2$. In the laboratory frame, M_{ES} can be determined from the measured three-momentum p_B of the B candidate without explicit knowledge of the masses of the decay products:

$$M_{ES} = \sqrt{(s/2 + p_B \times p_0)^2 / E_0^2 - p_B^2}$$

and in the c.m. frame

$$M_{ES} = \sqrt{E_{beam}^{*}{}^2 - p_B^{*}{}^2}$$

where p_B^* is the c.m. momentum of the B meson, derived from the momenta of its decay products, and the B-meson energy is substituted by E_{beam}^*. The resolution in M_{ES} is dominated by the spread in E_{beam}^* and $\sigma_{E_{beam}^*} = 2.6$ MeV.

2.2 The $B_A B_{AR}$ Detector

In order to meet its physics goals, $BABAR$ detector needs to have([6]):

- The maximum possible acceptance in the center-of-mass frame. The beam asymmetry causes a forward boost of the decay products in the laboratory frame ($\beta\gamma \simeq 0.56$), which leads to choosing an asymmetric detector design.

- Excellent vertex resolution. The detector has to be able to distinguish the decay vertices of the two opposite B mesons in the $B\overline{B}$ event. The typical

25

separation of these vertices is $250\mu m$, which means that vertexing resolution of $\sim 60 - 80\mu m$ is required for reliable separation.

- Good tracking performance over the range $\sim 60 \ MeV \ < \ p_t \ < \ 4 \ GeV$.

- Discrimination between e, μ, π, K and ρ over a wide kinematic range. This discrimination is required for reliable tagging of the flavor of B-meson decays - important for many analyses. Analyses of decays such as $B \rightarrow \pi\pi$ and $B \rightarrow K$ depend on π/K separation for background subtraction etc.

- To detect photons and $\pi^0 s$ over the wide energy range $\sim 20 \ MeV \ < \ E \ < \ 5GeV$.

- To have neutral hadron detection capability.

A summary of design performance parameters can be found in Table 2.3.

Parameter	BaBar value
Coverage	0.92
σ_{p_t}/p_t (%) (1 GeV pions at 90°)	0.36
σ_{z_0} (μm) (1 GeV pions at 90°)	52
σ_E/E (%) (1 GeV γ at all angles)	1.8
γ efficiency within acceptance (at 100 MeV)	0.92

Table 2.3: Designed *BABAR* performance parameters.

26

27
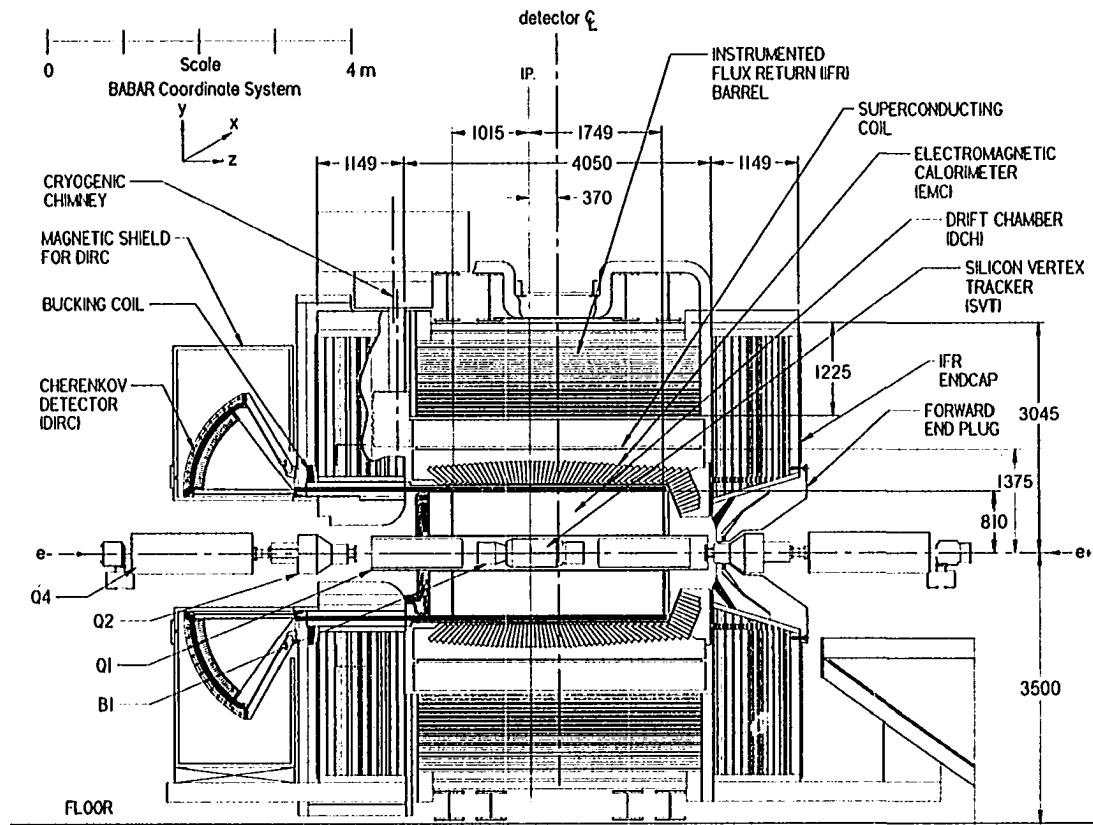
Figure 2.2: BaBar Detector design.

28
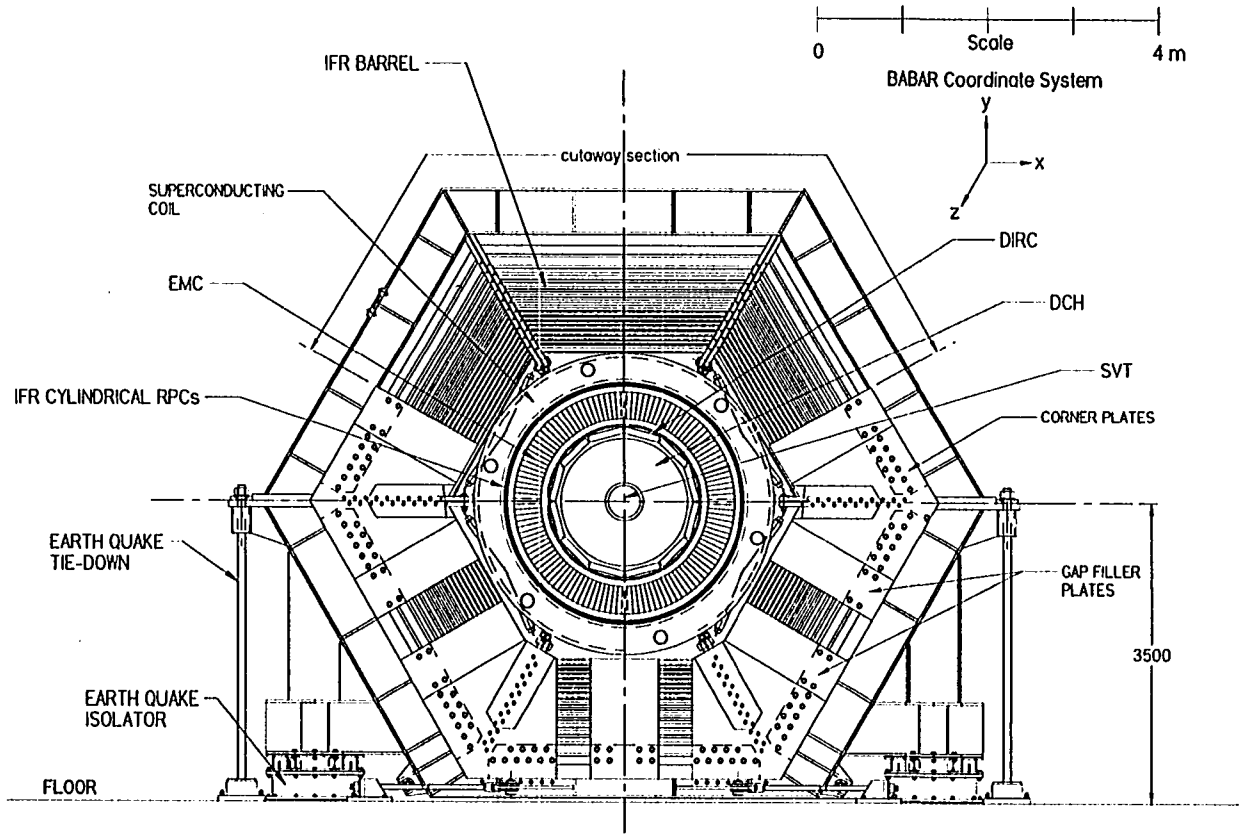
Figure 2.3: BaBar Detector - view from the back.

Electromagnetic Calorimeter

DIRC (Cerenkov)

Solenoid (1.5 T)

e^+(3.1 GeV)

e^- (9 GeV)

Drift Chamber

Silicon Vertex Tracker

Instrumented Flux Return
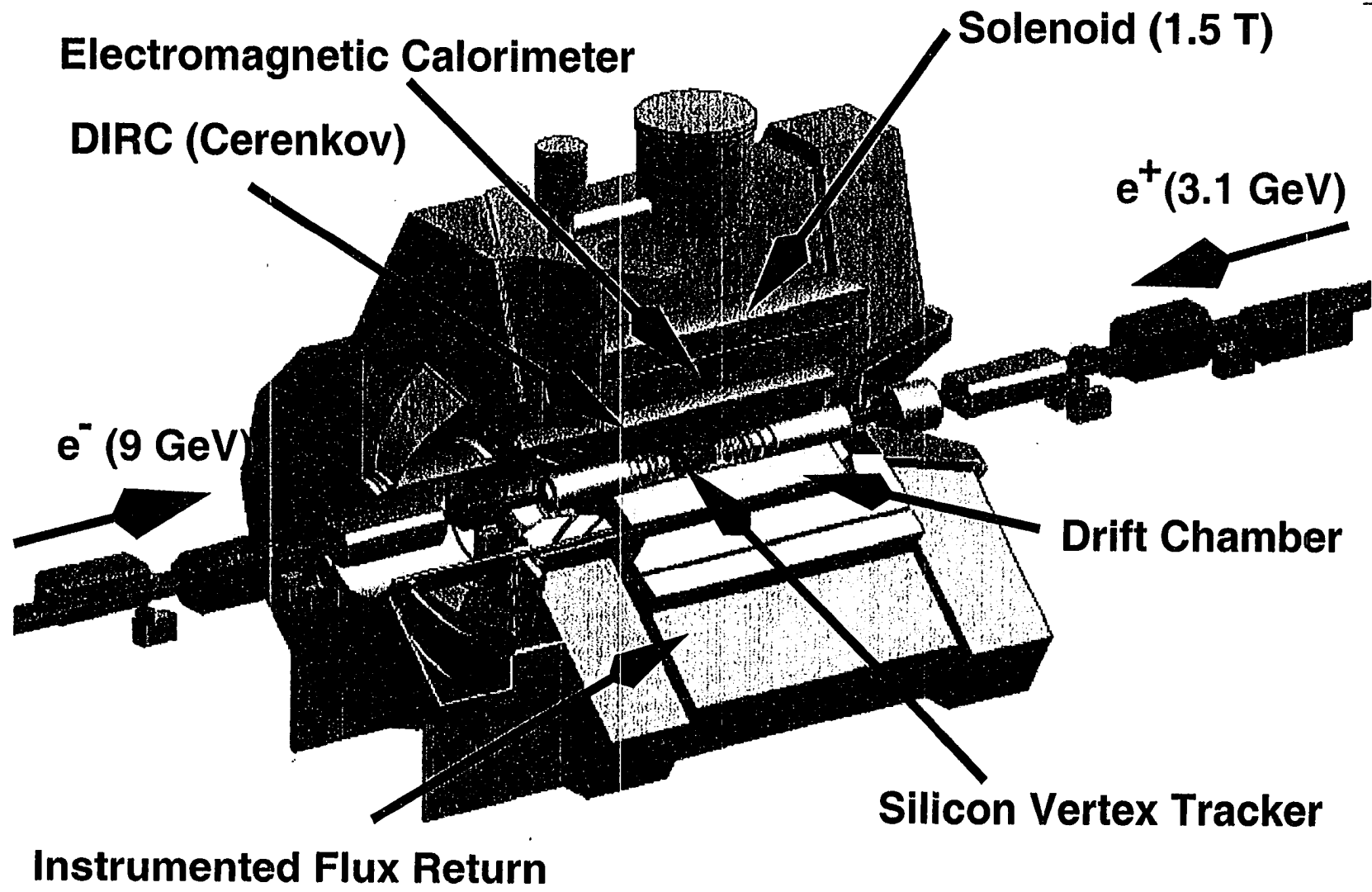
The *BABAR* detector was designed to meet all these requirements. A design of the detector is shown in Figures 2.2, 2.3. A schematic view of the detector is shown in Figures 2.4. It contains 6 major subsystems (three-letter acronyms (TLA) are listed after the name of each subsystem - we will be using them later in the text to refer to particular subsystem):

- 1. A Silicon Vertex Tracker (SVT) to provide precise position information on charged tracks and to track very low-energy charged particles.

- 2. A Drift Chamber (DCH) filled with a helium-based gas in order to minimize multiple coulomb scattering. This provides the main momentum measurement for charged particles and helps in particle ID through dE/dx measurement.

- 3. A Detector of Internally Reflected Cherenkov light (DRC or, more commonly, DIRC) for charged hadron particle ID.

- 4. A Caesium Iodide Calorimeter (EMC) for electron ID and neutral hadron ID.

- 5. A superconducting magnet to provide a 1.5 T magnetic field.

- 6. An Instrumented Flux Return (IFR) for muon ID down to about 0.6 GeV and neutral hadron ID.

The *BABAR* detector was commissioned in 1999 and recorded its first event on the 26th of May 1999.

2.2.1   The Silicon Vertex Tracker (SVT)

The Silicon Vertex Tracker is designed to provide precise position information on charged tracks and to track very low-energy charged particles. The physics principle behind silicon detectors is simple: a charged particle ionizes material of

the detector and the electric field between the sides of the detector pulls electrons and holes apart creating current. The primary design considerations for the SVT arose from the two sources: the physics goals of the experiment and the physical constraints imposed by the PEP-II interaction region design.

Physics Requirements

The CP-violating asymmetry is a function of the proper time difference (δt) between the two B decays, and vanishes in the integral over δt. The function of the vertex detector in the *BABAR* experiment is to determine the separation between the two B decay vertices, thus determining the time between decays $\delta t = \delta z / \beta \gamma c$. To avoid significant impact of the resolution on the CP asymmetry measurement, the mean vertex resolution along the z-axis for a fully reconstructed B decay must be better than 80 μm [11]. The required resolution in the x-y plane arises from the need to reconstruct final states in B decays as well as in τ and charm decays. To meet the corresponding requirements, the SVT needs to provide resolution of order $\sim 100 \mu m$ in the plane perpendicular to the beam line. To maintain the position resolution necessary to carry out physics analysis, relative positions of *individual* silicon sensors have to be stable over long time periods and a wide range of operating conditions. As a part of the *BABAR* tracking system, SVT also has to provide reliable tracking for the charged particles with transverse momentum less than 120 MeV/c, the minimum that can reliably be measured by the Drift Chamber alone.

PEP-II-imposed Constraints

The SVT is located inside the $\sim 4.5m$-long support tube that extends all the way through the center of the detector. To maximize the angular coverage in the asymmetric beam environment, the SVT must extend down to 20° in polar angle

31

from the beam line in the forward direction (in the backward direction, it is sufficient to extend the sensitive area only down to 30°). As the detector subsystem closest to the interaction point, the SVT must be able to withstand over 2Mrad of ionizing radiation. A radiation monitoring system capable of aborting beams in case of abnormally high backgrounds is required. Reliability and robustness of this detector subsystem are more critical than for any other subsystem - since it is located inside the support tube of the detector, the SVT is inaccessible during normal detector operations. The time needed for any replacement is 4-5 months. Hence, redundancies have to be built in the SVT whenever possible.

Design

A detailed description of the *BABAR* SVT can be found elsewhere [12]. The *BABAR* SVT is composed of 300 μm-thick double-sided silicon micro-strip detectors. The detectors are built on high-resistivity (6-15 kOhm · cm) n-type substrates with p^+ and n^+ strips implanted on both sides. The isolation of the strips on the n-side is achieved with individual p^+ implants (p-stops) surrounding each n^+ strip. The strips on the opposite sides of each sensor are oriented orthogonally to each other: the ϕ-measuring strips run parallel to the beam line and the z-measuring strips are oriented transversely to the beam axis. In order to achieve reasonable stand-alone tracking performance, 40 silicon strip modules are arranged into 5 layers of detecting plates: 6 modules in each of the first 3 layers, 16 modules in the fourth and 18 modules in the fifth layer. The motivation for the 5-layer configuration is as follows: 3 layers are necessary to calculate a track trajectory, 4 are needed to overconstrain the calculation and fifth layer provides reasonable redundancy level. The modules of the 3 inner layers are straight, while the modules for the 2 outer layers are arch-shaped to accommodate the angular acceptance requirements with minimal amount of material. The SVT design is

32

schematically shown in Figure 2.5.
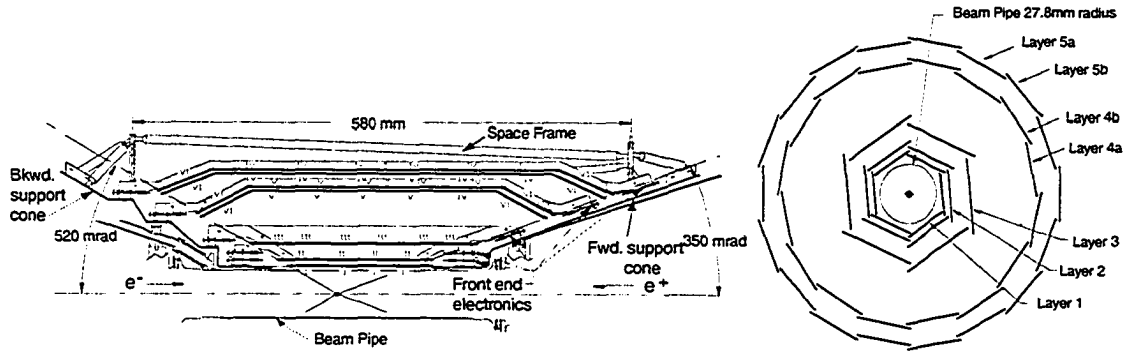
Figure 2.5: Design of the SVT detector

Electronics and Read-out System

The SVT design requires approximately 150,000 channels for data read-out. The actual number of micro-strips is higher because in outer layers 4 and 5, spatially separated z-strips are electrically connected in groups of two, reducing the number of channels. While decreasing the complexity of the SVT read-out system, this introduces an ambiguity in z coordinate detection which has to be resolved later using pattern-recognition software algorithms. In order to minimize the material in the acceptance region, the readout electronics is mounted entirely outside the active detector volume. Under normal operating conditions, the average SVT occupancy in a time window of $1\mu s$ is about 3% for the inner layers and less than 1% for the outer layers.

Performance

The BABAR Silicon Vertex Tracker has been performing close to its design expectations. Figure 2.6 shows SVT hit reconstruction efficiency as measured on $\mu\mu$ events, while Figure 2.7 shows hit resolutions in z and ϕ coordinates. The summary of achieved performance and design goals is presented in Table 2.4.

33
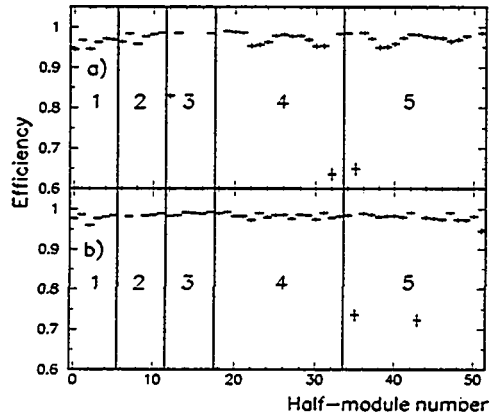
Figure 2.6: hit reconstruction efficiency of the SVT detector.
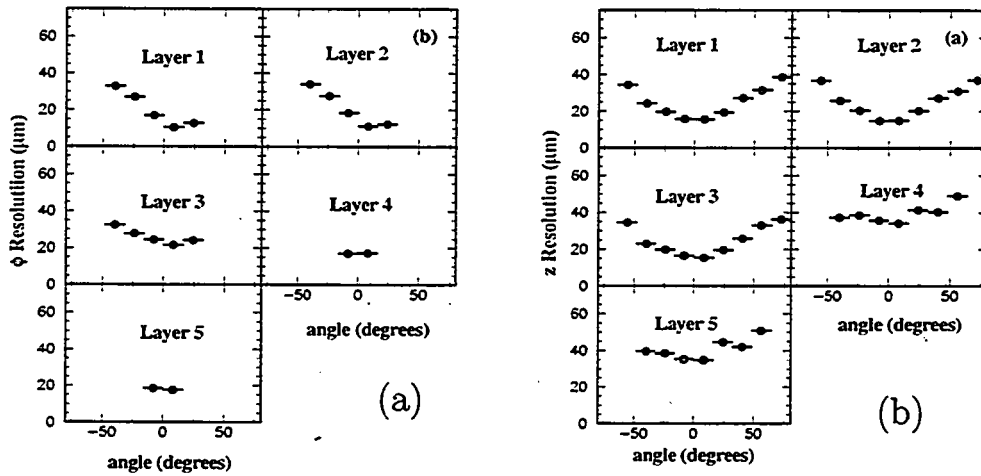
Figure 2.7: Resolution of the SVT detector; (a) - z resolution, (b) - ϕ.

34

Parameters	Design	Achieved (typical)
ϕ resolution, μm	80	< 40
z resolution, μm	80	< 50

Table 2.4: Comparison of the design and achieved performance for the *BABAR* SVT detector

2.2.2   The Drift Chamber (DCH)

The principal purpose of the drift chamber is the efficient detection of charged particles and the measurement of their momenta and angles with high precision. The DCH complements the tracking and position information from Silicon Vertex Tracker for optimal tracking and position resolution performance.

Physics Requirements

High precision measurements of particle momenta and positions are required for most of the physics tasks of *BABAR* experiment. They enable the effective reconstruction of exclusive B- and D-meson decays with minimal background as well as reconstruction of decays and interaction vertices outside of the SVT. For low momentum particles, the DCH is also required to provide particle identification by measurement of ionization loss (dE/dx). A resolution of about 7% will allow π/K separation up to 700 MeV/c and, in the extreme forward and backward directions, the DCH is the only detector subsystem that can provide discrimination of particles of different mass. Angular acceptance of the Drift Chamber has to be close to that of the SVT, which is determined by the overall detector acceptance goals. Due to the relatively low energy of the tracks from B- and D-meson decays, multiple scattering in the material of the DCH is largely responsible for the limitations on momentum and position resolutions. Therefore, the amount of

35

material in front of the first DCH layer as well as throughout the DCH volume has to be minimized. These physics requirements result in the stringent set of design parameters which are presented in the Table 2.5, column 2.

Gas System

In order to minimize the amount of material inside the DCH, a lightweight Helium-Isobutane (80:20) gas mixture has been selected. As a result, the combined radiation length for wires and 5.2 m^3 of gas inside the Chamber is as low as $0.2\% X_0$.

Mechanical Design

The *BABAR* Drift Chamber is a 280 cm long cylinder with an inner radius of 23.6 cm and the outer radius of 80.9 cm. The inner cylinder was built to minimize the amount of material in front of the first active DCH element. 1mm-thick berillium was chosen as the material for the inner cylinder while outer cylinder was made up of two carbon fiber layers on a Normex core. Corresponding radiation lengths (X_0) are 0.28% for the inner cylinder and 1.5% for the outer cylinder. The DCH endplates are made of aluminum. The backward endplate is 24mm thick while the forward endplate is 12mm in the region covered by the Electromagnetic Calorimeter (24mm in other regions), reflecting the requirement of low amount of material between DCH forward endplate and forward endcap of the Electromagnetic Calorimeter. Due to the asymmetry in the beam energies, the device is asymmetrically located with respect to the Interaction Point. The forward length of 1749mm is chosen to enable charged particles emitted at angles as low as 17.2^o to traverse at least half of the DCH layers. In the backward direction, the corresponding angle is chosen to be 152° (28° from the beam). The DCH design is schematically shown on the Figure 2.8, (a).

36

The Chamber itself is composed of 40 layers of 7104 hexagonal drift cells with a typical dimension of 1.2x1.9 cm^2, organized into 10 Axial (A) and Stereo (U, V) superlayers with 4 layers in each superlayer. These 10 superlayers are then set up in the A-U-V-A-U-V-A-U-V-A configuration (figure 2.8, (b)). For the stereo superlayers, the stereo angle varies from 40mr in the innermost layer to 70mr in the outermost layer. The individual drift cell is constructed of 6 (5 for the outer cells of each superlayer) $120\mu m$ gold-plated aluminum field wires and a $20\mu m$ gold-plated tungsten-rhenium wire. The outer cells of each superlayer also have 2 $80\mu m$ gold-plated aluminum guard wires on the outer side. Also, at the innermost boundary of layer 1 and the outermost boundary of layer 40, two $120\mu m$ gold-plated aluminum clearing wires were added per cell to collect charges created through photon conversions in the material of the support cylinders. During the operations, a potential of 1900-1960V is applied to each sense wire which, together with grounded field wires, creates the electric field in each cell (Figure 2.8, (c)). Guard wires are subject to the potential of 340 volts while 825 volts is applied to clearing wires.

Electronics and Read-out System

The DCH electronic system is designed to provide a measurement of the drift time and integrated charge, as well as a single bit to the trigger system for every wire with a signal. The small cell size, difficult access through the DIRC support tube and the requirement that no additional material has to be introduced between the DCH forward endplate and forward Calorimeter endcap result in very high density of electronic components. A compact and highly modular design has been chosen - the DCH amplifier and digitizer electronics are installed in so-called Front-End Assemblies (FEAs) that are mounted directly onto the rear endplate. The FEAs are organized into 16 sectors (wedges) with three FEA modules in each sector.

37
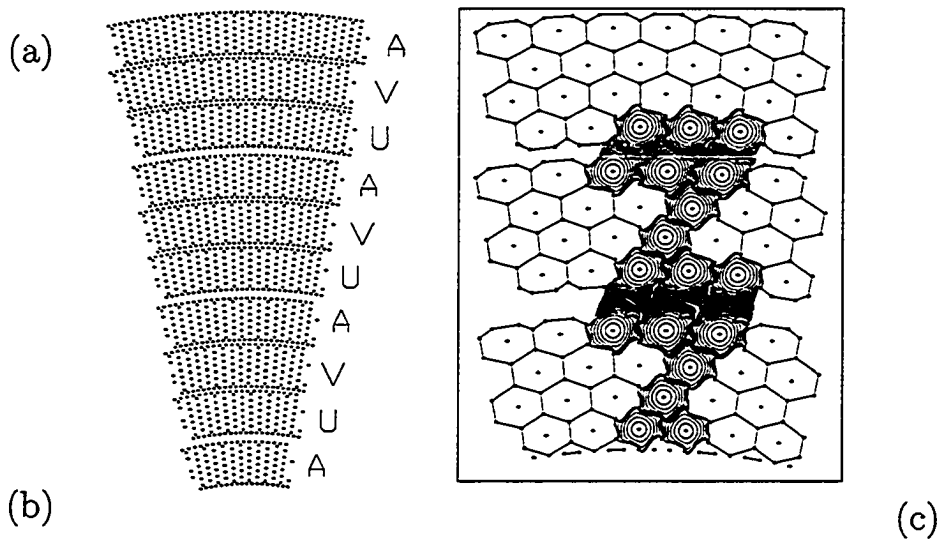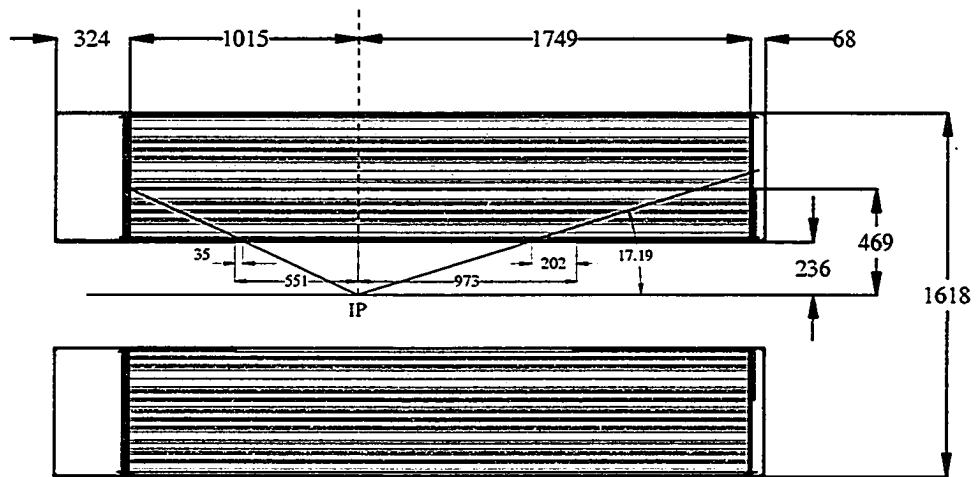
Figure 2.8: Design of the Drift Chamber detector; (a) - design side view, (b) - layer arrangement (one wedge is shown), (c) - cell configuration and maps of the electric field inside the cells.

The assemblies connect to the sense wires through service boards, which route the signals and High Voltage (HV) distribution. The data from the FEAs is, in turn, routed to high-speed optical fibers for transfer to the readout modules that are located outside of the detector building. The *BABAR* readout system consists of four Read-Out Modules (ROMs). These ROMs deploy drift chamber-specific feature extraction algorithms to convert raw information from FEAs into drift times, total charge and a status word. These values are then corrected for time offsets, pedestal bias and gain constants on a channel-by-channel basis. The involved processing takes about $1\mu s$ per channel and reduces the amount of data by a factor of four. The front-end electronics is calibrated daily to determine the channel-by-channel correction constants and thresholds.

Performance

The *BABAR* Drift Chamber has been performing close to its design expectations. Figure 2.9 shows the DCH track reconstruction efficiency, while Figure 2.10 shows dE/dx as a function of track momentum. As shown, clear $K - \pi - p$ separation is possible for tracks below 700 MeV/c using only Drift Chamber information. The summary of achieved performance and design goals is presented in the Table 2.5.

Parameters	Design	Achieved (typical)
x-y resolution, mm	0.14	0.1-0.4
z resolution, mm	1	1
dE/dx resolution, %	7	7.5

Table 2.5: Comparison of design and achieved performances for the *BABAR* DCH detector
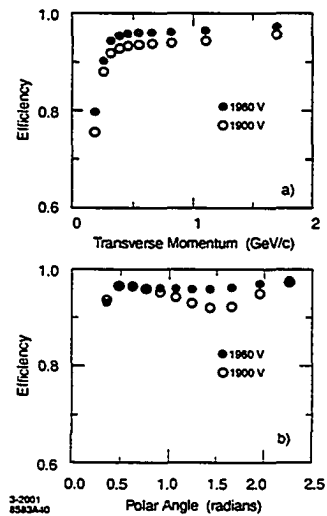
Figure 2.9: DCH track reconstruction efficiency.
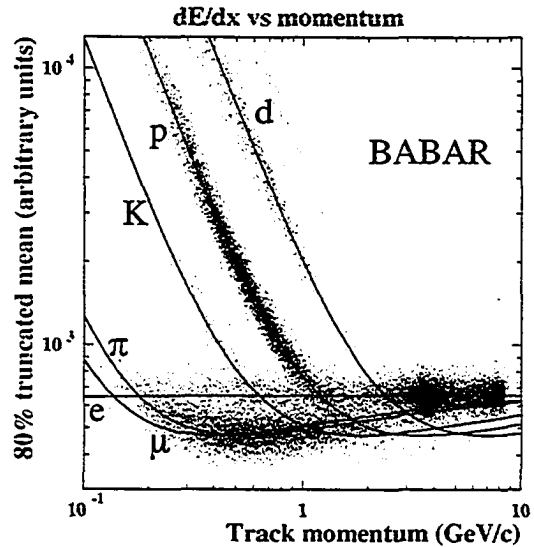
Figure 2.10: dE/dx measurement as a function of track momentum in the DCH detector.

2.2.3 The Tracking System

The Silicon Vertex Tracker along with the Drift Chamber compose the *BABAR* tracking system. Using the information mainly from these two devices, *BABAR* tracking reconstruction software extracts information about physical parameters of the charged particles traversing the detector. Overall performance of the entire *BABAR* tracking system with comparison to the design parameters is found in Table 2.6.

2.2.4 The DIRC

The principal purpose of the DIRC is to provide pion-kaon separation in the high-momentum region (above 700MeV/c, where Drift Chamber dE/dx separation power disappears).

40

Parameters	Design	Achieved (typical)
r (in x-y plane) resolution, μm	80	25
z resolution, μm	80	40
$tan(\theta)$ resolution, 10^{-3}	0.8	0.6
σ_{p_t}/p_t, constant term, %	0.36	0.45
σ_{p_t}/p_t, linear term, %/[GeV/c] (for $p_t > 1.0 GeV/c$)	0.3	0.13

Table 2.6: Comparison of design and achieved performances for BABAR tracking system. Achieved resolutions are given for the tracks with $p_t = 3 GeV/c$.

Physics Requirements

Excellent particle identification is of utmost importance for a systematic study of CP violation and B physics. In particular, Kaon/Pion separation is essential for many physics analyses in BABAR including study of the rare B-meson decay modes such as $B^0 \rightarrow \pi^+\pi^-$ and $B^0 \rightarrow K^{\pm}\pi^{\mp}$. This is accomplished by the Detector of Internally Reflected Cherenkov Radiation (DIRC), which uses the Cherenkov radiation emitted by charged particles traversing the material of the detector. The primary purpose of the detector is to provide pion-kaon separation for momenta of up to 4.0 GeV/c. Separation below 700 MeV/c relies mostly on dE/dx measurements from the DCH.

Design

A detailed description of the BABAR DIRC can be found elsewhere [12]. The DIRC is based on the principle that the magnitude of light incidence angles is maintained upon reflection from a flat surface. The radiator material of the DIRC is synthetic, fused silica in the form of long, thin bars with rectangular

41

cross-section. These bars serve both as radiators and as light pipes for the portion of the light trapped in the radiator by total internal reflection. To avoid placing photon detectors on both ends of the bar, a mirror is placed on the forward end, perpendicular to the axis. Once the photons arrive at the backward end, they enter a special water-filled expansion region, called the *standoff box*. The schematic view of the Cherenkov photon path is shown in Figure 2.11. The photons are detected by an array of densely packed photomultiplier tubes (PMTs), each surrounded by reflecting *catch cones* to capture light which would otherwise be lost in between the active region of PMTs. Overall, the DIRC is made up of 144 synthetic fused silica quartz bars which are 1.7cm thick, 3.5cm wide and 4.9m long. The quartz bars have an index of refraction of $n = 1.474$. The standoff box contains $6m^3$ of purified water. The amount of material present in DIRC amounts to approximately 14% of radiation length for a particle of normal incidence. Radially, it occupies only 8cm of space. Angular coverage of the DIRC is $\sim 87\%$ of the solid polar angle in $\Upsilon(4S)$ rest frame. The 144 bars are arranged into 12 modules. Due to the gaps between the sides of the resulting polygon, the azimuthal coverage is limited to 93%. The Cherenkov light is detected by an array of 10752 PMTs each with a diameter of 2.9cm. The PMTs operate at a voltage of 1.1kV with a maximum current per PMT of about $150\mu A$. The DIRC design is shown in Figure 2.12.

Electronics and Read-out System

The DIRC is essentially a three-dimensional imaging device capturing 2D light incidence position together with its time of arrival that is required to extract the necessary information. The DIRC front-end electronics (FEE) is designed to measure the arrival time to an accuracy limited by the intrinsic 1.5ns time spread of the PMTs. The FEE is mounted on the outside of the standoff box

42
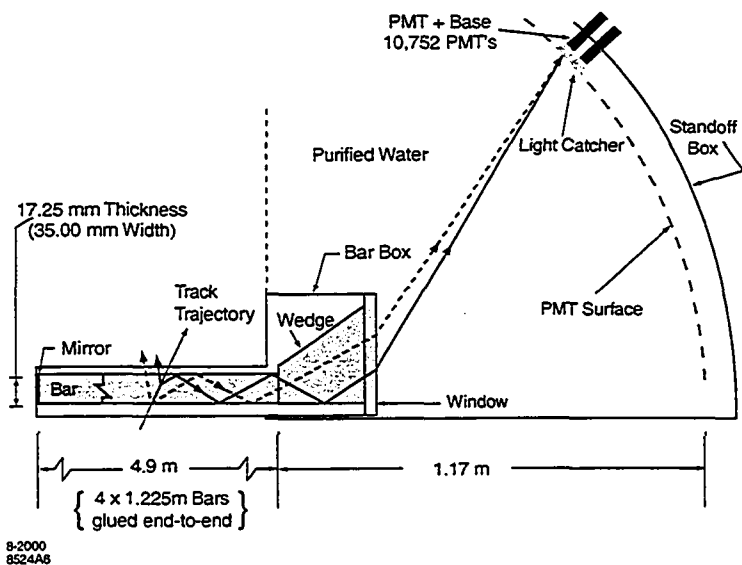
Figure 2.11: Photon pach in the *BABAR* DIRC detector
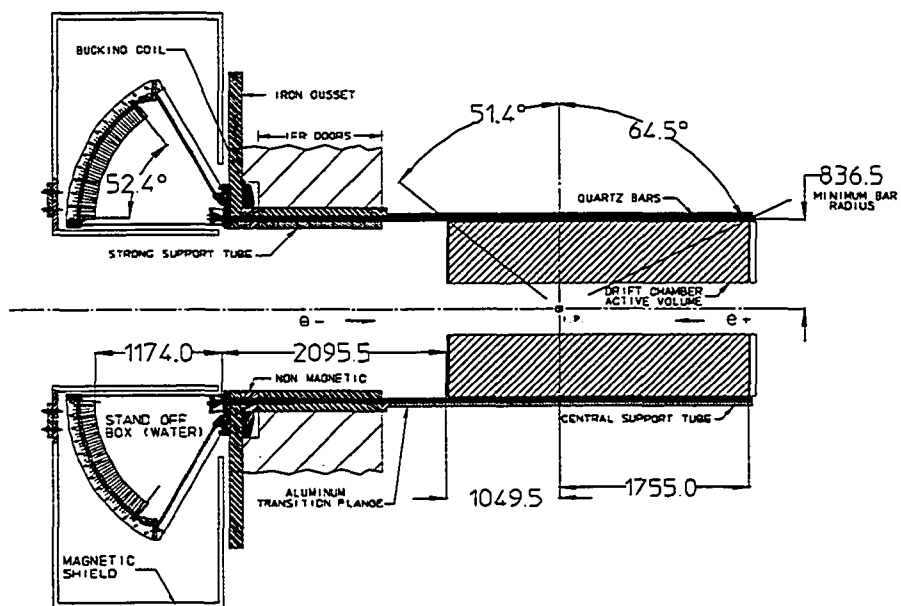
Figure 2.12: Design of the DIRC detector

43

and is highly integrated in order to minimize cable lengths and to retain the required single photoelectron sensitivity. Each of the 168 DIRC Front-End Boards processes signals from 64 PMTs. The data is further transmitted to 12 DIRC Crate controllers which send the information to six Read-Out Modules (ROMs) via 1.2 Gbit/s optical fibers. The ROMs translate raw data into the physical parameters of the detected particle, thereby reducing the data volume by 50%.

Performance

The *BABAR* Detector of Internally Reflected Cherenkov light has met its performance requirements. Figure 2.14 shows kaon identification efficiency and pion mis-ID, while Figure 2.13 shows the expected $\pi - K$ separation and the Cherenkov angle and time resolution of the DIRC system. The summary of achieved performance and design goals is presented in the Table 2.7.
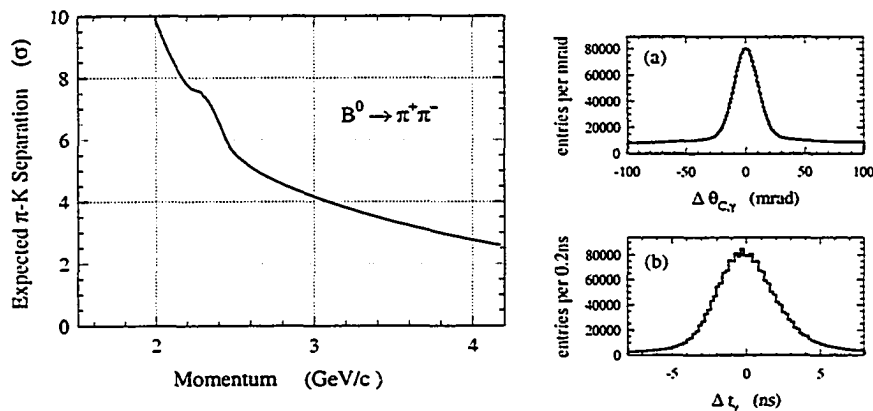
Figure 2.13: Expected $\pi - K$ separation and Cherenkov angle and time resolution of the DIRC detector.

2.2.5 The Electromagnetic Calorimeter (EMC)

The principal purpose of the EMC is reliable detection of electrons and photons from π^0 and η decays as well as from electromagnetic and radiative processes.

44
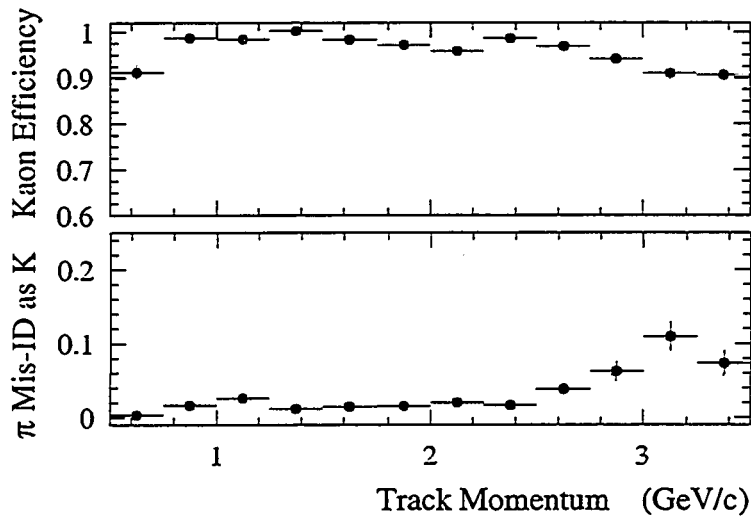
Figure 2.14: Kaon identification efficiency and pion mis-ID of the DIRC detector.

Parameters	Design	Achieved (typical)
π/K separation, 1.7-4.2 GeV/c	4σ	4.2σ (at 3 GeV/c)
	4σ	$> 10\sigma$ (at 1.7 GeV/c)
	4σ	2.8σ (at 4.2 GeV/c)
track angular resolution, mrad	2.2	2.5
mean kaon selection efficiency, %	95	96.2
mean pion misidentification as kaon, %	3	2.1

Table 2.7: Comparison of the design and achieved performance for the *BABAR* DIRC detector

45

Physics Requirements

As a large number of B-meson decay products contain a π^0 which in 99.9% of the cases decays into two photons, a calorimeter with very good energy resolution is required. The BABAR calorimeter was designed to have resolution given by the sum of two empirical contributions added in quadrature:

$$\frac{\sigma_E}{E} = \frac{\sigma_1}{\sqrt[4]{E}} \oplus \sigma_2, \%$$

where $\sigma_1 \approx 1\%$ and $\sigma_1 \approx 1.2\%$ for photons incident at a polar angle of 90°. The energy dependent term arises mostly from fluctuations in the photon statistics and is also impacted by electronic noise. This term is dominant at low energies. The constant term is due to the front and rear leakage from the crystals, inter-calibration errors and non-uniformity of light collection. This term is dominant at high energies. The angular resolution for photons incident at the polar angle of 90° is given by:

$$\sigma_{\theta, \phi} = \frac{3mr}{\sqrt{E(GeV)}} + 1mr$$

The minimum detectable energy for photons is in the range of 10-20 MeV.

Design

A detailed description of the BABAR EMC can be found elsewhere [12]. The EMC consists of 6580 thallium-doped CsI crystals organized into a cylindrical barrel and a conical forward endcap. The angular coverage is from 15.8^o to 141.8^o in polar angle and full in azimuth, representing 90% coverage in the $\Upsilon(4S)$ center of mass frame. The inner radius of the barrel is 90 cm and the outer radius is 136 cm. Individual crystals have length from 29.6 cm to 32.4 cm with a front face dimension of about 5 cm. The sensitivity of the individual crystals has a mean of 7300 and RMS of 890 photoelectrons per MeV. The total amount of the EMC material varies from $16X_0$ to $17.5X_0$ depending on the polar angle of incidence.

46

The amount of material in front of the active elements has been reduced to a minimum of $0.25X_0$ at normal incidence in the barrel region and $0.20X_0$ for the endcap. The EMC design is schematically shown in Figure 2.15.
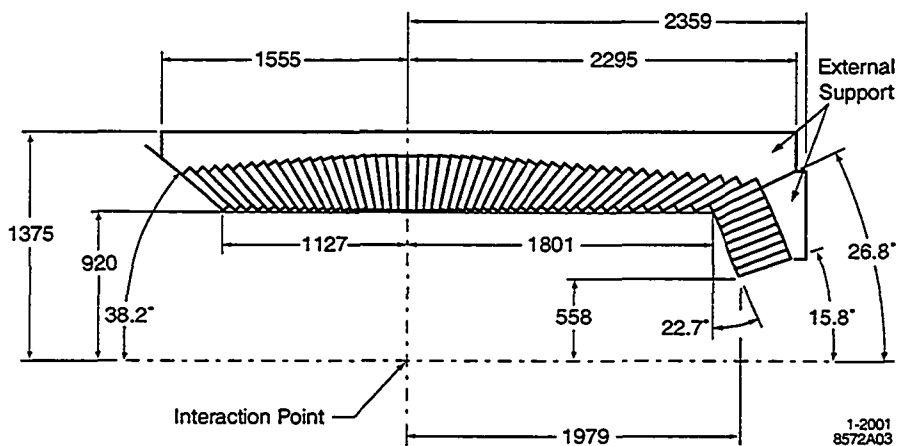
Figure 2.15: Design of the EMC detector

Electronics and Read-out System

The EMC electronics system is required to have a negligible impact on the energy resolution. This requirement limits the maximum allowed equivalent noise energy per crystal to 250 keV. This is achieved by deploying a highly efficient photon detector and a low-noise electronic readout. The PIN silicon photodiodes used have an efficiency of 85% for the CsI scintillation output. Two sets of photodiodes and low-noise pre-amplifiers are used for each crystal to provide necessary redundancy for inaccessible components. The dual signals are combined in postamplification-digitization boards installed in the accessible location.

Performance

The BABAR Electromagnetic Calorimeter has met its performance requirements. Figure 2.2.5 shows electron identification efficiency and pion mis-ID achieved

47

with the EMC inputs, while Figure 2.16 shows EMC energy resolution derived from multiple processes. A summary of achieved performance and design goals is presented in the Table 2.8.

The EMC is responsible for the most of the input to the *BABAR* electron identification algorithms. Electrons are separated from charged hadrons using the information on the shower energy, lateral momentum of the shower and track momentum. In addition, the dE/dx energy loss in the DCH and Cherenkov angle in the DIRC are required to be consistent with the hypothesis of an electron. The most important variable in the electron identification is the ratio E/p of the energy deposited by the track in the calorimeter to the momentum of the track. Figure 2.2.5 shows the achieved electron ID efficiency.

Parameters	Design	Achieved (typical)
σ_E/E, constant term, %	1-2	1.85 ± 0.12
σ_E/E, energy-dependant term, %	1-2	2.3 ± 0.3
σ_ϕ, constant term, mrad	1	0.00 ± 0.04
σ_ϕ, energy-dependant term, mrad	3	3.87 ± 0.07
lower energy threshold, MeV	20	10-20

Table 2.8: Comparison of the design and achieved performance for the *BABAR* EMC detector

2.2.6 The Instrumented Flux Return (IFR)

The principal purpose of the IFR is muon identification and detection of neutral hadrons (primarily K_L^0 and neutrons) over a wide range of momenta and angles.

(a)

σ_E / E

0.06
0.04
0.02

• π⁰ → γγ
▲ Bhabhas
○ χ_c → J/ψ γ
-- MonteCarlo

0.02

10⁻¹   1.0   10.0

3-2001
8583A41

Photon Energy (GeV)

(b)

σ_0 (mrad)

12
8
4
0

• π⁰ → γγ
--MonteCarlo

0   1   2   3

3-2001
8583A42

Photon Energy (GeV)
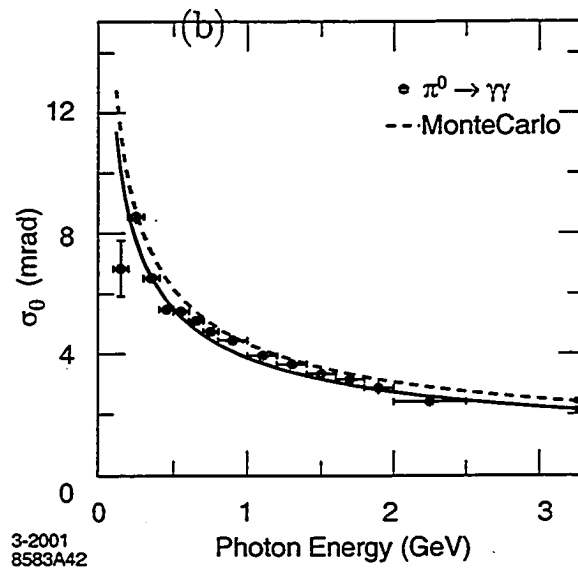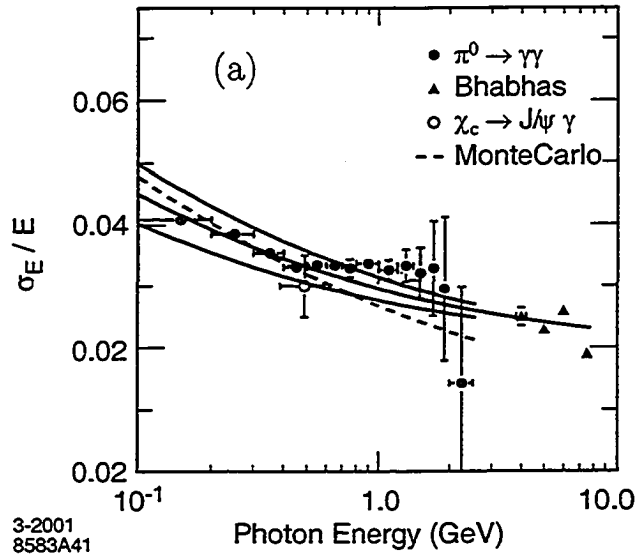
Figure 2.16: Energy (a) and Angular (b) resolution of the EMC detector.

49
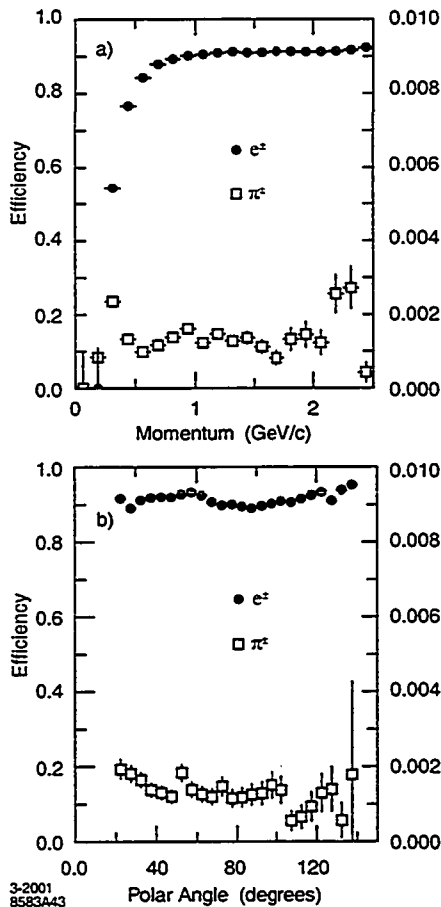
Figure 2.17: Electron ID efficiency and pion mis-identification rates achieved with the *BABAR* EMC. Efficiency and mis-ID rates are measured using radiative Bhabhas and $e^+e^- \rightarrow e^+e^-e^+e^-$ events. Pion mis-identification probabilities are measured using charged pions from K_S^0 decays and three-prong τ decays. Typical value for the efficiency is 95% for the "tight" selector (90% for the "very tight"), while pion mis-ID rate is 0.3% (0.1%). (a) - dependency of the efficiency on P_{LAB}, (b) - on polar angle θ.

50

Physics Requirements

Muon identification is rather important for the physics goals of the *BABAR* detector. It is crucial in the study of semileptonic *B*-meson decays as well as in the studies of vector mesons like J/ψ and studies of rare decays involving leptons from B and D mesons and τ leptons. Neutral hadron detection, especially K_L^0 allows the study of exclusive B decays in CP eigenstates. Overall, the primary physics requirements for the IFR are large angular coverage, good efficiency and reliable muon identification down to momenta of less than 1 GeV/c.

Design

A detailed description of the *BABAR* IFR can be found elsewhere [12]. To provide a good $\mu - \pi$ separation, the IFR has to contain a large amount of material to absorb all highly interacting hadron particles while affecting the muon propagation to a much less degree. The material (steel) of the IFR absorber is also used as a flux return for the *BABAR* magnet. Single gap resistive plate chambers (RPCs) with two-coordinate readouts have been chosen as active detectors for the IFR. The RPCs are operated at a voltage of $\sim 8kV$ in a limited streamer mode and the signals are read via capacitive readout strips. The readout strip pitch is varying from 38 to 38.5 mm for z- and ϕ strips. A non-flammable gas mixture of 56.7% Ar, 38.8% freon 134a and 4.5% isobutane fills the chambers at an absolute pressure of 1500-1600 Torr. A schematic view of the individual RPC is shown on the figure 2.19. The RPCs are installed in the gaps of finely segmented steel of the barrel and the end doors of the flux return. The steel is segmented into 18 layers with thickness varying from 2cm for the 9 innermost layers to 10cm for the rest of the system. The gap between the steel plates varies from 3.2cm to 3.5cm. 17 layers of RPCs are placed into the gaps and two layers are placed on the boundaries of the steel system. A total of 806 RPC modules

51

compose the active area of $\sim 2000m^2$. The IFR design is schematically shown in Figure 2.18.
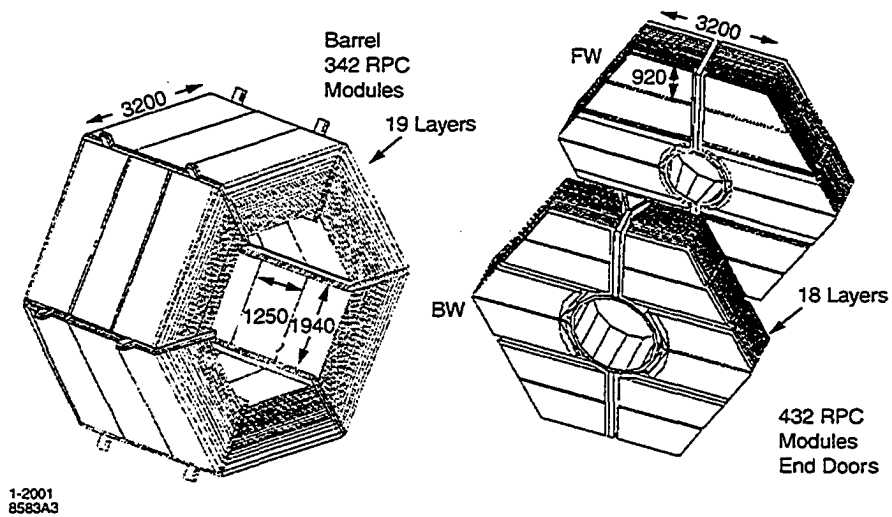
Figure 2.18: Design of the IFR detector
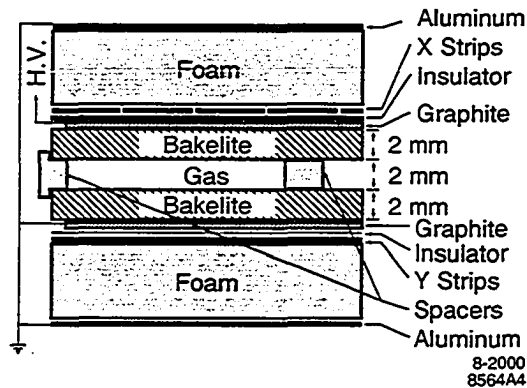
Figure 2.19: RPC design

Electronics and Read-out System

52,800 IFR readout channels are connected to the Front-End Cards (FECs), each serving 16 channels. The FECs shape and discriminate the input signals and set a bit for each strip with a signal above a certain theshold. Signals from the

52

FECs are further transmitted to eight custom IFR front-end crates that extract hit timing information from the raw data, synchronize it with external clock and transmit the resulting packages to the IFR readout modules (ROMs).

Performance

The *BABAR* Instrumented Flux Return initally met its performance requirements. Figure 2.20 shows muon identification efficiency and pion mis-identification rates based on the IFR inputs. However, during the first year of operation, inadequate cooling of the RPCs has resulted in the severe performance degradation in parts of the detector. This effect has since been linked to the instability of the linseed oil coating on the bakelite surface of the RPC plates. A special IFR Improvement task force has been established in order to suggest the solution to this problem. Several design types are currently under investigation.

2.2.7   The Trigger

The principal purpose of the *BABAR* trigger is the selection of the events of interest in terms of *BABAR* physics goals. It has to have high, stable and well-understood efficiency for such events while rejecting a large portion of the background to keep the event rate below 120 Hz, to be compatible with the throughput capacity of the *BABAR* Data Acquisition System.

Physics Requirements

The total trigger efficiency is required to exceed 99% for all $B\overline{B}$ events and to be at least 95% for continuum events. Requirements on the efficiency for the other event types such as $\tau^+\tau^-$ vary from 90% to 95% depending on the specific channel. The system must be able to operate under extreme background conditions while contributing no more than 1% to the total *BABAR* deadtime.

53
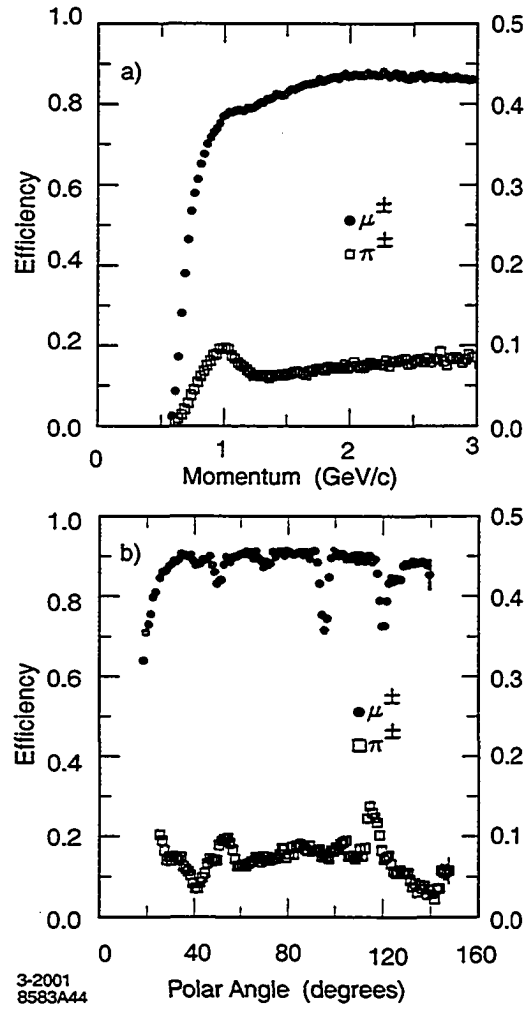
Figure 2.20: Muon efficiency and pion mis-ID rates of the IFR detector. (a) - dependency of the efficiency on P_{LAB}, (b) - on polar angle θ.

54

Design

The *BABAR* Trigger system is implemented as a two-level hierarchy, the Level 1 (L1) hardware trigger and the Level 3 (L3) software trigger. It is designed to accommodate up to 10 times the projected PEP-II background levels and to slowly and predictably deteriorate above that. Both trigger levels rely on the information from various detector subsystems described above. The L1 trigger uses information from 3 subsystems - DCH, EMC and IFR. The L1 system is therefore composed of three modules, each running subsystem-specific trigger processors: the Drift Chamber Trigger (DCT), the IFR trigger (IFT) and the electromagnetic calorimeter trigger (EMT). Each of the trigger processors generates trigger *primitives* - summary data on the position and energy of the particles. The DCT accepts tracks based on short or long track length and high p_t primitives, the EMT requires at least two clusters in the EMC with an energy deposit greater than 120 MeV. The IFT is used for triggering $\mu^+\mu^-$ and cosmic rays, mostly for diagnostic purposes. All three trigger processors send their data to the Global Trigger (GLT). The GLT processes all trigger inputs to form specific triggers, sending them to the Fast Control and Timing System (FCTS). The FCTS can be programmed to mask or prescale any of these specific triggers. If the valid trigger remains, the L1 Accept signal is issued to initiate L3 trigger processing. L3 operates by refining and augmenting the selection methods used in L1. The entire event information along with L1 trigger decisions are available to L3 processors. The L3 trigger is a software trigger designed to accomodate any event selection mechanism. The resulting processing algorithm has three phases. In the first phase, L3 input lines are formed by performing logical OR on any number of input bits from FCTS. In the second phase, the active (in logical 1 state) L3 input lines initiate execution of the independent trigger scripts which can use any information from the detector and L1 trigger to make a decision. In the

55

phase three, the outputs of these scripts are combined to produce an overall L3 Accept signal which initiates an event readout. A detailed description of the BABAR Trigger can be found elsewhere [12].

Performance

The BABAR Trigger System has met its performance requirements. The triggering efficiency for $B\overline{B}$ events is above 99.9% while the efficiency for the other event types of interest is above 92%. At a luminosity of $2.6 \times 10^{33} cm^{-2} s^{-1}$, the desired physics event acceptance runs at 16Hz representing 13% of all events accepted by L3 trigger. Another 40% is composed of diagnostic and calibration samples. Backgrounds represent the remaining 47% of the L3 accepts. A summary of achieved performance and design goals is presented in the Table 2.9. The configuration of a typical event accepted by the trigger system, along with some underlying trigger information, is shown in Figure 2.21.

Parameters	Design	Achieved (typical)
trigger efficiency, $B\overline{B}$ event , %	99	99.9
trigger efficiency, continuum event, %	95	>95.8
trigger efficiency, other event types, %	90	>92

Table 2.9: Comparison of the design and achieved performance for BABAR Trigger subsystem

atchouvi

Figure 2.21: An L3 event display. The small circles and small crosses in the DCH volume are DCH hits and Track Segment Finder (TSF) hit wires, respectively. The filled EMC crystals represent energy deposits in the calorimeter (fully filled crystal = 2 GeV). Small black triangles just in front of the calorimeter crystals show the location of the cluster centroids.

57

Chapter 3

B_AB_{AR} Computing

The PEP-II/*BABAR* B-factory produces over 10 gigabytes of event data each day. Each of the ~100,000 daily events have to undergo complicated tracking reconstruction processing. All these data are written to disks and then used in physics analysis by 10's of analysis groups. To control this very complicated data taking system as well as to provide the collaboration with analysis support tools, a sophisticated computing system has been designed and implemented. The *BABAR* Computing system includes the following elements:

- **Online** - currently encompasses detector control and monitoring, the upper levels of the data path, and various kinds of run control and partitioning

- **Offline** - organized into four areas: Reconstruction, Simulation, Databases and Code Releases

- **Software Environment** in which the computing work is done (including code development/management, user concerns, distributed computing issues etc.)

3.1 _BABAR_ Online Databases

Online databases are used to store all the information needed for effective operation of the BABAR detector. The BABAR online databases make use of Objectivity/DB [13], a commercial Object Oriented database engine with C++ language interface, as the underlying storage technology. Three types of online databases exist in BABAR :

- **Ambient Database.** It stores the readback values from the detector controls. Measurements are time-stamped and are used in online monitoring and offline analysis.

- **Conditions Database.** A special database used to track detector alignments, calibration constants, and other time-dependent records of the conditions under which the physics events are taken.

- **Configuration Database.** It is a BABAR unique feature to store all detector configuration data in a special database based on the commercial object-oriented product. This data is organized into configuration trees, each corresponding to the particular run type. Such a design has numerous benefits over plain-text configuration files:

    - Intuitive representation of the detector

    - Easy update tracking and backups

    - Improved security and data management

    There are configuration databases for each of the online subsystems. The configuration data are encapsulated in the configuration objects. Every stored configuration object has an identity - a quadruplet of the following entities:

59

— database name (susbsystem name, lower-case TLA, e.g. dch, svt etc.)

— class name of the object (e.g. "BdbConfigField")

— secondary key, which is an arbitrary string used to distiguish different configuration objects of the same class (can be empty)

— configuration key, which is a 32-bit integer number

Objects with the same class name and secondary key are stored in one "container". Every time a new object is created in the container, it is assigned a configuration key. Configuration keys of the objects in the same container are different. Configuration objects are never deleted or modified, thus guaranteeing that it will be possible to reconstruct the entire data-taking system configuration for any given point of time in the past. Configuration maps are used to organize the configuration objects into tree-like structures. Each subsystem has a set of maps which are stored in the subsystem's configuration database. Maps are also configuration objects - they are assigned configuration keys and are stored in the "Map Containers". The maps have named links to other objects. Following these links, one can navigate from the top-level map down to the basic objects. There is a special database with the name "top" which contains top-level maps referring to the subsystem maps. The top-level subsystem maps are roots of the configuration trees. They have the links named after each subsystem pointing to the subsystem's configuration maps. The top-level maps are instances of the special "BdbConfigTopMap" class and have no secondary key. Since the top-level configuration maps are used to root the particular configurations of the data-taking system, it is necessary to provide a convenient humanly readable naming infrastructure. The special objects - Alias Maps - have been designed for this. An alias map defines the type of

60

the run and is stored in the corresponding subsystem database. The subsystem's alias maps can have links to the top alias maps. Top alias maps define the type of run for the entire detector and have meaningful names such as "PHYSICS" for physics data taking, "COSMIC" for taking cosmic ray data to calibrate the detector, etc.

3.1.1 Configuration Browser

The structure and data handling policies of the configuration database described above result in a very large and constantly growing number of configuration objects. In order to effectively navigate and manage these configuration data, I developed a special software package, "BdbConfigBrowser". It provides an easy-to-use graphical interface to the underlying database structures enabling fast and efficient configuration updates. The software was developed in C++ within *BABAR* software release system. It uses the API from several core database packages to connect to the configuration database and to facilitate various transactions. A user-friendly interface has been developed using the Xmotif system of graphics libraries designed for Unix workstations.

A set of design requirements was created based on the input from the potential users of software:

- Application should be easy to use for any *BABAR* detector subsystem expert. Simple and efficient navigation is crucial

- Application should be fail-safe - no external event, such as power loss on the workstation application runs on, may result in the inconsistent data in the configuration database

- A subsystem expert should be able to create and edit the entire configuration map tree with the application without having to use any other database

61

tools

- All the changes made to the database have to be trackable by the appropriate expert

- Application should work on any workstation inside or outside of the SLAC network

The configuration browser has been designed to meet the above specifications, and the following set of functionality has been implemented:

- A graphical X-windows based interface representing all applicable configuration objects - configuration maps, top maps, aliases and leaf nodes

- An ergonomic user input interface to minimize the amount of interaction needed to perform most frequent functions

- A full set of editing functions

    - Create new element of configuration tree

    - Link an existing element to the tree

    - Replace an existing element with a new one

    - Remove an existing element

    - Create new alias map

    - Connect the current top configuration map to the alias map

    - Edit the content of the current element

- Efficient navigation throughout the entire set of configuration trees (over 1000) created in *BABAR* configuration database - random access and sequential; by configuration key or alias name

62

- Efficient navigation within the specific tree using two display modes – structural map mode and intuitive fold-down mode similar to the MS Windows File Explorer

- Database interface functions letting user control the commit transactions and rollback the changes if needed

- A set of administrative functions – help and application control

- An automatic expert notification sent to the subsystem and database experts every time the corresponding content is changed in the database

Some of this functionality is illustrated in Figures 3.1 and 3.2. The application was in active use by the entire collaboration for three years until July 2002 when it was replaced by the next generation configuration management tools.

63
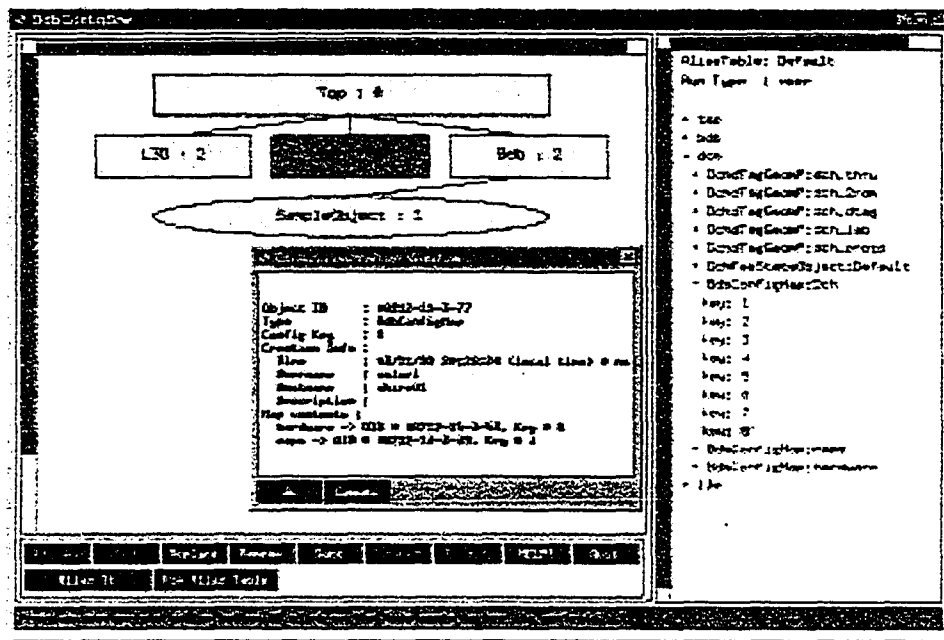
Figure 3.1: *BABAR* Configuration Browser. Rectangular boxes denote Configuration Map objects while ovals denote terminal nodes which actually contain configuration information. The top configuration map of the Drift Chamber detector subsystem is examined. In the Object COnfiguration window, one can see that the DCH map contains two second-level objects - "hardware" and "maps". The user can navigate through the overall *BABAR* detector configuration tree by clicking on the tree nodes in the main window. Alternatively, the Explorer-like interface is provided on the right side for quick access to an arbitrary tree node.
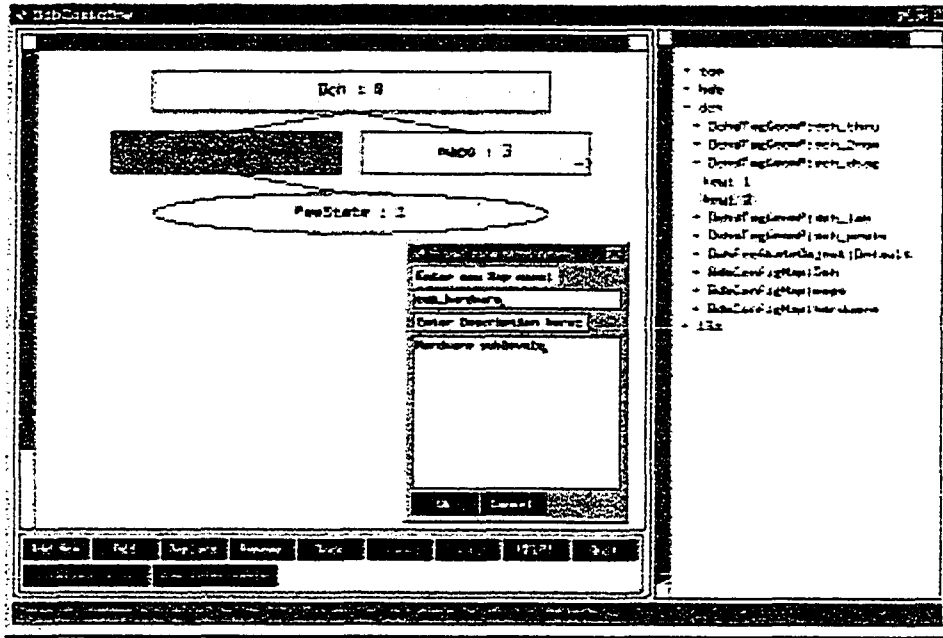
Figure 3.2: *BABAR* Configuration Browser. The Drift Chamber configuration map is now loaded in its expanded form and a new subnode of the "hardware" map element is being created. On the right side, one can see the entire content of the DCH configuration tree in a flat form. All versions of any object can be examined through the right-side interface while only linked objects can be accessed by the main graphical interface. For instance, one of the terminal nodes under "Maps" configuration map, "dch_dtag", is present in two versions. The version with *configuration key* $= 2$ is linked to the tree while *key* $= 1$ is available only through the right-side interface. This availability is important for tracking changes in configurations of particular elements of the subsystem.

65

Chapter 4

Analysis of the Inclusive

Semileptonic B-decays in B_AB_{AR}

The very large amount of data available for analysis in the BABAR experiment allows use of analysis methods which were previously statistically limited. Often, they have better systematic errors due to cleaner analysis algorithms. Also, some of them are of special interest because they allow measurements of decay asymmetries between different flavors of B mesons. The total amount of data available by the end of 2002 is over 100 fb^{-1}, more than a factor of 10 larger than for the previous experiment, CLEO.

4.1 Overview of the current Experimental Approaches

The experimental approaches used to extract the semileptonic branching fractions can be divided into two categories - Direct and Tagged Measurements.

- Direct Measurement.

  In this method, the branching fraction is measured directly from the inclusive spectrum of electrons detected in the event sample. As a result, very

66

high statistics can be obtained. However, systematic errors are high in this approach since very large background corections are needed to be estimated from simulated data. This method has been employed in early studies of semileptonic B decays [15], [14].

- Tagged Measurements.

  In these measurements, various methods are used to determine that a $B\overline{B}$ event has occured. This process is referred to as tagging a B meson decay. Various levels of B-meson tagging are possible. At a minimum we need sufficient information to say a BBbar event occurred. Furthermore, it would be helpful to separate the tracks coming from decays of each of the two B-mesons in the event. The higher the achieved level of separation, the less background one has to take care of in the analysis. The following tagging methods are currently used to provide different levels of tagging:

  - Lepton tags with charge correlation [and event topology].

    In this method, high-momentum leptons are used to tag B meson decay. The remaining leptons are then studied and branching fractions are determined from their spectra and tag count. Charge correlations between tag and "measured" leptons are exploited to suppress certain types of background. This method was first pioneered by ARGUS [16] and continued in CLEO [17], Belle [18] and $BABAR$ [19]. With the typical cut on lepton momentum in the $\Upsilon(4S)$ center-of-mass frame, 1.4 GeV/c, 96-97% of the tags correctly indicate a B meson decay. A small remainder is corrected for using simulated data. The advantages include relative model independence (most significant subtractions are possible to carry out in data using charge correlations) and high statistics. Disadvantages: separate measurements for neutral and charged

67

B mesons are not possible.

- Fully reconstructed B decays as tags.

   In this method, B decay is detected by fully reconstructing one of the B mesons. Leptons originating from the decay chain of the other B meson are then studied and the branching fraction is extracted from their spectra and tag count. This method was first used in *BABAR* [20] (preliminary result was obtained in 2001). Advantages: much cleaner spectra result in smaller backgrounds which, in turn, result in reduction in systematic errors. By fully reconstructing one of the B mesons, one knows the exact type and flavor of the other B meson in the event - this allows measurement of branching fractions separately for charged and neutral B mesons. Disadvantages: low statistics (full B meson reconstruction efficiency is less than 0.1%); new sources of systematic errors. **Measurements of the branching fraction of semileptonic B decays using this method have become feasible only now when large amounts of data have been accumulated at the two currently operating B-factories - Belle in Japan and** *BABAR* **in US**

- Partially reconstructed B decays as tags.

   Similar to the previous method except only a partial reconstruction of the *B*-meson is attempted. As a result, higher statistics can be obtained due to the higher efficiency of partial reconstruction w.r.t. full reconstruction. However, in events with partially reconstructed tags, a fraction of the tracks from the tag *B*-meson is mixed with the tracks from a "candidate" *B*-meson resulting in less clean events and higher systematic errors. Nevertheless, this tagging method finds use in ex-

68

periments with lower available statistics and provides an important cross-check on the results obtained using other methods.

For the first time in history of the semileptonic B decay studies, the large data samples from B-factories made it possible to obtain competitive results using fully reconstructed B mesons as tags.

69

4.2 Introduction to Inclusive Semileptonic Analysis in BABAR

4.2.1 Motivation

The main purpose of this analysis is the measurement of the primary lepton spectra and semileptonic branching fractions separately for B^0 and $B^\pm$ mesons. From this measurement, the ratio of branching fractions will be determined. Total (averaged over $B^\pm$ and B^0) branching fraction will also be obtained and used in determination of the CKM matrix element $|V_{cb}|$.

A set of phenomena related to the potential differences in $B^\pm$ and B^0 decay dynamics has been studied relatively poorly in the past. However, there are some compelling reasons to pursue such studies:

- It is often argued that the individual semileptonic branching fractions of $B^\pm$ and B^0 should be equal. This is based on the assumption that a heavy quark should decay weakly without regard to the light spectator quark. (In the case of charm quarks, the difference in the hadronic decay widths is known to be large due to non-spectator diagrams.) For B-mesons, the deviation from unity of the lifetime ratio τ_+/τ_0 is predicted to be of order 10% [23].

- There has also been some speculation that there are differences in the semileptonic decay spectra [24]. Namely, it is suggested that one of the spectator-level effects of the order $1/m_Q^3$, "Weak Annihilation", might result in a difference in total semileptonic branching fraction for $B^\pm$ vs. B^0

As a result, separate measurements of $B^\pm$ / B^0 decays represent special interest.

70

Measurements of the inclusive semileptonic branching fractions of B-mesons have been performed at many experiments including ARGUS, CLEO (I & II), Belle and *BABAR* . The summary of the measurements so far is given in Table 4.1 [25], and corresponding world average plots are given in Figures 4.1 and 4.2. Measurements of the branching fractions for B^0 and $B^{\pm}$ separately are at the level of $\sigma_{stat} \sim 6 - 8\%$, achieved in preliminary *BABAR* analysis [20]. Earlier results from CLEO analysis are at the level of $\sigma_{stat} \sim 6\%$ [17] and are based on partial reconstruction of both charged and neutral B-mesons. No statistically significant deviation from 1.0 for the ratio of the semileptonic branching fractions for B^0 and $B^{\pm}$ has been observed yet.

Experiment	Date	method used	BR
		$BR(B \rightarrow Xl\nu)$	
BELLE	2002	lepton tag, 5.1 fb^{-1}	$10.90 \pm 0.12 \pm 0.49$
BABAR	2002	lepton tag, 4.1 fb^{-1}	$10.84 \pm 0.21 \pm 0.34$
ADLO (LEP)	2002		10.65 ± 0.23
DELPHI	2001	lifetime and b-tagging	$10.70 \pm 0.08 \pm 0.21(+0.30 - 0.44)$
ALEPH	2001	charge correlation with other hemisphere	$10.70 \pm 0.1 \pm 0.23 \pm 0.26$
OPAL	1999	neural network, models fitted	$10.83 \pm 0.1 \pm 0.20(+0.20 - 0.13)$
L3	1999	double tag	$10.16 \pm 0.13 \pm 0.30$
CLEO	1996	electrons, lepton tagged	$10.49 \pm 0.17 \pm 0.43$
		$BR(B^{\pm} \rightarrow Xl\nu)$	
BABAR	2001	Tag with fully reconstructed B (prelim)	$10.3 \pm 0.6 \pm 0.5$
CLEO	1997	tag with partial reco	$10.25 \pm 0.57 \pm 0.5$
CLEO	1994		$10.1 \pm 1.8 \pm 1.5$
		$BR(B^0 \rightarrow Xl\nu)$	
BABAR	2001	Tag with fully reconstructed B (prelim)	$10.4 \pm 0.8 \pm 0.5$
CLEO	1997	tag with partial reco	$10.78 \pm 0.6 \pm 0.69$
CLEO	1994		$10.9 \pm 0.7 \pm 1.1$
		$BR(B^{\pm} \rightarrow Xl\nu)/BR(B^0 \rightarrow Xl\nu)$	
BABAR	2001	Tag with fully reconstructed B (prelim)	$0.99 \pm 0.1 \pm 0.03$
CLEO	1997	tag with partial reco	$0.95 \pm 0.08 \pm 0.091$
CLEO	1994		$0.93 \pm 0.18 \pm 0.12$

Table 4.1: Results on semileptonic branching fractions obtained to date.

72

SL Branching Fraction Results, B+-

BABAR, 2001, BRECO tag (prelim)

CLEO, 1997, tag with partial reco

CLEO, 1994

5   6   7   8   9   10   11   12   13
Branching Fraction, %

SL Branching Fraction Results, B0

BABAR, 2001, BRECO tag (prelim)

CLEO, 1997, tag with partial reco

CLEO, 1994

5   6   7   8   9   10   11   12   13
Branching Fraction, %
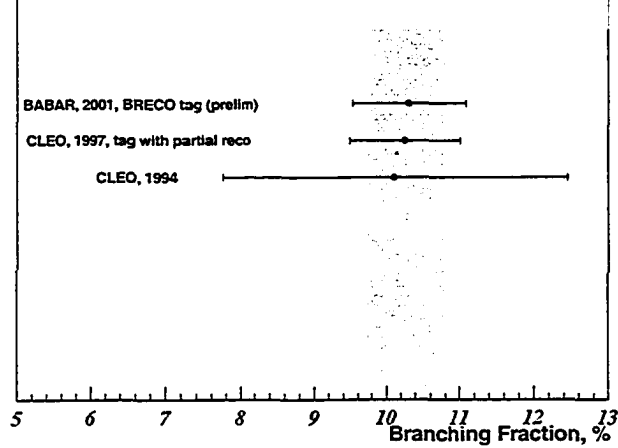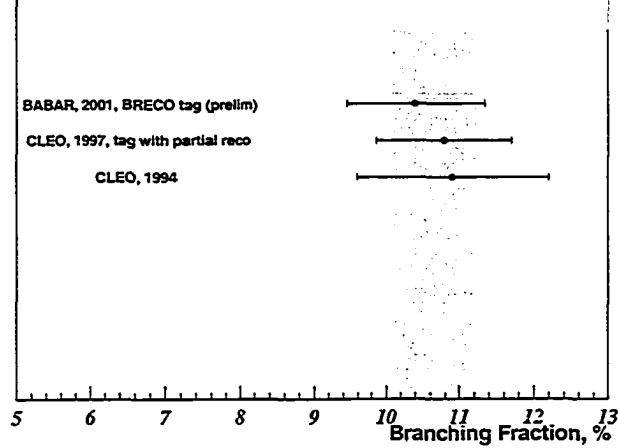
Figure 4.1: World averages for semileptonic B decay branching fractions before this measurement. Yellow bands show the prior world averages. (top) - BR($B^{\pm} \rightarrow Xe\bar{\nu}$), (bottom) - BR($B^{0} \rightarrow Xe\bar{\nu}$). World average values are calculated as an average of the individual measurements weighted with the corresponding errors.

73

SemiLeptonic Branching Fraction Results

BELLE, 2002, lepton tag
BABAR, 2002, lepton tag
ADLO (LEP), 2002
DELPHI, 2001, lifetime & B-tagging
ALEPH, 2001, charge corr
OPAL, 1999, neural net
L3, 1999, double tag
CLEO, 1996, lepton tag

8   8.5   9   9.5   10   10.5   11   11.5   12
Branching Fraction, %

SL Branching Fraction Ratio, B+-/B0

BABAR, 2001, BRECO tag (prelim)
CLEO, 1997, tag with partial reco
CLEO, 1994

0.4   0.5   0.6   0.7   0.8   0.9   1   1.1   1.2
Branching Fraction Ratio
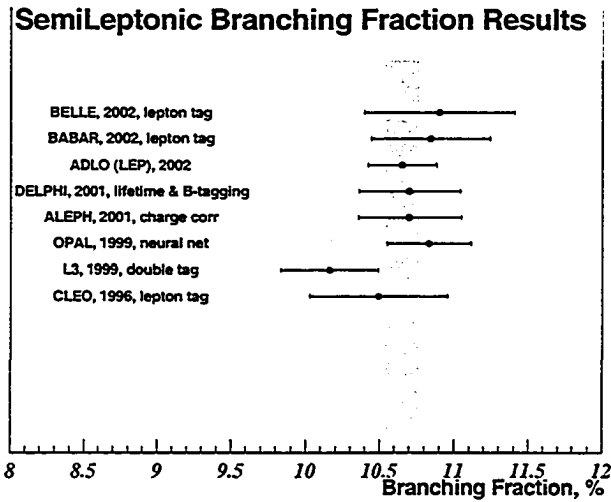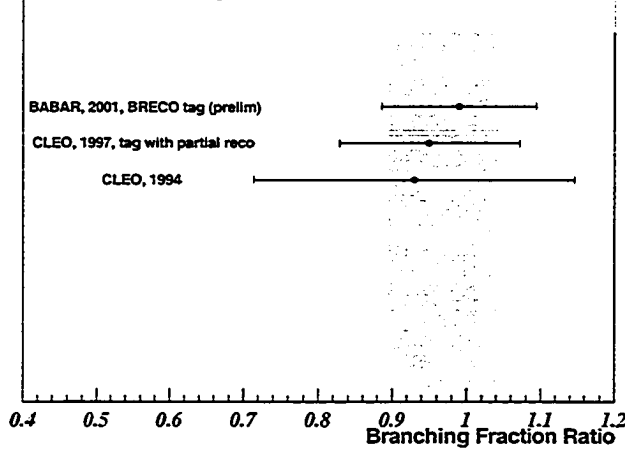
Figure 4.2: World averages for semileptonic B decay branching fractions before this measurement. Yellow bands show the prior world averages. (top) - BR($B \rightarrow$ $Xe\bar{\nu}$), (bottom) - BR($B^{\pm} \rightarrow Xe\bar{\nu}$)/BR($B^0 \rightarrow Xe\bar{\nu}$). World average values are calculated as an average of the individual measurements weighted with the corresponding errors.

74

4.2.2 Analysis Overview

We study the spectrum of primary electrons from B-meson decays generated in the PEP-II/$BABAR$ B-factory through the process $e^-e^+ \rightarrow \Upsilon(4S) \rightarrow B\overline{B}$.

- Primary spectrum definition: $b \rightarrow ce^-\overline{\nu}$ ($\overline{b} \rightarrow \overline{c}e^+\nu$). X_c includes: D^0 ($\overline{D^0}$), D^+ (D^-), D_s^+ (D_s^-).

- The Branching Fraction determination.

$$BR = \frac{N(B \rightarrow Xl\nu)/\epsilon_{SL}}{N_{tag}} \times \frac{\epsilon_{tag}}{\epsilon_{tag}^{SL}},$$

where

$N(B \rightarrow Xl\nu)$ is the integral over the detected semileptonic spectrum (after all background corrections)

ϵ_{SL} is the event selection efficiency for semileptonic events (in events with one B-meson fully reconstructed)

N_{tag} - number of tagged $B\overline{B}$ events

ϵ_{tag} is the efficiency to tag the $B\overline{B}$ event

ϵ_{tag}^{SL} is the efficiency to tag the $B\overline{B}$ event with the one B-meson decaying semileptonically

The concept for the present analysis is very straightforward. Events containing B-meson candidates are tagged with fully reconstructed hadronic B-decays (B_{reco} tags), where the standard software tools from BaBar analysis support system are employed. The electron (positron) spectrum from semileptonic decays of the other B-meson (B_{RECOIL}) is measured.

This method offers many advantages.

75

- It assures a very clean environment to study the properties of the recoil B-meson , as one of the two B mesons from the decay of the $\Upsilon(4S)$ is reconstructed in a fully hadronic mode . Thus we know that all the remaining particles of the event originate from the other B.

- The momentum of the recoiling B is also known and therefore the lepton can be boosted accurately into the B rest frame.

- The charge of the B is known, so the B^0s and the B^+s can be studied separately.

- The flavor of the B is known, so the correlation between the charge of the lepton and the flavor of the B can be used to reject $B \rightarrow D \rightarrow lepton$ events (the so-called cascade events).

The only drawback is that the efficiency of this method is very low and is dominated by the semi-exclusive reconstruction efficiency of $\sim 0.4\%$. In this analysis all the efficiencies will be calculated with respect to a sample with at least one fully reconstructed B.

The electron spectrum of the recoil B is measured for both B^0 and $B^\pm$. The correlation between the charge of the electron and the flavor of the reconstructed B-meson allows for the efficient separation of the primary and secondary contributions. The event sample is divided into 4 distinct classes, differentiated by the type of the B meson charged or neutral, and the charge of the electron (Table 4.2).

The right (wrong) sign refers to the charge of the electron expected from the flavor of the B-meson for a prompt b-decay (cascade c-decay). We distinguish between charmed mesons from the hadronization of the c-quark produced in the decay of the b-quark (wrong-sign cascade charm) or from hadronization of the $\bar{c}$-quark from the decay of the W (right-sign cascade charm). While the former

76

Event Class	Type of B	Charge of the electron w.r.t expected prompt electron charge
A	charged	right-sign - $Q_b \times Q_l < 0$
B	charged	wrong-sign - $Q_b \times Q_l > 0$
C	neutral	right-sign
D	neutral	wrong-sign

Table 4.2: Event class definition

contributes to wrong-sign leptons, the latter produces leptons of the same charge as prompt b-decay.

After the separation into the above event classes, the electron (positron) spectra in each class are corrected for the following background processes (in the order stated below):

- Pair Backgrounds

  - conversion pairs ($\gamma \rightarrow e^+ e^-$)

  - π^0 Dalitz decays ($\pi^0 \rightarrow \gamma e^+ e^-$, $\eta^c \rightarrow \gamma e^+ e^-$)

  - charmonium decays ($J/\psi \rightarrow e^+ e^-$)

- Hadron misidentification ($\pi, K, p(\overline{p})$, misidentified as electrons)

- Electrons from decays other than semileptonic B decays

  - $\tau \rightarrow e$ ($B \rightarrow \tau^+ \rightarrow e^+$, $B \rightarrow D_s^+ \rightarrow \tau^+ \rightarrow e^+$)

  - electrons from D, D_s, Λ_c ($B \rightarrow \overline{D}D, D \rightarrow e^+$, $B \rightarrow \overline{D}D_s^+, D \rightarrow e^+$, $B \rightarrow \Lambda_c^+ \rightarrow e^+$)

The pair and hadron misidentification backgrounds are derived from data with little input from Monte Carlo simulations. However, the contributions from elec-

77

trons from decays other than semileptonic B decays are derived from Monte Carlo based on the latest measured branching fractions for the corresponding decays.

At every step of the analysis, the electron (positron) spectra and corresponding background contributions are corrected for combinatorics in B-meson reconstruction through M_{ES} sideband subtraction, described in Section 4.3.4.

After the above corrections, the spectra have to be corrected for:

- Detector effects

- $B^0 \longleftrightarrow \overline{B^0}$ mixing

- systematic effects of full B-meson reconstruction

After the tag count has also been corrected for the systematic effects of full B-meson reconstruction, we use the number of $B^{\pm}$ or B^0 tags to normalize the spectra in the primary event classes (A and C). The resulting distribution is referred to as the visible/differential branching fraction for semileptonic decays of $B^{\pm}$ or B^0. Since in this analysis the electron spectrum is measured only for electrons with $p^* > 0.5$ GeV/c, we have to extrapolate the measured spectra to $p^* = 0$ by a fit to the sum of spectra predicted by Monte-Carlo for different semileptonic B decay channels.

The resulting full distribution is then integrated and the total semileptonic branching fraction of the B meson is obtained. This value is then used along with the latest theoretical input to determine the CKM matrix element $|V_{cb}|$.

78

4.3 Event Samples

4.3.1 Full Reconstruction of B-mesons

The primary event selection for this analysis relies on the semi-exclusive reconstruction of a B meson described in detail in [26]. The strategy of this reconstruction is designed to accumulate very large samples of decays of the type $B \to DY$. Here D refers to a charm meson, and Y represents a collection of hadrons of charge ± 1. The charm meson serves as a "seed" for the selection of decays, and we use four different seeds: $D^{\pm}$ and D^{*+} for B^0 and D^0 and D^{*0} for $B^{\pm}$. For each mode we define the "purity" of the mode as the ratio $\frac{S}{S+B}$ where S and B are the signal and combinatorial background respectively, as estimated from fits to the data, described in Section 4.3.4.

We define more than 800 decay chains (B_{reco} modes) which are characterized by different signal purities, depending on the multiplicity and on the composition of the hadrons making up the Y system. In events with more than one reconstructed B decay, the decay mode with the highest purity is selected. The data sample for this analysis consists only of events where the above semi-exclusive reconstruction succeeded and the resulting B_{reco} mode purity and event counts satisfy certain criteria described below in Section 4.3.4.

The combinatorial background is represented by both continuum and $B\overline{B}$ events. After the requirement on the presence of a lepton in the event the background is dominated by the $B\overline{B}$ background. In addition, there is also background which has an M_{ES} distribution similar to that of the signal, when the true mode differs from the reconstructed one by a single soft particle (e.g. a $B^0 \to D^{*-}\pi^+$ ($D^{*-} \to \overline{D^0}\pi^-$) confused with a $B^+ \to \overline{D^0}\pi^+$ event). If the soft particle which makes the difference is neutral the only effect is a marginal worsening of the resolution on kinematic quantities, while the situation is worse when a charged

79

particle is lost because the neutral and charged B samples get mixed up. This last case is called *cross-feed* and is studied in detail in Systematics section.

A detailed description of the data samples, the reconstruction of hadronic decays of B-mesons , the event selection, track requirements, and the electron identification used in the analysis follows in the next section. Some of these topics are covered in much more detail in separate *BABAR* analysis documents, [27], [28], and [29].

4.3.2 Monte-Carlo Sample

As with every data analysis, a detailed Monte-Carlo study provides important inputs to the overall analysis strategies. Similarly in this analysis a detail Monte-Carlo study has been performed to:

- Estimate the contribution to the electron spectrum from decays other than semileptonic B decays

- Determine B_{reco} *cross-feed* effects

- Obtain B_{reco} efficiency bias estimates ($\epsilon_{tag}/\epsilon_{tag}^{SL}$ - ratio of the efficiency of semi-exclusive B-meson reconstruction for all $B\overline{B}$ events to that for events with one of the B-mesons decaying semileptonically)

In these studies, the information about the generated decay sequences has been used to separate different types of decays. Each reconstructed track was matched to a generated particle candidate using standard *BABAR* Monte Carlo Truth Matching algorithm, described in more detail elsewhere [38].

In order to provide correct input on the above, a good description of the relevant variables by the Monte-Carlo simulation is important for this inclusive analysis.

A summary of the Monte-Carlo samples used in this analysis is provided in Table 4.3. These samples differ in terms of the decay modes of the tag B-meson

- *Cocktail* samples contain specific hadronic decay modes for one of the B-mesons (the B_{reco} candidate), corresponding to a subset of the modes used in the semi-exclusive reconstruction of the hadronic tag. The second B meson in the event decays generically (into all possible final states). Cocktail samples have been used only for cross-check purposes.

- *generic* samples, on the other hand, contain both of the B mesons decaying without restrictions. Generic $B\overline{B}$ MC represent the full simulation of all possible decays of the B meson and it should represent the data as an unbiased event sample.

In all Monte-Carlo simulations, the semileptonic B decay to charm mesons is generated using a mix of the specific decay models. For example, the decay mode $B \rightarrow D^*\ell\nu$ is generated using the parameterization of HQET form factors[30], the non-resonant decay $B \rightarrow D^{(*)}\pi\ell\nu$ is generated using the Goity and Roberts model [31], whereas the ISGW2 model [32] is used for all other semileptonic decays. The total Cabibbo-favored semileptonic branching fraction is set to $\mathcal{B}(b \rightarrow c\ell\nu) = 10.54\%$, which is somewhat lower than the most recent measurement performed by $BABAR$ [19].

The semileptonic branching fractions and decay dynamics for semileptonic decays of the B mesons are assumed to be identical for $B^\pm$ and B^0, as shown in Figure 4.3. The momentum-averaged ratio of primary electron spectra for charged and neutral B mesons obtained at the generator level in Monte-Carlo is $R_{\pm/0} = 1.003 \pm 0.011$ (using a limited sample of 5 Million generic $B\overline{B}$ events).
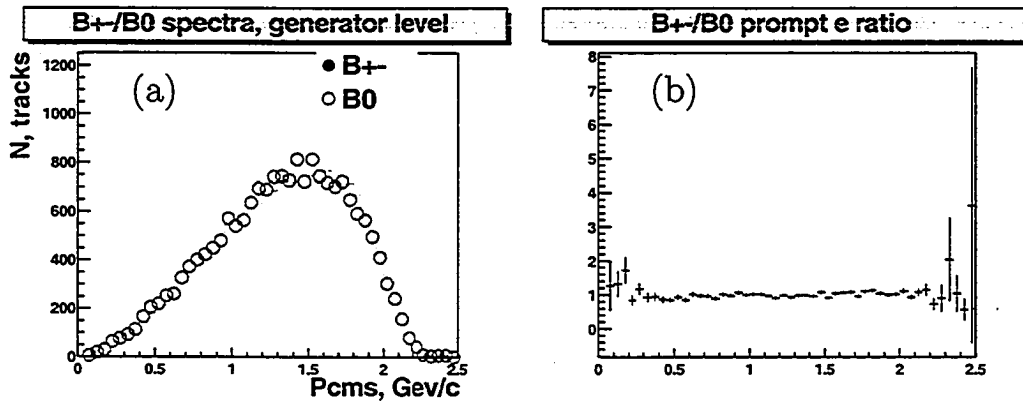
Figure 4.3: (a) Generator level electron spectra for charged and neutral B-mesons. (b) Ratio of the two spectra.

The generic Monte-Carlo simulated sample is used for various optimization studies, studies on the composition of the background tagged by B-meson candidate, and studies of the event reconstruction efficiency. The total MC sample corresponds to an integrated luminosity of $\mathcal{L} = \sim 240\,\text{fb}^{-1}$ both for $B^0/\overline{B}^0$ and for B^+/B^- (Table 4.3). Separate samples of uds ($u\bar{u} + d\bar{d} + s\bar{s}$) and $c\bar{c}$ events have also been added in the right proportions to arrive at a realistic sample that is identical in event composition to the data.

4.3.3 Data Sample

The present analysis is based on a total integrated luminosity of $82 \pm 0.7\ fb^{-1}$ (Table 4.4).

4.3.4 Event Reconstruction and Selection

All events used in this analysis are reconstructed in the semi-exclusive B meson reconstruction framework which is set up by the B_{reco} Analysis Working Group [33]. This framework is now used in a multitude of physics analyses including measurement of CP violation, $B^0 - \overline{B^0}$ mixing and many branching fractions.

82

Table 4.3: Monte-Carlo event samples used in this analysis.

Data set	Lumi [fb^{-1}]	Number of $B\overline{B}$ events, millions
B^0 cocktail	> 100	> 53
$B^{\pm}$ cocktail	> 300	> 158
B^0 generic	~ 240	~ 126
$B^{\pm}$ generic	~ 240	~ 126
$c\bar{c}$ generic	~ 35	$-$
$u\bar{u} + d\bar{d} + s\bar{s}$ generic	~ 29	$-$

Table 4.4: Data event samples used in this analysis.

Data set	Lumi [fb^{-1}]	Number of fully reconstructed B mesons (after mode selection, one per event)
2000	13	51,000
2001	42	197,000
2002	27	113,000
Total	82	361,000

83

Kinematic Selection of hadronic B Decays used to tag $B\overline{B}$ events

A possible choice of two largely independent variables to describe the decays of B-mesons on the $\Upsilon(4S)$ resonance are the energy-substituted mass M_{ES}, and the difference ΔE between the reconstructed and expected energy of the B-meson candidate. Both quantities can be evaluated either in the $\Upsilon(4S)$ rest frame or the laboratory frame. In this analysis, the lab-frame is chosen. The invariant energy difference of the B-meson candidate is calculated with

$$\Delta E = \frac{p_B \cdot p_i - s/2}{\sqrt{s}},$$

where $\sqrt{s}$ is the CMS energy, and where p_B and p_i denote the four-momenta (E, p) of the B-meson candidate and the initial state. The energy-substituted mass M_{ES} is calculated as

$$m_{ES} = \sqrt{(s/2 + \mathbf{p}_B \cdot \mathbf{p}_i)^2 / E_i^2 - \mathbf{p}_B^2}.$$

In this analysis, only events with $\Delta E < 0.1 GeV$ are used. Furthermore, B-meson candidates are selected by the requirement that the energy-substituted mass M_{ES} lies within a "signal box" chosen to be

$$5.27 \ GeV/c^2 < m_{ES} < 5.29 \ GeV/c^2,$$

Background studies and subtraction are done with B-meson candidates in a M_{ES} "sideband", defined as

$$5.21 \ GeV/c^2 < m_{ES} < 5.26 \ GeV/c^2.$$

The above parameters are justified by the M_{ES} plots generated using clean samples of $B\overline{B}$, $u\overline{u} + d\overline{d} + s\overline{s}$ and $c\overline{c}$ Monte-Carlo events (see Figure 4.4). On these plots, as well as in all other M_{ES} plots in this document, the following label conventions are used: S - number of signal entries in the "signal box" of

84

M_{ES} - equal to the integral of the fitted Crystal Ball function (defined below) over the "signal box" M_{ES} interval; B - number of background events in the "signal box" - equal to the integral of the fitted Argus function (defined below) over the "signal box" M_{ES} interval; m - B-meson mass from fitted function (the mean of the gaussian contribution in the fitted Crystal Ball function); s - σ of that gaussian contribution; P - purity of the M_{ES} distribution (S/(S+B)); R - "sideband subtraction" ratio (in %) - ratio of the number of background events in the "signal box" to that in M_{ES} "sideband".
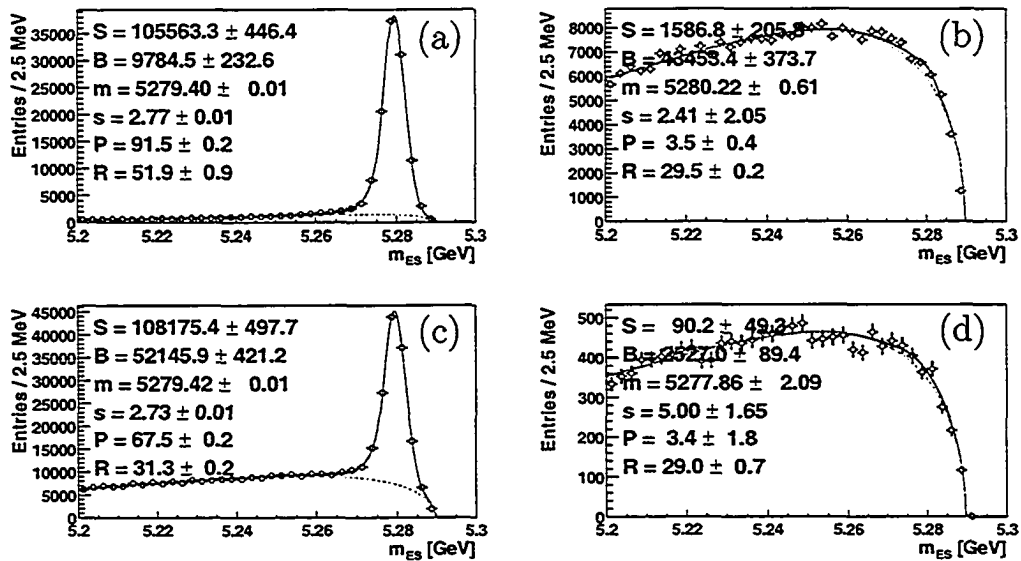
Figure 4.4: Motivation of the M_{ES} cuts used in signal box and sideband definitions. (a) - $B\overline{B}$ sample, (b) - $u\overline{u} + d\overline{d} + s\overline{s} + c\overline{c}$ sample from Monte-Carlo, (c) - correctly mixed MC sample (appropriate amounts of uds and $c\overline{c}$ events were added to $B\overline{B}$ sample), (d) - continuum DATA sample.

The background contributions to the events or electron spectra in the signal box are determined by extrapolating corresponding contributions from the sideband. A fit to the energy-substituted mass M_{ES} distribution is performed to separate signal ($B\overline{B}$) events from background (combinatorics, continuum). M_{ES}

85

is fitted to a sum of the empirical functions expected for signal and background M_{ES} distributions.

The signal component is fitted using a "Crystal Ball" function:

for $M_{ES} > m - \sigma \cdot a$:

$$\frac{dN}{dM_{ES}} = \frac{1}{N} \cdot \exp\left(-\frac{1}{2} \cdot \frac{(M_{ES} - m)^2}{\sigma^2}\right) \tag{4.1}$$

for $M_{ES} < m - \sigma \cdot a$:

$$\frac{dN}{dM_{ES}} = \frac{(n/a)^n}{N} \cdot \exp\left(-\frac{1}{2} \cdot a^2\right) \frac{1}{\left(\frac{(m-M_{ES})}{\sigma} + \frac{n}{a} - a\right)^n} \tag{4.2}$$

where m is the peak position, σ is the width of the gaussian distribution, a determines the crossover point from the gaussian distribution to the power law tail distribution, and n is a parameter describing the tail; smaller values generate a longer tail.

The tail of this function accounts for energy losses in the showers of reconstructed π^0 . Thus the tail of the distribution depends on the reconstructed B decay mode and in particular in the number of π^0 present in it.

The background shape in the M_{ES} distribution is described by the Argus function, first used by the ARGUS experiment as an empirical characterization of the mass spectrum of the continuum and other background events:

$$\frac{dN}{dM_{ES}} = N \cdot M_{ES} \cdot \sqrt{1 - x^2} \cdot \exp\left(-\xi \cdot (1 - x^2)\right) \tag{4.3}$$

where $x = M_{ES}/m_{\max}$ and the shape parameter ξ is determined from a fit. The endpoint of the Argus curve, $m_{\max}$, is fixed in the fit, since it depends only on the beam energy. The Argus function provides a good parametrization of both the continuum ($c\bar{c}$ and $u\bar{u} + d\bar{d} + s\bar{s}$) and the combinatoric background from $B\overline{B}$ events.

The maximum total number of floating parameters in the M_{ES} fits is seven. Two of them are for the Argus function, while the remaining five parameters are for the Crystal Ball function. The actual fitting is performed in two steps:

86

- 1. The ARGUS function is fitted to the sideband region of the M_{ES} distribution and two parameters of the ARGUS function are extracted.

- 2. The seven-parameter Crystal Ball + ARGUS function is fitted to the full M_{ES} distribution. Both ARGUS parameters are fixed to the values obtained in step 1.

For more details on the fitting method refer to Section 6.1.3.

B_{reco} mode selection for analysis

We apply special selection criteria to the modes used in the analysis based on their individual purity and relative fraction in the total number of tagged events.

Several parts of this analysis (such as the B_{reco} efficiency bias used to correct for different B_{reco} efficiencies for different types of events) depend on the correct description of the data by Monte-Carlo simulation. In order to simplify analysis and Data/Monte-Carlo comparison, we apply the following mode selection algorithm for both Data and Monte-Carlo event samples:

- First restrict ourselves to modes with the purity $> 50\%$

- and then reject all modes that contribute $< 0.2\%$ to the total number of $B\overline{B}$ events with one fully reconstructed B-meson .

Table 4.5 shows the effect of the above cuts on the event counts.

After this selection, 32 modes are retained : 14 for $B^{\pm}$ and 18 for B^0 . The mode statistics and relative contributions to total event counts for Data and Monte-Carlo samples are shown in Figure 4.5 and in Table 4.6. In the same table, the B_{reco} modes are also listed with relevant indices as used in $BABAR$ software. Good agreement between Data and Monte-Carlo is observed for our B_{reco} mode set. Another measure of the agreement between data and Monte-Carlo samples

87

Table 4.5: Result of the mode selection algorithm. The column labeled as Efficiency describes the fraction of the total number of events which survived the cut[s].

Cut	Data		Monte-Carlo	
	Event Count	Efficiency, %	Event Count	Efficiency, %
Total	500078 ± 2703	100.0	693187 ± 2403	100.0
purity > 50%	105037 ± 475	21	179998 ± 624	25.96
relative contribution to total > 0.2%	98266 ± 456	19.65	159470 ± 585	23

is the distribution of the number of tracks in the recoil (track multiplicity), found in Figure 4.6. Very good agreement is observed. The effect of the remaining deviation in relative contributions has been extensively studied and no systematic bias of the measured quantities has been observed (see Section 6.1). Several other cross-checks have been performed to test the Monte-Carlo description of the fully reconstructed $B\overline{B}$ events. More details on these studies are available in Section 6.1. Note that values in Tables and Figures in this section are based on the slightly lower statistics than that used in the analysis. Therefore, the total number of tags quoted is different for the two data samples (analysis counts are given in Figure 4.7).

Table 4.6: Mode statistics and relative contributions to total B_{reco} event counts in our sample

Index	BABAR Index	Mode	Data			MC		
			Signal	Fraction, %	Purity	Signal	Fraction, %	Purity
1	11001	$B^{\pm} \to D^0 K\pi, \pi$	7380 ± 118.3	7.51 ± 0.12	81.9 ± 0.8	11569 ± 149.2	7.25 ± 0.09	80.4 ± 0.7
2	11101	$B^{\pm} \to D^0 K\pi\pi^0, \pi$	13039 ± 170.9	13.26 ± 0.18	67.1 ± 0.6	21236 ± 219.7	13.31 ± 0.14	67.8 ± 0.5
3	11201	$B^{\pm} \to D^0 K3\pi, \pi$	10490 ± 153.4	10.67 ± 0.16	65.2 ± 0.7	18947 ± 202.1	11.88 ± 0.13	72.3 ± 0.5
4	12001	$B^0 \to D^- K_s\pi, \pi$	1233 ± 53.4	1.25 ± 0.05	64.8 ± 2	1752 ± 60.9	1.09 ± 0.03	63.9 ± 1.6
5	12101	$B^0 \to D^- K\pi\pi, \pi$	8610 ± 130	8.76 ± 0.13	77.7 ± 0.7	14585 ± 168.2	9.14 ± 0.11	80.4 ± 0.5
6	13001	$B^0 \to D^{*-} \to D^0\pi \to K\pi, \pi$	2074 ± 58.7	2.11 ± 0.06	97.2 ± 0.6	3132 ± 75.4	1.96 ± 0.04	95.7 ± 0.7
7	13003	$B^0 \to D^{*-} \to D^0\pi \to K\pi, \pi\pi^0$	3479 ± 82.9	3.54 ± 0.08	80.1 ± 1.1	5945 ± 111.4	3.72 ± 0.07	78.8 ± 0.9
8	13009	$B^0 \to D^{*-} \to D^0\pi \to K\pi, \pi\pi\pi$	2213 ± 65.7	2.25 ± 0.06	78.8 ± 1.4	3010 ± 78.3	1.88 ± 0.04	73.2 ± 1.2
9	13036	$B^0 \to D^{*-} \to D^0\pi \to K\pi$	535 ± 34.4	0.54 ± 0.03	61 ± 2.9	1080 ± 49.8	0.67 ± 0.03	60.7 ± 2.1
10	13101	$B^0 \to D^{*-} \to D^0\pi \to K\pi\pi^0, \pi$	3128 ± 73.9	3.18 ± 0.07	92 ± 0.9	5235 ± 97.7	3.28 ± 0.06	92.5 ± 0.7
11	13102	$B^0 \to D^{*-} \to D^0\pi \to K\pi\pi^0, K$	297 ± 24	0.3 ± 0.02	86.3 ± 3.2	378 ± 26.7	0.23 ± 0.01	84.6 ± 2.8
12	13103	$B^0 \to D^{*-} \to D^0\pi \to K\pi\pi^0, \pi\pi^0$	5886 ± 114	5.99 ± 0.11	69.7 ± 0.9	9629 ± 149.4	6.03 ± 0.09	67.1 ± 0.7
13	13109	$B^0 \to D^{*-} \to D^0\pi \to K\pi\pi^0, \pi\pi\pi$	3460 ± 87.7	3.52 ± 0.09	65.5 ± 1.1	4866 ± 108	3.05 ± 0.06	61.9 ± 0.9
14	13111	$B^0 \to D^{*-} \to D^0\pi \to K\pi\pi^0, KK\pi$	245 ± 21.3	0.24 ± 0.02	87.2 ± 3.4	465 ± 29.7	0.29 ± 0.01	85.5 ± 3
15	13138	$B^0 \to D^{*-} \to D^0\pi \to K\pi\pi^0$	342 ± 27.8	0.34 ± 0.02	64.8 ± 3.6	751 ± 42	0.47 ± 0.02	67.7 ± 2.5
16	13201	$B^0 \to D^{*-} \to D^0\pi \to K3\pi, \pi$	2290 ± 62.7	2.33 ± 0.06	93.5 ± 0.9	4133 ± 83.3	2.59 ± 0.05	93.1 ± 0.8
17	13203	$B^0 \to D^{*-} \to D^0\pi \to K3\pi, \pi\pi^0$	3820 ± 89.8	3.88 ± 0.09	69.5 ± 1.1	7443 ± 129.8	4.66 ± 0.08	69.2 ± 0.8
18	13209	$B^0 \to D^{*-} \to D^0\pi \to K3\pi, \pi\pi\pi$	2175 ± 69.5	2.21 ± 0.07	69.7 ± 1.5	3638 ± 90	2.28 ± 0.05	68.7 ± 1.1
19	13301	$B^0 \to D^{*-} \to D^0\pi \to K_s\pi^+\pi^-, \pi$	676 ± 35.1	0.68 ± 0.03	89 ± 2	1102 ± 43.9	0.69 ± 0.02	89.4 ± 1.8
20	13303	$B^0 \to D^{*-} \to D^0\pi \to K_s\pi^+\pi^-, \pi\pi^0$	1150 ± 53.9	1.17 ± 0.05	52.8 ± 1.9	2218 ± 78.7	1.39 ± 0.04	61.8 ± 1.4
21	13309	$B^0 \to D^{*-} \to D^0\pi \to K_s\pi^+\pi^-, \pi\pi\pi$	702 ± 42.7	0.71 ± 0.04	53.5 ± 2.4	1039 ± 49.5	0.65 ± 0.03	52.7 ± 1.9
22	14001	$B^{\pm} \to D^{*0} \to D^0\pi^0 \to K\pi, \pi$	2280 ± 62.7	2.32 ± 0.06	95.3 ± 0.9	3066 ± 74.5	1.92 ± 0.04	94.9 ± 0.8
23	14002	$B^{\pm} \to D^{*0} \to D^0\pi^0 \to K\pi, K$	222 ± 20.3	0.22 ± 0.02	87.4 ± 3.9	411 ± 0	0.25 ± 0	87.4 ± 3.2
24	14003	$B^{\pm} \to D^{*0} \to D^0\pi^0 \to K\pi, \pi\pi^0$	3169 ± 82.7	3.22 ± 0.08	71.5 ± 1.3	6526 ± 116.2	4.09 ± 0.07	80.5 ± 0.8
25	14009	$B^{\pm} \to D^{*0} \to D^0\pi^0 \to K\pi, \pi\pi\pi$	1908 ± 64.1	2 ± 0.06	74.2 ± 1.5	2514 ± 74.4	1.57 ± 0.04	69.8 ± 1.4
26	14036	$B^{\pm} \to D^{*0} \to D^0\pi^0 \to K\pi$	573 ± 38.1	0.58 ± 0.03	53.2 ± 2.6	1036 ± 49.7	0.64 ± 0.03	58 ± 2
27	14101	$B^{\pm} \to D^{*0} \to D^0\pi^0 \to K\pi\pi^0, \pi$	4108 ± 89.6	4.18 ± 0.09	79.9 ± 1.1	5393 ± 106.6	3.38 ± 0.06	75.9 ± 1
28	14201	$B^{\pm} \to D^{*0} \to D^0\pi^0 \to K3\pi, \pi$	2979 ± 76.8	3.03 ± 0.07	78.3 ± 1.2	4675 ± 98	2.93 ± 0.06	81.8 ± 0.9
29	15001	$B^{\pm} \to D^{*0} \to D^0\gamma \to K\pi, \pi$	2133 ± 63.8	2.17 ± 0.06	86.7 ± 1.4	2878 ± 75.9	1.8 ± 0.04	87.1 ± 1.2
30	15002	$B^{\pm} \to D^{*0} \to D^0\gamma \to K\pi, K$	233 ± 24.3	0.23 ± 0.02	69.2 ± 4.7	413 ± 28.8	0.25 ± 0.01	77.4 ± 3
31	15003	$B^{\pm} \to D^{*0} \to D^0\gamma \to K\pi, \pi\pi^0$	3690 ± 98.1	3.75 ± 0.1	55 ± 1.1	5212 ± 118.9	3.26 ± 0.07	54 ± 0.9
32	15101	$B^{\pm} \to D^{*0} \to D^0\gamma \to K\pi\pi^0, \pi$	3673 ± 100	3.73 ± 0.1	50.2 ± 1.1	5175 ± 120.6	3.24 ± 0.07	50.6 ± 0.9
–	–	All modes (sum of above)	98266.7 ± 456	99.99	–	159470 ± 585	99.99	–
–	–	All modes (from combined fit)	98377 ± 459	–	71.4 ± 0.2	159663 ± 589	–	72.4 ± 0.1
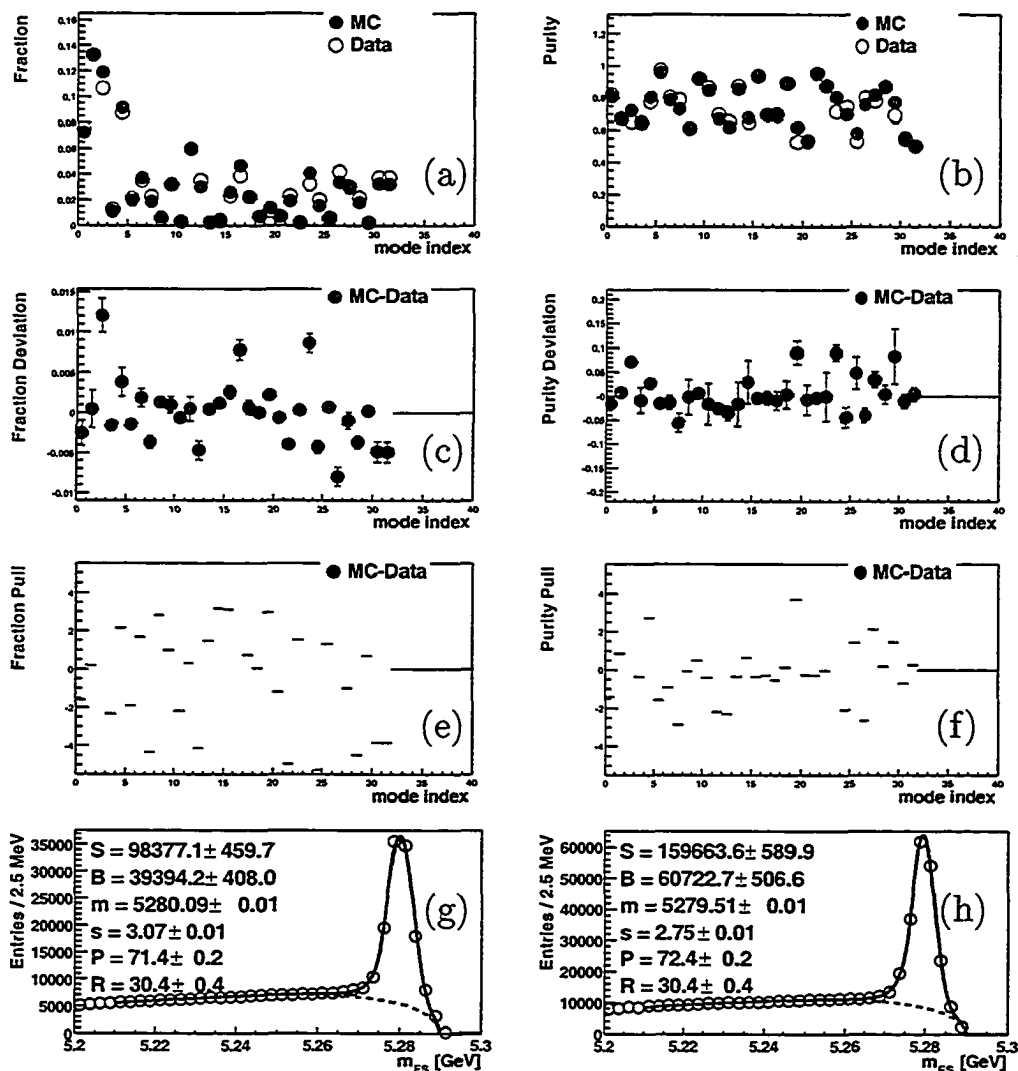
Figure 4.5: MC comparison for B_{reco} quantities. The mode index corresponds to the row number in Table 4.6. In the Figure: (a) relative contributions of various mode to total event counts, (b) B_{reco} purity, per mode, (c) absolute MC-Data difference in relative mode contribution ("fraction deviation"), (d) absolute MC-Data difference in purity ("purity deviation"), (e) pull of the MC-Data fraction deviation ($\frac{deviation}{\sigma_{deviation}}$), (f) pull of the MC-Data difference in purities, (g) M_{ES} distribution for all selected modes, data; (h) same for MC.

90
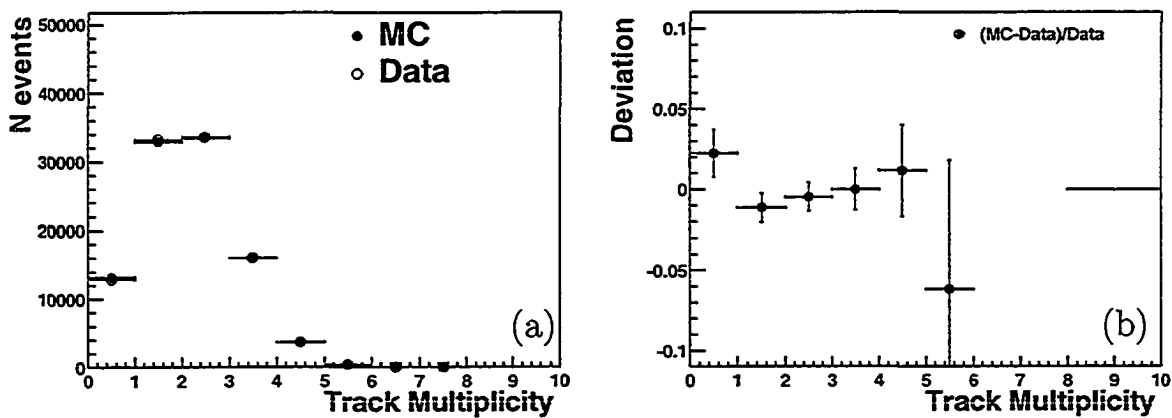
Figure 4.6: Track Multiplicity in the recoil, MC-Data comparison, sideband-subtracted, all events. (a) - distributions for data and Monte-Carlo samples, (b) - relative deviation, (MC-Data)/Data.

91

Table 4.7: Normalization of Monte-Carlo sample relative to Data, based on the tag-level M_{ES} distributions, per B type.

B type	MC tags	Data tags	scaling factor (as applied to MC)
$B^\pm$	194406 ± 656	56766 ± 354	0.2920 ± 0.0021
B^0	146617 ± 558	42951 ± 298	0.2929 ± 0.0023
all	341127 ± 861	99738 ± 462	0.2924 ± 0.0015

Yields correction and Data - Monte-Carlo normalization

Fig. 4.7 shows the total yields from Data and Monte-Carlo samples after mode selection criteria are applied. The M_{ES} distributions are fitted to the sum of a Crystal-Ball function (for the signal) and an ARGUS function (for the background). Any peaking background from continuum is extracted by fitting same distribution in the MC sample, once for the sample with mixed continuum events and once only for $B\overline{B}$ events. The relative difference in the under-the-peak counts is then applied to the under-the-peak count in Data.

These yields are also used in scaling Monte-Carlo corrections before they are applied to data. The scaling factors are given in the Table 4.7 separately for charged and neutral $B\overline{B}$ events.

Sideband Subtraction Method

The integral of the Argus function from the M_{ES} fit provides the total number of background events (N_{tot}^B). A fraction of this background lies in the signal box and needs to be subtracted from the total number of signal events. This is done as follows :

Integrating the Argus function obtained from the M_{ES} fit, we obtain the number of background events that lie in the signal box (N_S^B) and the sideband

92
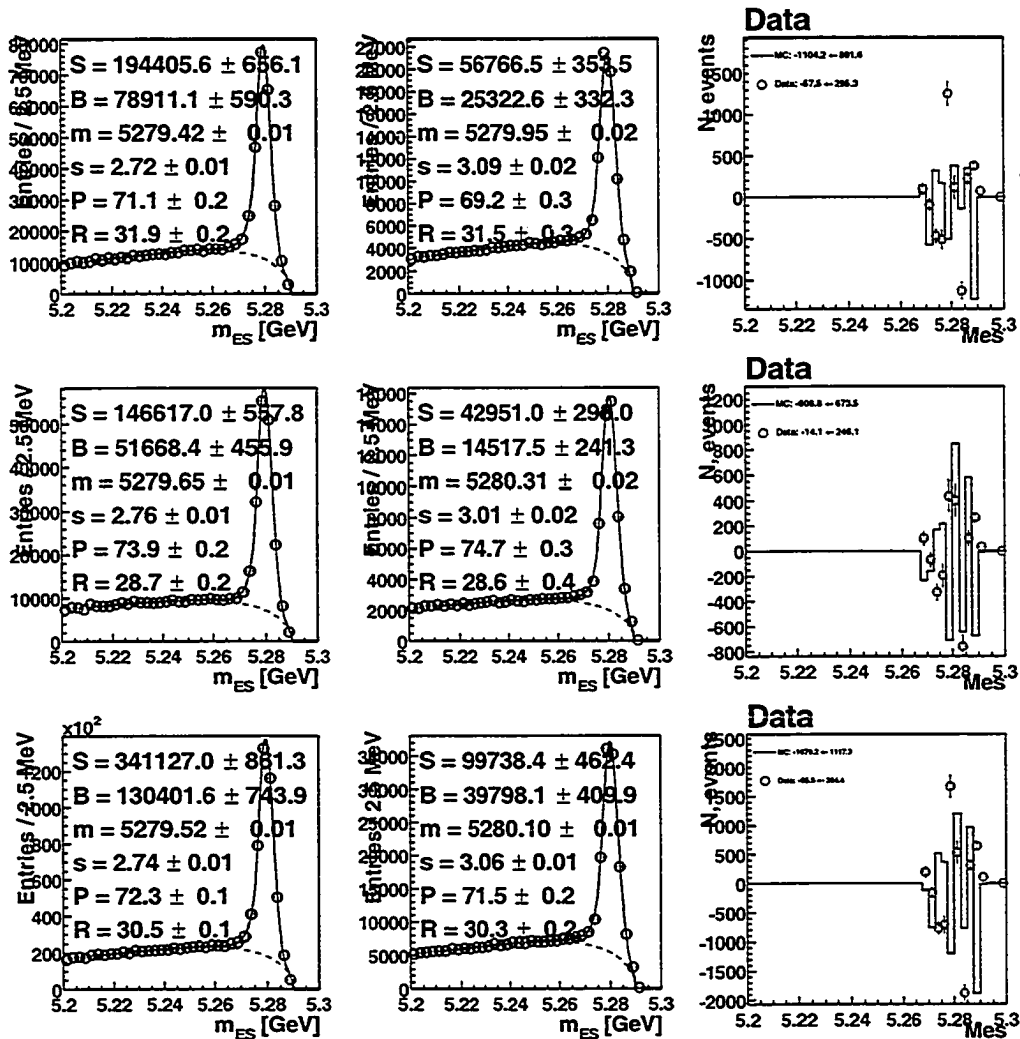
Figure 4.7: Tag Yields. From top to bottom: charged B decay modes, neutral B decay modes, sum of neutral and charged decay modes. From left to right: MC($B\overline{B}$, uds, and $c\overline{c}$ combined); Data; Difference between M_{ES} distribution and a resulting fit function, MC and Data.

93

region (N_{SB}^B). We use these two numbers to estimate the ratio,

$$f = \frac{N_S^B}{N_{SB}^B}$$

which is referred to as the sideband scaling factor. We use this scaling factor to subtract the sideband contribution to any electron spectrum obtained for the events falling into the M_{ES} signal box:

$$N^e = N^{es} - f \times N^{esB}$$

where N^{es} is the number of electrons detected in the signal box and N^{esB} – in the M_{ES} sideband.

Sideband scaling factors are determined separately for each event class from corresponding M_{ES} distributions (Figures 4.8 and 4.9) and are given in the Table 4.8.

The systematic effects of the sideband subtraction have been studied in detail and are described in the 'Systematic Studies' section later in this document.

Cross-Feed in B_{reco}

During the full reconstruction procedure, it is possible for a B meson to be reconstructed in a mode which is different from the actual mode (final state) to which the B originally decayed. We call this effect B_{reco} cross-feed. While some cross-feed effects do not change the apparent flavor of the B meson and thus do not affect this analysis, several others do:

- $B^{\pm} \longleftrightarrow B^0$

- $B^+ \longleftrightarrow B^-$

- $B^0 \longleftrightarrow \overline{B^0}$

94

Data

S = 18151.8 ± 182.8
B = 1378.5 ± 81.4
m = 5279.40 ± 0.03
s = 2.66 ± 0.02
P = 92.9 ± 0.4
R = 35.1 ± 1.5

m_{ES} [GeV]

S = 4805.3 ± 93.9
B = 458.6 ± 46.7
m = 5279.97 ± 0.05
s = 2.91 ± 0.04
P = 91.3 ± 0.8
R = 34.6 ± 2.6

m_{ES} [GeV]

Data

M_{ES}

S = 5248.5 ± 99.9
B = 797.4 ± 59.6
m = 5279.32 ± 0.05
s = 2.87 ± 0.04
P = 86.8 ± 0.9
R = 32.2 ± 1.8

m_{ES} [GeV]

S = 1347.7 ± 51.7
B = 303.4 ± 39.2
m = 5279.87 ± 0.11
s = 3.08 ± 0.10
P = 81.6 ± 2.0
R = 37.1 ± 3.6

m_{ES} [GeV]

M_{ES}
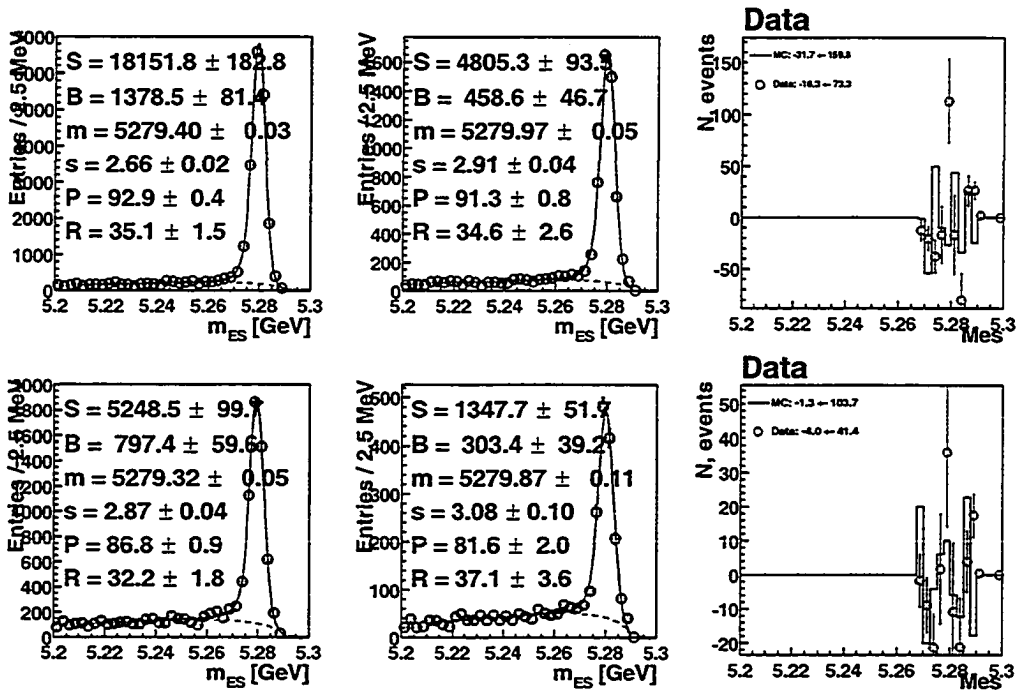
Figure 4.8: Event yields, for events with electrons of momentum $p_{cms} > 0.5$ GeV in recoil. From top to bottom: event class A; B. From left to right: MC ($B\overline{B}$ only); MC($B\overline{B}$, uds, and $c\bar{c}$ combined); Data; Difference between M_{ES} distribution and a resulting fit function, MC and Data.

95

Data

S = 12442.1 ± 155.5
B = 1209.3 ± 79.4
m = 5279.71 ± 0.03
s = 2.73 ± 0.03
P = 91.1 ± 0.5
R = 38.4 ± 1.9

S = 3243.7 ± 77.0
B = 330.5 ± 42.0
m = 5280.31 ± 0.06
s = 2.80 ± 0.05
P = 90.8 ± 1.1
R = 39.4 ± 3.7

S = 6233.0 ± 109.8
B = 1000.2 ± 69.3
m = 5279.71 ± 0.04
s = 2.70 ± 0.04
P = 86.2 ± 0.9
R = 35.0 ± 1.8

S = 1733.7 ± 55.4
B = 215.4 ± 29.8
m = 5280.35 ± 0.08
s = 2.99 ± 0.07
P = 88.9 ± 1.4
R = 29.5 ± 3.0
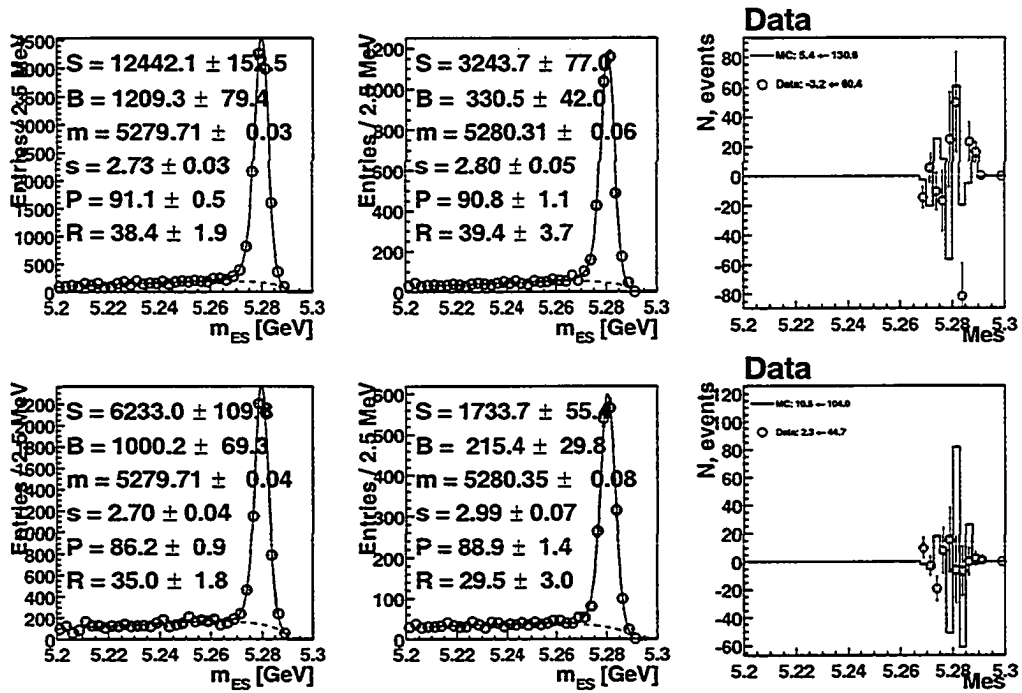
Figure 4.9: Event yields, for events with electrons of momentum $p_{cms} > 0.5\,\text{GeV}$ in recoil. From top to bottom: event class C; D. From left to right: MC ($B\overline{B}$ only); MC($B\overline{B}$, uds, and $c\bar{c}$ combined); Data; Difference between M_{ES} distribution and a resulting fit function, MC and Data.

96

Table 4.8: Normalization of sideband background to the signal region, based on the signal-level M_{ES} distributions, per event class.

Event Class	Sideband	Background in signal box	scaling factor
Data			
A	1326 ± 135	459 ± 47	0.346 ± 0.026
B	818 ± 106	303 ± 39	0.371 ± 0.036
C	838 ± 107	330 ± 42	0.394 ± 0.037
D	731 ± 101	215 ± 30	0.295 ± 0.030
Monte-Carlo			
A	3927 ± 232	1379 ± 81	0.351 ± 0.015
B	2478 ± 185	797 ± 60	0.322 ± 0.018
C	3150 ± 207	1209 ± 79	0.384 ± 0.019
D	2860 ± 198	1000 ± 69	0.350 ± 0.018

All of the above misidentification result in the change of the B flavor and therefore bias the charge-flavor correlation between the electron and B-meson . Cross-feed effects of these three types have been extensively studied. The details of these studies are given below.

4.3.5 B_{reco} cross-feed - from event type mismatch

The simplest way to quantitatively extract the cross-feed levels is to compare the type ($B^0\overline{B^0}$ or B^+B^-) of the generated event to that defined by the resulting B_{reco} mode in simulated data. The cross-feed in this case is described by the following parameter (cross-feed coefficient):

$$CF = \frac{S_{M_{ES}}^{all\ events} - S_{M_{ES}}^{correct\ B\ type}}{S_{M_{ES}}^{all\ events}}$$

where

$S_{M_{ES}}^{all\ events}$ is a signal count obtained from fitting an M_{ES} distribution for all tagged events

$S_{M_{ES}}^{correct\ B\ type}$ is a signal count obtained from fitting an M_{ES} distribution only for events where a generated B type matches that of the B_{reco} B type

This method gives the estimation on the $B^{\pm} \longleftrightarrow B^0$ cross-feed, and a list of related quantities derived through this algorithm is provided in Table 4.9. The same quantities for events which have a primary electron in the recoil are given in Table 4.10. Note that, by construction, these coefficients also absorb signal count biases resulting from any peaking non-$B\overline{B}$ M_{ES} components.

A similar study for different momentum ranges of the primary electron is shown in the appendix, Section 6.1.1. These studies confirm that the cross-feed coefficients do not have significant dependence on the primary electron momentum and therefore can be applied as overall corrections to the normalizations.

The cross-feed coefficients obtained from generic MC and averaged over all

98

B_{reco} modes (separately for $B^\pm$ and B^0 modes) are given in Table 4.11. These numbers are used later in the analysis to correct the normalization (tag counts) before extracting branching fractions from the electron spectra. Note that the cross-feed effect described above produces a peaking background, i.e. the M_{ES} distribution for background events has a non-zero area under the signal peak.

No significant dependency on the momentum of the electron in the recoil is observed for events where one B-meson decays semileptonically. Therefore all cross-feed corrections may be applied on a momentum-independent basis. Half of the observed weighted variation is 0.4%, which we take as an absolute systematic error on the cross-feed coefficients. Based on this absolute error, we assign a 10% relative systematic error to the total tag-level cross-feed and 30% - to the signal-level cross-feed.

Table 4.9: $B^{\pm} \longleftrightarrow B^0$ cross-feed related quantities, from generic Monte-Carlo.

BRECO Mode	Total	Wrong B flavor, M_{ES} fit	cross-feed
$B^{\pm} \to D^0 K\pi, \pi$	25430 ± 222	99 ± 90	0.0039 ± 0.0035
$B^{\pm} \to D^0 K\pi\pi^0, \pi$	45897 ± 324	3148 ± 165	0.0686 ± 0.0036
$B^{\pm} \to D^0 K3\pi, \pi$	41542 ± 299	2753 ± 142	0.0663 ± 0.0035
$B^0 \to D^- K_s\pi, \pi$	3749 ± 89	300 ± 47	0.080 ± 0.013
$B^0 \to D^- K\pi\pi, \pi$	30109 ± 242	1854 ± 113	0.0616 ± 0.0038
$B^0 \to D^{*-} \to D^0\pi \to K\pi, \pi$	6524 ± 107	0 ± 33	0 ± 0.0051
$B^0 \to D^{*-} \to D^0\pi \to K\pi, \pi\pi^0$	12305 ± 160	927 ± 62	0.0753 ± 0.0051
$B^0 \to D^{*-} \to D^0\pi \to K\pi, \pi\pi\pi$	6284 ± 112	343 ± 40	0.0546 ± 0.0065
$B^0 \to D^{*-} \to D^0\pi \to K\pi$	2270 ± 72	0 ± 19	0 ± 0.0085
$B^0 \to D^{*-} \to D^0\pi \to K\pi\pi^0, \pi$	10735 ± 131	75 ± 33	0.0070 ± 0.0031
$B^0 \to D^{*-} \to D^0\pi \to K\pi\pi^0, K$	841 ± 39	75 ± 14	0.089 ± 0.017
$B^0 \to D^{*-} \to D^0\pi \to K\pi\pi^0, \pi\pi^0$	20479 ± 218	1318 ± 98	0.0643 ± 0.0048
$B^0 \to D^{*-} \to D^0\pi \to K\pi\pi^0, \pi\pi\pi$	10072 ± 298	403 ± 264	0.040 ± 0.026
$B^0 \to D^{*-} \to D^0\pi \to K\pi\pi^0, KK\pi$	954 ± 43	0 ± 7.9	0 ± 0.0083
$B^0 \to D^{*-} \to D^0\pi \to K\pi\pi^0$	1531 ± 61	35 ± 27	0.023 ± 0.018
$B^0 \to D^{*-} \to D^0\pi \to K3\pi, \pi$	8437 ± 121	0 ± 4.6	0 ± 0.00055
$B^0 \to D^{*-} \to D^0\pi \to K3\pi, \pi\pi^0$	15627 ± 188	890 ± 79	0.0569 ± 0.0051
$B^0 \to D^{*-} \to D^0\pi \to K3\pi, \pi\pi\pi$	7426 ± 130	67 ± 54	0.0091 ± 0.0073
$B^0 \to D^{*-} \to D^0\pi \to K_s\pi^+\pi^-, \pi$	2275 ± 63	0 ± 6.6	0 ± 0.0029
$B^0 \to D^{*-} \to D^0\pi \to K_s\pi^+\pi^-, \pi\pi^0$	4671 ± 111	471 ± 61	0.101 ± 0.013
$B^0 \to D^{*-} \to D^0\pi \to K_s\pi^+\pi^-, \pi\pi\pi$	2155 ± 71	206 ± 37	0.095 ± 0.017
$B^{\pm} \to D^{*0} \to D^0\pi^0 \to K\pi, \pi$	6819 ± 111	184 ± 20	0.0270 ± 0.0030
$B^{\pm} \to D^{*0} \to D^0\pi^0 \to K\pi, K$	901.7 ± 2.5	0 ± 41	0 ± 0.045
$B^{\pm} \to D^{*0} \to D^0\pi^0 \to K\pi, \pi\pi^0$	14224 ± 171	376 ± 55	0.0264 ± 0.0039
$B^{\pm} \to D^{*0} \to D^0\pi^0 \to K\pi, \pi\pi\pi$	5202 ± 109	0 ± 82	0 ± 0.016
$B^{\pm} \to D^{*0} \to D^0\pi^0 \to K\pi$	2228 ± 73	143 ± 33	0.064 ± 0.015
$B^{\pm} \to D^{*0} \to D^0\pi^0 \to K\pi\pi^0, \pi$	11683 ± 156	105 ± 49	0.0090 ± 0.0042
$B^{\pm} \to D^{*0} \to D^0\pi^0 \to K3\pi, \pi$	10340 ± 144	244 ± 45	0.0236 ± 0.0044
$B^{\pm} \to D^{*0} \to D^0\gamma \to K\pi, \pi$	6282 ± 112	322 ± 37	0.0513 ± 0.0060
$B^{\pm} \to D^{*0} \to D^0\gamma \to K\pi, K$	889 ± 42	95 ± 19	0.107 ± 0.022
$B^{\pm} \to D^{*0} \to D^0\gamma \to K\pi, \pi\pi^0$	11640 ± 179	582 ± 90	0.0500 ± 0.0078
$B^{\pm} \to D^{*0} \to D^0\gamma \to K\pi\pi^0, \pi$	11201 ± 178	255 ± 95	0.0228 ± 0.0085
all $B^{\pm}$	194405 ± 656	7640 ± 288	0.0393 ± 0.0015
all B^0	146616 ± 558	6376 ± 222	0.0435 ± 0.0015

100

Table 4.10: Same as Table 4.9, events with primary electron.

BRECO Mode	Total	Wrong B flavor, M_{ES} fit	cross-feed
$B^{\pm} \to D^0 K\pi, \pi$	5404 ± 94	12.1 ± 8.8	0.0022 ± 0.0016
$B^{\pm} \to D^0 K\pi\pi^0, \pi$	9541 ± 130	40 ± 14	0.0042 ± 0.0015
$B^{\pm} \to D^0 K3\pi, \pi$	8371 ± 119	71 ± 18	0.0085 ± 0.0021
$B^0 \to D^- K_s\pi, \pi$	806 ± 37	20.3 ± 4.9	0.0252 ± 0.0062
$B^0 \to D^- K\pi\pi, \pi$	6101 ± 103	124 ± 29	0.0203 ± 0.0047
$B^0 \to D^{*-} \to D^0\pi \to K\pi, \pi$	1415 ± 48	0 ± 0.96	0 ± 0.00068
$B^0 \to D^{*-} \to D^0\pi \to K\pi, \pi\pi^0$	2571 ± 72	72 ± 15	0.0280 ± 0.0058
$B^0 \to D^{*-} \to D^0\pi \to K\pi, \pi\pi\pi$	1200 ± 38	0 ± 8.5	0 ± 0.0071
$B^0 \to D^{*-} \to D^0\pi \to K\pi$	564 ± 33	15 ± 33	0.027 ± 0.059
$B^0 \to D^{*-} \to D^0\pi \to K\pi\pi^0, \pi$	2285 ± 62	0 ± 8.5	0 ± 0.0037
$B^0 \to D^{*-} \to D^0\pi \to K\pi\pi^0, K$	174 ± 17	5.3 ± 2.9	0.030 ± 0.017
$B^0 \to D^{*-} \to D^0\pi \to K\pi\pi^0, \pi\pi^0$	4644 ± 97	149 ± 21	0.0322 ± 0.0046
$B^0 \to D^{*-} \to D^0\pi \to K\pi\pi^0, \pi\pi\pi$	2190 ± 66	48 ± 12	0.0221 ± 0.0056
$B^0 \to D^{*-} \to D^0\pi \to K\pi\pi^0, KK\pi$	205 ± 16	4.0 ± 2.3	0.019 ± 0.011
$B^0 \to D^{*-} \to D^0\pi \to K\pi\pi^0$	318 ± 24	8.6 ± 5.3	0.027 ± 0.017
$B^0 \to D^{*-} \to D^0\pi \to K3\pi, \pi$	1889 ± 55	6.9 ± 3.5	0.0037 ± 0.0019
$B^0 \to D^{*-} \to D^0\pi \to K3\pi, \pi\pi^0$	3462 ± 83	79 ± 17	0.0228 ± 0.0049
$B^0 \to D^{*-} \to D^0\pi \to K3\pi, \pi\pi\pi$	1732 ± 58	0.7 ± 7.5	0.0004 ± 0.0043
$B^0 \to D^{*-} \to D^0\pi \to K_s\pi^+\pi^-, \pi$	506 ± 30	10 ± 19	0.020 ± 0.038
$B^0 \to D^{*-} \to D^0\pi \to K_s\pi^+\pi^-, \pi\pi^0$	961 ± 44	42 ± 11	0.044 ± 0.012
$B^0 \to D^{*-} \to D^0\pi \to K_s\pi^+\pi^-, \pi\pi\pi$	455 ± 29	9.5 ± 6.3	0.021 ± 0.014
$B^{\pm} \to D^{*0} \to D^0\pi^0 \to K\pi, \pi$	1473 ± 49	0.7 ± 2.7	0.0004 ± 0.0018
$B^{\pm} \to D^{*0} \to D^0\pi^0 \to K\pi, K$	187 ± 19	2.1 ± 4.2	0.011 ± 0.022
$B^{\pm} \to D^{*0} \to D^0\pi^0 \to K\pi, \pi\pi^0$	3030 ± 77	39 ± 13	0.0130 ± 0.0042
$B^{\pm} \to D^{*0} \to D^0\pi^0 \to K\pi, \pi\pi\pi$	1169 ± 48	11 ± 12	0.009 ± 0.011
$B^{\pm} \to D^{*0} \to D^0\pi^0 \to K\pi$	491 ± 32	0 ± 5.5	0 ± 0.011
$B^{\pm} \to D^{*0} \to D^0\pi^0 \to K\pi\pi^0, \pi$	2553 ± 68	28.1 ± 8.0	0.0110 ± 0.0031
$B^{\pm} \to D^{*0} \to D^0\pi^0 \to K3\pi, \pi$	2144 ± 62	28.0 ± 10.0	0.0131 ± 0.0047
$B^{\pm} \to D^{*0} \to D^0\gamma \to K\pi, \pi$	1322 ± 49	42.2 ± 8.4	0.0319 ± 0.0065
$B^{\pm} \to D^{*0} \to D^0\gamma \to K\pi, K$	164 ± 17	0 ± 1.1	0 ± 0.0069
$B^{\pm} \to D^{*0} \to D^0\gamma \to K\pi, \pi\pi^0$	2462 ± 73	92 ± 16	0.0373 ± 0.0067
$B^{\pm} \to D^{*0} \to D^0\gamma \to K\pi\pi^0, \pi$	2394 ± 69	49 ± 13	0.0203 ± 0.0055
all $B^{\pm}$	40735 ± 274	366 ± 42	0.0090 ± 0.0010
all B^0	31754 ± 244	598 ± 45	0.0188 ± 0.0014

101

Table 4.11: $B^{\pm} \longleftrightarrow B^0$ cross-feed related quantities, from generic Monte-Carlo.

All events

BRECO Mode	Total	Wrong B flavor, M_{ES} fit	cross-feed
all $B^{\pm}$	194405 ± 656	7640 ± 288	0.0393 ± 0.0015
all B^0	146616 ± 558	6376 ± 222	0.0435 ± 0.0015

Events with primary electron

BRECO Mode	Total	Wrong B flavor, M_{ES} fit	cross-feed
all $B^{\pm}$	40735 ± 274	366 ± 42	0.0090 ± 0.0010
all B^0	31754 ± 244	598 ± 45	0.0188 ± 0.0014

events with primary electron of $p^* < 1.0$ GeV/c

BRECO Mode	Total	Wrong B flavor, M_{ES} fit	cross-feed
all $B^{\pm}$	9465 ± 131	100 ± 19	0.0105 ± 0.0020
all B^0	7390 ± 116	129 ± 20	0.0175 ± 0.0028

events with primary electron of $1.0 < p^* < 2.0$ GeV/c

BRECO Mode	Total	Wrong B flavor, M_{ES} fit	cross-feed
all $B^{\pm}$	20786 ± 192	210 ± 29	0.0101 ± 0.0014
all B^0	16186 ± 174	265 ± 31	0.0164 ± 0.0019

events with primary electron of $2.0 < p^*$ GeV/c

BRECO Mode	Total	Wrong B flavor, M_{ES} fit	cross-feed
all $B^{\pm}$	10486 ± 141	55 ± 35	0.0052 ± 0.0033
all B^0	8170 ± 126	209 ± 21	0.0255 ± 0.0026

102

4.3.6 B_{reco} cross-feed - from studying events with $b \to cl\nu$ and $b \to c \to Xl\nu$ decays in recoil

To determine the effect B_{reco} cross-feed has on the electron spectra we detect in this analysis, the following method has been used: the origin of all reconstructed electrons has been identified using MC truth information. If the origin of an electron is a semileptonic B decay or the cascade decay of D meson, the information on the flavor of B-meson is obtained from the charge of the electron. Since the reconstructed electron belongs to the recoil B-meson decay chain, this directly provides the information on the true flavor of the other B meson which was reconstructed hadronically by the B_{reco} process. A direct comparison of this true flavor with the flavor obtained from the B_{reco} output allows the derivation of the appropriate cross-feed quantities. The benefit of this method is that the cross-feed ratios can be directly applied to electron spectra in all event classes after background subtractions allowing reliable cross-feed corrections.

Table 4.13 shows the cross-feed quantities derived from the events with semileptonic B decay ($b \to e$). The same quantities derived from events with cascade B decay ($b \to c \to e$) are provided in Table 4.14. The explanation of the values in the above tables is given in Table 4.12. $B^0 \leftrightarrow \overline{B^0}$ mixing effects are properly taken into account in all cross-feed coefficient calculations.

These coefficients, $CF^{generated\ B\ flavor}_{B_{reco}\ B\ flavor}$, are then applied to the final spectra in each of the 4 classes (Table 4.2) to derive corrections by subtracting fractions of spectra in other event classes to account for events moved from those classes.

Generally, flavor-changing cross-feed effects (such as $B^0 \to B^-$ or $B^+ \to B^-$) will move events from wrong-sign to right-sign events and vice versa, while flavor-conserving cross-feed (such as $B^0 \to B^+$) will keep the correlation. Formulas similar to the above are applied to all event classes. To correct right-sign event classes (A, C), the cross-feed ratios derived from the events with semileptonic B

Table 4.12: Template table for cross-feed matrices below. All numbers and co-efficients are calculated for a certain B_{reco} mode or mode set. The top number in the B^-/B^+ ($B^0/\overline{B^0}$) columns represents the total number of B events (from M_{ES} fit) reconstructed with a certain flavor of the B_{reco} B-meson . In the N_{gen} column, the total numbers of B events (from the M_{ES} fit) where a B-meson was generated in a certain flavor AND reconstructed into a certain flavor, not neces-sarily identical to the generated flavor. In the inner cells of the table we show the ratio of the event counts generated in a certain flavor to the event counts reconstructed in a certain flavor.

B_{reco} mode: all $B^{\pm}$			
True	N_{gen}	Reconstructed as	
		B^-	B^+
		$N^{reconstructed}_{as\ B-}$	$N^{reconstructed}_{as\ B+}$
B^-	$N^{generated}_{as\ B-}$	CF^{B-}_{B-}	CF^{B-}_{B+}
B^+	$N^{generated}_{as\ B+}$	CF^{B+}_{B-}	CF^{B+}_{B+}
B^0	$N^{generated}_{as\ B0}$	CF^{B0}_{B-}	CF^{B0}_{B+}
$\overline{B^0}$	$N^{generated}_{as\ \overline{B^0}}$	$CF^{\overline{B^0}}_{B-}$	$CF^{\overline{B^0}}_{B+}$

104

decays are applied. To correct wrong-sign event classes (B, D), the cross-feed ratios derived from the events with cascade B decays are applied.

We define the following cross-feed correction matrix:

$$
M_{CF} = \begin{pmatrix}
-- & {}^{C}CF_{B+}^{B-} + {}^{C}CF_{B-}^{B+} & {}^{SL}CF_{B^0}^{B+} + {}^{SL}CF_{\overline{B^0}}^{B-} & {}^{C}CF_{\overline{B^0}}^{B-} + {}^{C}CF_{B^0}^{B-} \\
{}^{SL}CF_{B+}^{B-} + {}^{SL}CF_{B-}^{B+} & -- & {}^{SL}CF_{B^0}^{B-} + {}^{SL}CF_{\overline{B^0}}^{B+} & {}^{C}CF_{B^0}^{B+} + {}^{C}CF_{\overline{B^0}}^{B-} \\
{}^{SL}CF_{B+}^{B^0} + {}^{SL}CF_{B-}^{\overline{B^0}} & {}^{C}CF_{B+}^{\overline{B^0}} + {}^{C}CF_{B-}^{B^0} & -- & {}^{C}CF_{B^0}^{\overline{B^0}} + {}^{C}CF_{\overline{B^0}}^{B^0} \\
{}^{SL}CF_{B+}^{\overline{B^0}} + {}^{SL}CF_{B-}^{B^0} & {}^{C}CF_{B+}^{B^0} + {}^{C}CF_{B-}^{\overline{B^0}} & {}^{SL}CF_{B^0}^{\overline{B^0}} + {}^{SL}CF_{\overline{B^0}}^{B^0} & --
\end{pmatrix}
$$

Using this matrix, the resulting cross-feed correction to the spectrum can be expressed as

$$
\begin{pmatrix} A \\ B \\ C \\ D \end{pmatrix}_{BG} = \frac{M_{CF}}{2} \times \begin{pmatrix} A \\ B \\ C \\ D \end{pmatrix}_{reco}
$$

The above expression assumes equal number of $B^{\pm}$ and B^0 events in the sample, which is a valid assumption for the Monte-Carlo and Data samples used in this analysis. Contamination of the electron spectrum is then subtracted from each of the four event classes according to the above matrix. Coefficients marked as $^{SL}CF_{rec}^{gen}$ are used in correcting for contributions from events detected in classes A and C, while coefficients marked as $^{C}CF_{rec}^{gen}$ are used in correcting for contributions from events detected in classes B and D.

The other effect of the cross-feed is that some fraction of events of true class A are reconstructed as events of another class thereby decreasing the efficiency to detect class A events. When this decrease in the efficiency is different from the corresponding decrease in $B^{\pm}$ tag count, the correction has to be applied. This correction is absorbed in the Efficiency Bias Correction described later in Section

105

Table 4.13: Cross-feed coefficients from generic Monte-Carlo, for all $B^{\pm}$ and B^0 B_{reco} modes, from studying B_{reco} side in Semileptonic decays of the recoil B.

BRECO mode: all $B^{\pm}$			
True	N_{gen}	Reconstructed as	
		B^-	B^+
		7765 ± 118.7	7907 ± 118.0
B^-	7741 ± 118.0	$0.997^{+0.0033}_{-0.022}$	0 ± 0.0021
B^+	7788 ± 117.9	0 ± 0.00016	$0.987^{+0.013}_{-0.021}$
B^0	106 ± 16.7	0.00060 ± 0.00039	0.01302 ± 0.00073
$\overline{B^0}$	34 ± 14.2	0.0044 ± 0.0018	0.00002 ± 0.00024

BRECO mode: all B^0			
True	N_{gen}	Reconstructed as	
		B^0	$\overline{B^0}$
		6117 ± 105.3	6109 ± 105.1
B^-	122 ± 19.0	0.00205 ± 0.00065	0.0180 ± 0.0026
B^+	92 ± 17.8	0.0150 ± 0.0029	0.00043 ± 0.00018
B^0	6005 ± 104.7	$0.981^{+0.019}_{-0.024}$	0.00143 ± 0.00047
$\overline{B^0}$	6003 ± 103.9	0.00197 ± 0.00079	$0.980^{+0.020}_{-0.024}$

Table 4.14: Cross-feed related quantities from generic Monte-Carlo, for all B^0 and $B^{\pm}$ B_{reco} modes, from studying B_{reco} side in $b \rightarrow c \rightarrow Xl\nu$ decays of the recoil B.

BRECO mode: all $B^{\pm}$			
True	N_{gen}	Reconstructed as	
		B^-	B^+
		868 ± 38.8	904 ± 40.1
B^-	869 ± 39.8	$1.000^{+0}_{-0.063}$	0 ± 0.0017
B^+	878 ± 38.9	0.0056 ± 0.0021	$0.972^{+0.028}_{-0.061}$
B^0	27 ± 7.9	0.0034 ± 0.0031	0.0258 ± 0.0095
$\overline{B^0}$	2 ± 2.6	0 ± 0.0048	0.0083 ± 0.0043

BRECO mode: all B^0			
True	N_{gen}	Reconstructed as	
		B^0	$\overline{B^0}$
		938 ± 41.7	959 ± 41.8
B^-	8 ± 7.6	0 ± 0.0018	0.0124 ± 0.0075
B^+	24 ± 7.9	0.0161 ± 0.0089	0.0061 ± 0.0013
B^0	930 ± 42.0	$0.994^{+0.0055}_{-0.062}$	0 ± 0.0014
$\overline{B^0}$	941 ± 42.2	0 ± 0.0020	$0.984^{+0.016}_{-0.061}$

107

4.5.1.

108

4.3.7 Track Selection

Charged particle tracks are taken from one of the standard *BABAR* track lists referred to as the *GoodTracksLoose* list. But in this analysis, the track selection criteria are then tightened for electrons to suppress background and to ensure a reliable measurement of the identification efficiency. Hence the following additional cuts are applied to the tracks found in the GoodTracksLoose list :

- $p_{lab} > 0.5\,\text{GeV}/c$, where p_{lab} refers to the laboratory momentum of the track,

- $p^* > 0.5\,\text{GeV}/c$, where p^* refers to the momentum of the track in the rest frame of the recoil B-meson , and

- the polar angle acceptance is restricted to $0.36 < \theta_{lab} < 2.37$.

Table 4.15 shows the generator level efficiency of applying these cuts. The single cuts on p^* and p_{lab} have an inefficiency of roughly 4%. The loss of efficiency due to the angular cuts is approximately 14%. The latter is used later in the analysis to correct for the geometric acceptance. All other efficiencies in Table 4.15 are given for reference purposes as an estimate of the effect our track selection cuts have on the electron spectrum. The geometric acceptance efficiency has also been calculated analytically assuming a uniform angular distribution for tracks of primary electrons in the rest frame of the recoil B-meson . The two estimates agree within errors.

4.3.8 Electron Identification

Electrons are identified using a likelihood-based selector [34], which uses a number of discriminating variables:

Table 4.15: Efficiency of kinematic cuts imposed on electron candidates on the generator level. The cuts in the first three rows indicate the efficiency applying one cut only. The last three rows show the cumulative efficiency.

Sample	$B[\%]$	$B^{\pm}[\%]$	$B^0[\%]$
$p_{lab} > 0.5\,\text{GeV}/c$	0.9568 ± 0.0013	0.9549 ± 0.0020	0.9586 ± 0.0018
$p^* > 0.5\,\text{GeV}/c$	0.9597 ± 0.0013	0.9582 ± 0.0019	0.9612 ± 0.0018
$20.6° < \theta < 135.9°$	0.8626 ± 0.0023	0.8622 ± 0.0033	0.8629 ± 0.0032
p_{lab}, p^*	0.9445 ± 0.0015	0.9423 ± 0.0022	0.9466 ± 0.0021
p^*, θ	0.8272 ± 0.0025	0.8262 ± 0.0036	0.8282 ± 0.0035
p_{lab}, p^*, θ	0.8177 ± 0.0026	0.8168 ± 0.0037	0.8186 ± 0.0035

- E_{cal}/p_{lab}, the ratio of E_{cal}, the energy deposited in the EMC, and p_{lab} the momentum in the laboratory frame measured using the tracking system; LAT, the lateral shape of the calorimeter deposit; $\Delta\Phi$, the azimuthal distance between the centroid of the EMC cluster and the impact point of the track on the EMC; and N_{cry}, the number of crystals in the EMC cluster;

- dE/dx, the specific energy loss in the DCH;

- the Cherenkov angle θ_C and N_C, the number of photons measured in the DRC.

First, muons are eliminated based on the dE/dx and shower energy relative to their momentum. For the remaining tracks, separate likelihood functions are computed assuming the particle is an electron, pion, kaon, or proton. These likelihood functions are based on probability density functions that are derived from pure particle data control samples for each of the discriminating variables. For hadrons, we take into account the correlations between energy and shower-

110

shapes. Using combined likelihood functions

$$L(\xi) = P(E/p, LAT, \Delta\Phi, dE/dx, \theta_C|\xi)$$

$$= P_{Emc}(E/p, LAT, \Delta\Phi|\xi) \, P_{Dch}(dE/dx|\xi) \, P_{Drc}(\theta_C|\xi)$$

for the hypotheses ξ in $\{e, \pi, K, p\}$, the fraction

$$F_e = \frac{f_e L(e)}{\sum_\xi f_\xi L(\xi)} \, , \tag{4.4}$$

is defined, where, for the relative particle fractions, $f_e : f_\pi : f_K : f_p = 1 : 5 : 1 : 0.1$ is assumed. A track is identified as an electron if $F_e > 0.95$.

The electron identification efficiency has been measured using radiative Bhabha events, as a function of laboratory momentum p_{lab} and polar angle θ_{lab}. The misidentification rates for pions, kaons, and protons are extracted from selected data samples. Pure pions are obtained from kinematically selected $K_S^0 \to \pi^+\pi^-$ decays and three prong $\tau^\pm$ decays. Two-body Λ and D^0 decays provide pure samples of protons and charged kaons.

The performance of the likelihood-based electron identification algorithm is summarized in Figure 4.10, in terms of the electron identification efficiency and the per track probability that a hadron is misidentified as an electron.

The average hadron fake rates per track are determined separately for positive and negative particles, taking into account relative abundances from Monte Carlo simulation of $B\overline{B}$ events. The resulting average fake rate per hadron track of $p_{lab} > 0.5\,\mathrm{GeV}/c$ is of the order of 0.05% for pions and 0.4% for kaons.

The raw spectra of the detected electrons after all event and track selections are given in the Figure 4.11. The corresponding electron yields are given in the Table 4.16.

111
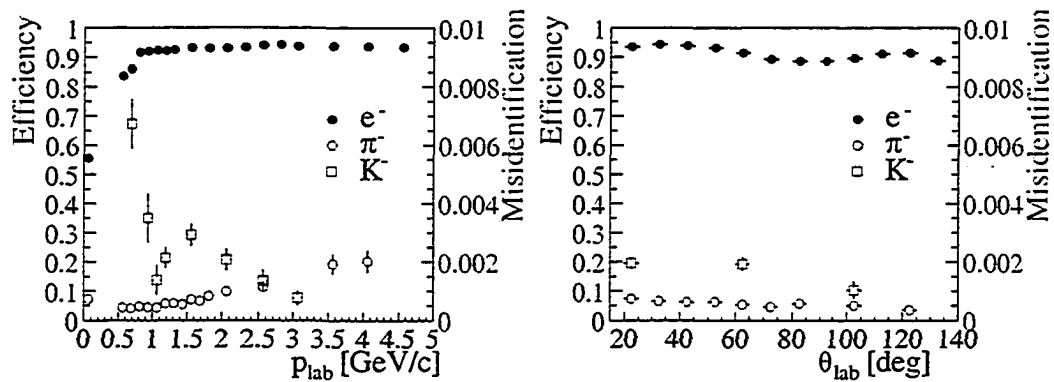
Figure 4.10: Electron identification and hadron misidentification probability for the likelihood-based electron selector as a function of momentum (left) and polar angle (right). Scales for identification and misidentification are the left and right ordinates, respectively.

Table 4.16: Electron Spectrum: Sideband subtraction before any corrections. The error given corresponds to the statistical error.

Sample	A	B	C	D
Signal box	5362 ± 73	1738 ± 42	3686 ± 61	2032 ± 45
Unscaled Sideband	1363 ± 37	843 ± 29	850 ± 29	746 ± 27
Sideband-subtracted	4891 ± 74	1425 ± 43	3351 ± 62	1812 ± 46
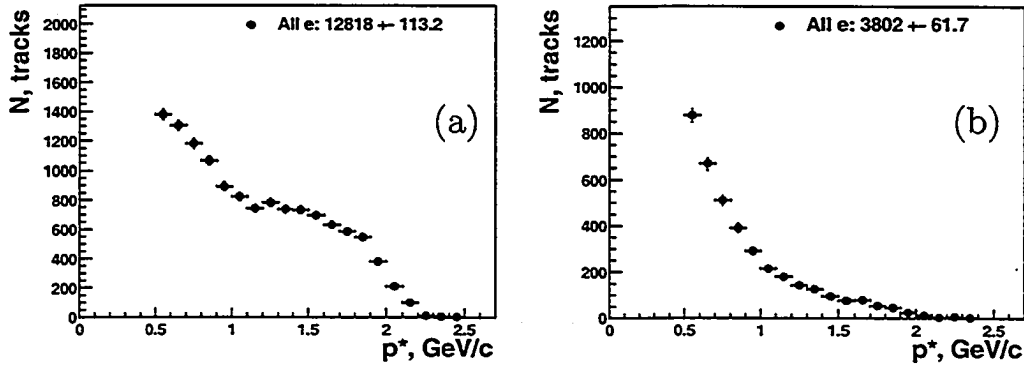
Figure 4.11: Raw electron spectra before any background corrections, as detected. (a) - signal box, (b) - unscaled contribution from M_{ES} sideband region.

4.4 Electron Background Subtraction

The raw measured electron spectra obtained from Data for the signal box and sideband are shown in Figure 4.11. These raw spectra contain electrons from prompt and cascade B-meson decays plus various background sources that need to be subtracted. The spectra also have to be corrected for the efficiency of detecting an electron track in a tagged event. The corrections are performed in the following order:

- Correction for electrons from converted photons, Dalitz and J/ψ decays

    Estimated by counting the number of pair vertices that satisfy specific sets of kinematic cuts.

- Correction for hadrons mis-identified as electrons

    Estimated for each of the three hadron types (π, K, p) using mis-ID rates determined from hadron control samples, relative abundance of hadrons of each type determined from the Monte-Carlo sample and the detected non-electron spectrum.

113

- Correction for tracking and electron identification efficiencies

  Determined from the efficiency tables provided by the *BABAR* tracking and PID groups, respectively.

- Correction for $B^0 \leftrightarrow \overline{B^0}$ mixing effects

  Due to the mixing, electron spectra from B^0 decay chain in classes C and D are linear combinations of the prompt and cascade electron spectra. The corresponding mixing equations are solved for the prompt spectrum. Latest PDG 2002 value for the mixing parameter, χ_d is used.

- Correction for electrons from decays other than semileptonic B decays (decays of, *e.g.*, D-mesons, τ, Λ_c, *etc.*)

  Determined from Monte-Carlo. Predicted spectra for all decay modes are adjusted for differences between Monte-Carlo branching fractions and the latest experimental results by applying corresponding rescaling factors.

- Correction for cross-feed effects

  Cross-feed coefficients and methodology are defined in Section 4.3.6.

- Correction for electrons lost due to bremsstrahlung

  Monte-Carlo simulation is used to populate a three-dimentional matrix translating reconstructed p^*, θ into the generated ones. The matrix is applied to the fully corrected spectra from Data to arrive at the true $b \rightarrow e$ spectrum.

- Correction for P_{LAB} cut efficiency and Geometric Acceptance

  Monte-Carlo simulation is used to derive corresponding correction coefficients.

The rest of this section will deal with each correction in detail.

114

4.4.1 Pair Background

ISL pair-finder

Electrons from photon conversions and Dalitz decays are identified with the ISL pair-finder [37], which is a significant improvement with respect to the standard conversion finder of BABAR . The improvements include an introduction of an additional parameter, the radial coordinate of the pair vertex, as well as better parameter settings. As a result, much cleaner separation of the conversion electrons and electrons from Dalitz decays becomes possible.

Figure 4.12a shows a schematic explanation of the pair finder algorithm.

The algorithm finds a vertex position and a distance between two tracks of opposite charge. It uses first the projection of the two helixes in the x-y plane.

From the track parameters R, the radius, d_0, the distance of the closest approach to the x-axis (doca) and ϕ_0, the angle at the point of closest approach, one can calculate the position of the points A and B which are the two points on the tracks where the tangents are parallel.

Δxy is defined as the distance between the points A and B. The center M of $[A, B]$ is defined as the conversion point or the vertex point. When the two circles intersect, a negative sign is assigned to Δxy. The point M is still the center of $[A, B]$, defined as given in Figure 4.12b.

Δz is the z-coordinate difference between the points A and B. To calculate it, the parameters z_0, the z coordinate of the point of closest approach, and $\tan \theta$, the elevation of the track above z axis, are necessary inputs.

$$z_A = z_0 + S_A \times \tan \theta \qquad (4.5)$$

where S_A is the length on the circle between the point of doca and the point A
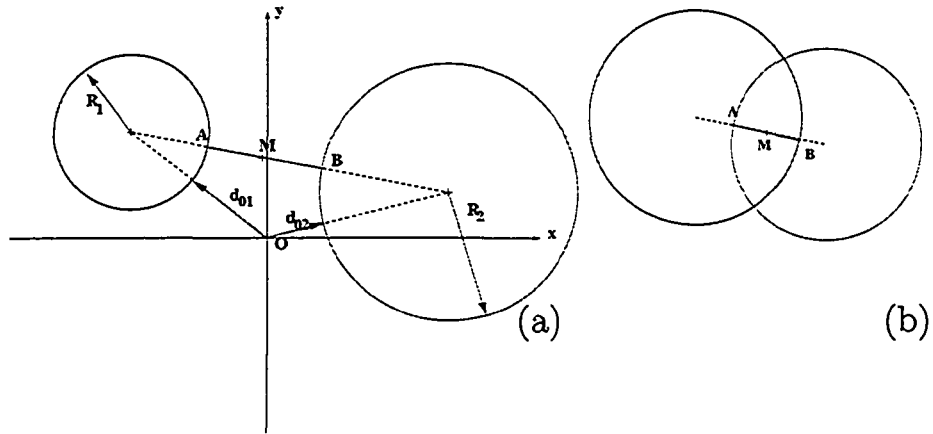
Figure 4.12: (a) Principle of the ISL pair finder algorithm, for (a) positive and (b) negative Δxy definitions.

Table 4.17: ISL Pair Finder cuts used in the detection of pair background. d is the distance of the closest approach of the momentum vector of an electron pair to the interaction point. r is the distance of the conversion point from the interaction point in x-y plane. m_{ee} is the invariant mass of the electron pair.

Background	$m_{ee}[\text{GeV/c}^2]$	$|\Delta_{xy}|[cm]$	$|\Delta_z|[\text{cm}]$	$d[\text{cm}]$	$r[\text{cm}]$
Conversions	< 0.01	< 0.3	< 1.0	< 2.5	> 1.6
Dalitz decays	< 0.02	< 0.2	< 1.0	< 2.5	< 1.6

116

Photon Conversion Background

The standard ISL Pair Finder described above is used to detect pairs of electrons originating from photon (γ) conversions. We apply cuts on the values of Δxy, Δz and of the mass of the γ candidate (Table 4.17). The efficiency of the finder has been determined in generic $B\overline{B}$ Monte Carlo events,

$$\varepsilon_{\gamma \rightarrow ee} = 36.4 \pm 2.6\%(stat).$$

This efficiency is relatively low, mainly due to asymmetric conversion pairs where one of the electrons is lost. The contribution of conversion electrons to the total electron spectrum is quite large at low momenta. Figure 4.13 shows a comparison of the detected (reconstructed, sideband-subtracted and corrected for finder efficiency) yield in **Monte-Carlo** with the number of generated (and reconstructed) electrons from converted photons (as determined from Monte Carlo Truth). Figure 4.14 shows a comparison of the reconstructed track yield after sideband subtraction and correction for finder efficiency in **Data** with the yield predicted by Monte-Carlo. Good agreement is observed in both cases. The conversion finder has a misidentification rate of less than 8% in the statistically relevant part of the electron spectrum [39]. This impurity is taken into account in the efficiency correction.

To examine the systematic uncertainty for this background estimate, we rewrite the finder efficiency ϵ_c in terms of three factors

$$\epsilon_c = \epsilon_c^{pair} \epsilon_c^{trk} \epsilon_c^{vtx} \tag{4.6}$$

where

- ϵ_c^{pair} is the probability for the other track to exceed $p_t > 0.1$ GeV/c, which is required to assure high tracking efficiency. ϵ_c^{pair} depends on the underlying photon spectrum. To check how well this spectrum is reproduced in

117

the Monte Carlo simulation, we compare the p_t distributions of found conversions in MC and data. Another check is the comparison of the energy spectrum of found conversions in data and MC. Checks performed in [19] indicate good agreement. From this we derive an estimate of $\left(\Delta\epsilon_c^{pair}/\epsilon_c^{pair}\right)_{sys}$ = 10%.

- ϵ_c^{trk} is the probability for the second track to be reconstructed. ϵ_c^{trk} depends on the tracking efficiency, which at low momenta is known to 1% for *GoodTracksLoose*. We accept larger impact parameters for the second track than specified in *GoodTracksLoose*, and we estimate $\left(\Delta\epsilon_c^{trk}/\epsilon_c^{pair}\right)_{trk}$ = 1.5%.

- ϵ_c^{vtx} is the probability that once both tracks are reconstructed, they also pass the vertexing criteria listed in Table 4.17. We determine the uncertainty in this procedure by comparing the distributions of Δ_{xy}, Δ_z, and invariant mass M_{ee} for data and MC. While leaving the cuts on two of these variables fixed, the cut on the third is loosened, and the change in the yield is observed. From this study we arrive at a relative systematic uncertainty of $\left(\Delta\epsilon_c^{vtx}/\epsilon_c^{vtx}\right)_{sys}$ = 8%.

In summary, by adding the relative uncertainties in the individual efficiency factors in quadrature we arrive at a total uncertainty. Specifically, for conversion background we obtain

$$\left(\frac{\Delta\epsilon_c}{\epsilon_c}\right)_{sys} = 13\%. \tag{4.7}$$

Dalitz Decay Background

The electrons from the $\pi^0 \to e^+e^-\gamma$ decays are identified with the same pair finder as used for detecting photon conversions, with an additional cut on the position of the electron production vertex (Table 4.17). The very small lifetime

118

of the π^0 results in most Dalitz electrons being confined within a very small distance from the beam spot. Photon conversions, on the other hand, tend to be produced by photon interaction with the material of the detector and therefore are not abundant near the beam spot. This distinction allows efficient separation of γ conversion and Dalitz electrons. The efficiency for detection of an e^+e^- pair from a π^0 Dalitz decay is

$$\epsilon_{\pi^0 \rightarrow eeX} = 22.3 \pm 4.8\%(stat)$$

The main contributions to the inefficiency comes from the requirement on the second track (mainly $N_{Dch} \geq 12$). This could be remedied by combining electron candidates with tracks from the ChargedTracks list, but this would result in a significant increase in the systematic error associated with the track finding efficiency and an increase in combinatoric background for the finder. Figure 4.13 shows a comparison of the detected (reconstructed, sideband-subtracted and corrected for finder efficiency) yield in **Monte-Carlo** with the number of generated (and reconstructed) electrons from Dalitz decays (as determined from Monte Carlo Truth). Figure 4.14 shows a comparison of the reconstructed track yield after sideband subtraction and correction for finder efficiency in **Data** with the yield predicted by Monte-Carlo. Good agreement is observed in both cases. The Dalitz finder has a misidentification rate of $\sim 20\%$ in the statistically relevant part of the electron spectrum [40]. This impurity is taken into account in the efficiency correction.

The systematic uncertainty for this background is estimated using the same procedure as described above for conversions. For Dalitz decays, ϵ_d^{vtx} is lower compared to conversions, which results in a higher relative error, $\left(\Delta\epsilon_d^{vtx}/\epsilon_d^{vtx}\right)_{sys}$ = 16%. Furthermore, since we require a loose electron identification for the second track, we have $\left(\Delta\epsilon_d^{trk}/\epsilon_d^{trk}\right)_{sys}$ = 2%. Combined with $\left(\Delta\epsilon_d^{pair}/\epsilon_d^{pair}\right)_{sys}$

119

= 10%, the systematic error on the Dalitz electron efficiency is

$$\left(\frac{\Delta \epsilon_d}{\epsilon_d} \right)_{sys} = 19\%. \tag{4.8}$$

J/ψ Background

Electrons from J/ψ decays are identified by combining each signal electron candidate with all tracks from the GoodTrackLoose list identified with the "tight" electron selector. The mass of the J/ψ candidate is calculated after constraining the two electron candidates to come from a common vertex. If multiple combinations occur for a signal electron candidate, the combination with the highest vertex probability is chosen. Requiring the second track to be identified as an electron lowers the J/ψ reconstruction efficiency by about 10% (absolute), but decreases the combinatoric background substantially. This allows us to neglect combinatoric background in the mass window $2.95 < m_{ee} < 3.14\,\mathrm{GeV}$. The efficiency of detecting the electron from J/ψ decay is determined from Monte-Carlo simulation by comparing the number of reconstructed electrons whose parent is a J/ψ to the number of electrons detected by the above algorithm:

$$\epsilon_{J/\psi \to ee} = 68.3 \pm 5.5\% (stat).$$

Within the statistical error, the reconstruction efficiency is the same for all electron subsamples (positive and negative electrons in all event classes). Figure 4.15c compares the m_{ee} distributions from reconstructed electrons in the Monte Carlo sample with the generated distributions for electrons from J/ψ decays.

The systematic uncertainty for this background is conservatively estimated at 10% based on the observed differencies in detected yields for Data sample and true yields for Monte-Carlo sample (Figure 4.14).

The actual corrections for the pair backgrounds are shown on Figure 4.16

120
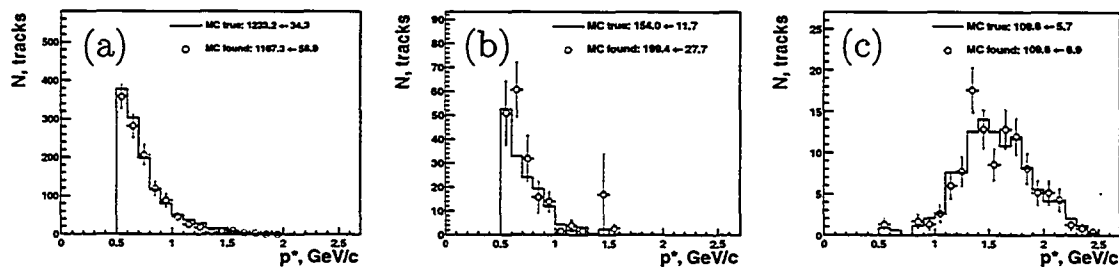
Figure 4.13: Comparison of the detected (efficiency-corrected but not sideband subtracted) momentum spectrum of background electrons with the true yield of reconstructed electrons from same source (all in Monte Carlo sample, used to cross-check the pair finders). (a) - Conversion photons, (b) - Dalitz decays, (c) - J/ψ.
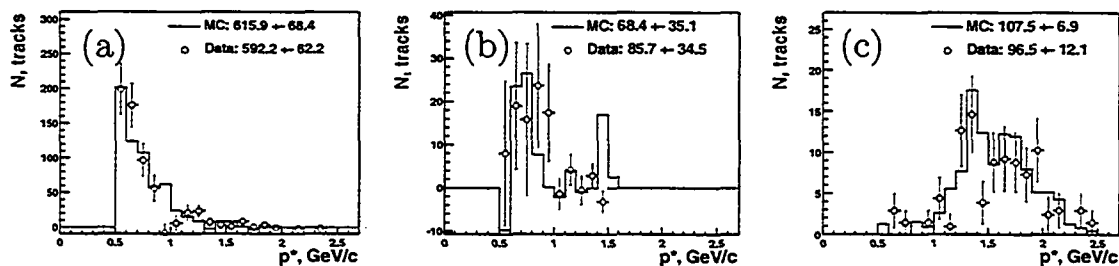
Figure 4.14: Comparison of the reconstructed (efficiency-corrected and sideband subtracted) momentum spectrum of background electrons from: (a) - Converted photons, (b) - Dalitz decays, (c) - J/ψ, in DATA and Monte Carlo. The histogram indicates the yield expected from Monte Carlo truth where as the solid markers show the reconstructed yield from data.

121
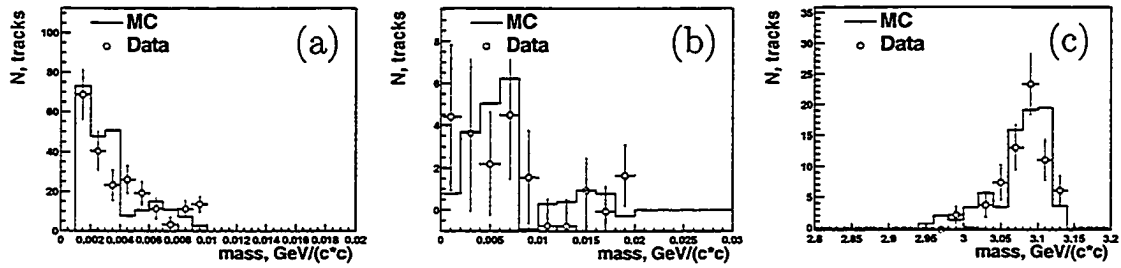
Figure 4.15: Invariant mass distribution for electron pairs (positrons included) in Monte Carlo and Data for (a) - Conversion (b) - Dalitz and (c) - J/ψ candidates. All distributions are sideband-subtracted *but not* adjusted for detection efficiencies.

(for total electron spectrum) and Figure 4.17 (events in classes A and C). The corresponding subtraction statistics is shown in Table 4.19. Comparison of the detected pair backgroud in data with the expected yield determined from MC is shown for all event classes in Table 4.18.

122
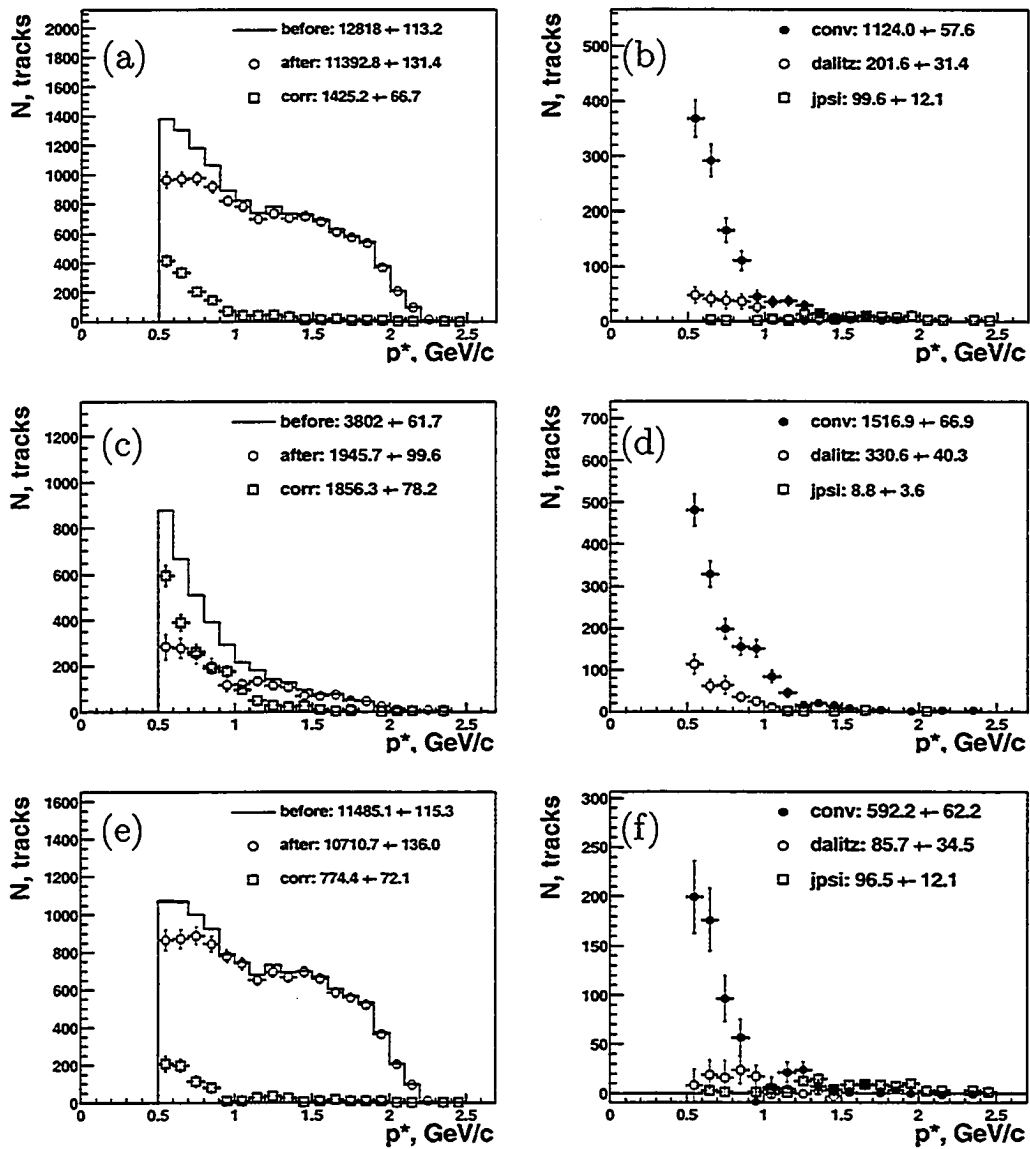
Figure 4.16: Pair Background Subtraction - Signal Box (a,b), Sideband (c,d), Sideband-subtracted (e,f). Left side - subtraction of the combined pair background, Right side - background spectra.

123
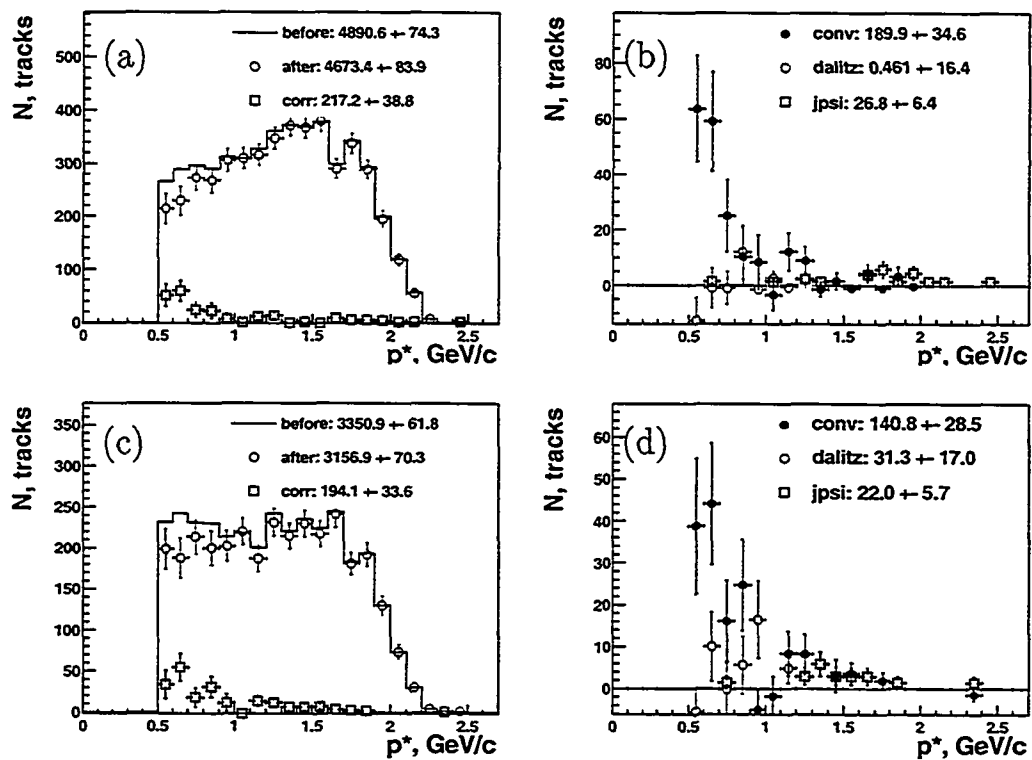
Figure 4.17: Pair Background Subtraction from sideband-subtracted raw electron spectra. (a) - subtraction of the combined pair background, event class A; (b) - background spectra, event class A; (c) - subtraction of the combined pair background, event class C; (d) - background spectra, event class C.

124

Table 4.18: Comparison of Data and Monte Carlo yields of backgrounds from converted photons, π^0 Dalitz decays, and J/ψ decays. The column labeled as "fraction" denotes the contribution relative to all electrons observed in B-meson decays in Data sample. The "MC Truth" label denotes the reconstructed electrons matched to true electrons from the appropriate pair background source.

leptons	Background	DATA	MC Truth	Fraction (DATA) [%]
$e^\pm$, all event classes signal box	Conversions	1124 ± 58	—	8.76 ± 0.45
	Dalitz	202 ± 31	—	1.57 ± 0.24
	J/ψ	100 ± 12	—	0.530 ± 0.060
$e^\pm$, all event classes sideband	Conversions	1517 ± 67	—	39.9 ± 1.9
	Dalitz	331 ± 40	—	8.7 ± 1.1
	J/ψ	8.8 ± 3.6	—	0.150 ± 0.060
$e^\pm$, all event classes sideband-subtracted	Conversions	592 ± 62	616 ± 68	5.15 ± 0.54
	Dalitz	86 ± 34	68 ± 35	0.74 ± 0.30
	J/ψ	97 ± 12	107.5 ± 6.9	0.570 ± 0.070
$e^\pm$, class A sideband-subtracted	Conversions	190 ± 35	211 ± 38	3.88 ± 0.71
	Dalitz	0 ± 16	8 ± 14	0 ± 0.33
	J/ψ	26.8 ± 6.4	34.2 ± 3.9	0.370 ± 0.080
$e^\pm$, class B sideband-subtracted	Conversions	140 ± 34	180 ± 35	9.8 ± 2.4
	Dalitz	40 ± 20	30 ± 21	2.8 ± 1.4
	J/ψ	29.1 ± 6.8	33.0 ± 3.8	1.39 ± 0.32
$e^\pm$, class C sideband-subtracted	Conversions	141 ± 28	128 ± 33	4.20 ± 0.85
	Dalitz	31 ± 17	-5 ± 14	0.93 ± 0.50
	J/ψ	22.0 ± 5.7	20.4 ± 3.0	0.44 ± 0.11
$e^\pm$, class D sideband-subtracted	Conversions	121 ± 27	99 ± 31	6.7 ± 1.5
	Dalitz	16 ± 15	36 ± 19	0.86 ± 0.82
	J/ψ	18.6 ± 5.3	20.0 ± 3.0	0.70 ± 0.20

Table 4.19: Electron Spectrum: Pair background yields. The error corresponds to the statistical error.

Sample	A	B	C	D
Conversions	190 ± 35	140 ± 34	141 ± 28	121 ± 27
Dalitz	0 ± 16	40 ± 20	31 ± 17	16 ± 15
J/ψ	26.8 ± 6.4	29.1 ± 6.8	22.0 ± 5.7	18.6 ± 5.3
Total	217 ± 39	209 ± 40	194 ± 34	155 ± 31

126

4.4.2 Hadron Misidentification

Hadrons can be misidentified as electrons (for overview of electron identification methodology used in this analysis, see Section 4.3.8). This has been studied in detail and is *not* well described in the Monte Carlo simulation. The deficiency of the MC shows up most prominently in a failure to describe the interactions of hadrons in the Calorimeter (EMC), leading to a significant underestimation of the hadron misidentification when applying electron selectors on MC simulated events. The remedy is to use specially generated efficiency tables ("Particle Identification Tables" or "PidTables") for the misidentification probability. Hadron control samples from Data are used to generate these efficiency tables for different types of electron identification settings. The tables are then used in the analysis to determine the misidentification probability on a track-by-track basis. It is crucial to include all stable hadrons in the background studies for misidentification. For example, even though the absolute fraction of anti-protons is quite small (a few %), their misidentification probability is very large at certain momenta (due to annihilation in the EMC). Kaons have relatively large misidentification probabilities at low momenta, where they dominate the fake background. The high fake rates of kaons and anti-protons are also due to their dE/dx bands crossing the electron band. Studies are underway to suppress this contamination with a kaon veto (this degrades the electron identification efficiency at low momenta) and improved cuts on both the DRC and Drift Chamber variables.

Due to different interaction cross-sections and processes, the misidentification probability is significantly different for positive and negative hadrons. This is fully corrected with the PidTables, which allow us to weight all hadron tracks with a weight

127

$$w = \eta(p, \theta, \phi, q) = \sum_{i=\pi, K, p} f_i(p, \theta, \phi, q) \cdot \eta_i(p, \theta, \phi, q),$$

where η_i denotes the probability that a particle of type i is misidentified as an electron. f_i is the fraction of particle i relative to the sum of all charged hadrons. The values of f_i are taken from a Monte Carlo sample of generic B-decays. Figure 4.18 shows projections of the hadron fractions averaged over B flavors along with hadronic fractions separately for $B^{\pm}$ and B^0 decays. There is a significant difference between the same fractions in B^0 and $B^{\pm}$, mainly due to the different composition of B decay modes including kaons. In this analysis, we use separate fractions for $B^{\pm}$ and B^0 decays. The mean fractions for the angular and momentum range covered by this analysis are shown in the Table 4.20.

Sample	Hadron type	Positive Hadrons	Negative Hadrons
$B^{\pm} + B^0$	$\pi^{\pm}$	0.7134 ± 0.0037	0.7209 ± 0.0038
	$K^{\pm}$	0.2441 ± 0.0013	0.2421 ± 0.0013
	$p, \bar{p}$	0.04253 ± 0.00024	0.03702 ± 0.00021
$B^{\pm}$	$\pi^{\pm}$	0.6978 ± 0.0058	0.7047 ± 0.0059
	$K^{\pm}$	0.2567 ± 0.0022	0.2567 ± 0.0022
	$p, \bar{p}$	0.04559 ± 0.00041	0.03851 ± 0.00035
B^0	$\pi^{\pm}$	0.7304 ± 0.0081	0.7387 ± 0.0083
	$K^{\pm}$	0.2326 ± 0.0026	0.2269 ± 0.0026
	$p, \bar{p}$	0.03697 ± 0.00045	0.03435 ± 0.00043

Table 4.20: Mean Hadronic fractions as determined from generic Monte-Carlo. Errors are statistical errors on hadron counts only - statistical error from control samples is included in the systematic error

Figure 4.19 shows the misidentification probability for pions, kaons and pro-

128

tons as taken from the "PidTables".

The following describes the methodology of the hadron mis-ID correction. All quantities shown below are estimated separately for each bin in the electron momentum.

The hadron fake contribution to the electron spectrum

$$
\begin{aligned}
N_{fake} &= (f_\pi \eta_\pi + f_K \eta_K + f_p \eta_p) \times N_h \\
&= <\eta> \times N_h
\end{aligned}
$$

is determined from the measured hadron and electron samples without using muon identification. The measured sample of tracks not identified as electrons consists of

$$
N_{not-e}^{meas} = N_h + N_\mu + (1 - \epsilon_e)N_e, \tag{4.9}
$$

where N_h, N_μ, N_e are the numbers of reconstructed tracks belonging to "true" hadrons, muons and electrons, respectively. The last term represents electrons missed because of inefficiencies in the electron selector. The spectrum of true muons can be related to the true electron spectrum, which can be determined from the measured electron spectrum (approximation in the second equation is made only for determination of the true hadron spectrum):

$$
\begin{aligned}
N_\mu &= r_{\mu/e} N_e \\
N_e^{meas} &= \epsilon_e N_e + \eta N_h \sim \epsilon_e N_e
\end{aligned}
$$

where $r_{\mu/e}$ is a function describing the ratio of the muon and electron spectra and is determined from the Monte Carlo simulation using generator-level particle ID information for reconstructed tracks. The spectra of muons and electrons differ

129
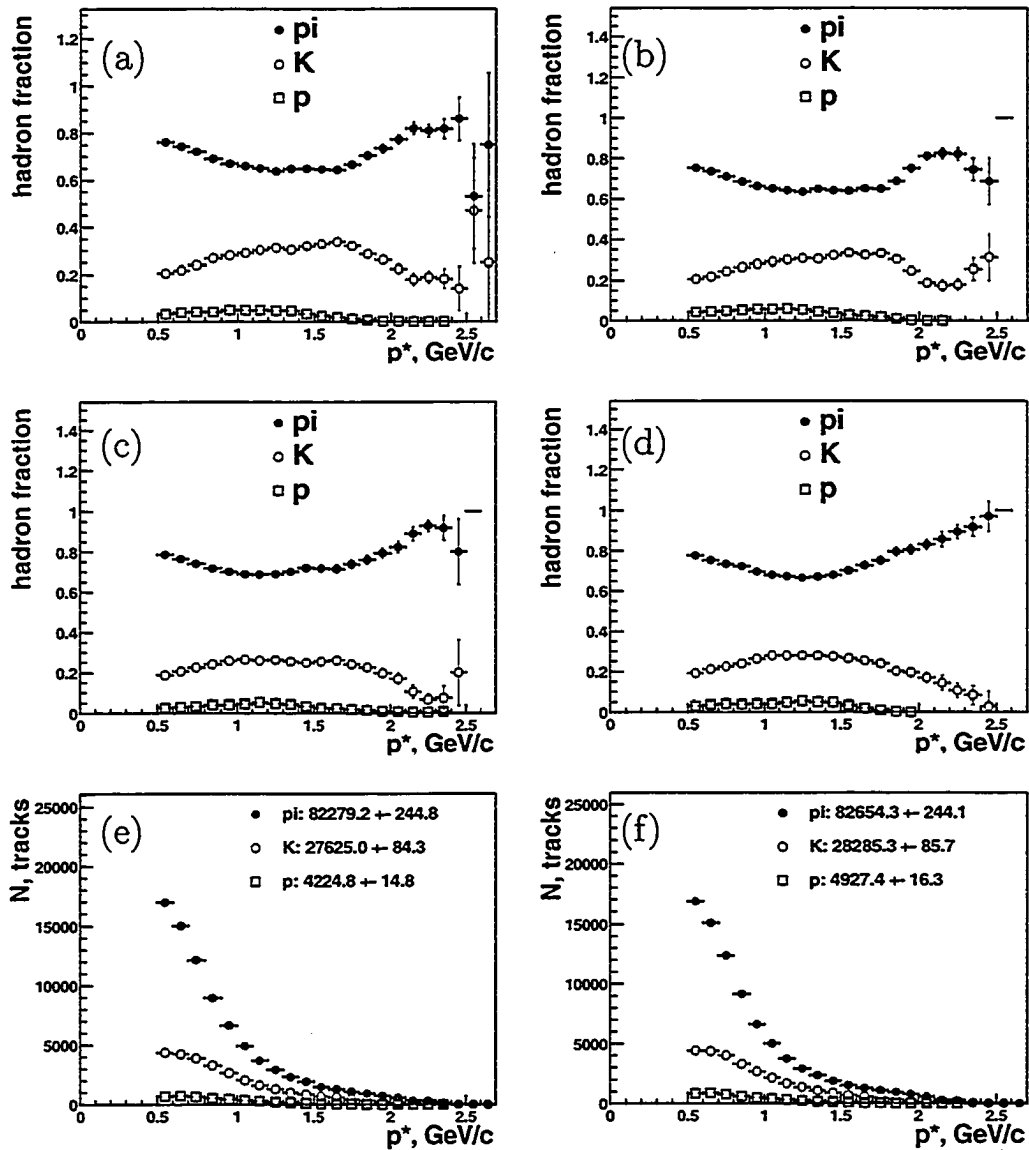
Figure 4.18: Hadron fractions as functions of momentum in the C.M.S. (a) negative particles, charged B events; (b) same for positive; (c) negative particles, neutral B events; (d) same for positive; (e) projected hadron spectra, negative particles, "signal box"; (f) same for positive

130
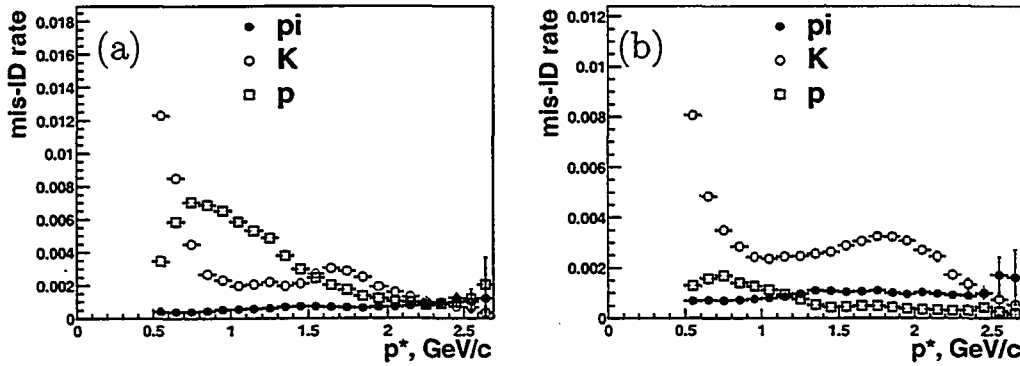
Figure 4.19: Hadron misidentification probability. (a) raw values from mis-ID tables, negative hadron particles; (b) same for positive.

due to different background processes (*e.g.* photon conversions and Dalitz decays for electrons, Kaon decay for muons) and due to bremsstrahlung. This ratio is determined and applied separately for each event class. The results are shown on Figure 4.20.

Equations 4.9 and 4.10 can be solved for the true hadron spectrum:

$$N_h = N_{not-e}^{meas} - \left(\frac{1 + r_{\mu/e} - \epsilon_e}{\epsilon_e}\right) N_e^{meas}. \qquad (4.10)$$

The second term contains the subtraction of the muon contribution to the hadron spectrum and the correction of the hadron sample for electrons not identified by the electron selector. The underestimation of the lepton corrections to the hadron spectrum due the approximation in Equation 4.10 is of the order of 0.5% and thus much smaller than the statistical or systematic error associated with the fake hadron subtraction.

Table 4.21 lists all the parameters used in determining the hadron fake contributions to the electron spectra. The summary of the hadron mis-ID correction for all event classes is given in Table 4.22.

131
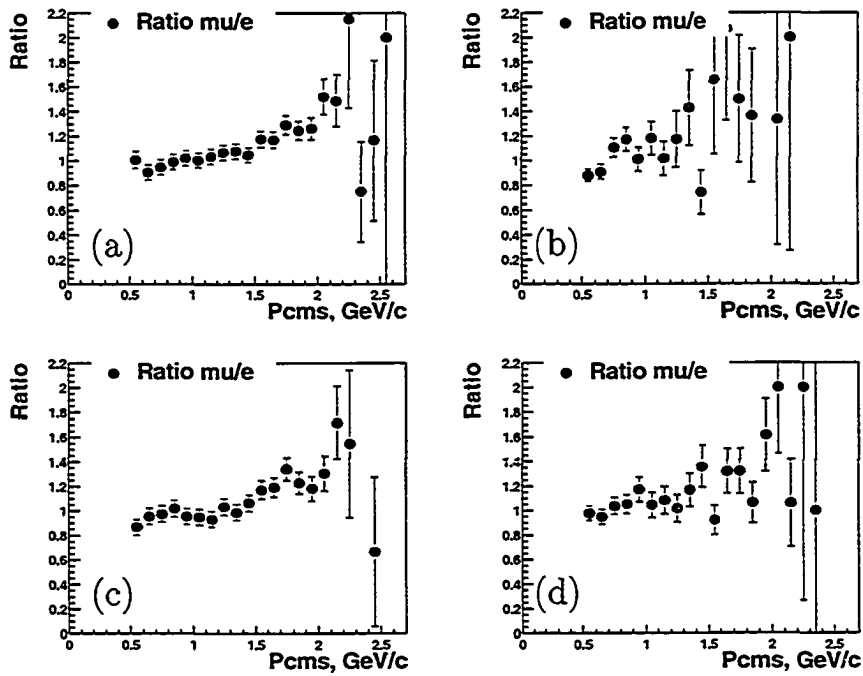
Figure 4.20: Correction function $r_{\mu/e} = N_\mu/N_e$ determined from a Monte Carlo simulation. (a) event class A, (b) - class B; (c) - class C; (d) - class D.
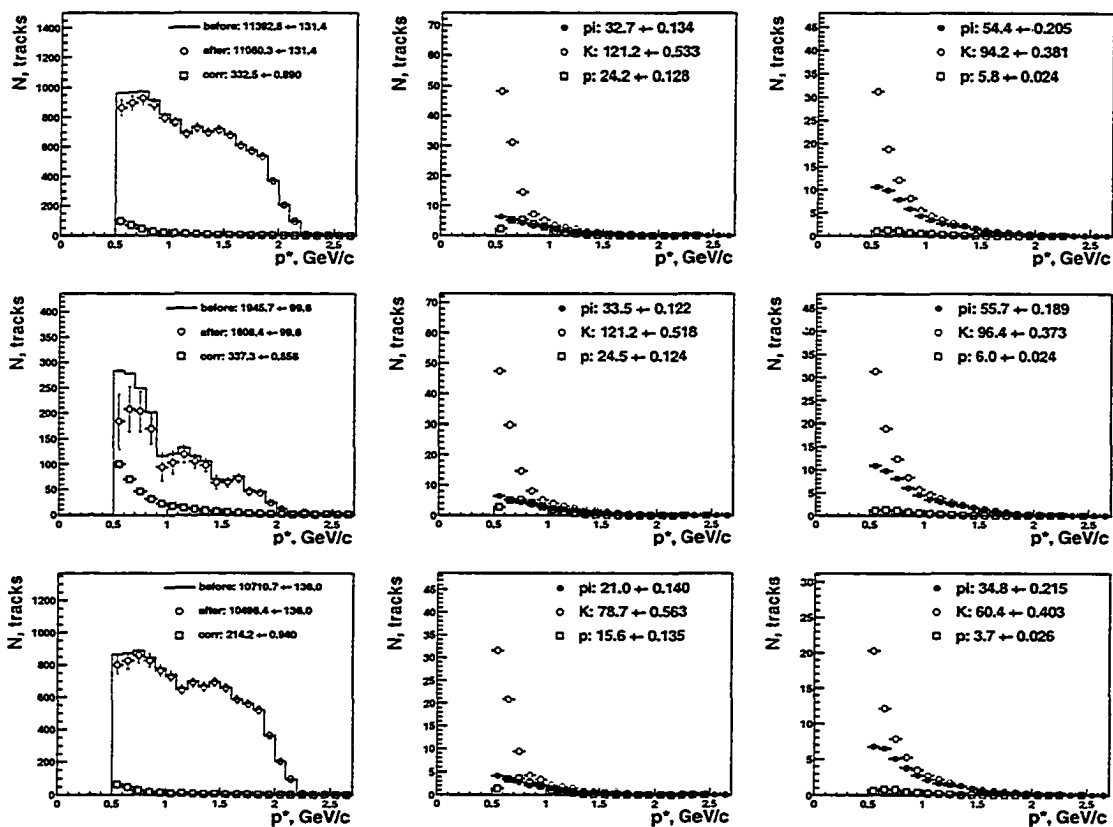
Figure 4.21: Hadron Mis-ID subtraction, all event classes. From left to right: subtraction, negative hadrons per particle type, positive per particle type. From top to bottom: signal box, unscaled sideband, sideband-subtracted. Corresponding numbers for the signal box subtraction are given in table 4.21.

133
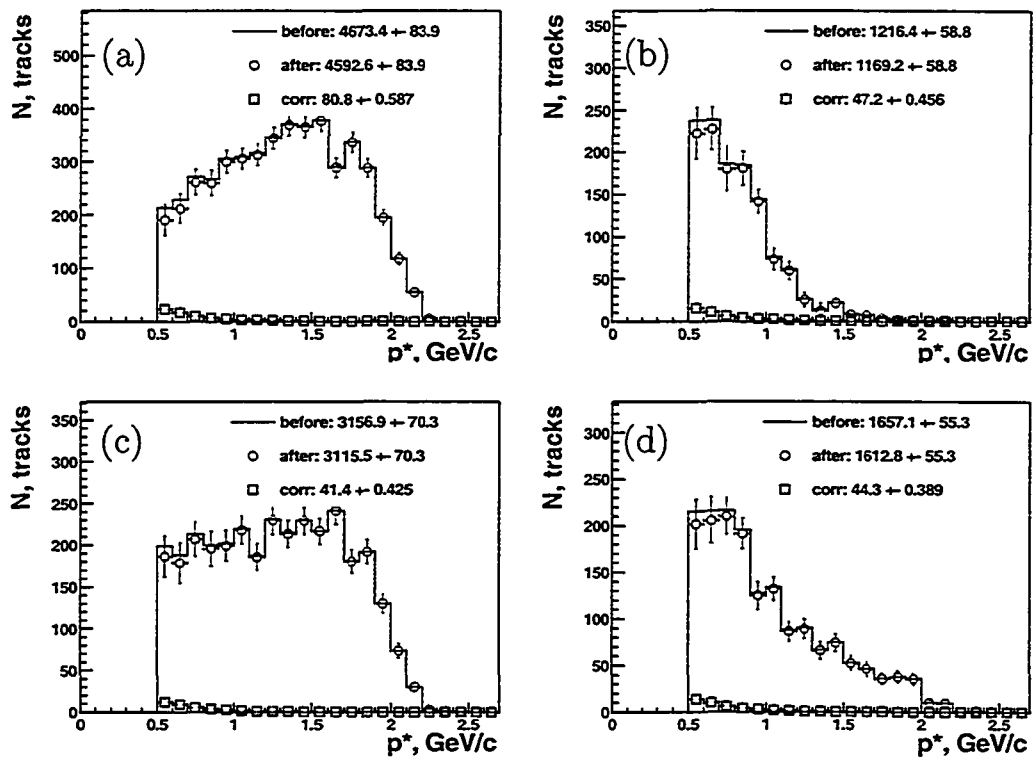
Figure 4.22: Hadron Mis-ID subtraction, sideband-subtracted spectra before and after the correction are shown along with the correction. (a) - event class A, (b) - class B; (c) - class C; (d) - class D.

134

Table 4.21: Hadron fake contributions to the electron spectra in the **signal box**. Summary for data presented in Figure 4.21 (all event classes). The "fraction" column indicates the fraction of particle i relative to the total *hadron* sample. η is the average misidentification probability (not weighted with the fraction). N_w represents the absolute contribution to the electron spectrum. Errors are the statistical errors associated with the hadron sample (error due to the control samples statistics is absorbed in the appropriate systematic error).

Event Class	Particle	Tracks	Hadron Fraction	η	N_w
All	$\pi-$	82279 ± 245	0.7209 ± 0.0038	0.000398	32.71 ± 0.13
	K-	27625 ± 84	0.2421 ± 0.0013	0.00439	121.21 ± 0.53
	p-	4225 ± 15	0.03702 ± 0.00021	0.00572	24.16 ± 0.13
	$\pi+$	82654 ± 244	0.7134 ± 0.0037	0.000658	54.36 ± 0.20
	K+	28285 ± 86	0.2441 ± 0.0013	0.00333	94.21 ± 0.38
	p+	4927 ± 16	0.04253 ± 0.00024	0.00118	5.825 ± 0.024
class A	$\pi-$	31275 ± 149	0.7047 ± 0.0059	0.000402	12.557 ± 0.085
	K-	11393 ± 56	0.2567 ± 0.0022	0.00409	46.64 ± 0.33
	p-	1709.0 ± 9.6	0.03851 ± 0.00035	0.00570	9.745 ± 0.083
	$\pi+$	30669 ± 147	0.6978 ± 0.0058	0.000655	20.10 ± 0.13
	K+	11281 ± 55	0.2567 ± 0.0022	0.00316	35.69 ± 0.24
	p+	2004 ± 11	0.04559 ± 0.00041	0.00117	2.341 ± 0.016
class C	$\pi-$	18534 ± 118	0.7387 ± 0.0083	0.000382	7.085 ± 0.067
	K-	5693 ± 37	0.2269 ± 0.0026	0.00417	23.75 ± 0.23
	p-	861.8 ± 6.6	0.03435 ± 0.00043	0.00543	4.676 ± 0.054
	$\pi+$	18679 ± 117	0.7304 ± 0.0081	0.000635	11.85 ± 0.10
	K+	5948 ± 38	0.2326 ± 0.0026	0.00315	18.71 ± 0.17
	p+	945.5 ± 6.8	0.03697 ± 0.00045	0.00112	1.0564 ± 0.0099

135

Table 4.22: Electron Spectrum: Hadron mis-identification background yields. The error given corresponds to the statistical error. Note that sideband-subtracted yields are shown, corresponding to plots on Figure 4.22.

Sample	A	B	C	D
$\pi-$	7.908 ± 0.089	4.205 ± 0.058	4.355 ± 0.070	4.470 ± 0.058
K-	29.99 ± 0.35	17.82 ± 0.28	14.76 ± 0.25	15.99 ± 0.23
p-	6.150 ± 0.087	3.491 ± 0.067	2.958 ± 0.058	2.956 ± 0.052
Total negative	44.04 ± 0.37	25.52 ± 0.29	22.08 ± 0.26	23.41 ± 0.25
$\pi+$	12.73 ± 0.13	7.149 ± 0.093	7.21 ± 0.11	7.624 ± 0.092
K+	22.54 ± 0.25	13.67 ± 0.20	11.47 ± 0.18	12.56 ± 0.16
p+	1.489 ± 0.017	0.880 ± 0.013	0.644 ± 0.011	0.7039 ± 0.0097
Total positive	36.75 ± 0.29	21.70 ± 0.22	19.32 ± 0.21	20.89 ± 0.19
Total	80.80 ± 0.59	47.22 ± 0.46	41.39 ± 0.42	44.30 ± 0.39

136

The systematic error for the hadron mis-identification correction is composed of the three parts:

- 1. Hadron fraction systematics.

  Due to the extremely large statistics available in Monte-Carlo for determination of these fractions, the corresponding statistical error is negligible. The dominant error for this term arises from the possible inadequacy of the Monte-Carlo description of the hadron spectra. This has been checked by comparing the fractions obtained from the *BABAR* Monte-Carlo with the experimentally obtained fractions in the ARGUS experiment that also used $\Upsilon(4S) \rightarrow B\overline{B} \rightarrow X$ decays [41]. As shown in Figure 4.23, the agreement is reasonable - we take half of the difference as a systematic error contribution from this term. The error corresponding to each hadron type is weighted with the relative contribution of that hadron type to the total misidentification rate. The weighted errors are then added together in quadrature to arrive at the error for the total mis-ID correction. The details on the hadronic fractions systematics are given in Table 4.23, column f_h.

Table 4.23: Contributions to the total systematic error for the hadron mis-identification correction. Weight denotes the relative contribution to the overall mis-ID correction from the particular hadron type. Resulting absolute errors (in number of mis-identified electrons) are given for event classes A and C.

Sample	Weight	$\delta\eta_h/\eta_h$	$\delta f_h/f_h$	combined	A, absolute	C, absolute
π	0.255	0.1000	0.1000	0.141	2.92	1.64
K	0.650	0.150	0.150	0.212	11.1	5.56
p	0.0945	0.200	0.200	0.283	2.16	1.02
Total	1.00	0.103	0.103	0.145	11.7	5.89

137
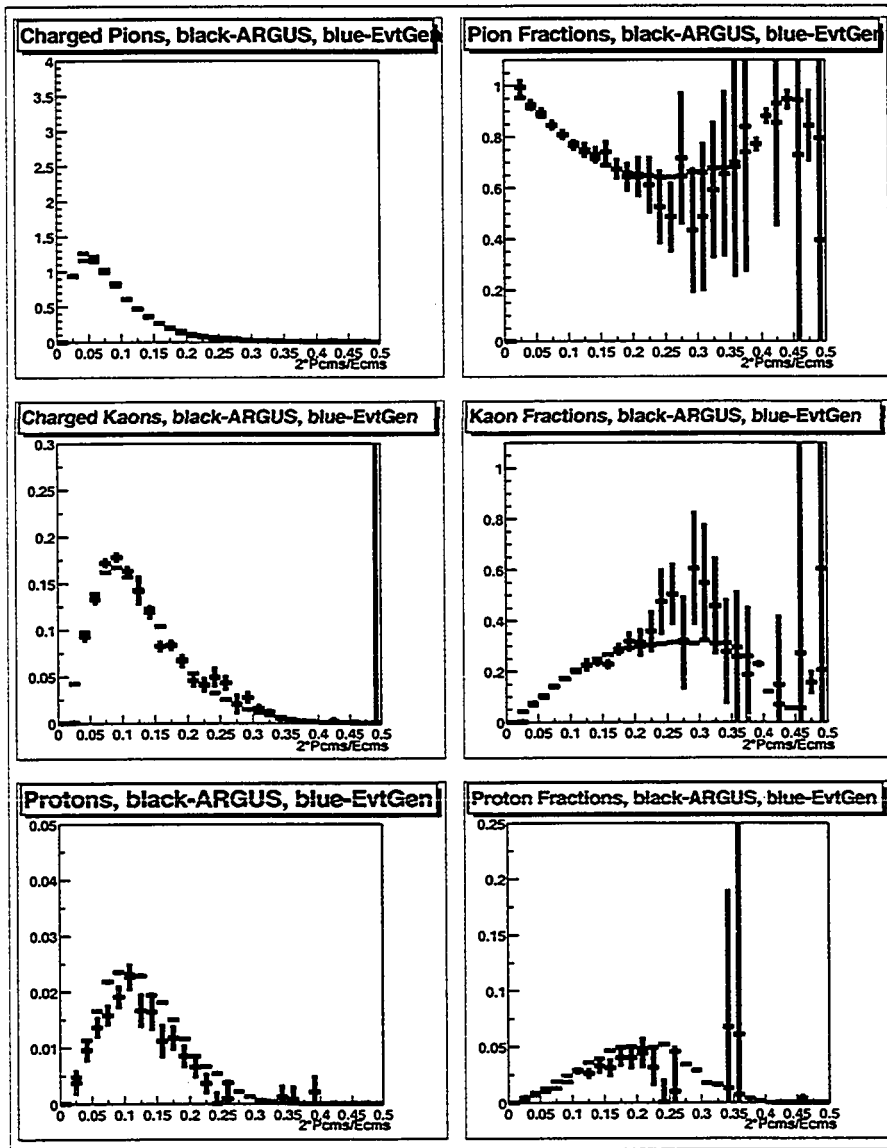
Figure 4.23: Comparison of the hadronic multiplicities and fractions observed in ARGUS experiment, with the corresponding distributions obtained from *BABAR* Monte-Carlo sample. On the left, the track multiplicity (per event) for a given hadron type is shown. E_{CMS} in the X axis label is the center-of-mass energy of the event.

138

- 2. Hadron fake rate systematics.

  The corresponding error is described in detail elsewhere [19]. The details on the hadronic fractions systematics are given in Table 4.23, column η_h.

- 3. Systematic effects in determination of the true hadron spectrum in Data.

  This is mostly affected by the uncertainties in tracking efficiencies and detecting lepton particles. Due to the small magnitude of these errors, this term has negligible contribution to the total error associated with hadron misidentification correction.

139

4.4.3 Tracking and Electron ID Efficiency Correction

The data sample used in this analysis has been accumulated using three different Drift Chamber High Voltage settings - 1900V, 1930V, and 1960V. Approximately 80% of the data were taken at 1930V, while 1900V and 1960V settings contribute approximately 10% each. Since the tracking efficiency correction depends on these settings, it has been applied to the respective parts of the data sample separately. No significant charge dependance of the tracking efficiency has been observed, therefore we use the same efficiency for negative and positive tracks.

In tracking efficiency corrections, efficiency tables containing absolute Data sample efficiencies are used. The tables contain tracking efficiency binned in θ, ϕ, P_{LAB} and event multiplicity. The appropriate efficiency is applied to each track based on its kinematic properties as well as the total event multiplicity. Tracking efficiency weighted with the analysis spectra is shown in Figure 4.4.3b.

In order to enable direct comparison of Data and Monte-Carlo spectra, the average of the absolute Monte-Carlo sample tracking efficiency ($\sim 97\%$) is applied to all Monte-Carlo spectra. The error introduced by this approximation is very small since it only affects certain physics background corrections ($< 7\%$ of total electron yield).

The correction for electron ID efficiency is applied separately for each charge of the electron. In this correction, two sets of efficiency tables are used. The first set of tables contains the electron ID efficiency as determined from the electron control samples, mostly radiative bhabha (electron-electron scattering) events. It has been observed [43], however, that particle identification efficiency may depend significantly on the event topology. Since this analysis is performed on the multihadron events, which have notably different topology from bhabha events, an adjustment to the electron ID efficiency has to be applied. This adjusment has been derived in [19] and is represented by the second set of efficiency tables.

140

The adjustment results in lowering the effective electron ID efficiency by 1-4%, with the largest effect being in the lower part of the spectrum. Averaged over the detected electron spectra, this adjustment amounts to $\sim$ 2.4% for the spectra in event classes A and C (average efficiency changes from 91.8% to 89.6%. Electron ID efficiency weighted with the analysis spectra is shown in Figure 4.4.3a.

Unlike the tracking efficiency correction, the Electron ID efficiency correction does not need to be applied to Monte-Carlo spectra since all electron spectra in Monte-Carlo sample presented in this analysis are based on the Monte-Carlo truth-matched electrons (effective electron ID efficiency of 100%). The details on both tracking and electron ID efficiency corrections are given in Table 4.24.
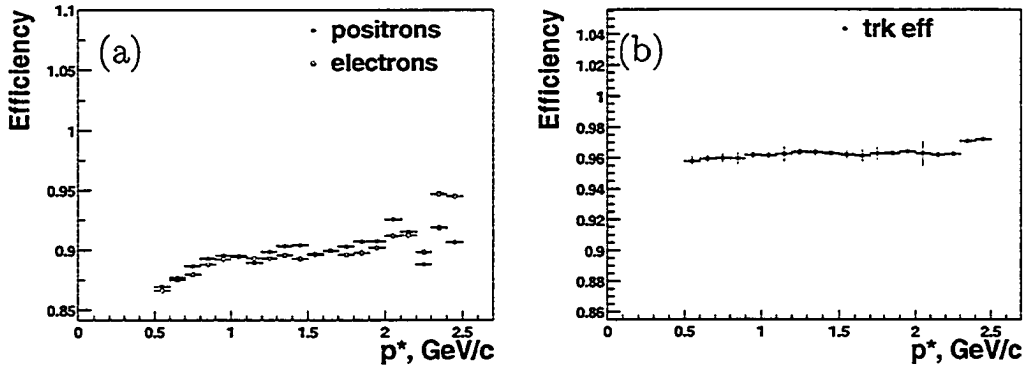
Figure 4.24: (a) - Electron ID Efficiency, (b) - Tracking Efficiency. Both efficiencies are shown only for the range of momenta used in the analysis.

Systematics of these corrections are well-described elsewhere [44], [34]. The systematic error for tracking efficiency correction is set to 0.7% while the systematic error for the electron ID efficiency is set to 1.0%. We also add half of the event topology adjustment to the systematic error in the electron ID correction to arrive at a total electron ID efficiency systematic error of 1.5%.

141

Table 4.24: Electron Spectrum: Electron ID and Tracking efficiency corrections. Errors are statistical only.

Sample	A	B	C	D
Before	4593 ± 84	1169 ± 59	3115 ± 70	1613 ± 55
After Eff. Corr(ID)	5130 ± 94	1325 ± 67	3485 ± 79	1817 ± 63
After Eff. Corr(Trk)	5309 ± 98	1378 ± 70	3639 ± 83	1898 ± 66

4.4.4 Efficiency-corrected Electron Spectra after Pair and Mis-ID subtractions

Figure 4.25 shows the efficiency-corrected spectra in all four event classes after Pair and Mis-ID subtraction. Table 4.45 shows the numbers corresponding to Figure 4.25.

4.4.5 Unmixing of the electron spectra in B^0 samples

The extraction of the branching fraction is performed using the measured number of electrons, the reconstruction efficiency, the mixing parameter χ_d, and the number of produced B-mesons .

Measurements of the total $B^0 \leftrightarrow \overline{B^0}$ mixing probability χ_d (probability of B^0 meson to decay as $\overline{B^0}$) have been published by many experiments, with the world average [45] (including recent BABAR measurements) currently given by

$$\chi_d = 0.181 \pm 0.004.$$

However, the value of the mixing probability is fixed in BABAR Monte-Carlo at

$$\chi_d = 0.175$$

142
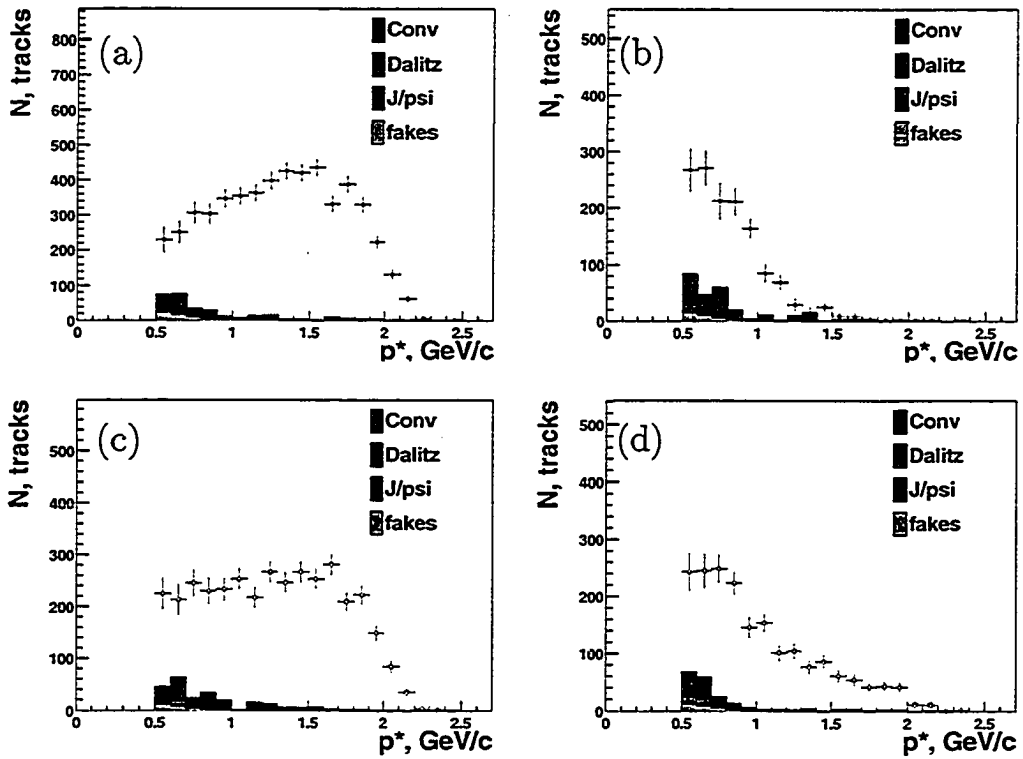
Figure 4.25: Electron spectrum after pair and hadron mis-ID corrections and all subtracted components for all four event classes: (a) - class A, (b) - class B, (c) - class C, (d) - class D.

This value is used instead of the world average value to correct for the mixing of the Monte-Carlo B^0 spectra. This difference affects, among other things, the subtraction of backgrounds for B^0 spectra and cross-feed corrections.

For charged B-mesons , there is a simple relation between the number of prompt (cascade) electrons $N_p^\pm$ ($N_c^\pm$) and the charge of the lepton expected from the charge of the B-meson :

$$N_p^\pm = N_{right-sign}^\pm$$

$$N_c^\pm = N_{wrong-sign}^\pm$$

once the contribution from same-sign cascade charm decays, τ-decays, and the remaining background sources have been subtracted. The contribution from incorrectly reconstructed B-mesons is taken into account in the spectra cross-feed correction step described below.

However, in case of neutral B-mesons , $B^0 \leftrightarrow \overline{B^0}$ mixing complicates this simple picture:

$$N_{right-sign}^0 = N_p^0(1 - \chi_d) + N_c^0 \chi_d$$

$$N_{wrong-sign}^0 = N_p^0 \chi_d + N_c^0(1 - \chi_d)$$

where electrons from the prompt decays of mixed B-mesons contribute to the wrong-flavor sample and opposite-sign cascade charm decays of mixed B-mesons contribute to the sample of right-sign electrons. This set of equations can be solved for the prompt spectrum:

$$N_p^0 = \frac{(1 - \chi_d)N_{right-sign}^0 - \chi_d N_{wrong-sign}^0}{1 - 2\chi_d}.$$

and the result is shown in Figure 4.26. Corresponding electron yields are given in Table 4.25. After this correction, we will refer to the B^0 event classes as

144

C' and D' to reflect that their definition as right/wrong-sign events is no longer valid.
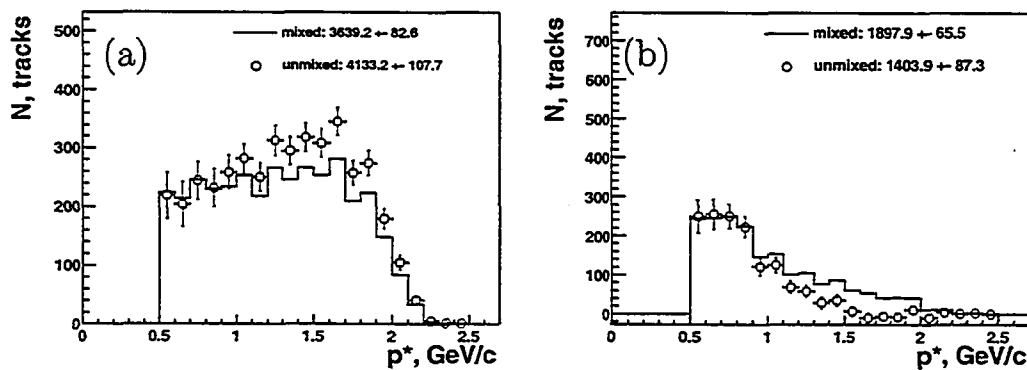
Figure 4.26: Correction to the lepton spectra in B^0 events due to $B^0\overline{B}^0$ mixing. The plots are the following : (a) - class C' and (b) - class D'.

Table 4.25: Electron Spectrum: Correction for $B^0 \leftrightarrow \overline{B^0}$ mixing effects. Error are statistical only.

Sample	C	D
Before	3639 ± 83	1898 ± 66
	C'	D'
After	4133 ± 108	1404 ± 87

Special care has to be taken of any pair or hadron mis-ID background remaining in event classes C and D before the unmixing is applied. Below, we estimate a systematic error due to these residuals.

The above set of mixing equations is modified as

$$N^0_{right-sign} = N^0_p(1 - \chi_d) + N^0_c \chi_d + \Delta x$$

$$N^0_{wrong-sign} = N^0_p \chi_d + N^0_c(1 - \chi_d) + \Delta y$$

145

where $\triangle x$ and $\triangle y$ represent the background residual contribution to the right-sign and wrong-sign respectively.

This set of equations can be resolved for the prompt spectrum:

$$N_p^0 = \frac{(1 - \chi_d)N_{right-sign}^0 - \chi_d[N_{wrong-sign}^0 - (\triangle x + \triangle y)] - \triangle x}{1 - 2\chi_d}. \qquad (4.11)$$

Thus, the term corresponding to the residuals can be written as

$$\triangle' = \frac{(\chi_d - 1) \cdot \triangle x}{1 - 2\chi_d} + \frac{\chi_d \cdot \triangle y}{1 - 2\chi_d}. \qquad (4.12)$$

Since $\triangle x$ and $\triangle y$ are correlated quantities, we add the errors corresponding to these residual contributions linearly to arrive at the resulting systematic error contribution to the prompt spectra:

$$\triangle = \frac{(\chi_d - 1) \cdot \triangle x + \chi_d \cdot \triangle y}{1 - 2\chi_d}. \qquad (4.13)$$

Thus $\triangle$ can be evaluated using the values of χ_d and $\triangle x$ and $\triangle y$. This formula is used to determine the systematic errors for all corrections applied before unmixing: all pair backgrounds and hadron mis-ID.

The following example deals with the conversion pair background. From the earlier section on the conversion subtraction, we know that the relative systematic error for this background is 13%. Based on the detected yield for conversion background, we estimate the absolute systematic error of $\triangle x = 25$ for the right-sign sample and $\triangle y = 21$ for the wrong-sign sample. Substituting these values into 4.13 gives $\triangle = 26$, which has to be normalized to the number of prompt electrons after unmixing, 4133 ± 108 , to obtain contribution to the relative systematic error. The resulting systematic error due to conversion subtraction is set to 0.6%. Similarly, systematic errors on Dalitz, J/psi and hadron mis-ID

146

backgrounds are determined. Corresponding values are given in Table 4.46 in systematics section of this document.

147

4.4.6 Physics Background

All background sources discussed so far are determined from data (with some input from Monte Carlo simulation). This section describes background sources not easily identifiable in data, arising from e.g. decays of $D^{0,+}$-mesons, τ-leptons, kaons, Λ_c, etc. .
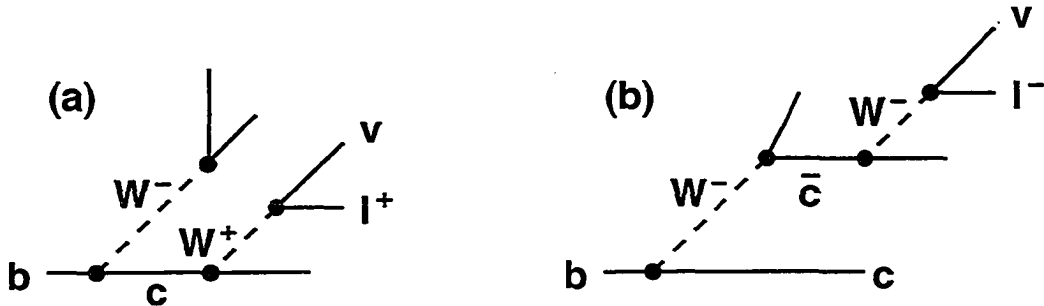
Figure 4.27: Feynman diagrams for background electrons from $D^{0,+}$ decays. (a) Electron from opposite-sign cascade charm decays (separated from prompt electrons by event classification), (b) electron from same-sign cascade charm decays (so-called "Upper Vertex" decays, need to be corrected for by subtraction).

Branching fraction rescaling in Monte-Carlo simulation

The corrections for contributions from these sources are determined from Monte-Carlo simulation. However, due to the recent experimental progress made in studying various decay modes, the updated branching fractions for a number of processes are significantly different from the branching fractions used for these processes in the *BABAR* Monte-Carlo simulations. A separate study has been performed in order to derive the corresponding scaling factors using the latest experimental results. These scaling factors are then applied to Monte-Carlo prediction for the background sources mentioned above to arrive at the correct background estimates. Line numbers in the following discussion refer to line numbers

in the master decay file used in Monte-Carlo simulation.

4.4.7 Background from Upper Vertex $D_s^+ \overline{D} X$ and $D\overline{D}$ process

Upper vertex processes $\overline{b} \to \overline{c}(\overline{c}s)$ give rise to a secondary lepton from charm decays which have the same sign charge as primary leptons from $\overline{b} \to \overline{c}\ell\nu$ decays Here we discuss two upper vertex processes $B \to D_s^+ \overline{D} X$ and $B \to D\overline{D}X$ which are the source of background.

$D_s^+ \to X e^+ \nu$ Branching Ratio

We derive the poorly measured inclusive branching fraction $\mathcal{B}(D_s^+ \to X e^+ \nu)$ from $\mathcal{B}(D^0 \to X e\nu)$ and $\mathcal{B}(D^+ \to X e^+ \nu)$ and the lifetime ratios τ_{D^0}/τ_{D_s} and $\tau_{D^\pm}/\tau_{D_s}$ separately, assuming equal semileptonic decay widths for D and D_s. Finally, we take the average of the two values as the mean value for $\mathcal{B}(D_s \to X e\nu)$.

$$\frac{\Gamma(D_s \to X e\nu)}{\Gamma(D^{0,+} \to X e\nu)} \cdot \frac{\tau_{D_s}}{\tau_{D^{0,+}}} = \frac{\mathcal{B}(D_s \to X e\nu)}{\mathcal{B}(D^{0,+} \to X e\nu)} \qquad (4.14)$$

which gives rise to

$$Br(D_s \to X e\nu) = Br(D^{0,+} \to X e\nu) \cdot \frac{\tau_{D_s}}{\tau_{D^{0,+}}} \qquad (4.15)$$

The values given in Table 4.26 is used to calculate the above branching fraction and the result is provided in Table 4.27.

$B \to D_s^+ DX$ Production via $\overline{b} \to \overline{c}(c\overline{s})$

- Wrong flavor D_s^+ ($b \to \overline{c}(\overline{c}s)$) production (external W-emission) at upper vertex gives a secondary lepton of right sign (i.e. same sign as the primary leptons from $B \to D\ell\nu$ decays).

- D_s production possible via internal W-emission is negligible.

149

Table 4.26: Lifetimes of D_s, $D^{\pm}$ and D^0 mesons.

Lifetimes	PDG'00 (ps)	PDG'02 (ps)
τ_{D^0}	0.413 ± 0.0028	0.412 ± 0.0027
τ_{D^+}	1.051 ± 0.013	1.051 ± 0.013
τ_D^{avg}	0.441 ± 0.0027	0.438 ± 0.0026
τ_{D_s}	0.496 ± 0.010	0.490 ± 0.009
Lifetime Ratio	PDG'00	PDG'02
τ_{D_s}/τ_D^{avg}	1.124 ± 0.024	1.118 ± 0.022

Table 4.27: Evalution of Eqn.(4.15) using values from table 4.26

Parent of electron	Decay Chain Link	BR, PDG'00 (%)	BR, PDG'02 (%)
D^0	$D^0 \to Xe\nu$	6.75 ± 0.29	6.87 ± 0.28
D^+	$D^+ \to Xe\nu$	17.2 ± 1.9	17.2 ± 1.9
	$D^{avg} \to Xe\nu$	6.99 ± 0.29	7.09 ± 0.28
Average	$D_s \to Xe\nu$	7.85 ± 0.36	7.92 ± 0.35

- Right flavor D_s^- ($\bar{b} \to \bar{c}$) production (color suppressed) at lower vertex gives wrong sign lepton. The relative fraction is (0.16 ± 0.085) of the total D_s production [47].

From Table 4.28, it is evident that the electron production from upper vertex D_s process in MC is underestimated compared to the PDG'00 and PDG'02 values. According to the latest PDG values, this leads to a reweighting of the electron spectrum from D_s by 1.003.

150
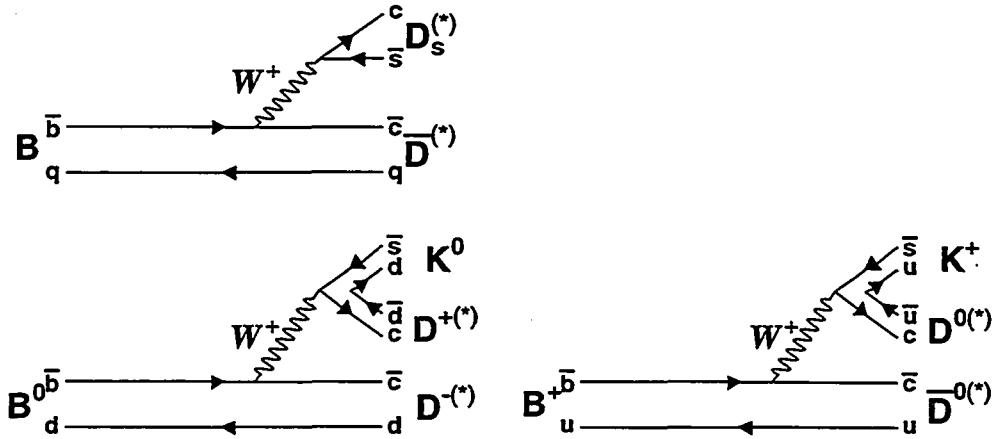
Figure 4.28: Diagrams for D_s and $D\overline{D}K$ production

Table 4.28: Branching Ratios for $B \rightarrow D_s^+ \rightarrow Xe^+\nu$. Right sign leptons from D_s^+ via $\overline{b} \rightarrow \overline{c}(c\overline{s})$, where the lepton originates from c.

$b \rightarrow c$	$c \rightarrow e$	MC (%)	PDG'00 (%)	PDG'02 (%)
$B \rightarrow D_s^\pm X$	—	11.89	10.0 ± 2.5	10.5 ± 2.6
—	$D_s \rightarrow Xe\nu$	5.86	7.85 ± 0.36	7.92 ± 0.35
$B \rightarrow D_s^\pm \rightarrow Xe\nu$		0.697	0.785 ± 0.2	0.832 ± 0.209
$\mathcal{F} = $ (upper-vertex/total)		100.0	84.0 ± 8.5 [47]	
$(\overline{b} \rightarrow c \rightarrow e^+) =$ $(B \rightarrow D_s^+ \rightarrow Xe\nu) \times \mathcal{F}$		0.697	0.660 ± 0.181	0.699 ± 0.189

According to the latest result (Belle) the error on the measurement of $D_s^\pm \rightarrow \phi\pi^\pm$ has improved from 25% to 16%. This brings down the error on the upper vertex $B \rightarrow D_s^+ \rightarrow Xe\nu$ to 0.136 from 0.189 in Table 4.28, which along with the central value of 0.699 (PDG'02), results in the systematic error of 20%.

151

$B \rightarrow D\overline{D}X$ production via $\overline{b} \rightarrow \overline{c}(c\overline{s})$

As shown in Fig.4.28, wrong flavor $D^{(*)}$ are produced at upper vertex which give right sign leptons. It is evident from Table 4.29 that the branching fraction

Table 4.29: Branching fractions of $B \rightarrow D^0 \rightarrow Xe\nu$ and $B \rightarrow D^+ \rightarrow Xe\nu$. Value of $\mathcal{B}(D^+ \rightarrow Xe\nu)$ is underestimated in MC.

$b \rightarrow c/\overline{c}$	$c/\overline{c} \rightarrow e$	MC (%)	PDG'00 (%)	PDG'02 (%)
$B \rightarrow DX$	—	8.895	8.2 ± 1.3	8.2 ± 1.3
—	$D^0 \rightarrow Xe\nu$	6.61	6.75 ± 0.29	6.85 ± 0.28
—	$D^+ \rightarrow Xe\nu$	13.72	17.2 ± 1.9	17.2 ± 1.9
—	$D^{*+} \rightarrow D^0 X$	68.3	67.7 ± 0.5	67.7 ± 0.5
$B \rightarrow D^{(*)} \rightarrow Xe\nu$		0.755	0.84 ± 0.21	0.841 ± 0.21

$\mathcal{B}(D^+ \rightarrow Xe\nu)$ is underestimated in MC by a factor 1.25 compared to the latest PDG values.

The above correction to the electron counting was justified by comparing the $\mathcal{B}(B \rightarrow D^{(*)} \rightarrow Xe\nu)$ branching fraction estimation in MC and data. The value of $\mathcal{B}(B \rightarrow DX)$ for MC was obtained directly from the particle decay table and is given in Table 4.29. For data, the estimation was done using the value $\mathcal{B}(B \rightarrow DX) = (8.2 \pm 1.3)\%$ [49] for D production at upper vertex. Details about the MC and data estimation of the branching fraction of $\mathcal{B}(B \rightarrow D^{(*)} \rightarrow Xe\nu)$ is described in Section 4.4.11.

4.4.8 $B \rightarrow \Lambda_c X \rightarrow e^+ X$

- No information available about upper vertex production $\overline{b} \rightarrow \overline{c}(c\overline{s})$, thus we assume a negligible contribution.

152

- Wrong flavor Λ_c^+ production ($\bar{b} \to c$) through "internal W^+-emission ($c\bar{s}$)" decays to right sign lepton.

- Right flavor Λ_c^- production ($\bar{b} \to \bar{c}$) through "internal/external W^+-emission($u\bar{d}$)" decays to wrong sign/charge lepton.

Table 4.30: Right-sign lepton production through wrong flavor Λ_c decay in $\bar{b} \to c$.

$\bar{b} \to \bar{c}$	$\bar{c} \to \ell^-$	MC (%)	PDG'00 (%)	PDG'02 (%)
$B \to \Lambda_c X$	—	6.4	6.4 ± 1.1	6.4 ± 1.1
—	$\Lambda_c \to eX$	4.5	4.5 ± 1.7	4.5 ± 1.7
$B \to \Lambda_c \to Xe\nu$		0.288	0.288 ± 0.12	0.288 ± 0.12
$\mathcal{F} = (\bar{b} \to c(\Lambda_c^+))/\text{total} = 19.0 \pm 13.6$ [48]				
$(\bar{b} \to c \to \ell^-) = (B \to \Lambda_c \to Xe\nu) \times \mathcal{F}$		0.055	0.055 ± 0.046	0.055 ± 0.046

- $B \to \Lambda_c^- X$ is 6.4% in MC, which includes $B \to \Lambda_c X$, $B \to \Sigma_c X$ and $B \to \Xi_c X$, (Lines 553-561, 1000-1008, 1337-1343, 1751-1757)

- $\Lambda_c^- \to e^- X$ is 4.5% in MC, (Lines 4488-4494)

As evident from Table 4.30 the MC and latest PDG values for lepton production from upper vertex Λ_c agree. This leads to no reweighting of the right sign electron counting from Λ_c.

4.4.9 $\quad B \to \tau \to e^+ \nu\nu$ ($\bar{b} \to \bar{c}$)

There are two principal sources of $\tau^\pm$ that can contribute electrons to the right sign lepton sample: $B \to X\tau^+\nu$ and $B \to D_s^+ X$, $D_s^+ \to \tau^+\nu_\tau$ with $\tau^+ \to e^+\nu\nu$.

153

$B \rightarrow X\tau\nu, \ \tau \rightarrow e^+\nu\nu$

In MC, we have :

- $\text{Br}(B \rightarrow X_c\tau\nu) = 2.96\%$ (Lines 611-616 for B^0, Lines 1436-1441 for B^+)

- $\text{Br}(B^0 \rightarrow X_u\tau\nu) = 0.0257\%$ (Lines 648-656)

- $\text{Br}(B^+ \rightarrow X_u\tau\nu) = 0.0337\%$ (Lines 1493-1510)

- $\text{Br}(\tau \rightarrow e\nu_e\nu_\tau) = 18\%$ (Line 2653)

The branching fraction for $B \rightarrow \tau \rightarrow \ell$ is provided in Table 4.31, where the value of $B \rightarrow X\tau^+\nu_\tau$ for MC is the sum of the above three branching fractions.

Table 4.31: Branching fraction of $B \rightarrow \tau \rightarrow \ell$.

$\bar{b} \rightarrow \tau^+$	$\tau^+ \rightarrow \ell^+$	MC (%)	PDG'00 (%)	PDG'02 (%)
$B \rightarrow X\tau^+\nu_\tau$	—	3.0194	2.6 ± 0.4	2.48 ± 0.26
—	$\tau^+ \rightarrow e^+\nu\nu$	18.0	17.83 ± 0.06	17.84 ± 0.06
$B \rightarrow \tau \rightarrow \ell$ (Right Sign)		0.543	0.464 ± 0.07	0.442 ± 0.046

$B \rightarrow D_s^+X, \ D_s^+ \rightarrow \tau^+\nu, \ \tau^+ \rightarrow e^+\nu\nu$

The branching fraction for $B \rightarrow D_s \rightarrow \tau \rightarrow \ell$ is provided in Table 4.32. Only the upper vertex D_s that subsequently decays to τ are taken into account.

As mentioned before, the error on the $B \rightarrow D_s^+X$ (due to $D_s^\pm \rightarrow \phi\pi^\pm$) measurement is improved by 9%, which brings down the error from 2.36 to 1.4 (PDG'02)in Table 4.32. Thus the error on $B \rightarrow D_s \rightarrow \tau \rightarrow \ell$ reduces to 0.029 from 0.036.

Adding the MC and PDG'02 results for $B \rightarrow \tau \rightarrow \ell$ from Table 4.31 with the results of $B \rightarrow D_s \rightarrow \tau \rightarrow \ell$ from Table 4.32 for MC and the updated value with

154

Table 4.32: Branching fraction of $B \to D_s \to \tau \to \ell$. Only upper vertex D_s is taken into account.

$\overline{b} \to c$	$c \to \ell^+$	MC (%)	PDG'00 (%)	PDG'02 (%)
$B \to D_s^+ X$	—	11.89	8.4 ± 2.27	8.82 ± 2.36
—	$D_s^\pm \to \tau^\pm \nu_\tau$	7.0	7.0 ± 4.0	6.4 ± 1.5
—	$\tau^+ \to e^+ \nu \nu$	18.0	17.83 ± 0.06	17.84 ± 0.06
$B \to D_s \to \tau \to \ell$ (Right Sign)		0.15	0.105 ± 0.066	0.101 ± 0.036

reduced error (described above) for data, gives the following :

$$MC : (B \to \tau^+ X \to \ell^+) = 0.693\%$$

$$PDG'02 : (B \to \tau^+ X \to \ell^+) = (0.543 \pm 0.0544)\%$$

which requires in the rescaling of electrons from the τ cascade extracted from MC by 0.78, and the resulting systematics error from this correction is 10%.

4.4.10 $B \to J/\psi$ and $B \to \Psi(2S)$ decays

Electrons from J/ψ decays are considered as pair backgrounds and are removed at the early stage of the background subtraction procedure.

The branching fractions of $B \to J/\psi X \to e^+ e^-$ and $B \to \Psi(2S)X \to e^+ e^-$ are given in Table 4.33 and Table 4.34 respectively.

4.4.11 $B \to D\overline{D}X$ decays

$\mathcal{B}(B \to D^{(*)} \to Xe\nu)$ estimation for Data

The inclusive branching fraction $\mathcal{B}(B \to \overline{D}DX)$ for D production at the upper vertex is determined to be $(8.2 \pm 1.3)\%$ [49] by combining measurements from CLEO [50], ALEPH [51] and DELPHI [52]. Apart from the branching ratios

155

Table 4.33: Branching fraction of $B \to J/\psi X \to e^+ e^-$.

$\bar{b} \to \bar{c}c\bar{s}$	$\bar{c} \to \ell^+$	PDG'00 (%)	PDG'02 (%)
$B \to J/\psi X$	—	1.15±0.06	1.06±0.042
—	$J/\psi \to e^+ e^-$	5.93±0.1	5.93±0.1
$B \to J/\psi X \to e^+ e^-$ (W/R Sign)		$(6.82\pm0.38)\times 10^{-4}$	$(6.29\pm0.27)\times 10^{-4}$

Table 4.34: Branching fraction of $B \to \Psi(2S)X \to e^+ e^-$.

$\bar{b} \to \bar{c}c\bar{s}$	$\bar{c} \to \ell^+$	PDG'00 (%)	PDG'02 (%)
$B \to \Psi(2S)X$	—	0.35±0.05	0.297±0.028
—	$\Psi(2S) \to e^+ e^-$	0.88±0.13	0.73±0.04
$B \to \Psi(2S)X \to e^+ e^-$ (W/R Sign)		$(0.31\pm0.06)\times 10^{-4}$	$(0.22\pm0.024)\times 10^{-4}$

for the semileptonic decays of neutral and charged D mesons, we need to know the relative occurences of D^0 and D^+ mesons at these upper vertex processes. We assume that the total number of charged D and D^* mesons equals the total number of neutral D and D^* mesons. This assumption is motivated by the same number of B and anti-B mesons in our sample, resulting in an equal number of W^+ and W^- bosons contributing in the upper vertices. Further, if we assume equal probabilities for D and D^* production during the fragmentation of the W, we can use

- $\mathcal{B}(D^{*0} \to D^0 X) = 1$

- $r := \mathcal{B}(D^{*+} \to D^0 X) = (67.7 \pm 0.5)\%, \quad \mathcal{B}(D^{*+} \to D^+ X) = 1 - r$

156

to compute

$$\mathcal{B}(B \to D^{(*)} \to Xe\nu) =$$
$$\mathcal{B}(B \to DX) \times \left[\mathcal{B}(D^0 \to Xe\nu)\left(\frac{1}{2} + \frac{r}{4}\right) + \mathcal{B}(D^+ \to Xe\nu)\left(\frac{1}{2} - \frac{r}{4}\right) \right] \quad (4.16)$$

Using the latest PDG values mentioned in Table 4.29 as input, we arrive at

$$\mathcal{B}(D^0 \to Xe\nu)\left(\frac{1}{2} + \frac{r}{4}\right) + \mathcal{B}(D^+ \to Xe\nu)\left(\frac{1}{2} - \frac{r}{4}\right) = (10.24 \pm 0.66)\%$$

and

$$\mathcal{B}(B \to D^{(*)} \to Xe\nu) = (0.84 \pm 0.14)\%$$

However, there is no experimental measurement confirming that the number of excited D mesons equals the number of ground state D mesons in the fragmentation of the W bosons. In the case of no D^* production at all, we would have

$$\mathcal{B}(B \to D^{(*)} \to Xe\nu) = 0.9856\% \quad (W \to D \text{ only})$$

while in the case where only excited D meson states were produced in W fragmentation, we would have

$$\mathcal{B}(B \to D^{(*)} \to Xe\nu) = 0.6931\% \quad (W \to D^* \text{ only})$$

To be conservative, we used the difference between the central value and the values obtained in the extreme cases as additional systematic error, so that finally we arrive at

$$\mathcal{B}(B \to D^{(*)} \to Xe\nu) = (0.84 \pm 0.21)\% \quad (4.17)$$

$\mathcal{B}(B \to D^{(*)} \to Xe\nu)$ estimation for MC

For neutral B mesons, our MC models

- 1.5 % direct $B^0 \to D^0 X$ transitions (Lines 895, 897, 900, 905, 916-919);

157

- 3.3 % direct $B^0 \rightarrow D^{*0}X$ transitions (Lines 902, 907, 910, 912, 920-923); the D^{*0} decays to 100% into a D^0(Lines 2694-2701).

- 1.307 % direct $B^0 \rightarrow D^+X$ transitions (Lines 864, 965, 896, 898, 901, 906);

- 2.88 % direct $B^0 \rightarrow D^{*+}X$ transitions (Lines 866, 867, 903, 908, 911, 913). $\mathcal{B}^{MC}(D^{+*} \rightarrow D^0X) = 68.3\%$ (Lines 2685 and 2690). $\mathcal{B}^{MC}(D^{+*} \rightarrow D^+X) = 31.7\%$ (Lines 2686, 2687, 2691, 2692). This leads to 1.967 % B^0's decaying to D^0 and 0.91 % B^0's decaying to D^+ via a D^{*+} cascade.

This combines to

$$\mathcal{B}^{MC}(B^0 \rightarrow D^0X) = 6.77\%$$
$$\mathcal{B}^{MC}(B^0 \rightarrow D^+X) = 2.22\%$$

For charged B mesons, our MC models

- 1.25 % direct $B^+ \rightarrow D^0X$ transitions (Lines 1670, 1672, 1675, 1680);

- 1.5 % direct $B^+ \rightarrow D^+X$ transitions (Lines 1671, 1673, 1674, 1681, 1691, 1692, 1695, 1696);

- 2.75 % direct $B^+ \rightarrow D^{*0}X$ transitions (Lines 1677, 1682, 1685, 1687);

- 3.3% direct $B^+ \rightarrow D^{*+}X$ transitions (Lines 1678, 1683, 1686, 1688, 1693, 1694, 1697, 1698); this leads to to 2.2539 % B^+'s decaying to D^0 and 1.0461 % B^+'s decaying to D^+ via a D^{*+} cascade.

This combines to

$$\mathcal{B}^{MC}(B^+ \rightarrow D^0X) = 6.25\%$$
$$\mathcal{B}^{MC}(B^+ \rightarrow D^+X) = 2.55\%$$

For the semileptonic decay of D - mesons, we have

158

- $\mathcal{B}^{MC}(D^0 \rightarrow Xe\nu) = 6.61\%$ (Lines 2892 - 2897)

- $\mathcal{B}^{MC}(D^+ \rightarrow Xe\nu) = 13.72\%$ (Lines 2716 - 2725)

Combining all these branching ratios, we have

$$\mathcal{B}^{MC}(B \rightarrow D^{(*)} \rightarrow Xe\nu) = 0.755\% \tag{4.18}$$

Since the value of $\mathcal{B}^{MC}(D^+ \rightarrow Xe\nu)$ in MC is underestimated, we weight every electron coming from a charged D meson by 1.25 in the process of electron counting, this correction will lead to a value of 0.84, identical to Eqn. 4.17.

The errors on the branching fractions calculated above are used in determining systematic errors for the physics corrections.

Corrections to the spectra

In event classes A and C' (for description of classes, see Table 4.2 and Section 4.4.5), the following sources contribute to the right-sign background:

- Same-sign cascade charm mesons $D^{0,+}$ and D_s from tree level and color-suppressed penguin decays $B \rightarrow D_{(s)}^{(*)}\overline{D}^{(*)}$

- Semileptonic B-meson decays $B \rightarrow \tau\nu_\tau X$, $\tau \rightarrow e$.

In event classes B and D' (after unmixing), the following sources contribute to the wrong-sign background:

- Λ_c, predominantly produced as cascade products in the B-decay .

- Electrons from lower vertex decays $B \rightarrow D_s \rightarrow e$.

Monte Carlo simulations are used to obtain the shape and normalization of contributions to the electron spectrum not associated with either prompt b- or cascade c-decays. The corrections are shown in Figures 4.29-4.30.

159

Corresponding statistics is given in Table 4.35. Comparison of the prompt spectra in Data with the expected spectrum from Monte-Carlo simulation is shown in Figure 4.31.
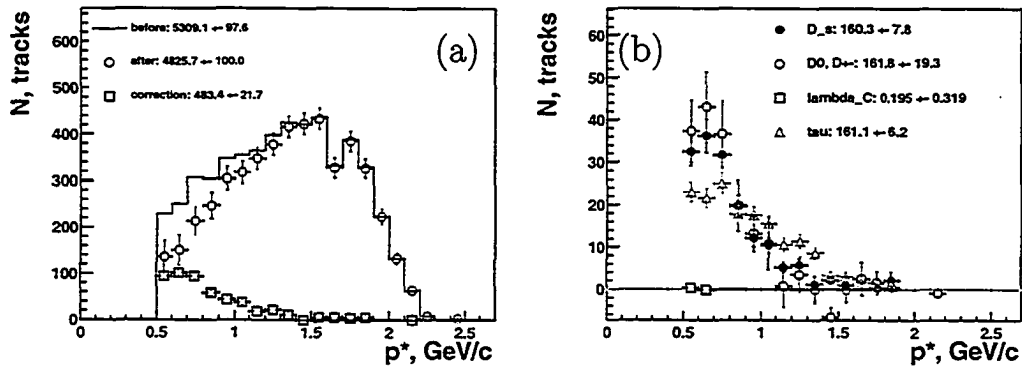
Figure 4.29: Physics background subtraction, event class A. (a) - τ and charm subtraction, (b) - backgrounds per type.
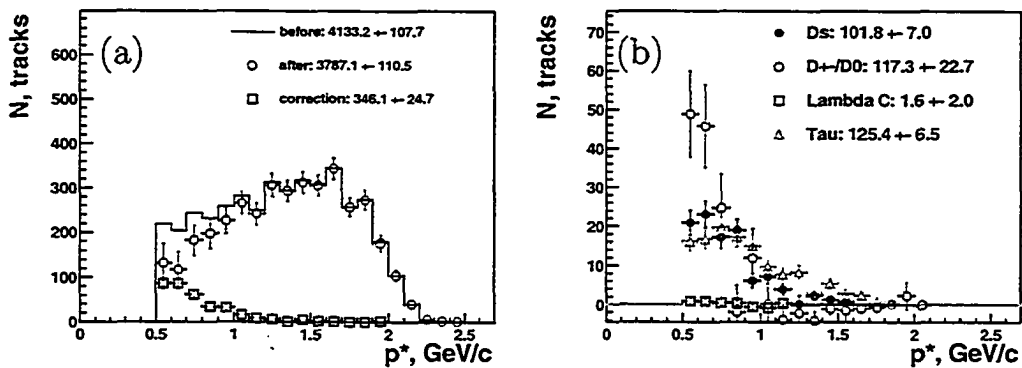
Figure 4.30: Physics background subtraction, event class C'. (a) - τ and charm subtraction, (b) - backgrounds per type.
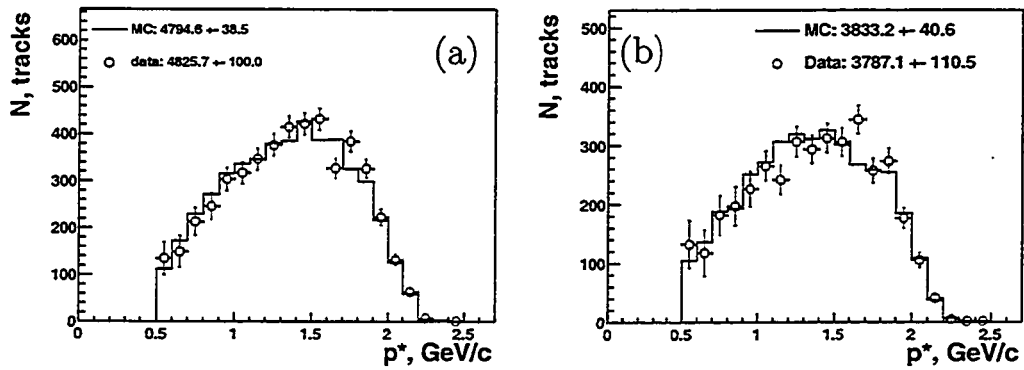
Figure 4.31: Comparison of the prompt spectrum determined from Data with the prompt spectrum as expected from MC. (a) - $B^{\pm}$, (b) - B^0 .

Table 4.35: Electron Spectrum: Physics background yields. Errors are statistical only.

Sample	A	B	C'	D'
D_s	160.3 ± 7.8	7.9 ± 3.0	101.8 ± 7.0	5.5 ± 5.2
$D^0, D\pm$	162 ± 19	—	117 ± 23	—
Λ_c	0.20 ± 0.32	26.2 ± 4.3	1.6 ± 2.0	24.6 ± 5.0
τ	161.1 ± 6.2	3.9 ± 1.0	125.4 ± 6.5	4.7 ± 3.5
Total	483 ± 22	38.1 ± 5.3	346 ± 25	34.8 ± 8.0

161
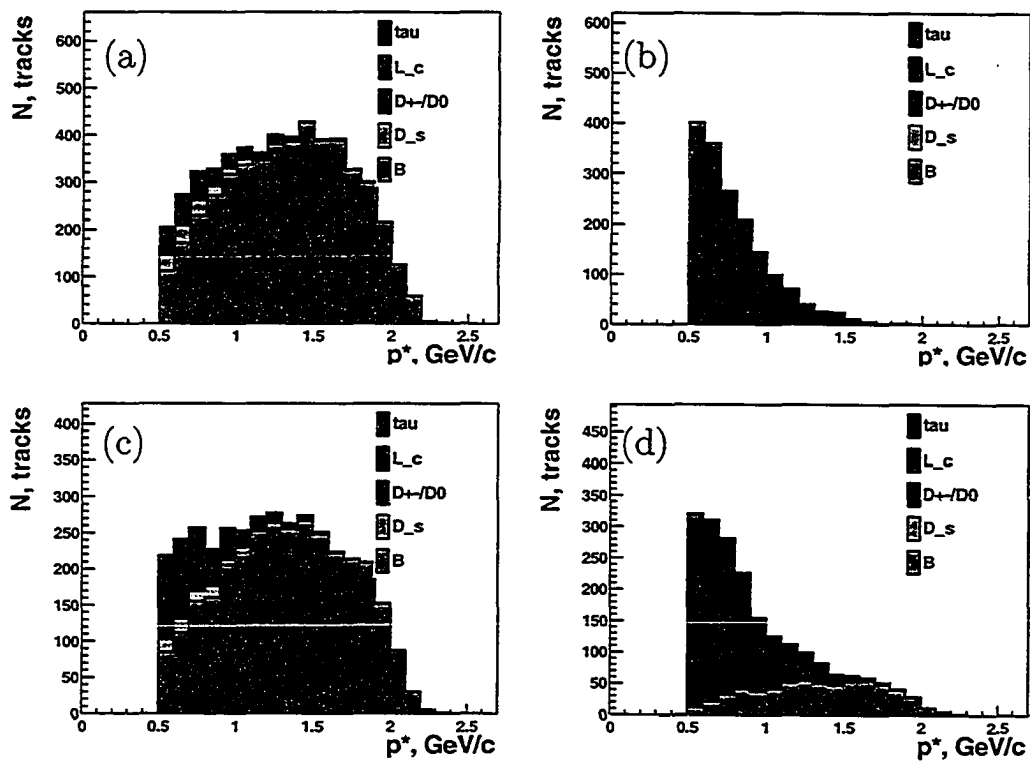
Figure 4.32: Sources for electrons in the four event classes as determined from Monte Carlo simulation: (1) - event class A, (b) - B, (c) - C, (d) - D. Same-sign cascade charm decays are not separated from opposite-sign cascade charm decays in these plots. Electrons from sources eliminated by the pair-finders (photon conversion, π^0 Dalitz decays, J/ψ) are not displayed. B^0 spectra are shown before unmixing.

162

4.4.12 Cross-feed correction to the spectra

Certain types of cross-feed will change the class of the event, affecting the spectra within individual event classes. Such types include flavor-changing cross-feed effects such as $B^0 \leftrightarrow \overline{B^0}$, $B^+ \leftrightarrow B^-$, $B^0 \leftrightarrow B^-$, , $\overline{B^0} \leftrightarrow B^+$. To derive the corresponding cross-feed coefficients, we have studied B_{reco}-generated B flavor correlation in events with one B decaying semileptonically. In such events, one can exactly determine the flavor of the B meson that has been reconstructed into a B_{reco} mode (see Section 4.3.6 for more details on the methodology). The final results of the corrections to the spectra are shown in Figure 4.33. The corresponding electron yields are given in Table 4.36.

Table 4.36: Electron Spectrum: Spectra cross-feed correction. The error given corresponds to the statistical error.

Sample	into class A	into class C'
Before	4826 ± 100	3787 ± 110
from class A	–	79.6 ± 1.6
from class B	3.77 ± 0.20	4.12 ± 0.21
from class C'	32.97 ± 0.96	–
from class D'	8.00 ± 0.51	0
After	4781 ± 100	3703 ± 110

Systematic errors for the cross-feed correction to the electron spectra are discussed in Section 4.3.4. They are composed of the uncertainty due to limited statistics of the Monte-Carlo sample used to derive corresponding cross-feed coefficients (30%) and a systematic error determined from variation of cross-feed coefficients for different bins in recoil electron momentum (30%).

163
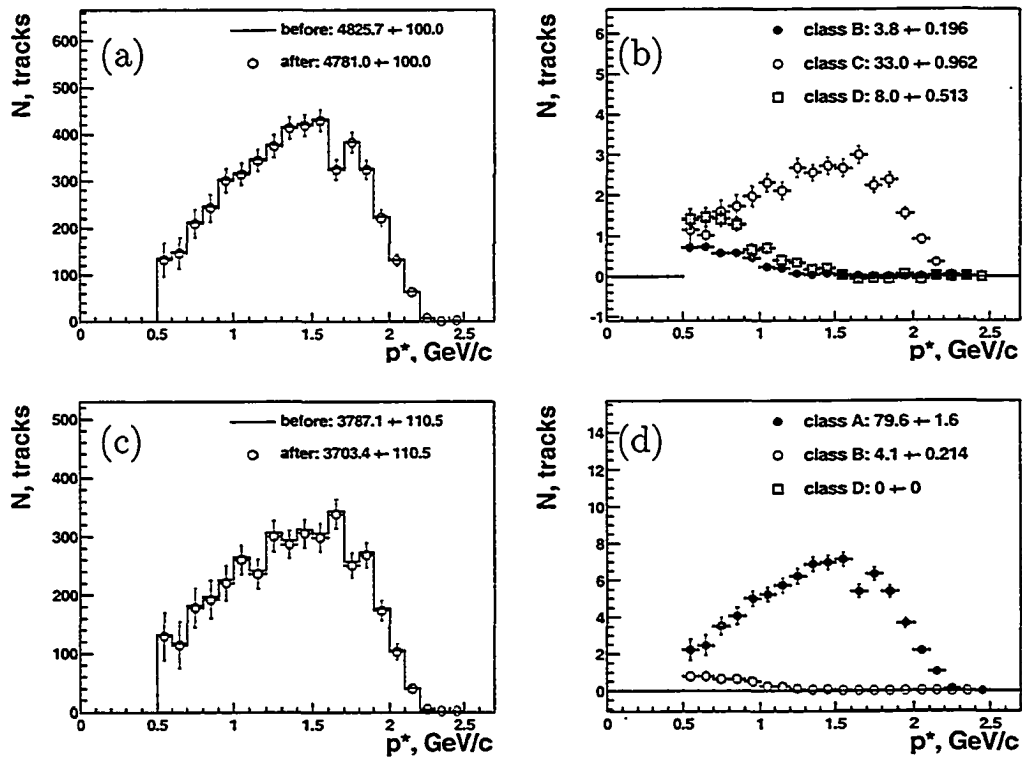
Figure 4.33: Correction to the lepton spectrum due to B_{reco} cross-feed effects. (a) - spectra before/after correction, class A, (b) - contributions from all event classes to the spectrum in class A (contributions from classes B, C', D' are subtracted), (c) - spectra before/after correction, class C', (b) - contributions from all event classes to the spectrum in class C' (contributions from classes A, B, D' are subtracted).

164

4.4.13 Correction for radiative effects

Generally speaking, radiative effects result in the softer electron spectrum being detected. The correction is dependent on the amount of material a track has to traverse and on the momentum of the track. Also, the momentum of the track changes which makes it impossible to derive an efficiency histogram independent of the spectrum to be corrected. Instead, we have analyzed a significant number of generated Monte Carlo electron tracks to populate the matrix describing $P_{CMS} - \theta$-dependent momentum transformation. We use a 3-dimensional matrix (generated θ (same as reconstructed), generated P_{CMS}, reconstructed P_{CMS}) describing the conversion of the reconstructed momentum and θ into generated ones. This matrix is then applied to the detected prompt electron spectrum to arrive at the generated prompt electron spectrum. The cross-check on the procedure is shown in Figure 4.34 and the actual application to the spectra from Data is shown in Figure 4.35.
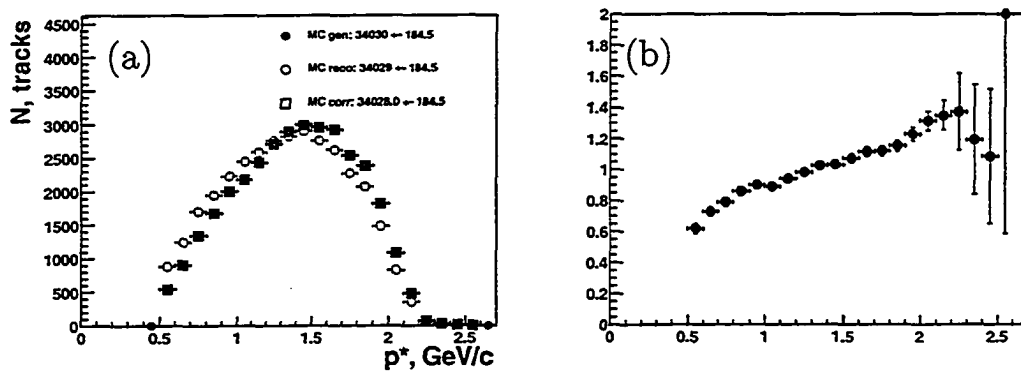
Figure 4.34: Bremsstrahlung correction to the lepton spectrum. (a) - check on MC to make sure we can return to generated spectrum by applying the correction to reconstructed MC spectrum, (b) - correction function.

In addition to changing a shape of the detected spectrum, bremsstrahlung also results in a loss of the electrons. A certain portion of the electrons generated

165
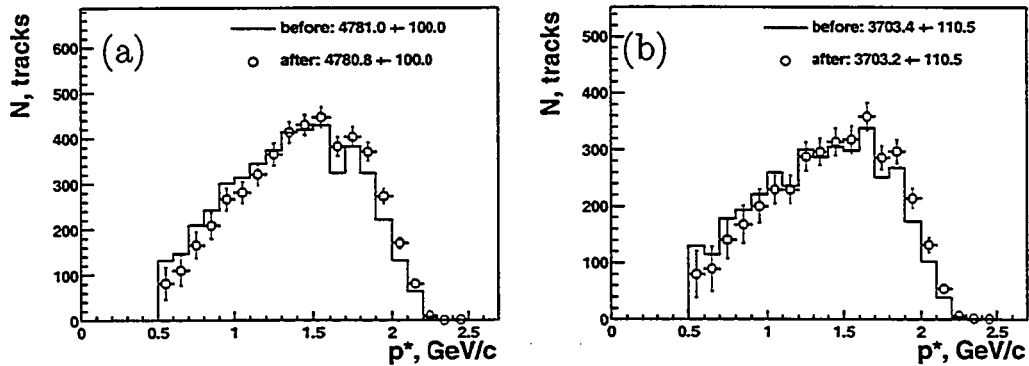
Figure 4.35: Bremsstrahlung correction to the lepton spectrum. (a) - correction applied to Data (class A), (b) - class C'.

at momenta above 0.5 Gev/c is reconstructed with momenta below 0.5 Gev/c due to bremsstrahlung effects. This was corrected for using Monte-Carlo simulations (efficiency of 99.14±0.13 is obtained). The corresponding correction and efficiency plots are shown in Figure 4.36.
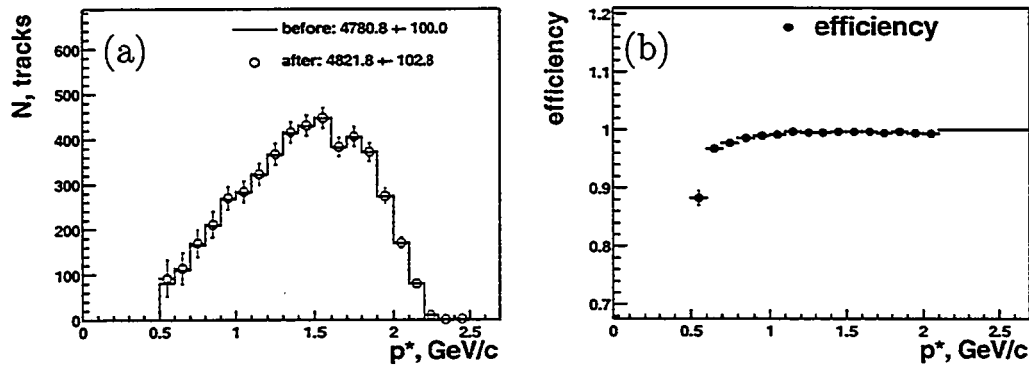
Figure 4.36: Loss of the electrons due to Bremsstrahlung. (a) - correction applied to class A, (b) - corresponding effective effficiency.

The systematic error for the bremsstrahlung corrections is estimated at 20% based on the statistics of the Monte-Carlo sample used to determine this correction.

166

4.4.14 Corrections for P_{LAB} cut efficiency and Acceptance

At this point, we have true prompt spectra of electrons from $B^{\pm}$ and B^0 , as generated. All electrons in these distributions come from desired physical sources. However, the spectra still have to be corrected for:

- momentum-dependent efficiency of the plab cut

- geometrical acceptance

First, we correct for plab cut efficiency. The correction is based on Monte-Carlo generator-level spectra of the primary electrons and is shown in Figure 4.37. Overall efficiency of the plab cut applied in this analysis is determined to be $(98.82 \pm 0.15)\%$ for prompt spectrum.
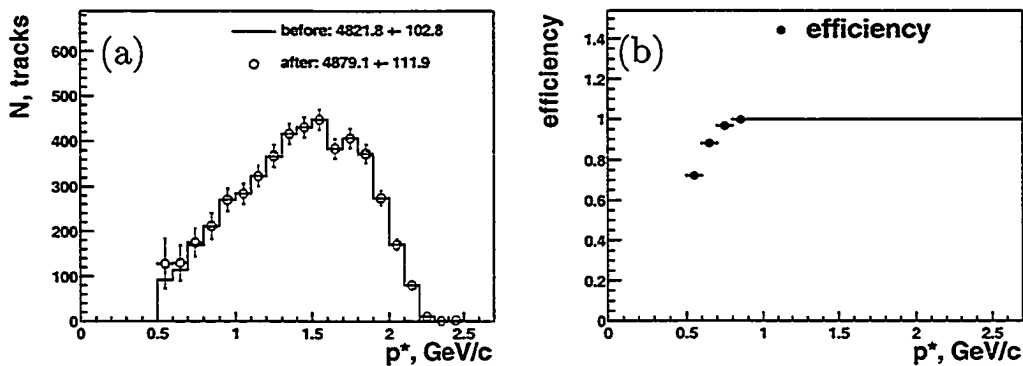
Figure 4.37: Correction for momentum-dependent efficiency of the plab cut. (a) - correction for class A, (b) - corresponding plab cut efficiency.

Finally, the spectra are corrected for geometrical acceptance (efficiency of 86.24 ± 0.45 % for $B^{\pm}$ and 86.22 ± 0.51 % for B^0). For more details on correlations of the geometrical acceptance efficiencies with other track cut efficiencies, refer to Table 4.15. The result of this correction is shown in Figure 4.38 and Table 4.37.
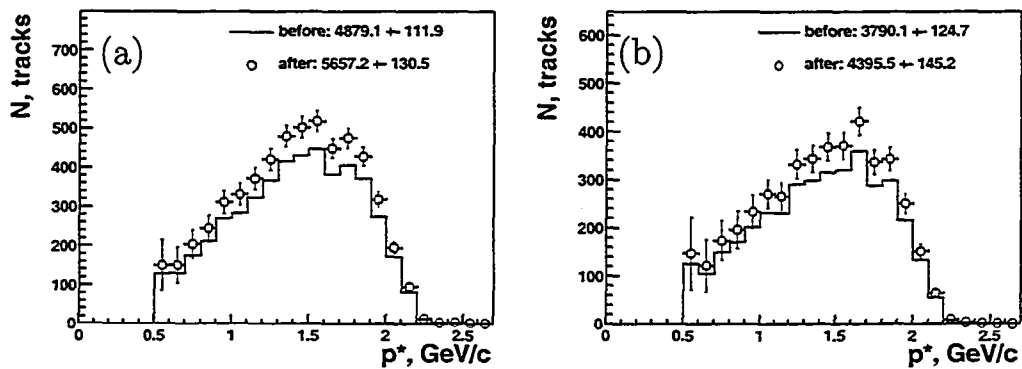
Figure 4.38: Correction for geometrical acceptance. (a) - correction applied to spectrum in event class A, (b) - same for class C'.

Table 4.37: Electron Spectrum: Acceptance, P_{LAB} momentum cut and Radiative corrections. The error given corresponds to the statistical error.

Sample	A	C'
Before	4781 ± 100	3703 ± 110
After loss due to bremsstrahlung	4822 ± 103	3738 ± 114
After $P_{LAB} > 0.5$	4879 ± 112	3790 ± 125
After Geometry	5657 ± 130	4396 ± 145

168

Systematic of the acceptance correction is determined from statistics of the Monte-Carlo sample used to derive the efficiency - an error of 0.5% is taken (see Table 4.15). The systematic uncertainty of the P_{LAB} cut efficiency correction is also determined from the statistics of Monte-Carlo sample used - an error of 0.15% is taken.

The resulting spectrum is compared to the true prompt electron spectrum derived from the MOnte-Carlo sample in Figure 4.39.
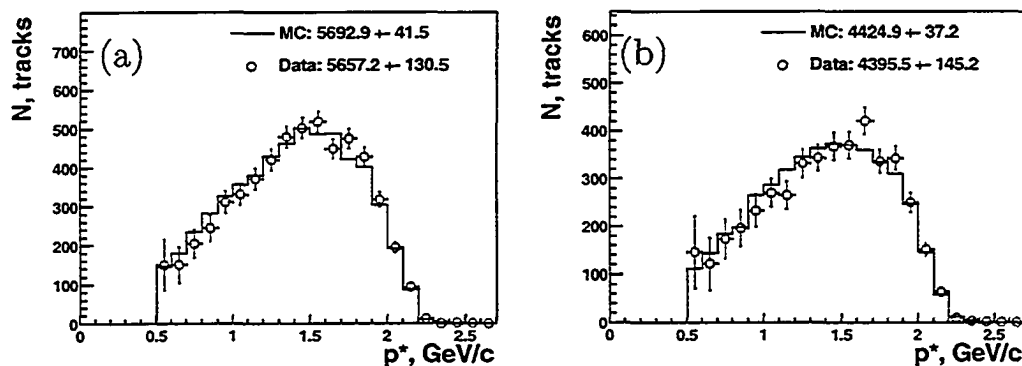
Figure 4.39: Comparison of the final fully corrected spectrum to the true prompt electron spectrum in Monte-Carlo. (a) - event class A, (b) - same for class C'.

169

4.5 Results

4.5.1 Measurement of the Detected Branching Fractions

The branching fraction is derived from the number of tags and the signal spectrum via

$$\mathcal{B}(sl) = \frac{N^e}{N^{tot}} = \frac{N^e_{tag}/\epsilon^e_{tag}}{N^{tot}_{tag}/\epsilon^{tot}_{tag}}$$

where

ϵ^e_{tag} is a fraction of $B\overline{B}$ events tagged by B_{reco} in which one of the B decays semileptonically to an electron, the other hadronically

ϵ^{tot}_{tag} - a fraction of $B\overline{B}$ events tagged by B_{reco} , only one B_{reco} per event

ϵ^{had}_{tag} - a fraction of $B\overline{B}$ events tagged by B_{reco} in which both B mesons decay to hadrons

N^e - the number of detected electrons from semielectronic B-meson decays in all $B\overline{B}$ events in our sample, corrected for fakes and non-prompt electrons

N^{tot} - the total number of detected $B\overline{B}$ events

N^e_{tag} - the number of detected electrons from semielectronic B-meson decays in $B\overline{B}$ events tagged by B_{reco} , corrected for fakes, combinatorics from sidebands in M_{ES} , non-prompt electrons and electron selection efficiency $(\epsilon^e_{sel} = \epsilon^e_{PID}\epsilon^e_{trk}\epsilon^e_{plab}\epsilon^e_{geom.}\epsilon^e_{brems})$

N^{tot}_{tag} - the number of detected $B\overline{B}$ events tagged by B_{reco} , corrected for combinatorics from sidebands in M_{ES} , one B_{reco} /event

170

Efficiency Bias Correction

Since we do not want to rely on the MC to have the correct mix of hadronic and semileptonic decays we rewrite N_{tag}^{tot} as the sum of events with semileptonic and hadronic decays in the recoil:

$$N_{tag}^{tot} = N_{tag}^{SE} + N_{tag}^{SM} + N_{tag}^{had} = 2N_{tag}^{SE} + (N_{tag}^{tot} - 2N_{tag}^{SE})$$

where

N_{tag}^{SE} is the number of B_{reco}-tagged events with semielectronic decay of the recoil B-meson

N_{tag}^{SM} - same for semimuonic B decay in the recoil

N_{tag}^{had} - same for hadronic B decay in the recoil

In the following, we assume that the number of $B\overline{B}$ events where one B-meson decays semi-*electronically* is identical to the number of $B\overline{B}$ events where one B-meson decays semi-*muonically*. Then the total number of detected $B\overline{B}$ events can be written as

$$N^{tot} = 2N_{tag}^{SE}/\epsilon_{tag}^{e} + N_{tag}^{had}/\epsilon_{tag}^{had}$$

Thus we obtain

$$\mathcal{B}(sl) = \frac{N^e}{N^{tot}} = \frac{N_{tag}^e/\epsilon_{tag}^e}{2N_{tag}^{SE}/\epsilon_{tag}^e + N_{tag}^{had}/\epsilon_{tag}^{had}} = \frac{N_{tag}^e}{2N_{tag}^e + (N_{tag}^{tot} - 2N_{tag}^e)\frac{\epsilon_{tag}^e}{\epsilon_{tag}^{had}}}$$

The efficiencies are determined by MC simulation:

171

$$\epsilon^e_{tag} = \frac{N^{SE}_{tag}(MC)}{2N_{BB}\mathcal{B}^{MC}_{sl}(1 - 2\mathcal{B}^{MC}_{sl})}$$

$$\epsilon^{had}_{tag} = \frac{N^{had}_{tag}(MC)}{2N_{BB}(1 - 2\mathcal{B}^{MC}_{sl})^2}$$

where $\mathcal{B}^{MC}_{sl} = 10.54\%$ is the default Monte-Carlo semileptonic branching fraction and N_{BB} is the total number of generated $B\overline{B}$ events in Monte-Carlo sample.

In order to reliably determine these efficiencies, events with different types of recoil B-meson decay have to be cleanly separated. Since the generator-level information from MC is used to determine the type of recoil B-meson decay, we have to correctly match one of the generated B-mesons to the recoil B-meson . To achieve this, we require the type of the the generated B-meson to match that of the reconstructed B_{reco} candidate. All surviving events are used in the efficiency calculations. The resulting efficiency bias estimates are given in Table 4.38.

Table 4.38: Event selection efficiency for events where both B-mesons decay hadronically and where one decays semileptonically. Errors are statistical only.

ϵ	B_{reco} + s.l	B_{reco} hadronic	$\frac{\epsilon^e_{tag}}{\epsilon^{had}_{tag}}$
$B^\pm$	0.0009506 ± 0.0000067	0.0009341 ± 0.0000024	1.018 ± 0.010
B^0	0.0007335 ± 0.0000059	0.0006972 ± 0.0000021	1.052 ± 0.012

172

Tag Cross-Feed Correction

Before we derive branching fractions, the tag count, N_{tag}, has to be corrected for cross-feed effects as discussed in Section 4.3.5. Namely, cross-feed effects which change the type of B event result in a bias in the tag counts. The correction could be expressed as:

$$N_{true}^{B^0 \ tag} = N_{B_{reco}}^{B^0 \ tag} \times (1 - CF_{B^0}^{B^\pm})$$

$$N_{true}^{B^\pm \ tag} = N_{B_{reco}}^{B^\pm \ tag} \times (1 - CF_{B^\pm}^{B^0})$$

where $CF_{B^0}^{B^\pm}$ is the fraction of the events reconstructed into B^0 modes while being true $B^\pm$ events.

For this analysis, corresponding corrections are given in the Table 4.39. Table 4.40 shows the final tag and signal yields that are used to determine branching fractions.

Table 4.39: Tag count correction due to the B_{reco} cross-feed effects. Errors on the correction are statistical only. For systematic error discussion refer to the Systematics section below.

	Detected	Correction	Correction, %	True Count
$B^\pm$	56766 ± 354	-2231 ± 89	-0.0393 ± 0.0016	54536 ± 365
B^0	42951 ± 298	-1868 ± 75	-0.0435 ± 0.0017	41083 ± 307

Final Signal and Tag Yields

Using the expressions above, the spectra are scaled as shown in Figure 4.40 and the resulting branching fractions for $p^* > 0.5$ GeV/c are:

173

$$BR(B^{\pm})_{p^{*}>0.5\ GeV/c} \quad = \quad 0.1023 \pm 0.0024$$

$$BR(B^{0})_{p^{*}>0.5\ GeV/c} \quad = \quad 0.1028 \pm 0.0034$$

where the error indicates the statistical uncertainty only.

Table 4.40: Electron yields in data

B-meson	Tag count	Prompt electrons
$B^{\pm}$	54536 ± 365	5657 ± 130
B^{0}	41083 ± 307	4396 ± 145
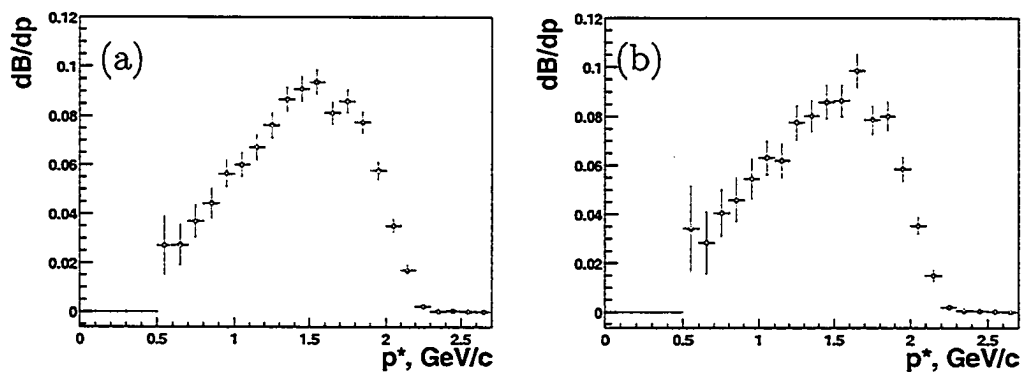
Figure 4.40: Electron spectra normalized to the number of B_{reco} tags taking into account the efficiency ratio for generic recoil side vs. semielectronic one. (a) - charged B, (b) - neutral B.

174

4.5.2 Extrapolation to full Semileptonic Branching Fraction

The extension of the measurement from the limited p^* range to the full inclusive semileptonic branching fraction requires a correction for the undetected part ($p^* < 0.5 GeV/c$) of the electron spectrum. This correction is derived from Monte Carlo simulations and amounts to $\sim 4\%$ as determined from fits to a sum of predicted spectra shapes for individual semileptonic decay modes. Fits are shown on Figure 4.41 and described in detail below.
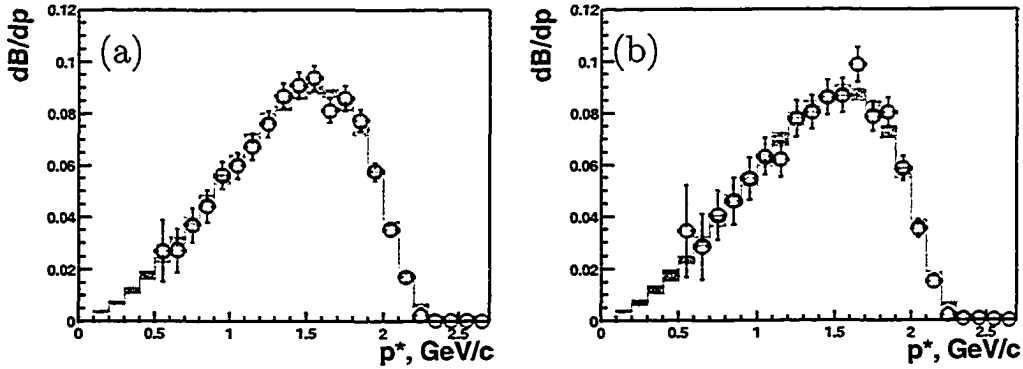
Figure 4.41: Extrapolation of the lepton spectrum to $P^* = 0$. (a),(b) - fit with error band showing one-sigma variation in fitted bin content when input bin content is varied according to its mean value and error (assuming gaussian distribution): (a) - for $B^{\pm}$; (b) - for B^0.

Fitting procedure

We fit the spectrum corrected for bremsstrahlung to the theoretical models. The relative branching fractions for the $B \rightarrow X_c l\nu$ modes according to our event generator are:

$$(\mathcal{B}(D^* l\nu) : \mathcal{B}(B \rightarrow Dl\nu) : \mathcal{B}(B \rightarrow D^{**} l\nu) : \mathcal{B}(B \rightarrow D(*)\pi l\nu)) =$$

175

$$= (c_{D^*} : c_D : c_{D^{**}} : c_{D(*)\pi}) = (0.54 : 0.20 : 0.14 : 0.12)$$

In the data spectra there is also a small contribution of $b \to u$ electrons. The default event generator predicts that such electrons contribute 1.3% to the total semileptonic rate. However, more recent results [56] on $b \to u$ suggest that fraction to be 2.24% so we renormalize our $b \to u$ branching fraction before including it into a fit function.

To predict shapes of the involved $b \to c$ exclusive modes the models described in Table 4.41 are used.

Table 4.41: Models used to predict contributions from the individual decay channels to the total semileptonic decay spectrum. Current experimental errors on observed branching fractions are given.

mode	$B \to D^*l\nu$	$B \to Dl\nu$	$B \to D^{**}l\nu$	$B \to D(*)(n)\pi l\nu$
model	HQET	ISGW2	ISGW2	Goity-Roberts
$\frac{\delta B(mode)}{B(mode)}$	15%	10%	25%	–

The standard *BABAR* event generator is used (EvtGen package) to produce 5 Million $B\overline{B}$ events.

In the fit, we allow the branching fractions of $B \to D^{**}l\nu$, $B \to D^*l\nu$ and $B \to Dl\nu$ to float while the fraction of $B \to D(*)\pi l\nu$ is determined from normalization constraints. Finally, the sum of all modes is allowed to float.

The fit is set up to minimize the χ^2 function, which includes a "penalty" term for deviation of the branching fractions for exclusive modes from their measured world average values:

176

$$\chi^2 = \sum (\frac{x(p_i) - f(p_i))}{\sigma x(p_i)})^2 \tag{4.19}$$

$$+ (\frac{BR(B \to Dl\nu)^{fitted} - BR(B \to Dl\nu)^{meas}}{\sigma BR(B \to Dl\nu)^{meas}})^2 \tag{4.20}$$

$$+ < same \; for \; other \; exclusive \; modes > \tag{4.21}$$

The fit function is constructed in the following way: all resonant decay spectra are scaled by the individual fit parameters and the non-resonant spectrum is scaled in such a way that a sum of all fitted $B \to X_c l\bar{\nu}$ branching fractions inside the square brackets is equal to 1.00. Also, the $b \to u$ spectrum is added as a fixed contribution to the expression in the square brackets. Finally, everything is scaled using one more parameter, a_0. The resulting function is

$$F(p^*) = a_0[a_1 f_{D^*}(p^*) + a_2 f_D(p^*) + a_3 f_{D^{**}}(p^*)$$
$$+ \frac{1 - a_1 c_{D^*} - a_2 c_D - a_3 c_{D^{**}}}{c_{D^{non-res}}} f_{D^{non-res}}(p^*) + f_{b \to u}(p^*)]$$

where a_n are fit parameters, $f_{xxx}(p^*)$ are the spectra for specific channels predicted by the event generator and c_{D^x} are the relative branching fractions defined above in 4.19. The fit parameters define how large the specific contribution or fraction is compared to the generator default.

Figure 4.42 shows the result of the fit. The Table 4.43 shows the branching fraction of each channel from default EvtGen decay files and obtained through the fitting procedure. Note that the fit calls for a significantly lower fraction of the non-resonant $B \to D(*)(n)\pi l\nu$ decays.

The fit for the charged B spectrum has $\chi^2/DOF = 0.638$ and predicts the fraction of electrons with $p^* < 0.5 GeV/c$ to be 4.08 ± 0.10 % of the total rate. The same fit for the neutral B spectrum has $\chi^2/DOF = 0.711$ and predicts the fraction of electrons with $p^* < 0.5 GeV/c$ to be 4.14 ± 0.13 % of the total rate.

177
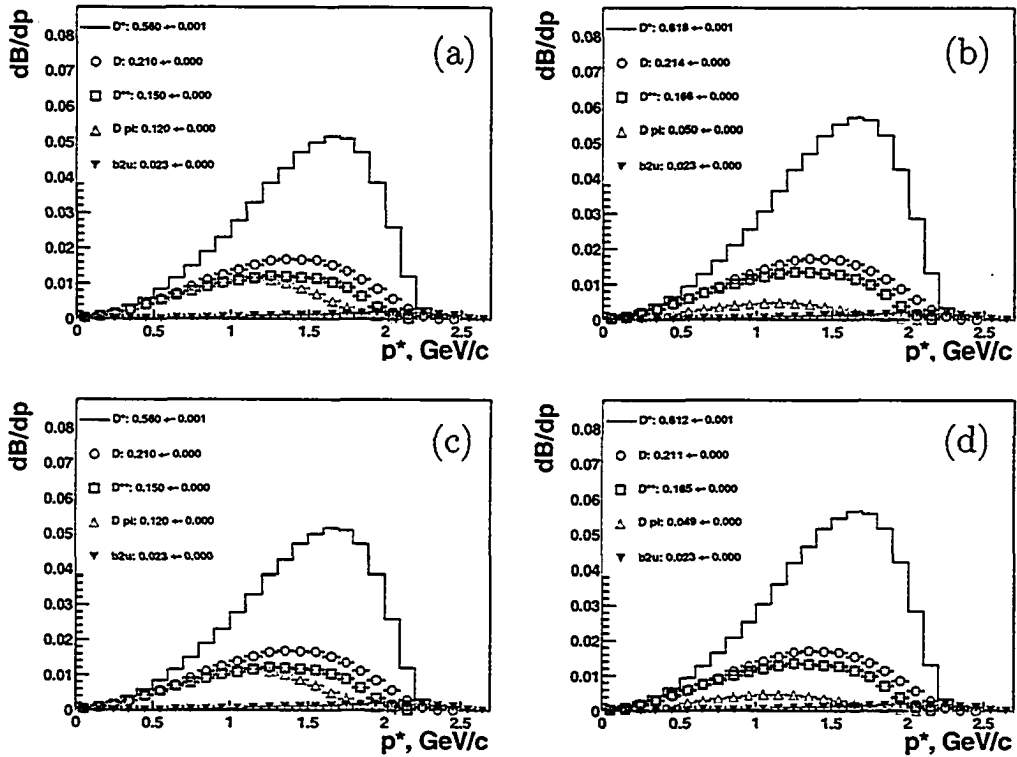
Figure 4.42: Results of the fit to the theoretical shapes. (a) - the default decomposition of $B^{\pm} \rightarrow X_c e\nu$ spectrum into 4 exclusive modes and $b \rightarrow u$, (b) - the fitted decomposition of $B^{\pm} \rightarrow X_c e\nu$ spectrum into 4 exclusive modes and $b \rightarrow u$, (c) - the default decomposition of $B^0 \rightarrow X_c e\nu$ spectrum into 4 exclusive modes and $b \rightarrow u$, (d) - the fitted decomposition of $B^0 \rightarrow X_c e\nu$ spectrum into 4 exclusive modes and $b \rightarrow u$.

To determine the error on these corrections, the following procedure is used. We observe fit variations when changing bin content of the differential branching fraction histogram in accordance with errors on contents of its bins. In this process, each variation is obtained by assuming gaussian distribution with mean=bin content and sigma=bin error for each bin content and generating new bin content based on that distribution. We use this method to obtain 100s of variations of

178

the input histogram. We then run fits on each of them accumulating values of the fit function at the center of each bin and the value of the $p^* = 0$ extrapolation factor. At the end of this process, we fit accumulated distributions to a gaussian function to obtain the error on the fitted bin content and the extrapolation factor. The resulting error estimates for each of the bins are shown in Figure 4.43. The errors on the extrapolation factor are extracted from the distributions in Figure 4.44.
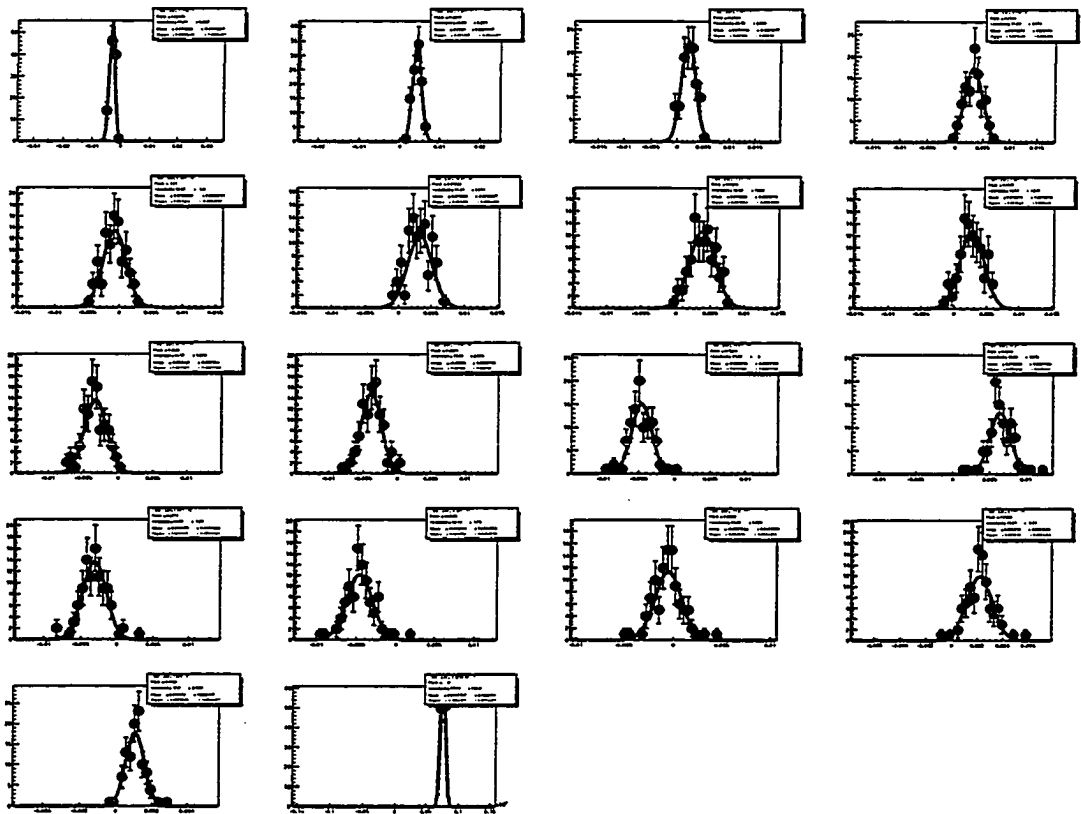
Figure 4.43: Error estimation for $p^* = 0$ extrapolation fit. Bin-by-bin error estimation is shown
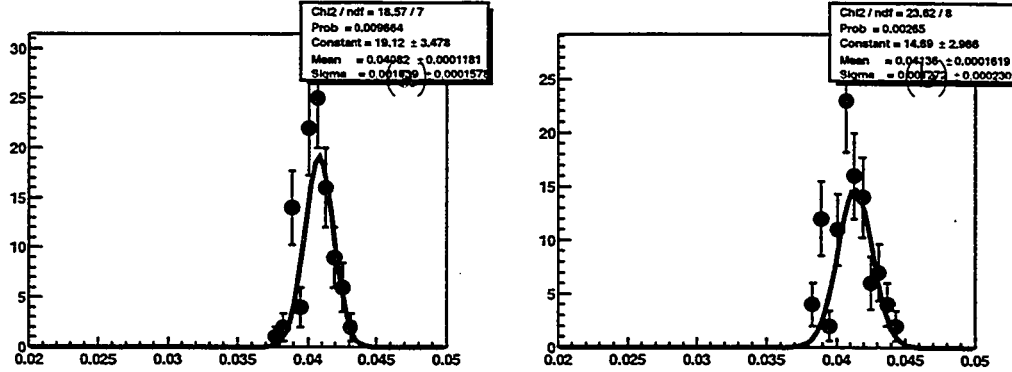
Figure 4.44: Error estimation for $p^* = 0$ extrapolation fit. (a) - distribution of the $p^* = 0$ extrapolation, $B^{\pm}$; (b) - same for B^0 .

Table 4.42: Fit results.

parameter	floating D/D^* ratio	
	$B^{\pm}$	B^0
a_0^{fit}	1.008 ± 0.019	0.998 ± 0.027
a_1^{fit}	1.094 ± 0.052	1.095 ± 0.064
a_2^{fit}	1.010 ± 0.095	1.008 ± 0.095
a_3^{fit}	1.10 ± 0.23	1.10 ± 0.24
$\chi 2/DOF$	$\frac{8.93}{14.0} = 0.638$	$\frac{9.95}{14.0} = 0.711$
Conf. Level	0.776	0.697
p=0 correction, % (relative)	4.08 ± 0.10	4.14 ± 0.13

180

mode	$B \to D^* l\nu$	$B \to Dl\nu$	$B \to D^{**} l\nu$	$B \to D(*)(n)\pi l\nu$	$b \to u$	total
$B^{\pm}$, float D/D^*	6.18 ± 0.30	2.14 ± 0.20	1.66 ± 0.35	0.50 ± 0.50	0.233	10.72 ± 0.21
B^0, float D/D^*	6.12 ± 0.36	2.11 ± 0.20	1.65 ± 0.36	0.49 ± 0.54	0.233	10.61 ± 0.28

Table 4.43: Individual channel and total branching fractions, default and fitted, %. $b \to u$ branching fraction is fixed to 2.24% of the $b \to c$ combined fraction, per latest experimental results.

Branching fractions before and after this correction are given in Table 4.44.

Table 4.44: Branching Fraction extrapolation to the full momentum range.

Sample	BR ($p^* > 0.5$ GeV/c)	$p^* = 0$ correction	full BR, %
$B^\pm$	0.1023 ± 0.0024	0.00404	$10.63 \pm 0.24 \pm 0.29$
B^0	0.1028 ± 0.0034	0.00403	$10.68 \pm 0.34 \pm 0.31$
average	–	–	$10.65 \pm 0.19 \pm 0.27$

4.5.3 Summary of the analysis steps

A summary of all corrections and normalizations described above is given in Table 4.45.

Table 4.45: Electron Spectrum: Signal and background yields. Errors are statistical only. Rows labeled "raw" are not efficiency corrected. The other rows include corrections for *e.g.* electron identification efficiency, finder- and reconstruction-efficiency, *etc.*.

Sample	A	B	C	D
Electrons (raw)				
Signal box	5362 ± 73	1738 ± 42	3686 ± 61	2032 ± 45
Sideband (unscaled)	1363 ± 37	843 ± 29	850 ± 29	746 ± 27
Sideband-subtracted	4891 ± 74	1425 ± 43	3351 ± 62	1812 ± 46
Pair Background	217 ± 39	209 ± 40	194 ± 34	155 ± 31
Hadron fakes	80.80 ± 0.59	47.22 ± 0.46	41.39 ± 0.42	44.30 ± 0.39
Electrons	4593 ± 84	1169 ± 59	3115 ± 70	1613 ± 55
After Eff. Corr(ID)	5130 ± 94	1325 ± 67	3485 ± 79	1817 ± 63
After Eff. Corr(Trk)	5309 ± 98	1378 ± 70	3639 ± 83	1898 ± 66
Sample	A	B	C'	D'
After Unmixing	5309 ± 98	1378 ± 70	4133 ± 108	1404 ± 87
Physics Bg	483 ± 22	38.1 ± 5.3	346 ± 25	34.8 ± 8.0
Final spectrum	4826 ± 100	1340 ± 70	3787 ± 110	1369 ± 88
MC (truth-matched)	4795 ± 39	–	3833 ± 41	–
Cross-feed	4781 ± 100	–	3703 ± 110	–
bremsstrahlung loss	4822 ± 103	–	3738 ± 114	–
$P_{LAB} > 0.5$	4879 ± 112	–	3790 ± 125	–
Geometry	5657 ± 130	–	4396 ± 145	–
MC (truth-matched)	5693 ± 41	–	4425 ± 37	–
Final Normalizations				
Raw N_{tags}	56766 ± 354		42951 ± 298	
cross-feed	54536 ± 365		41083 ± 307	
B_{reco} Efficiency Bias	1.018 ± 0.010		1.052 ± 0.012	
$p^* = 0$, absolute	0.00403	–	0.00401	–
Branching Fraction, %	$10.63 \pm 0.24 \pm 0.29$	–	$10.68 \pm 0.34 \pm 0.31$	–

183

4.5.4 Systematic Errors

The systematic errors for this analysis are presented in Table 4.46. The errors are separated into several categories reflecting the sources of the errors and the way they affect the final result. This section summarizes all the systematic errors that are relevant to this analysis. Some errors are determined separately for B^0 and $B^{\pm}$ events:

- Error on the ratio of B_{reco} efficiencies for events with semileptonic vs. hadronic recoil side is estimated from:

  - Error due to the limited Monte-Carlo statistics used in calculation of these coefficients.

  - Possible differences in this ratio in Data and Monte-Carlo. This error is estimated from the variation of this ratio for different B_{reco} mode compositions (Section 6.1.7).

- Error on the cross-feed correction to the tag counts, taken from:

  - Error due to the limited Monte-Carlo statistics used in calculation of the corresponding coefficients.

  - Dependency on the momentum of the electron in the recoil (Sections 4.3.5 and 6.1.1).

- Error on the cross-feed correction to the signal spectra, taken from:

  - Error due to the limited Monte-Carlo statistics used in calculation of the corresponding coefficients.

  - Dependency on the momentum of the electron in the recoil (Sections 4.3.5 and 6.1.1).

- Error on the sideband subtraction is determined from

Reproduced with permission of the copyright owner. Further reproduction prohibited without permission.

- The variation of the sideband scaling factors observed when different M_{ES} fitting methods are used (Section 6.1.3).

- Dependency of the sideband scaling factors on the momentum of the electron in the recoil (Section 6.1.6).

- Error due to the limited Monte-Carlo statistics used in calculation of the sideband scaling factors.

• Error on the $B^0 - \overline{B^0}$ mixing parameter, χ_d. The latest available values from PDG2002 were taken [46].

The errors from the list above are derived through detailed systematic studies presented in Section 6.1.

The remaining errors are common to both charged and neutral B events:

• Tracking systematics (Section 4.4.3).

• Particle identification systematics (Sections 4.4.3 and 4.4.2). Electron identification and hadron misidentification systematic effects are studied in detail in [29]. The error on the hadronic fraction is determined from Monte-Carlo statistics used in deriving said fractions.

• Pair background systematics (Section 4.4.1).

• Physics correction systematics, taken from the known uncertainties on the corresponding branching fractions (Section 4.4.6).

• Errors on the acceptance, P_{LAB} cut and bremsstrahlung corrections, due to limited statistics of the Monte-Carlo samples used to derive these corrections.

185

- Error on the extrapolation of the spectrum to $p^* = 0$. The error is determined by varying the fit parameters (branching fractions of underlying decays) within their respective standard deviations (Section 4.5.2).

These errors are derived in the preceding sections at the same time the corresponding correction is applied.

The systematic error in the ratio of the branching fractions will be obtained from the errors in the individual $B^\pm$ and B^0 measurements, taking into account correlations between the corresponding errors. The following procedure is used:

- errors for individual measurements are grouped (by adding in quadrature) into correlated ($\sigma_c^\pm$, σ_c^0 for $B^\pm$, B^0), uncorrelated ($\sigma_u^\pm$, σ_u^0) and anti-correlated ($\sigma_a^\pm$, σ_a^0).

- the total covariance matrix is written as

$$
V = \begin{pmatrix} BR_{B\pm}^2 \times (\sigma_c^{\pm 2} + \sigma_u^{\pm 2} + \sigma_a^{\pm 2}) & BR_{B^0} \times BR_{B\pm} \times (\sigma_c^\pm \sigma_c^0 - \sigma_a^\pm \sigma_a^0) \\ BR_{B^0} \times BR_{B\pm} \times (\sigma_c^\pm \sigma_c^0 - \sigma_a^\pm \sigma_a^0) & BR_{B^0}^2 \times (\sigma_c^{0\,2} + \sigma_u^{0\,2} + \sigma_a^{0\,2}) \end{pmatrix}
$$

- the error on the ratio of branching fractions (R) is propagated according to

$$
\sigma R = R \sqrt{\frac{V^{11}}{BR_{B\pm}^2} + \frac{V^{22}}{BR_{B^0}^2} - 2\frac{V^{12}}{BR_{B\pm} \times BR_{B^0}}}
$$

4.5.5 Branching Fractions

The fully corrected semileptonic branching fractions measured in this analysis are:

$$
BR(B^0 \rightarrow Xl\nu) = 10.68 \pm 0.34 \pm 0.31
$$

$$
BR(B^\pm \rightarrow Xl\nu) = 10.63 \pm 0.24 \pm 0.29
$$

186

Table 4.46: Analysis systematics. x denotes the relative (normalized to the branching fraction) size of the correction applied, $\delta x/x$ - its relative error, $\delta BR/BR$ - contribution to the relative error on the appropriate branching fraction from this source. Second column indicates whether the error for B^0 branching fraction from that particular source is correlated (not correlated, anti-correlated) with the same error for $B^\pm$ branching fraction.

Contribution	Corr?	B^0			$B^\pm$			$\frac{\delta BR}{BR}$, %
		x	$\delta x/x$, %	$\frac{\delta BR}{BR}$, %	x	$\delta x/x$, %	$\frac{\delta BR}{BR}$, %	
B-reco eff ratio								
statistics	–	1.05	1.1	1.16	1.018	0.9	0.92	0.72
B-reco cross-feed								
TAG-level - statistics	–	0.035	6	0.21	0.043	8	0.34	0.22
TAG-level - p* in recoil	–	0.035	10	0.35	0.043	10	0.43	0.29
SIGNAL-level - statistics	–	0.008	30	0.24	0.016	25	0.4	0.25
SIGNAL-level - p* in recoil	–	0.008	30	0.24	0.016	30	0.48	0.29
Sideband subtraction								
fit methodology	Corr	0.11	1.3	0.14	0.1	1.3	0.13	0.14
p* in recoil	Corr	0.11	7	0.77	0.1	4.5	0.45	0.59
M_{ES} statistics	–	0.11	5	0.55	0.1	5	0.5	0.37
Mixing								
Uncertainty in χ_d	–	0.181	2.5	0.45	0	0	0	0.19
Tracking Efficiency	Corr	1.04	0.7	0.73	1.04	0.7	0.73	0.73
Particle Identification								
electron ID	Corr	1.1	1.5	1.65	1.1	1.5	1.65	1.65
hadron misid	Corr	0.009	17	0.16	0.015	13	0.2	0.18
Pair Backgrounds								
conversions	Corr	0.04	15	0.6	0.04	13	0.52	0.55
Dalitz	Corr	0.01	20	0.2	0	19	0.2	0.2
J/ψ	Corr	0.005	10	0.05	0.005	10	0.05	0.05
Physics Corrections								
τ bkg	Corr	0.025	10	0.25	0.032	10	0.32	0.29
$D_s bkg$	Corr	0.027	20	0.54	0.032	20	0.65	0.6
$D^0, D^\pm bkg$	Corr	0.037	25	0.94	0.032	25	0.8	0.86
$\Lambda_c bkg$	Corr	0.001	83	0.08	0	83	0.08	0.08
Acceptance	–	1.16	0.5	0.58	1.16	0.5	0.58	0.41
Bremsstrahlung	Corr	0.009	10	0.09	0.009	10	0.09	0.09
P_{LAB} cut	Corr	1.02	0.2	0.2	1.02	0.2	0.2	0.2
Extrapolation uncertainty	–	0.04	10	0.4	0.04	10	0.4	0.29
Total				2.9			2.7	2.5

187

One of the interesting results of this analysis is the ratio of the branching fractions for B^0 vs. $B^\pm$. Based on the results above, we obtain the following measurement:

$$\frac{BR(B^\pm)}{BR(B^0)} = 0.996 \pm 0.039 \pm 0.015$$

The last term denotes the systematic error which is smaller than in the individual branching fraction measurements due to the fact that many of the systematic errors are correlated for both B^0 and $B^\pm$ and therefore largely cancel out when the ratio is constructed. The procedure used to derive the error on the ratio of branching fractions is described in the previous Section 4.5.4.

Furthermore, we calculate a weighted average of the individual $B(B^\pm \to Xe\bar{\nu})$ and $B(B^0 \to Xe\bar{\nu})$ branching fractions. Statistical errors of these two measurements are used to weight the two results to arrive at

$$BR(B \to Xe\bar{\nu}) = 10.65 \pm 0.19 \pm 0.27\% \qquad (4.22)$$

The last term denotes the systematic error, which is larger than what would be expected from addition of the individual systematic errors in quadratures. This is due to the fact that correlated errors have to be added linearly rather than in quadrature.

4.5.6 $|V_{cb}|$ CKM matrix element

Finally, the value of $|V_{cb}|$ CKM matrix element is obtained from the weighted average of the two branching fractions:

$$|V_{cb}| = (0.0419)\sqrt{\frac{B(B \to X_c e\bar{\nu})}{10.5\%} \times \frac{1.55 ps}{\tau_B}} \qquad (4.23)$$

188

$$\times(1 - 0.012\frac{\mu_\pi^2 - 0.5 GeV/c^2}{0.1 GeV/c^2}) \tag{4.24}$$

$$\times(1 \pm 0.015_{perturb} \pm 0.010_{m_b} \pm 0.012_{1/m_Q^3}) \tag{4.25}$$

where

$\tau_B = (\tau_{B^\pm} + \tau_{B^0})/2 = 1.61 \pm 0.012 ps$, $\tau_{B^\pm} = 1.674 \pm 0.018 ps$, $\tau_{B^0} = 1.546 \pm$ $0.016 ps$ - mean lifetimes of corresponding B-mesons , [46],

$B(B \rightarrow X_c e\bar{\nu})$ is the weighted average branching fraction, obtained from (4.22) by subtracting $b \rightarrow u$ component (2.24% relative),

$\mu_\pi^2 = 0.5\ GeV/c^2$ is related to the average kinetic energy of the b quark moving inside the B-meson .

$$|V_{cb}| = 0.0409 \pm 0.00074 \pm 0.0010 \pm 0.000858 \tag{4.26}$$

The first error is statistical, second - systematic from this measurement and the third - theoretical. The experimental error is taken from the measurement of the weighted average branching fraction (4.22). The theoretical error is composed of three terms:

- 1. Perturbative corrections.

- 2. Correction for imprecise knowledge of the mass of b-quark.

- 3. $O(1/m_Q^3)$ correction in expansion series.

All of these components are thoroughly discussed in [10] and final estimates are given in (4.25).

189

Chapter 5

Conclusions

We have been able to perform an analysis of semileptonic decays of B-mesons using fully reconstructed B-mesons as tags for the first time in *BABAR* . The large amount of statistics, made available by the joint effort of *BABAR* scientists, detector experts and PEP-II engineers, allowed us to reach levels of statistical errors competitive with the world average results. For the first time, the branching fractions of $B^{\pm}$ and B^0 were measured with a precision previously attainable only for a measurement averaged over all B-meson types. As a result, much more stringent limits are placed on the ratio of $B^{\pm}$ and B^0 branching fractions. And most importantly, a new value of the $|V_{cb}|$ CKM matrix element was obtained and can now be used along with a set of similar results from other experiments to overconstrain the Standard Model unitarity triangle - one of the major purposes stated in the beginning of this report. An updated set of world average plots is shown in Figures 5.1 and 5.2.

190

SL Branching Fraction Results, B+-

BABAR, 2001, BRECO tag (prelim)

CLEO, 1997, tag with partial reco

CLEO, 1994

THIS ANALYSIS

Branching Fraction, %

SL Branching Fraction Results, B0

BABAR, 2001, BRECO tag (prelim)

CLEO, 1997, tag with partial reco

CLEO, 1994

THIS ANALYSIS
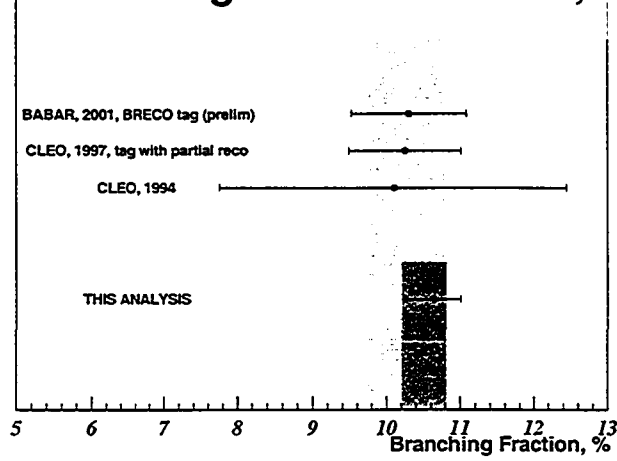
Branching Fraction, %
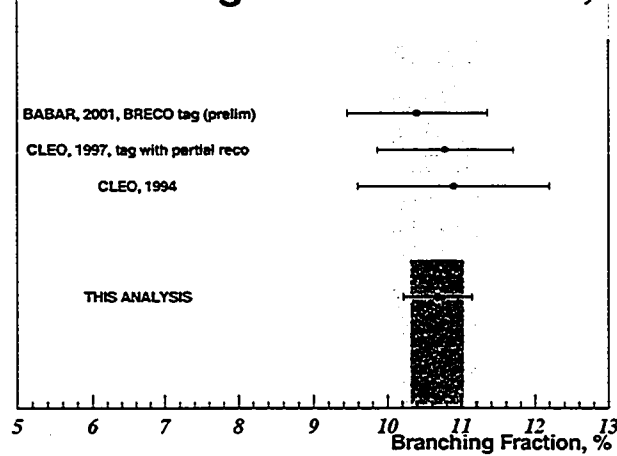
Figure 5.1: World averages for semileptonic B decay branching fractionst. The lighter bands show the prior world averages. The darker bands indicate the world averages recalculated after additional input from this analysis. (top) - BR($B^{\pm} \rightarrow Xe\bar{\nu}$), (bottom) - BR($B^0 \rightarrow Xe\bar{\nu}$). World average values are calculated as an average of the individual measurements weighted with the corresponding errors.

191

SemiLeptonic Branching Fraction Results

BELLE, 2002, lepton tag
BABAR, 2002, lepton tag
ADLO (LEP), 2002
DELPHI, 2001, lifetime & B-tagging
ALEPH, 2001, charge corr
OPAL, 1999, neural net
L3, 1999, double tag
CLEO, 1996, lepton tag

THIS ANALYSIS

8   8.5   9   9.5   10   10.5   11   11.5   12
Branching Fraction, %

SL Branching Fraction Ratio, B+-/B0

BABAR, 2001, BRECO tag (prelim)
CLEO, 1997, tag with partial reco
CLEO, 1994

THIS ANALYSIS

0.4   0.5   0.6   0.7   0.8   0.9   1   1.1   1.2
Branching Fraction Ratio

Figure 5.2: World averages for semileptonic B decay branching fractions. The lighter bands show the prior world averages. The darker bands indicate the world averages recalculated after additional input from this analysis. (top) - BR($B \to Xe\bar{\nu}$), (bottom) - BR($B^{\pm} \to Xe\bar{\nu}$)/BR($B^0 \to Xe\bar{\nu}$). World average values are calculated as an average of the individual measurements weighted with the corresponding errors.

192

5.1 Prospects for studies of B_{reco} -tagged semileptonic decays of B mesons in BABAR

Due to the lack of reliable muon identification, this analysis has been restricted to the electron track sample only. In the near future we expect to get access to a better muon ID system - this will allow us to further increase the statistics and reduce some of the systematic errors (such as particle identification, radiative corrections, hadron misidentification etc.). Since this analysis is likely to be systematically limited once larger data sample becomes available later this year, these reductions in systematic errors will help us make the most precise measurement possible.

Another extension of the current analysis might involve measurement of leptonic moments using detected electron (muon) spectra. The leptonic moments are important input parameters into a series of theoretical models and their precise measurement is one of the priority topics in today's studies of semileptonic B decays.

With further increase in the size of available data sample, it will also become feasible to perform scans across different B_{reco} subsamples in order to extract branching fraction dependencies on the B_{reco} mode compositions. Such studies have a potential to greatly reduce the systematic errors associated with B_{reco} processing (cross-feed, B_{reco} efficiency bias etc.) - the dominant set of systematic errors in this analysis.

5.2 Concluding Summary

As we have seen in the preceding chapters, analysis of the semileptonic B decays with fully reconstructed B decays used as tags, while already giving some very competitive results, has a great potential for further improvement. It is undoubt-

193

edly one of the great tools to probe further into the underlying principles behind B physics phenomena. This thesis is one of the first successful attempts to utilize this novel analysis method to measure fundamental particle physics parameters. I am sure that it will be soon used to run even more sophisticated analyses and I hope that my work will be a good foundation for those future studies.

194

Chapter 6

Appendices

6.1 Systematic Studies

6.1.1 Tag B_{reco} Cross-Feed

In Table 6.1, 6.2 and 6.3 we list the $B^{\pm} \longleftrightarrow B^0$ cross-feed related quantities for three momentum ranges of the primary electron in the recoil: $p_e^* < 1.0$ GeV/c, $1.0 < p_e^* < 2.0$ GeV/c and $p_e^* > 2.0$ GeV/c. These tables confirm that crossfeed coefficients do not have significant dependency on the primary electron momentum and therefore may be applied as momentum-independent normalization corrections.

195

Table 6.1: $B^{\pm} \longleftrightarrow B^0$ cross-feed related quantities, from generic Monte-Carlo, events with primary electron, $p_e^* < 1.0$ GeV/c.

BRECO Mode	Total	Wrong B flavor, M_{ES} fit	cross-feed
$B^{\pm} \to D^0 K\pi, \pi$	1259 ± 45	0 ± 5.3	0 ± 0.0042
$B^{\pm} \to D^0 K\pi\pi^0, \pi$	2214 ± 62	8.4 ± 7.2	0.0038 ± 0.0033
$B^{\pm} \to D^0 K3\pi, \pi$	2006 ± 59	24 ± 10	0.0121 ± 0.0052
$B^0 \to D^- K_s\pi, \pi$	180 ± 14	5.1 ± 4.0	0.028 ± 0.022
$B^0 \to D^- K\pi\pi, \pi$	1438 ± 50	35 ± 12	0.0242 ± 0.0084
$B^0 \to D^{*-} \to D^0\pi \to K\pi, \pi$	317 ± 23	4.3 ± 4.3	0.013 ± 0.014
$B^0 \to D^{*-} \to D^0\pi \to K\pi, \pi\pi^0$	602 ± 34	21.9 ± 7.0	0.036 ± 0.012
$B^0 \to D^{*-} \to D^0\pi \to K\pi, \pi\pi\pi$	308 ± 0	6.26 ± 0	0.0203 ± 0
$B^0 \to D^{*-} \to D^0\pi \to K\pi$	147 ± 17	4.6 ± 4.3	0.031 ± 0.029
$B^0 \to D^{*-} \to D^0\pi \to K\pi\pi^0, \pi$	555 ± 31	0 ± 3.5	0 ± 0.0063
$B^0 \to D^{*-} \to D^0\pi \to K\pi\pi^0, K$	49.0 ± 7.7	1.7 ± 7.7	0.03 ± 0.16
$B^0 \to D^{*-} \to D^0\pi \to K\pi\pi^0, \pi\pi^0$	1009 ± 44	0 ± 6.9	0 ± 0.0068
$B^0 \to D^{*-} \to D^0\pi \to K\pi\pi^0, \pi\pi\pi$	505 ± 30	13.3 ± 4.9	0.0262 ± 0.0097
$B^0 \to D^{*-} \to D^0\pi \to K\pi\pi^0, KK\pi$	50.3 ± 9.3	0 ± 2.1	0 ± 0.042
$B^0 \to D^{*-} \to D^0\pi \to K\pi\pi^0$	76 ± 12	1.9 ± 2.3	0.024 ± 0.030
$B^0 \to D^{*-} \to D^0\pi \to K3\pi, \pi$	484 ± 28	3.3 ± 3.3	0.0069 ± 0.0069
$B^0 \to D^{*-} \to D^0\pi \to K3\pi, \pi\pi^0$	800 ± 39	22.3 ± 8.6	0.028 ± 0.011
$B^0 \to D^{*-} \to D^0\pi \to K3\pi, \pi\pi\pi$	412 ± 28	0 ± 3.1	0 ± 0.0076
$B^0 \to D^{*-} \to D^0\pi \to K_s\pi^+\pi^-, \pi$	122 ± 14	2.0 ± 1.9	0.016 ± 0.015
$B^0 \to D^{*-} \to D^0\pi \to K_s\pi^+\pi^-, \pi\pi^0$	222 ± 21	5.6 ± 4.6	0.025 ± 0.021
$B^0 \to D^{*-} \to D^0\pi \to K_s\pi^+\pi^-, \pi\pi\pi$	72.0 ± 9.5	2.7 ± 2.6	0.038 ± 0.037
$B^{\pm} \to D^{*0} \to D^0\pi^0 \to K\pi, \pi$	332 ± 23	0 ± 5.5	0 ± 0.017
$B^{\pm} \to D^{*0} \to D^0\pi^0 \to K\pi, K$	48.1 ± 8.9	0 ± 0	0 ± 0
$B^{\pm} \to D^{*0} \to D^0\pi^0 \to K\pi, \pi\pi^0$	661 ± 35	8 ± 46	0.013 ± 0.070
$B^{\pm} \to D^{*0} \to D^0\pi^0 \to K\pi, \pi\pi\pi$	252 ± 22	9.6 ± 1.6	0.0379 ± 0.0071
$B^{\pm} \to D^{*0} \to D^0\pi^0 \to K\pi$	120 ± 15	6.5 ± 3.5	0.054 ± 0.030
$B^{\pm} \to D^{*0} \to D^0\pi^0 \to K\pi\pi^0, \pi$	605 ± 32	3.1 ± 3.3	0.0052 ± 0.0055
$B^{\pm} \to D^{*0} \to D^0\pi^0 \to K3\pi, \pi$	503 ± 30	0 ± 2.8	0 ± 0.0055
$B^{\pm} \to D^{*0} \to D^0\gamma \to K\pi, \pi$	266 ± 22	0 ± 22	0 ± 0.083
$B^{\pm} \to D^{*0} \to D^0\gamma \to K\pi, K$	35.4 ± 7.1	0 ± 0	0 ± 0
$B^{\pm} \to D^{*0} \to D^0\gamma \to K\pi, \pi\pi^0$	542 ± 33	25.8 ± 5.7	0.048 ± 0.011
$B^{\pm} \to D^{*0} \to D^0\gamma \to K\pi\pi^0, \pi$	519 ± 32	10.0 ± 6.6	0.019 ± 0.013
all $B^{\pm}$	9465 ± 131	100 ± 19	0.0105 ± 0.0020
all B^0	7390 ± 116	129 ± 20	0.0175 ± 0.0028

196

Table 6.2: Same as Table 6.1, events with primary electron, $1.0 < p_e^* < 2.0$ GeV/c.

BRECO Mode	Total	Wrong B flavor, M_{ES} fit	cross-feed
$B^\pm \to D^0 K\pi, \pi$	2745 ± 66	14.8 ± 3.9	0.0054 ± 0.0014
$B^\pm \to D^0 K\pi\pi^0, \pi$	4864 ± 92	31 ± 12	0.0064 ± 0.0024
$B^\pm \to D^0 K3\pi, \pi$	4252 ± 84	45 ± 15	0.0105 ± 0.0035
$B^0 \to D^- K_s\pi, \pi$	412 ± 22	12.3 ± 6.6	0.030 ± 0.016
$B^0 \to D^- K\pi\pi, \pi$	3133 ± 73	46 ± 15	0.0148 ± 0.0049
$B^0 \to D^{*-} \to D^0\pi \to K\pi, \pi$	757 ± 35	0 ± 2.6	0 ± 0.0034
$B^0 \to D^{*-} \to D^0\pi \to K\pi, \pi\pi^0$	1311 ± 51	26.6 ± 8.8	0.0203 ± 0.0067
$B^0 \to D^{*-} \to D^0\pi \to K\pi, \pi\pi\pi$	620 ± 27	0 ± 2.9	0 ± 0.0047
$B^0 \to D^{*-} \to D^0\pi \to K\pi$	285 ± 24	6.0 ± 5.5	0.021 ± 0.019
$B^0 \to D^{*-} \to D^0\pi \to K\pi\pi^0, \pi$	1139 ± 44	0 ± 5.1	0 ± 0.0045
$B^0 \to D^{*-} \to D^0\pi \to K\pi\pi^0, K$	80.9 ± 9.0	3.36 ± 0.97	0.042 ± 0.013
$B^0 \to D^{*-} \to D^0\pi \to K\pi\pi^0, \pi\pi^0$	2383 ± 68	84 ± 15	0.0351 ± 0.0065
$B^0 \to D^{*-} \to D^0\pi \to K\pi\pi^0, \pi\pi\pi$	1112 ± 47	27 ± 11	0.024 ± 0.010
$B^0 \to D^{*-} \to D^0\pi \to K\pi\pi^0, KK\pi$	88 ± 13	4.7 ± 6.9	0.053 ± 0.079
$B^0 \to D^{*-} \to D^0\pi \to K\pi\pi^0$	167 ± 17	4.3 ± 3.3	0.026 ± 0.020
$B^0 \to D^{*-} \to D^0\pi \to K3\pi, \pi$	968 ± 39	4.5 ± 5.1	0.0047 ± 0.0052
$B^0 \to D^{*-} \to D^0\pi \to K3\pi, \pi\pi^0$	1688 ± 58	24 ± 10	0.0145 ± 0.0062
$B^0 \to D^{*-} \to D^0\pi \to K3\pi, \pi\pi\pi$	914 ± 42	10.5 ± 7.6	0.0114 ± 0.0083
$B^0 \to D^{*-} \to D^0\pi \to K_s\pi^+\pi^-, \pi$	245 ± 16	153.4 ± 6.1	0.626 ± 0.048
$B^0 \to D^{*-} \to D^0\pi \to K_s\pi^+\pi^-, \pi\pi^0$	494 ± 31	12.5 ± 6.4	0.025 ± 0.013
$B^0 \to D^{*-} \to D^0\pi \to K_s\pi^+\pi^-, \pi\pi\pi$	259.1 ± 5.2	4 ± 21	0.016 ± 0.081
$B^\pm \to D^{*0} \to D^0\pi^0 \to K\pi, \pi$	748 ± 35	2.0 ± 1.9	0.0027 ± 0.0025
$B^\pm \to D^{*0} \to D^0\pi^0 \to K\pi, K$	94 ± 13	2.0 ± 2.8	0.021 ± 0.030
$B^\pm \to D^{*0} \to D^0\pi^0 \to K\pi, \pi\pi^0$	1596 ± 55	25 ± 10	0.0154 ± 0.0065
$B^\pm \to D^{*0} \to D^0\pi^0 \to K\pi, \pi\pi\pi$	601 ± 34	3 ± 12	0.004 ± 0.020
$B^\pm \to D^{*0} \to D^0\pi^0 \to K\pi$	246 ± 18	0 ± 18	0 ± 0.073
$B^\pm \to D^{*0} \to D^0\pi^0 \to K\pi\pi^0, \pi$	1293 ± 47	17.2 ± 6.0	0.0133 ± 0.0047
$B^\pm \to D^{*0} \to D^0\pi^0 \to K3\pi, \pi$	1085 ± 43	21.5 ± 6.7	0.0198 ± 0.0062
$B^\pm \to D^{*0} \to D^0\gamma \to K\pi, \pi$	682 ± 35	24.6 ± 6.2	0.0361 ± 0.0093
$B^\pm \to D^{*0} \to D^0\gamma \to K\pi, K$	85 ± 12	0 ± 0.99	0 ± 0.012
$B^\pm \to D^{*0} \to D^0\gamma \to K\pi, \pi\pi^0$	1259 ± 51	53 ± 11	0.0417 ± 0.0087
$B^\pm \to D^{*0} \to D^0\gamma \to K\pi\pi^0, \pi$	1232 ± 49	16.0 ± 7.2	0.0130 ± 0.0059
all $B^\pm$	20786 ± 192	210 ± 29	0.0101 ± 0.0014
all B^0	16186 ± 174	265 ± 31	0.0164 ± 0.0019

197

Table 6.3: Same as Table 6.1, events with primary electron, $p_e^* > 2.0$ GeV/c.

BRECO Mode	Total	Wrong B flavor, M_{ES} fit	cross-feed
$B^\pm \to D^0 K\pi, \pi$	1383 ± 49	3 ± 16	0.002 ± 0.012
$B^\pm \to D^0 K\pi\pi^0, \pi$	2462 ± 66	3.0 ± 7.7	0.0012 ± 0.0031
$B^\pm \to D^0 K3\pi, \pi$	2110 ± 60	0 ± 8.9	0 ± 0.0042
$B^0 \to D^- K_s\pi, \pi$	213 ± 19	2.4 ± 2.4	0.011 ± 0.011
$B^0 \to D^- K\pi\pi, \pi$	1524 ± 50	47 ± 12	0.0307 ± 0.0077
$B^0 \to D^{*-} \to D^0\pi \to K\pi, \pi$	372 ± 24	2.4 ± 2.6	0.0065 ± 0.0069
$B^0 \to D^{*-} \to D^0\pi \to K\pi, \pi\pi^0$	651 ± 38	21 ± 11	0.032 ± 0.017
$B^0 \to D^{*-} \to D^0\pi \to K\pi, \pi\pi\pi$	282 ± 19	2.5 ± 2.8	0.0090 ± 0.0099
$B^0 \to D^{*-} \to D^0\pi \to K\pi$	137 ± 13	4.1 ± 3.0	0.030 ± 0.022
$B^0 \to D^{*-} \to D^0\pi \to K\pi\pi^0, \pi$	586 ± 31	2.2 ± 1.9	0.0038 ± 0.0032
$B^0 \to D^{*-} \to D^0\pi \to K\pi\pi^0, K$	43.4 ± 8.3	0 ± 0	0 ± 0
$B^0 \to D^{*-} \to D^0\pi \to K\pi\pi^0, \pi\pi^0$	1244 ± 52	72 ± 11	0.0579 ± 0.0095
$B^0 \to D^{*-} \to D^0\pi \to K\pi\pi^0, \pi\pi\pi$	576 ± 34	8.7 ± 6.0	0.015 ± 0.010
$B^0 \to D^{*-} \to D^0\pi \to K\pi\pi^0, KK\pi$	64.6 ± 1.3	1.3 ± 8.6	0.02 ± 0.13
$B^0 \to D^{*-} \to D^0\pi \to K\pi\pi^0$	73 ± 12	1.7 ± 2.4	0.023 ± 0.033
$B^0 \to D^{*-} \to D^0\pi \to K3\pi, \pi$	431 ± 27	0 ± 2.2	0 ± 0.0050
$B^0 \to D^{*-} \to D^0\pi \to K3\pi, \pi\pi^0$	974 ± 46	34 ± 10	0.035 ± 0.011
$B^0 \to D^{*-} \to D^0\pi \to K3\pi, \pi\pi\pi$	403 ± 28	0 ± 2.1	0 ± 0.0051
$B^0 \to D^{*-} \to D^0\pi \to K_s\pi^+\pi^-, \pi$	134 ± 12	2.0 ± 1.6	0.015 ± 0.012
$B^0 \to D^{*-} \to D^0\pi \to K_s\pi^+\pi^-, \pi\pi^0$	243 ± 25	22 ± 17	0.091 ± 0.069
$B^0 \to D^{*-} \to D^0\pi \to K_s\pi^+\pi^-, \pi\pi\pi$	126 ± 15	3.4 ± 2.5	0.027 ± 0.020
$B^\pm \to D^{*0} \to D^0\pi^0 \to K\pi, \pi$	388 ± 25	0.0000 ± 0.0013	0.0000000 ± 0.0000033
$B^\pm \to D^{*0} \to D^0\pi^0 \to K\pi, K$	53.7 ± 9.2	0 ± 0	0 ± 0
$B^\pm \to D^{*0} \to D^0\pi^0 \to K\pi, \pi\pi^0$	763 ± 40	6.3 ± 5.7	0.0083 ± 0.0075
$B^\pm \to D^{*0} \to D^0\pi^0 \to K\pi, \pi\pi\pi$	318 ± 19	0.0 ± 2.5	0.0001 ± 0.0079
$B^\pm \to D^{*0} \to D^0\pi^0 \to K\pi$	127 ± 0	0 ± 16	0 ± 0.13
$B^\pm \to D^{*0} \to D^0\pi^0 \to K\pi\pi^0, \pi$	655 ± 35	9.0 ± 4.5	0.0137 ± 0.0069
$B^\pm \to D^{*0} \to D^0\pi^0 \to K3\pi, \pi$	556 ± 0	7 ± 31	0.013 ± 0.056
$B^\pm \to D^{*0} \to D^0\gamma \to K\pi, \pi$	333 ± 25	9.0 ± 3.9	0.027 ± 0.012
$B^\pm \to D^{*0} \to D^0\gamma \to K\pi, K$	42.0 ± 8.2	0 ± 0.085	0 ± 0.0020
$B^\pm \to D^{*0} \to D^0\gamma \to K\pi, \pi\pi^0$	656 ± 39	19.1 ± 8.6	0.029 ± 0.013
$B^\pm \to D^{*0} \to D^0\gamma \to K\pi\pi^0, \pi$	633 ± 36	19.1 ± 8.7	0.030 ± 0.014
all $B^\pm$	10486 ± 141	55 ± 35	0.0052 ± 0.0033
all B^0	8170 ± 126	209 ± 21	0.0255 ± 0.0026

198

6.1.2 Additional DOCA cuts to reduce conversion background

Studies [37] have shown that electrons from photon conversions can be efficiently reduced with a stringent cut on the distance of closest approach to the beam spot in the $x - y$ plane ($|d_{xy}|$) and along the z axis ($|d_z|$). These two variables are referred to as the "doca" variables. The distribution of $|d_{xy}|$ and $|d_z|$ are shown in Figure 6.1.2.

MC docaXY comparisons, all   **MC docaXY comparisons, electrons**

(a)   (b)

MC docaZ comparisons, all   **MC docaZ comparisons, electrons**

(c)   (d)
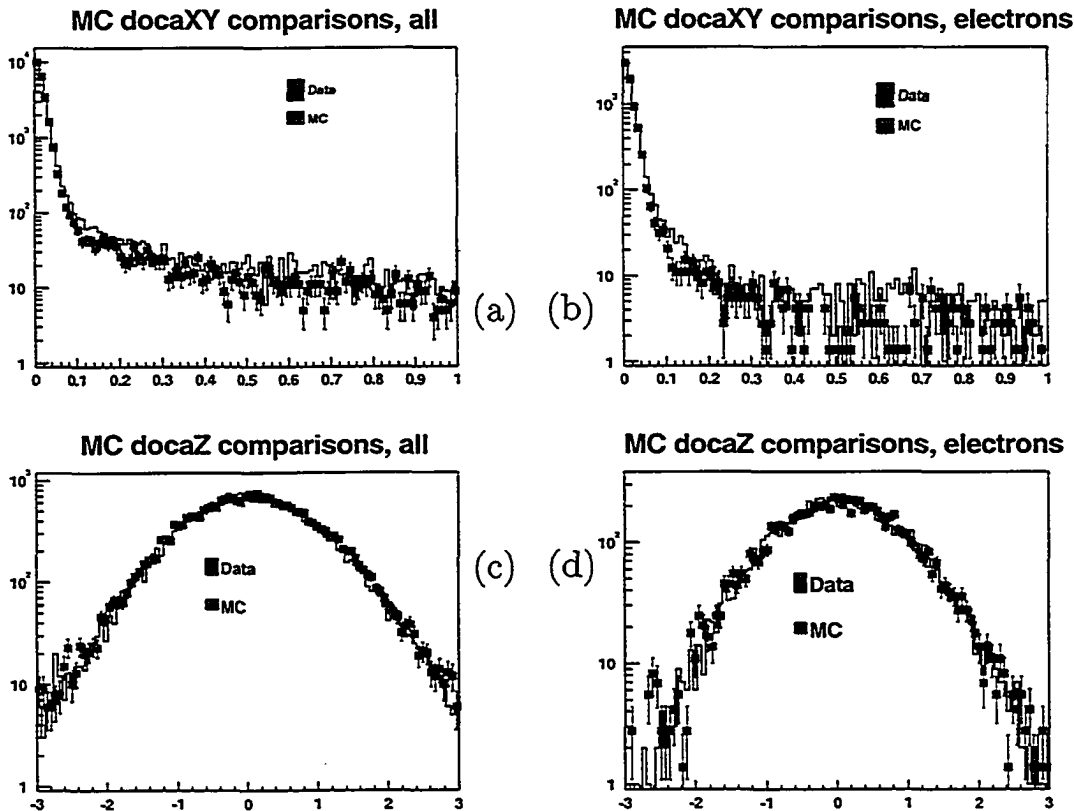
Figure 6.1: Distribution of the distance of closest approach (doca), X axis is in cm. (a) all tracks, in the transverse plane; (b) same for electron tracks; (c) all tracks, direction along the beam line; (d) same for electron tracks.

However, applying additional doca cuts increases the systematic error in the

tracking efficiency - this is a non-standard cut for which no efficiency studies have been done. A separate study has been performed in order to make an informed decision whether to apply additional doca cuts. From the distributions of the doca parameters ($|d_{xy}|$, $|d_z|$), one can derive the following set of efficient doca cuts on the electron tracks:

- $|d_{xy}| < 0.25$ cm, and

- $|d_z| < 3$ cm,

A conservative estimate of the tracking efficiency systematics when above cuts are used is $\sim 1.5\%$, to be compared with the standard tracking efficiency systematic error of $\sim 0.7\%$. To determine whether the overall error suffers from the introduction of the additional doca cuts, the analysis has been performed 8 times: 4 times with the above additional doca cuts and 4 times without them as given in Table 6.4. In each set, a scan on a p^* cut was performed ranging the minimum momentum of the signal electron from 0.5 GeV/c to 0.8 GeV/c with 100 Mev/c intervals. Systematic error on the tracking efficiency of 1.5% was assumed for the first set of 4 runs and 0.7% for the second set. This error was then combined in quadrature with the part of the statistical error on the final result obtained from conversion background subtraction. The resulting value was compared for all runs and the decision was made to NOT apply additional doca cuts. More details on this study are available in the Table 6.4.

6.1.3 Study of M_{ES} fit algorithm performance

Fits to the M_{ES} distributions play significant role in our analysis. They are used in sideband subtraction, tag normalization, cross-feed corrections, B_{reco} efficiency bias determination etc. This short study was designed to achieve better understanding of the M_{ES} fits. It also provides another estimate of the systematic

200

Table 6.4: Effect of the DOCA cuts on the error for the final electron count after all corrections. The error quoted for conversion background includes a systematic error on the corresponding correction.

P^* Cut	Doca Cuts	Total Spectrum	Conv (X)	Final Spectrum (Y)	Relative Correction (X/Y)	Combined Error, %
0.5	yes	4081±70	101±33	4038±91	0.025±0.0080	1.7
0.6	yes	3704±65	74±25	3764±81	0.0197±0.0065	1.6
0.7	yes	3415±62	54±20	3546±76	0.0152±0.0056	1.6
0.8	yes	3178±59	35±15	3380±71	0.0104±0.0045	1.6
0.5	no	4244±72	175±48	4133±98	0.042±0.012	1.5
0.6	no	3803±67	98±34	3843±86	0.026±0.009	1.14
0.7	no	3476±63	70±26	3598±79	0.0195±0.007	1.0
0.8	no	3216±60	38±20	3418±72	0.0111±0.0058	0.9

errors associated with sideband subtraction. Monte-Carlo sample has been used in this study.

The study resulted in the change of the M_{ES} fit procedure. Previously, M_{ES} histogram was fitted to the sum of Crystal Ball and ARGUS functions without fixing any of the significant parameters. The new implementation first performs fit of the M_{ES} region from 5.21 to 5.26 to the pure ARGUS function. The ARGUS function parameters obtained through such procedure are then used to fix the ARGUS function parameters in the fit of the complete M_{ES} distribution to the sum of Crystal Ball and ARGUS.

Details of this study are given in Figures 6.2 - 6.4. Plots corresponding to the old fitting procedure are shown on the right, while those from the new procedure - on the left.

Firstly, we study the dependency of the fit results on addition of the continuum MC mix. From the figure 6.2, one can see that the both fitting procedures result in overestimation of the signal count when continuum background is added

201

to the event sample. A part of such excess results from the peaking background in continuum sample, part - from imperfection in the fitting procedures. By utilizing the new fitting method, we are able to decrease overestimation of the signal count from 4% to 2%. In the analysis, the remaining overestimation is corrected for through the application of the 'cross-feed' corrections to the tag counts and signal spectra.

Furthermore, sideband subtraction scaling factor changes from 30.8% to 31.6% (2.7% relative change) when the fitting method is changed. This is the largest deviation we have observed during this study. We take half of this difference, 1.4%, as one of the estimates of a systematic error of sideband subtraction.

Figure 6.2: Peaking Background estimate. Top M_{ES} distribution is derived from $B\overline{B}$ events, bottom - from the correctly mixed MC sample (appropriate amounts of uds and $c\overline{c}$ events were added to $B\overline{B}$ sample). The difference indicates the amount of peaking background corresponding to the addition of the continuum M_{ES} distribution. Plots corresponding to the old fitting procedure are shown on the right, while those from the new procedure - on the left.

202

Secondly, we determine the fit bias due to the addition of the pure ARGUS background. If the fit procedure is ideal, there should not be any change in the signal count in this case. From Figure 6.3, we conclude that there is no significant dependency.
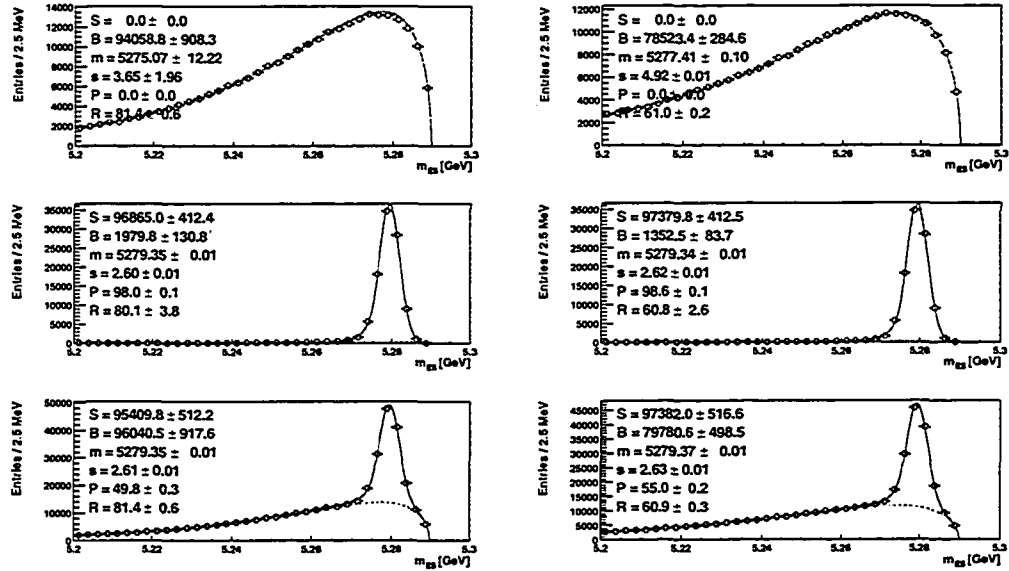
Figure 6.3: Fit bias due to addition of the pure ARGUS background. ARGUS function was used to generate background M_{ES} distribution shown in the top row plots. M_{ES} fit to that distrubution is shown. Then, purely $B\overline{B}$ M_{ES} distribution from the central row is added to this purely ARGUS M_{ES} distribution and the fit is repeated (bottom row plots). Plots corresponding to the old fitting procedure are shown on the right, while those from the new procedure - on the left.

Finally, we compare the fits to the data and MC samples consisting entirely of continuum events. We observe a very good agreement between data and Monte-Carlo fit parameters and conclude that M_{ES} -fit-based continuum background estimation in data is adequate.

203
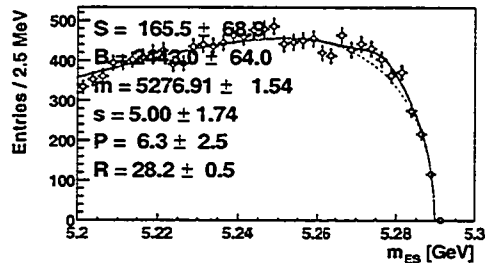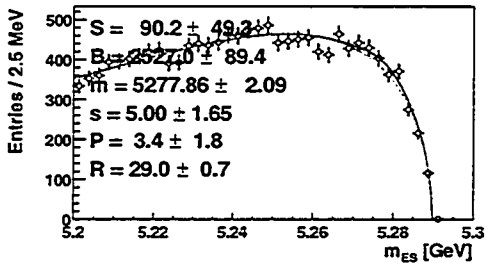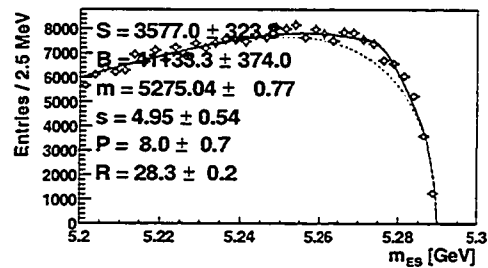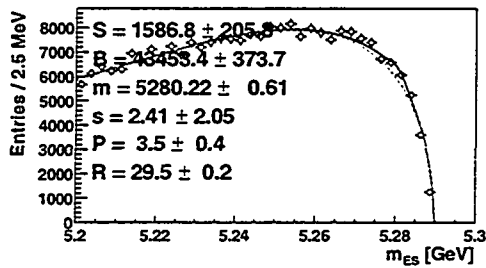
Figure 6.4: Continuum study. The fit of the continuum MC sample (top) is compared to the fit of the continuum DATA sample (bottom). The ARGUS shape parameters for the 2 fits are consistent within [small] errors. The difference in the detected peaking background levels is 3.5% vs. 3.4% (8% vs. 7% for the old procedure). Plots corresponding to the old fitting procedure are shown on the right, while those from the new procedure - on the left.

204

6.1.4 Study of M_{ES} fit algorithm performance - no crystal ball fit

Details of this study are given in Figures 6.5 - 6.7. Plots corresponding to the old fitting procedure are shown on the right, while those from the new procedure - on the left.
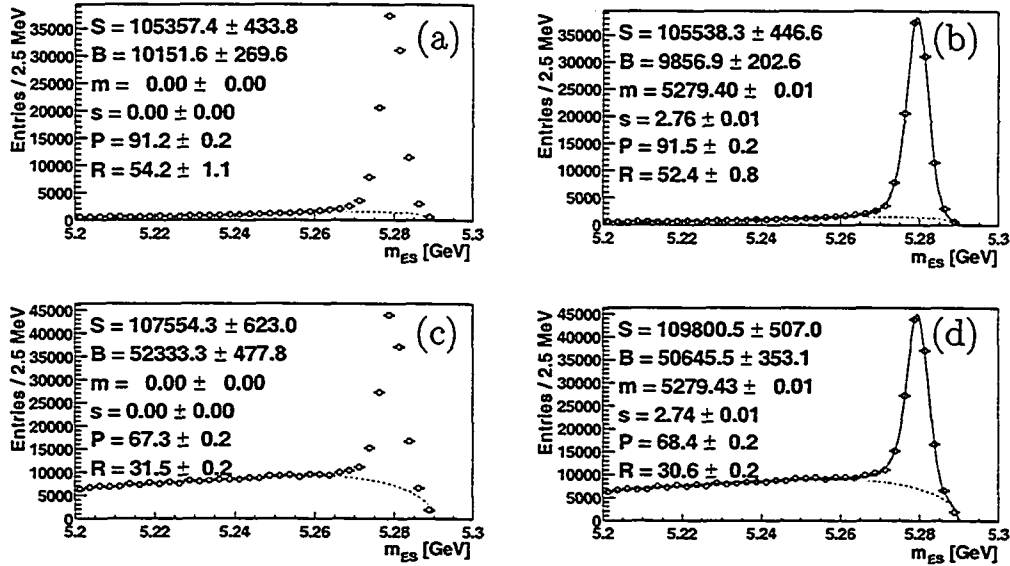
Figure 6.5: Peaking Background estimate. Top M_{ES} distribution is derived from $B\overline{B}$ events, bottom - from the correctly mixed MC sample (appropriate amounts of uds and $c\bar{c}$ events were added to $B\overline{B}$ sample). The difference indicates the amount of peaking background corresponding to the addition of the continuum M_{ES} distribution. Plots corresponding to the old fitting procedure are shown on the right, while those from the new procedure - on the left.

Secondly, we determine the fit bias due to the addition of the pure ARGUS background. If the fit procedure is ideal, there should not be any change in the signal count in this case. From Figure 6.6, we conclude that there is no significant dependency.

205

Figure 6.6: Fit bias due to addition of the pure ARGUS background. ARGUS function was used to generate background M_{ES} distribution shown in the top row plots. M_{ES} fit to that distrubution is shown. Then, purely $B\overline{B}$ M_{ES} distribution from the central row is added to this purely ARGUS M_{ES} distribution and the fit is repeated (bottom row plots). Plots corresponding to the old fitting procedure are shown on the right, while those from the new procedure - on the left.

206

Finally, we compare the fits to the data and MC samples consisting entirely of continuum events. We observe a very good agreement between data and Monte-Carlo fit parameters and conclude that M_{ES} -fit-based continuum background estimation in data is adequate.

Figure 6.7: Continuum study. The fit of the continuum MC sample (top) is compared to the fit of the continuum DATA sample (bottom). The ARGUS shape parameters for the 2 fits are consistent within [small] errors. The difference in the detected peaking background levels is 3.5% vs. 3.4% (8% vs. 7% for the old procedure). Plots corresponding to the old fitting procedure are shown on the right, while those from the new procedure - on the left.

6.1.5 Study of M_{ES} fit dependency on recoil quantities

In this analysis, a number of correction factors is applied in a momentum-independent way. To make sure that we do not distort the detected spectrum by doing so, a set of studies has been performed to justify the current methodics.

Momentum of the electron in the recoil

One of the important parameters in this analysis is the B_{reco} efficiency bias calculated using MC and showing how B_{reco} efficiency differs for events with and without an electron in the recoil. This parameter is then used to rescale the resulting electron spectrum before branching fraction extraction. The bias value is obviously dependent on the momentum of the electron in the recoil. Therefore, correct application of this correction is heavily dependant on the correct description of recoil electrons by MC. In the Figure 6.8, we compare the M_{ES} distributions for different bins in momentum of the recoil electron in Data and MC. The relative fraction of events is extracted for each bin - the summary is given in the Table 6.5 .

Table 6.5: Relative fraction of events in each bin of electron momentum in recoil.

Momentum bin	Events (relative fraction)		
	MC (selector-based PID)	Data Data	MC (truth-based PID)
all	100.0%	100.0%	100.0%
0.5-1.0 GeV/c	43±0.8%	41.4±1.3%	42.2±0.8%
1.0-1.5 GeV/c	31.2±0.7%	30.7±1%	32.2±0.7%
1.5-2.0 GeV/c	22.3±0.5%	24.7±0.9%	22.4±0.5%
2.0+ GeV/c	2.8±0.2%	3.1±0.3%	2.7±0.2%
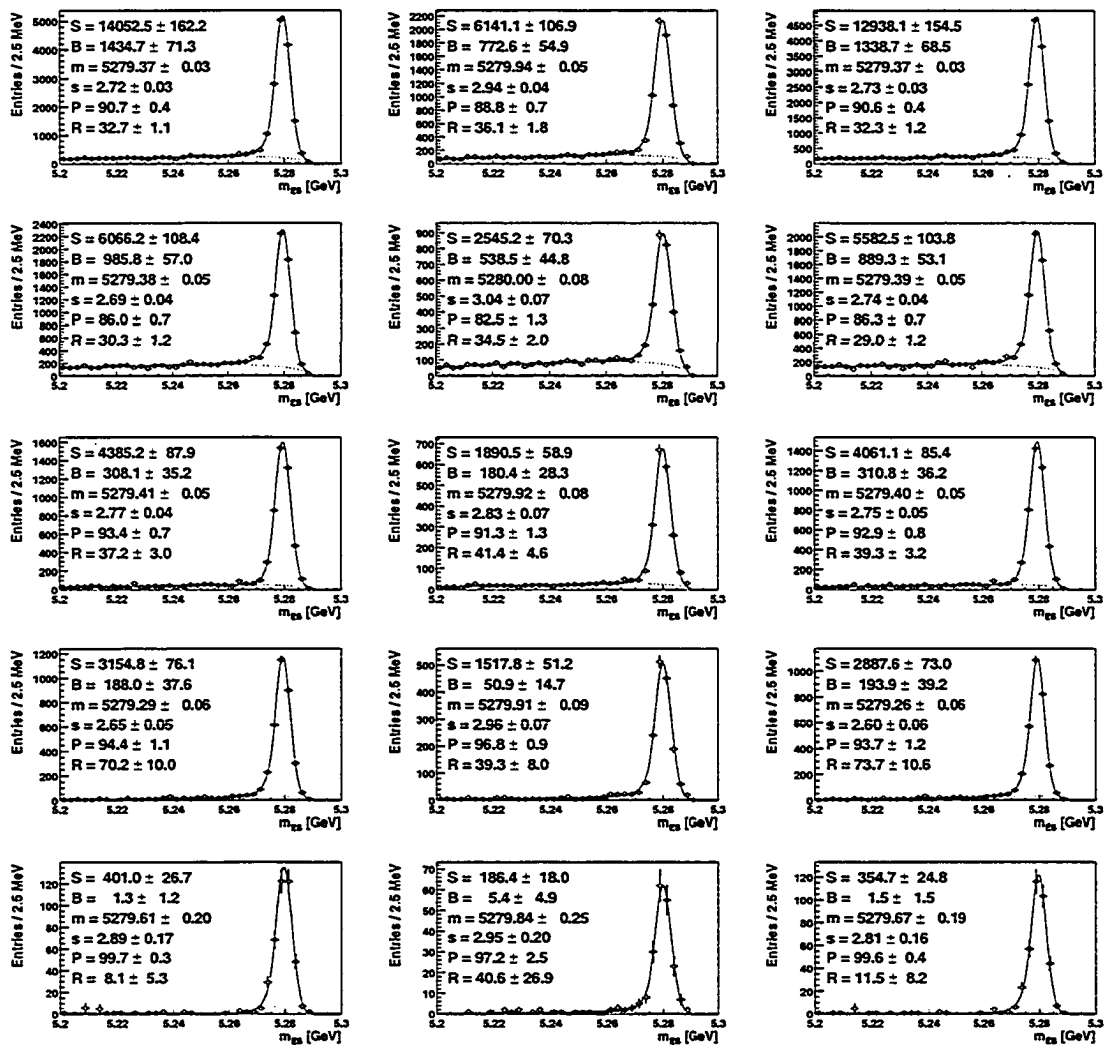
Figure 6.8: M_{ES} histograms used for extraction of the relative fraction of events in each bin of recoil electron momentum. From left to right in each plot set: MC (selector-based PID) distributions are show; Data; MC (truth-based PID). Top to bottom - bins in momentum: 0-3.0, 0.5-1.0, 1.0-1.5, 1.5-2.0, 2.0+ GeV/c.

209

No significant difference between Data and Monte-Carlo has been observed. Therefore, corrections dependent on the electron momentum in the recoil can be determined from Monte-Carlo and then safely applied to Data sample.

210

6.1.6 Dependency of the Sideband Subtraction coefficients on the electron momentum in the recoil

M_{ES} sideband subtraction techniques are used extensively throughout the analysis to correct for continuum and background caused by combinatorics of the B_{reco} process. It is a sizeable correction ($\sim 10\%$ of the prompt spectrum) and any related systematic effects must be well understood. In one of the preceding sections, an estimate has been made on the systematic error of sideband subtraction by varying fit methodology. This section attempts to derive a systematic error from studying dependency of the sideband subtraction parameters on the electron momentum in the recoil system. Monte-Carlo sample has been used in this study.

Separate M_{ES} distributions have been used in this study:

- 1. All events with an electron in the recoil.

- 2. Same as (1) except only events with an electron of $p^* < 1.0$ GeV have been used.

- 3. Same as (1) except only events with an electron of $1.0 < p^* < 2.0$ GeV have been used.

- 4. Same as (1) except only events with an electron of $p^* > 2.0$ GeV have been used.

For each M_{ES} histogram, sideband scaling factor has been determined. All M_{ES} distributions are shown in Figure 6.9 and corresponding numbers are given in Table 6.6.

The observed absolute variation in sideband scaling factors is $\sim 9.9\%$ for B^0 and $\sim 5.8\%$ for $B^\pm$, corresponding to relative variations of $\sim 24\%$ for B^0 and $\sim 14\%$ for $B^\pm$. The scaling factors are systematically lower than average
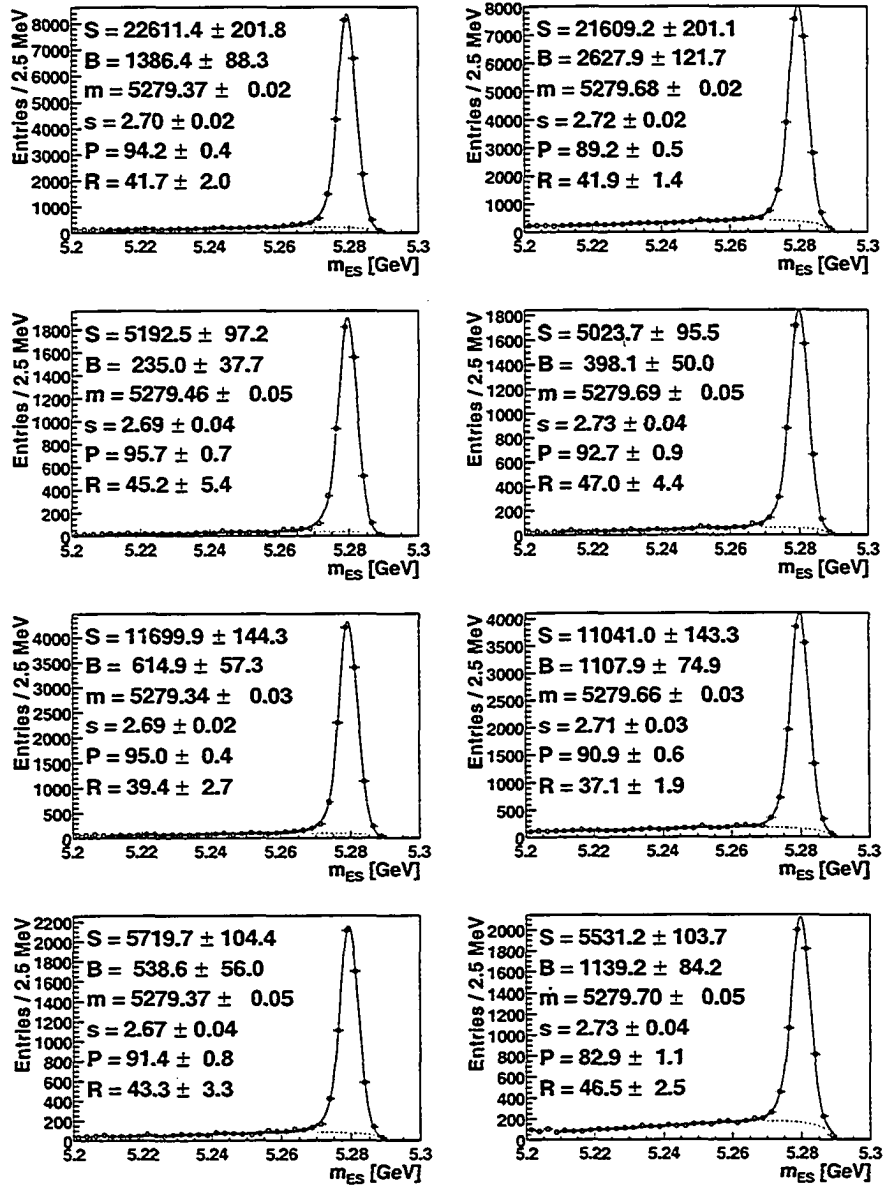
Figure 6.9: M_{ES} histograms for different bins in the recoil electron momentum. From top to bottom: All events with an electron in recoil, events with an electron of $p^* < 1.0$ GeV, events with an electron of $1.0 < p^* < 2.0$ GeV, events with an electron of $p^* > 2.0$ GeV. Left column - $B^{\pm}$, right column - B^0 .

212

Table 6.6: Sideband scaling factors for different bins in the recoil electron momentum..

Momentum bin	Scaling Factor	
	$B^{\pm}$	B^0
All	0.417 ± 0.020	0.419 ± 0.014
$p^* < 1.0$ GeV	0.452 ± 0.054	0.470 ± 0.044
$1.0 < p^* < 2.0$ GeV	0.394 ± 0.027	0.371 ± 0.019
$p^* > 2.0$ GeV	0.433 ± 0.033	0.465 ± 0.025

for the central momentum bin and higher for the lower and highest momentum bins. This means that by applying an average scaling factor as a momentum-independent quantity, we undersubtract sideband background in the lowest and highest momentum bins while oversubtracting in the central bin. The typical case of the sideband subtraction for event class A is shown in Figure 6.10. If we apply the correction for over-(under-)subtraction per above estimates, the sideband subtraction changes by -0.79% for B^0 and by -0.46% for $B^{\pm}$ relative to the sideband-subtracted yield. Therefore, we estimate the contribution to the total systematic error from sideband subtraction to be $\sim 0.8\%$ for B^0 and $\sim 0.5\%$ for $B^{\pm}$ using this method. From Figure 6.10, the sideband subtraction amounts to $\sim 11.3\%$ of the sideband-subtracted electron yield. Hence, our calculation results in 7% error relative to the magnitude of the sideband subtraction in class A and 4.5% - in class C. This is the largest error we observe in all studies of sideband subtraction systematics and therefore we use it as a main estimate for that error.

In the future, the analysis might benefit from migration to the binned sideband subtraction method. This will be especially beneficial for measurements of

213
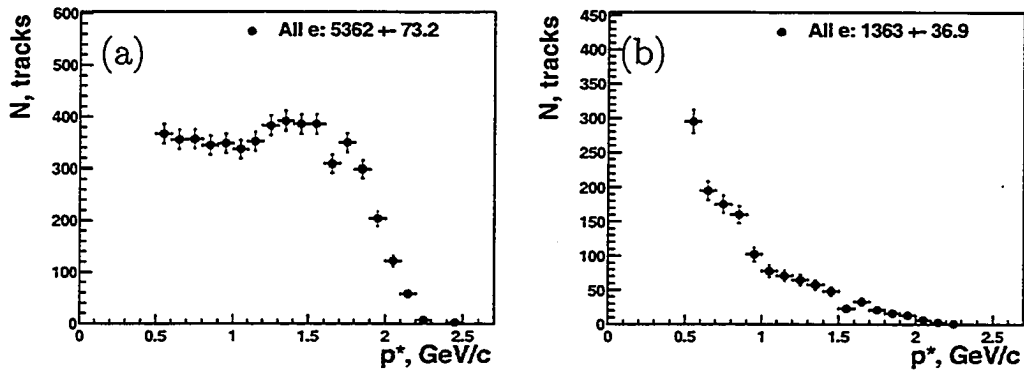
Figure 6.10: Raw electron spectra before any background corrections, as detected, event class A. (a) - signal box, (b) - unscaled contribution from M_{ES} sideband region. Sideband scaling factor for this sample is ~ 0.4.
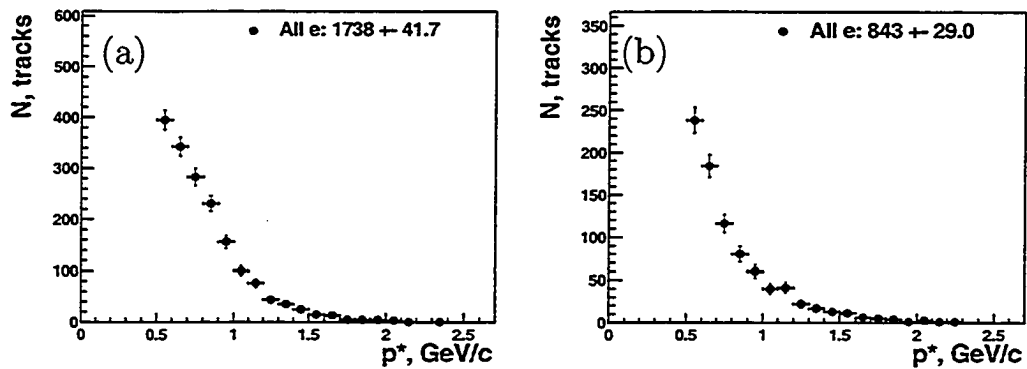
Figure 6.11: Raw electron spectra before any background corrections, as detected, event class B. (a) - signal box, (b) - unscaled contribution from M_{ES} sideband region. Sideband scaling factor for this sample is ~ 0.4.

214

the secondary ($b \rightarrow c \rightarrow e$) electron spectrum since the sideband subtraction is much more significant in that sample as evident from Figure 6.11

215

6.1.7 B_{reco} mode rescaling in Monte-Carlo sample

As evident from the Figure 6.12, even after the careful selection of B_{reco} modes used in the analysis, the relative contributions of the individual modes to the total number of tagged events do not quite agree between data and Monte-Carlo. This can potentially affect any correction that is dependant on the B_{reco} mode. Such corrections include cross-feed, B_{reco} efficiency bias and sideband subtraction. Also, variation of the final result, semileptonic branching fraction, can be expected. To assess the significance of the concerns listed above, a special study has been performed.
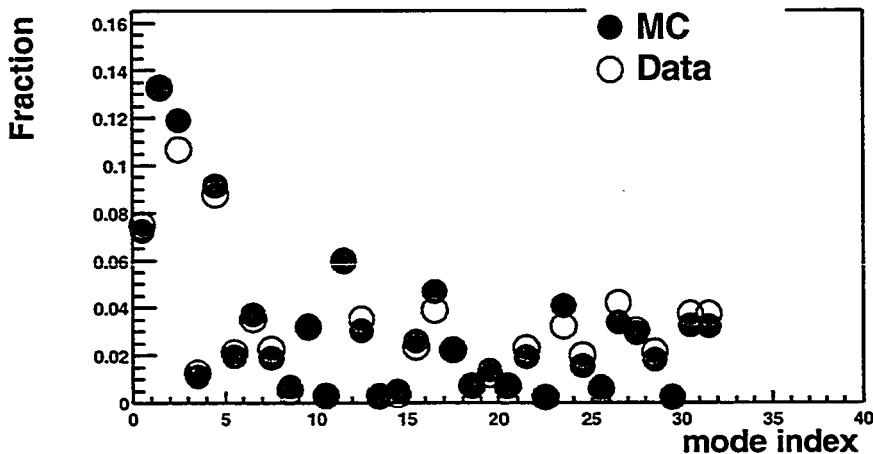
Figure 6.12: MC comparison for B_{reco} quantities. Mode index corresponds to the row number in Table 4.6. Relative mode contribution to total event counts is shown.

The analysis has been rerun with reweighting of all Monte-Carlo events with the factors determined from the Figure 6.12 such that the relative contributions of the individual modes agree perfectly between reweighted Monte-Carlo and Data samples. The variations in cross-feed and efficiency bias coefficients, as well as final branching fraction, have been examined.

216

Table 6.7: $B^{\pm} \longleftrightarrow B^0$ cross-feed related quantities, from generic Monte-Carlo. Comparison of the coefficients for analysis with rescaled B_{reco} modes with the default analysis routine.

All events - B_{reco} modes ARE rescaled

BRECO Mode	Total	Wrong B flavor, M_{ES} fit	cross-feed
all $B^{\pm}$	198148 ± 663	7460 ± 290	0.0377 ± 0.0015
all B^0	143033 ± 551	6265 ± 220	0.0438 ± 0.0015

All events - B_{reco} modes ARE NOT rescaled

BRECO Mode	Total	Wrong B flavor, M_{ES} fit	cross-feed
all $B^{\pm}$	194405 ± 656	7640 ± 288	0.0393 ± 0.0015
all B^0	146616 ± 558	6376 ± 222	0.0435 ± 0.0015

Cross-feed coefficients

The new set of tag-level cross-feed coefficients along with the default set is shown in Table 6.7. The observed variation is under 5%, which is negligible compared to the corresponding systematic error.

The new set of signal-level cross-feed coefficients along with the default set is shown in Tables 6.8 and 6.9. The observed variation is under 5%, which is negligible compared to the corresponding systematic error.

B_{reco} efficiency bias

The new set of B_{reco} efficiency bias coefficients along with the default set is shown in Table 6.10. The observed variation is under 0.2%, which is negligible compared to the corresponding systematic error.

217

Table 6.8: Cross-feed coefficients from generic Monte-Carlo, for all $B^\pm$ and B^0 B_{reco} modes, from studying B_{reco} side in Semileptonic decays of the recoil B. Comparison of the coefficients for analysis with rescaled B_{reco} modes with the default analysis routine.

Semileptonic events - B_{reco} modes ARE rescaled

BRECO mode: all $B^\pm$			
True	N_{gen}	Reconstructed as	
		B^-	B^+
		7898 ± 119.9	8061 ± 119.2
B^-	7879 ± 119.3	$0.997^{+0.0035}_{-0.021}$	0 ± 0.0018
B^+	7934 ± 119.1	0 ± 0.00018	$0.986^{+0.014}_{-0.021}$
B^0	111 ± 17.2	0.00064 ± 0.00040	0.01389 ± 0.00100
$\overline{B^0}$	39 ± 14.7	0.0048 ± 0.0018	0.00057 ± 0.00055

BRECO mode: all B^0			
True	N_{gen}	Reconstructed as	
		B^0	$\overline{B^0}$
		5957 ± 103.9	5957 ± 103.0
B^-	112 ± 18.9	0.00140 ± 0.00057	0.0181 ± 0.0022
B^+	82 ± 17.4	0.0142 ± 0.0028	0.0008 ± 0.0021
B^0	5852 ± 103.4	$0.982^{+0.018}_{-0.024}$	0.00149 ± 0.00043
$\overline{B^0}$	5853 ± 102.6	0.00252 ± 0.00087	$0.979^{+0.021}_{-0.048}$

Table 6.9: Cross-feed coefficients from generic Monte-Carlo, for all $B^{\pm}$ and B^0 B_{reco} modes, from studying B_{reco} side in Semileptonic decays of the recoil B. Comparison of the coefficients for analysis with rescaled B_{reco} modes with the default analysis routine.

Semileptonic events - B_{reco} modes ARE NOT rescaled

BRECO mode: all $B^{\pm}$			
True	N_{gen}	Reconstructed as	
		B^-	B^+
		7765 ± 118.7	7907 ± 118.0
B^-	7741 ± 118.0	$0.997^{+0.0033}_{-0.022}$	0 ± 0.0021
B^+	7788 ± 117.9	0 ± 0.00016	$0.987^{+0.013}_{-0.021}$
B^0	106 ± 16.7	0.00060 ± 0.00039	0.01302 ± 0.00073
$\overline{B^0}$	34 ± 14.2	0.0044 ± 0.0018	0.00002 ± 0.00024

BRECO mode: all B^0			
True	N_{gen}	Reconstructed as	
		B^0	$\overline{B^0}$
		6117 ± 105.3	6109 ± 105.1
B^-	122 ± 19.0	0.00205 ± 0.00065	0.0180 ± 0.0026
B^+	92 ± 17.8	0.0150 ± 0.0029	0.00043 ± 0.00018
B^0	6005 ± 104.7	$0.981^{+0.019}_{-0.024}$	0.00143 ± 0.00047
$\overline{B^0}$	6003 ± 103.9	0.00197 ± 0.00079	$0.980^{+0.020}_{-0.024}$

Table 6.10: B_{reco} efficiency bias coefficients calculated for individual B_{reco} modes. Comparison of the coefficients for analysis with rescaled B_{reco} modes with the default analysis routine.

Semileptonic events - B_{reco} modes ARE rescaled

BRECO Mode	Tag^h	Tag^e	$\frac{\epsilon^e_{tag}}{\epsilon^h_{tag}}$
all $B^\pm$	149705 ± 531.8	20310 ± 190.4	1.016 ± 0.010
all B^0	106713 ± 448.7	15002 ± 163.1	1.053 ± 0.012

Semileptonic events - B_{reco} modes ARE NOT rescaled

BRECO Mode	Tag^h	Tag^e	$\frac{\epsilon^e_{tag}}{\epsilon^h_{tag}}$
all $B^\pm$	146614 ± 525.4	19927 ± 188.4	1.018 ± 0.010
all B^0	109363 ± 2187.3	15375 ± 165.2	1.053 ± 0.024

Semileptonic branching fractions

The new set of branching fractions obtained is

$$BR(B^0 \rightarrow Xl\nu) = 10.70 \pm 0.34 \pm 0.31$$

$$BR(B^\pm \rightarrow Xl\nu) = 10.64 \pm 0.24 \pm 0.29$$

We conclude that the observed differences in B_{reco} mode compositions between Data and Monte-Carlo do not affect this analysis in a significant way.

6.1.8 $p^* = 0$ extrapolation fit studies

Fitting the combined electron spectrum for both $B^{\pm}$ and B^0

Figures 6.13 and 6.14 shows the result of the fit. The Table 6.12 shows the branching fraction of each channel from default EvtGen decay files and obtained through the fitting procedure. Note that the fit calls for a significantly lower fraction of the non-resonant $B \rightarrow D(*)(n)\pi l\nu$ decays. We vary a_1, a_2 and a_3 within the fit errors to obtain another independent estimate on the error of the low-momentum correction.
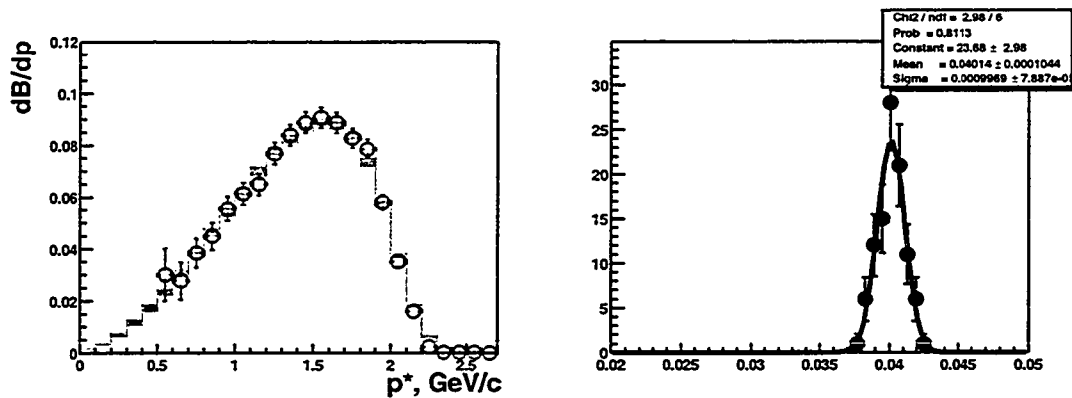
Figure 6.13: Extrapolation of the lepton spectrum to $P^* = 0$. (a) - fit to combined $B^{\pm}$ and B^0 spectrum, (b) - extraction of the $p^* = 0$ extrapolation factor.

The fit for the combined B spectrum has $\chi^2/DOF = 0.677$ and predicts the fraction of electrons with $p^* < 0.5 GeV/c$ to be 4.014 ± 0.100 % of the total rate. To determine the error on these corrections, we use the procedure described in detail in Section 4.5.2.
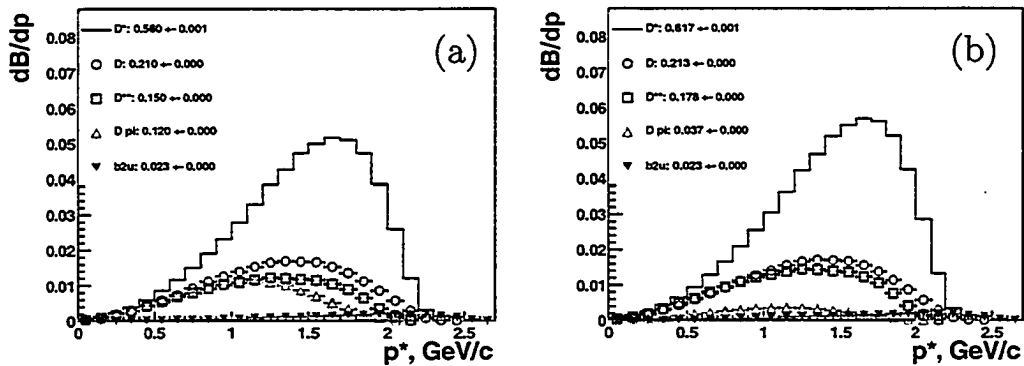
Figure 6.14: Results of the fit to the theoretical shapes. (a) - the default decomposition of $B \to X_c e\nu$ spectrum into 4 exclusive modes and $b \to u$, (b) - the fitted decomposition of $B \to X_c e\nu$ spectrum into 4 exclusive modes and $b \to u$.

Table 6.11: Fit results.

parameter	floating D/D^* ratio
a_0^{fit}	1.004 ± 0.016
a_1^{fit}	1.096 ± 0.047
a_2^{fit}	1.009 ± 0.095
a_3^{fit}	1.18 ± 0.23
$\chi 2/DOF$	$\frac{9.47}{14.0} = 0.677$
Conf. Level	0.734
p=0 correction, % (relative)	4.014 ± 0.100

222

mode	$B \to D^*l\nu$	$B \to Dl\nu$	$B \to D^{**}l\nu$	$B \to D(*)(n)\pi l\nu$	$b \to u$	total
default	5.6020 ± 0.0079	2.0998 ± 0.0048	1.5008 ± 0.0041	1.1951 ± 0.0036	0.233	10.6
$B^{\pm} + B^0$	6.17 ± 0.26	2.13 ± 0.20	1.78 ± 0.35	0.37 ± 0.48	0.233	10.67 ± 0.17

Table 6.12: Individual channel and total branching fractions, default and fitted, %. No penalty functions are applied. $b \to u$ branching fraction is fixed to 2.24% of the $b \to c$ combined fraction, per latest experimental results.

Scanning the penalty function parameters

The "penalty factors" in the fit function shown in (4.21) are varied in order to test for any dependancy of the extrapolation results on the input values for errors on branching fractions for individual decay modes (Table 4.41).

The errors are scaled by a factor of 2

Figures 6.15 and 6.16 shows the result of the fit. The Table 6.14 shows the branching fraction of each channel from default EvtGen decay files and obtained through the fitting procedure. Note that the fit calls for a significantly lower fraction of the non-resonant $B \rightarrow D(*)(n)\pi l \nu$ decays. We vary a_1, a_2 and a_3 within the fit errors to obtain another independent estimate on the error of the low-momentum correction.
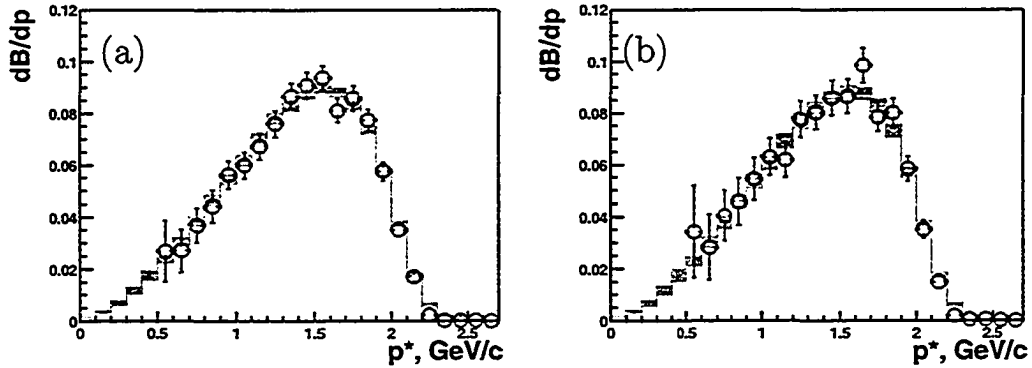
Figure 6.15: Extrapolation of the lepton spectrum to $P^* = 0$, errors on branching fractions of individual decay modes are rescaled by a factor of 2. (a) - fit with error band showing deviations in the fitted spectrum for $B^{\pm}$ and (b) - same for B^0.

The fit for the charged B spectrum has $\chi^2/DOF = 0.594$ and predicts the fraction of electrons with $p^* < 0.5 GeV/c$ to be 4.20 ± 0.12 % of the total rate. The same fit for the neutral B spectrum has $\chi^2/DOF = 0.663$ and predicts the

224
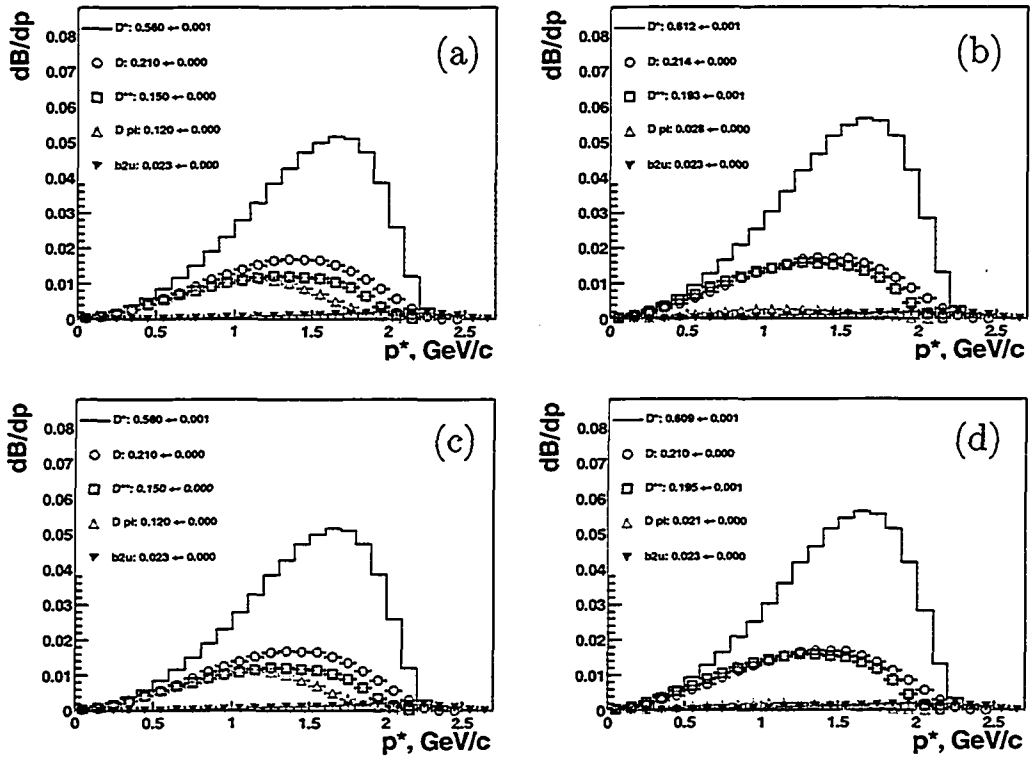
Figure 6.16: Results of the fit to the theoretical shapes, errors on branching fractions of individual decay modes are rescaled by a factor of 2. (a) - the default decomposition of $B^{\pm} \to X_c e\nu$ spectrum into 4 exclusive modes and $b \to u$, (b) - the fitted decomposition of $B^{\pm} \to X_c e\nu$ spectrum into 4 exclusive modes and $b \to u$, (c) - the default decomposition of $B^0 \to X_c e\nu$ spectrum into 4 exclusive modes and $b \to u$, (d) - the fitted decomposition of $B^0 \to X_c e\nu$ spectrum into 4 exclusive modes and $b \to u$.

fraction of electrons with $p^* < 0.5 GeV/c$ to be 4.23 ± 0.18 % of the total rate. To determine the error on these corrections, we use the procedure described in detail in Section 4.5.2.

225
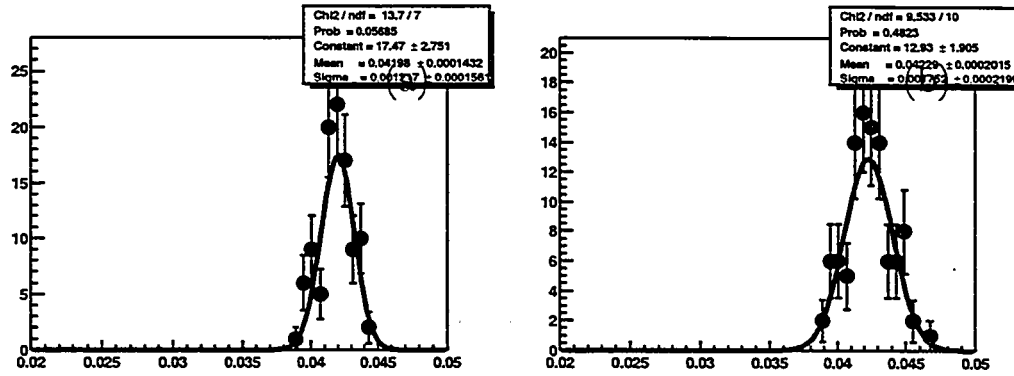
Figure 6.17: Error estimation for $p^* = 0$ extrapolation fit, errors on branching fractions of individual decay modes are rescaled by a factor of 2. (a) - distribution of the $p^* = 0$ extrapolation, $B^{\pm}$; (b) - same for B^0 .

Table 6.13: Fit results, errors on branching fractions of individual decay modes are rescaled by a factor of 2.

parameter	floating D/D^* ratio	
	$B^{\pm}$	B^0
a_0^{fit}	1.007 ± 0.020	0.996 ± 0.027
a_1^{fit}	1.086 ± 0.072	1.092 ± 0.083
a_2^{fit}	1.01 ± 0.17	1.00 ± 0.17
a_3^{fit}	1.28 ± 0.41	1.31 ± 0.42
$\chi 2/DOF$	$\frac{8.32}{14.0} = 0.594$	$\frac{9.28}{14.0} = 0.663$
Conf. Level	0.819	0.749
p=0 correction, % (relative)	4.20 ± 0.12	4.23 ± 0.18

226

mode	$B \to D^*l\nu$	$B \to Dl\nu$	$B \to D^{**}l\nu$	$B \to D(*)(n)\pi l\nu$	$b \to u$	total
default	5.6020 ± 0.0079	2.0998 ± 0.0048	1.5008 ± 0.0041	1.1951 ± 0.0036	0.233	10.6
$B^{\pm}$	6.12 ± 0.40	2.14 ± 0.35	1.93 ± 0.62	0.28 ± 0.82	0.233	10.70 ± 0.21
B^0	6.09 ± 0.46	2.10 ± 0.35	1.95 ± 0.63	0.21 ± 0.86	0.233	10.59 ± 0.29

Table 6.14: Individual channel and total branching fractions, default and fitted, %. Errors on branching fractions of individual decay modes are rescaled by a factor of 2. $b \to u$ branching fraction is fixed to 2.24% of the $b \to c$ combined fraction, per latest experimental results.

227

The errors are scaled by a factor of 5

Figures 6.18 and 6.19 shows the result of the fit. The Table 6.16 shows the branching fraction of each channel from default EvtGen decay files and obtained through the fitting procedure. Note that the fit calls for a significantly lower fraction of the non-resonant $B \rightarrow D(*)(n)\pi l\nu$ decays. We vary a_1, a_2 and a_3 within the fit errors to obtain another independent estimate on the error of the low-momentum correction.
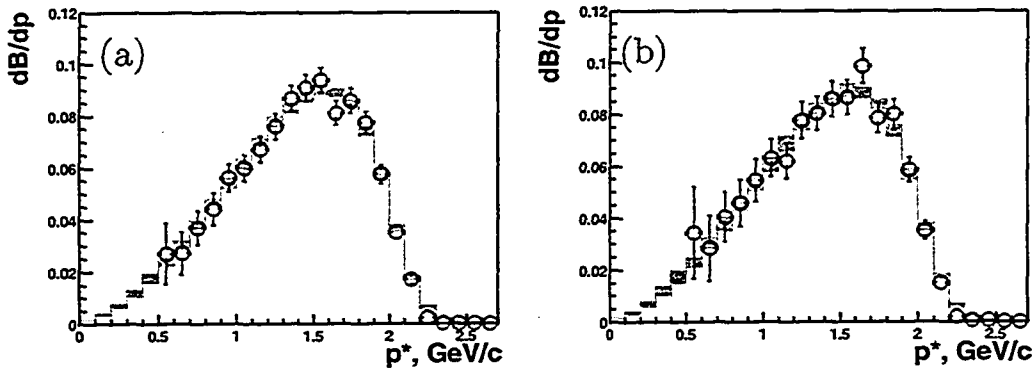
Figure 6.18: Extrapolation of the lepton spectrum to $P^* = 0$, errors on branching fractions of individual decay modes are rescaled by a factor of 5. (a) - fit with error band showing deviations in the fitted spectrum for $B^{\pm}$ and (b) - same for B^0.

The fit for the charged B spectrum has $\chi^2/DOF = 0.538$ and predicts the fraction of electrons with $p^* < 0.5 GeV/c$ to be 4.48 ± 0.15 % of the total rate. The same fit for the neutral B spectrum has $\chi^2/DOF = 0.588$ and predicts the fraction of electrons with $p^* < 0.5 GeV/c$ to be 4.51 ± 0.18 % of the total rate. To determine the error on these corrections, we use the procedure described in detail in Section 4.5.2.
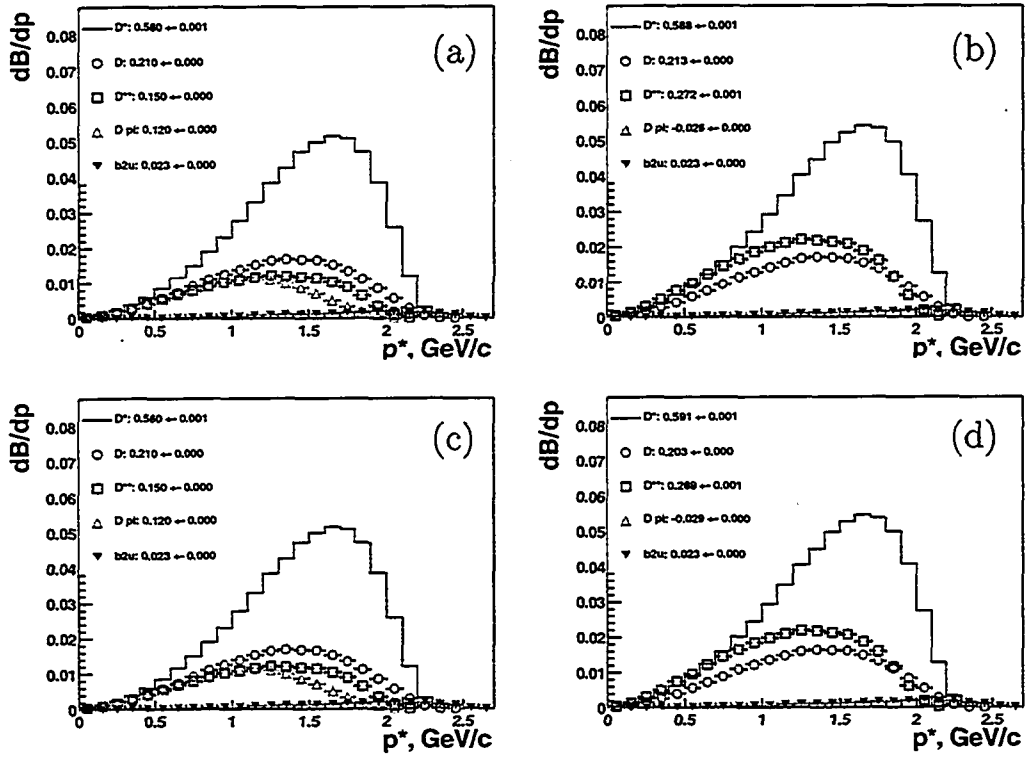
Figure 6.19: Results of the fit to the theoretical shapes, errors on branching fractions of individual decay modes are rescaled by a factor of 5. (a) - the default decomposition of $B^{\pm} \rightarrow X_c e\nu$ spectrum into 4 exclusive modes and $b \rightarrow u$, (b) - the fitted decomposition of $B^{\pm} \rightarrow X_c e\nu$ spectrum into 4 exclusive modes and $b \rightarrow u$, (c) - the default decomposition of $B^0 \rightarrow X_c e\nu$ spectrum into 4 exclusive modes and $b \rightarrow u$, (d) - the fitted decomposition of $B^0 \rightarrow X_c e\nu$ spectrum into 4 exclusive modes and $b \rightarrow u$.

229
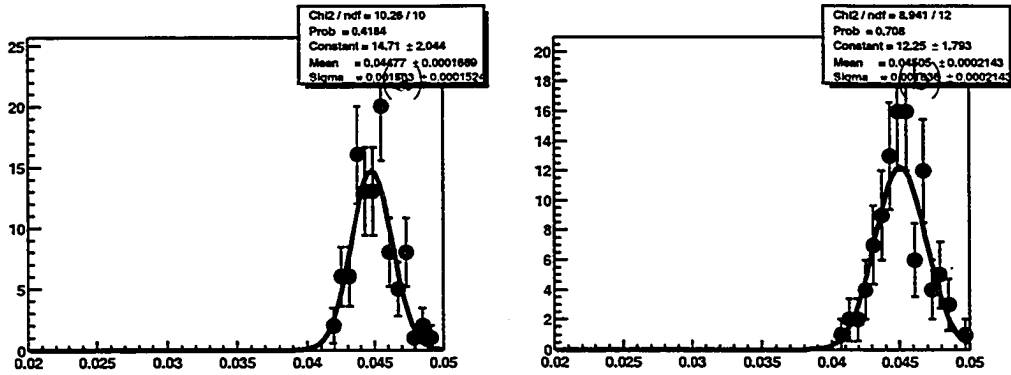
Figure 6.20: Error estimation for $p^* = 0$ extrapolation fit, errors on branching fractions of individual decay modes are rescaled by a factor of 5. (a) - distribution of the $p^* = 0$ extrapolation, $B^\pm$; (b) - same for B^0 .

Table 6.15: Fit results, errors on branching fractions of individual decay modes are rescaled by a factor of 5.

parameter	floating D/D^* ratio	
	$B^\pm$	B^0
a_0^{fit}	1.007 ± 0.020	0.995 ± 0.027
a_1^{fit}	1.04 ± 0.11	1.06 ± 0.12
a_2^{fit}	1.01 ± 0.27	0.97 ± 0.24
a_3^{fit}	1.80 ± 0.87	1.8 ± 1.1
$\chi2/DOF$	$\frac{7.53}{14.0} = 0.538$	$\frac{8.23}{14.0} = 0.588$
Conf. Level	0.867	0.825
p=0 correction, % (relative)	4.48 ± 0.15	4.51 ± 0.18

230

mode	$B \to D^*l\nu$	$B \to Dl\nu$	$B \to D^{**}l\nu$	$B \to D(*)(n)\pi l\nu$	$b \to u$	total
default	5.6020 ± 0.0079	2.0998 ± 0.0048	1.5008 ± 0.0041	1.1951 ± 0.0036	0.233	10.6
$B^{\pm}$	5.88 ± 0.61	2.13 ± 0.58	2.7 ± 1.3	-0.3 ± 1.6	0.233	10.70 ± 0.21
B^0	5.91 ± 0.65	2.03 ± 0.49	2.7 ± 1.7	-0.3 ± 1.9	0.233	10.58 ± 0.29

Table 6.16: Individual channel and total branching fractions, default and fitted, %. Errors on branching fractions of individual decay modes are rescaled by a factor of 5. $b \to u$ branching fraction is fixed to 2.24% of the $b \to c$ combined fraction, per latest experimental results.

No penalty function is applied

Figures 6.21 and 6.22 shows the result of the fit. The Table 6.18 shows the branching fraction of each channel from default EvtGen decay files and obtained through the fitting procedure. Note that the fit calls for a significantly lower fraction of the non-resonant $B \rightarrow D(*)(n)\pi l\nu$ decays. We vary a_1, a_2 and a_3 within the fit errors to obtain another independent estimate on the error of the low-momentum correction.
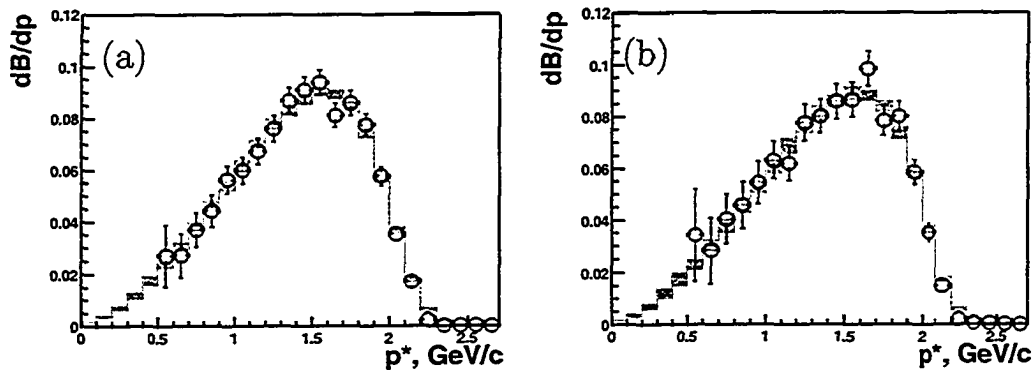
Figure 6.21: Extrapolation of the lepton spectrum to $P^* = 0$, no penalty functions are applied. (a) - fit with error band showing deviations in the fitted spectrum for $B^{\pm}$ and (b) - same for B^0.

The fit for the charged B spectrum has $\chi^2/DOF = 0.508$ and predicts the fraction of electrons with $p^* < 0.5 GeV/c$ to be 4.32 ± 0.15 % of the total rate. The same fit for the neutral B spectrum has $\chi^2/DOF = 0.554$ and predicts the fraction of electrons with $p^* < 0.5 GeV/c$ to be 4.40 ± 0.24 % of the total rate. To determine the error on these corrections, we use the procedure described in detail in Section 4.5.2.

232
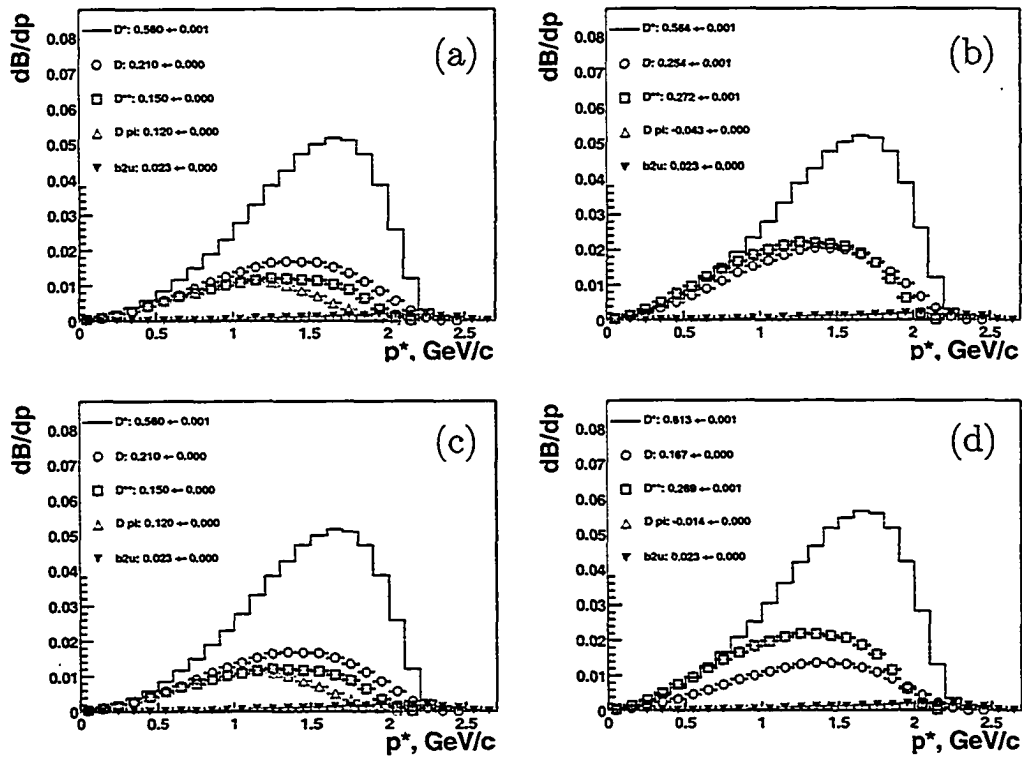
Figure 6.22: Results of the fit to the theoretical shapes, no penalty functions are applied. (a) - the default decomposition of $B^{\pm} \rightarrow X_c e\nu$ spectrum into 4 exclusive modes and $b \rightarrow u$, (b) - the fitted decomposition of $B^{\pm} \rightarrow X_c e\nu$ spectrum into 4 exclusive modes and $b \rightarrow u$, (c) - the default decomposition of $B^0 \rightarrow X_c e\nu$ spectrum into 4 exclusive modes and $b \rightarrow u$, (d) - the fitted decomposition of $B^0 \rightarrow X_c e\nu$ spectrum into 4 exclusive modes and $b \rightarrow u$.

233
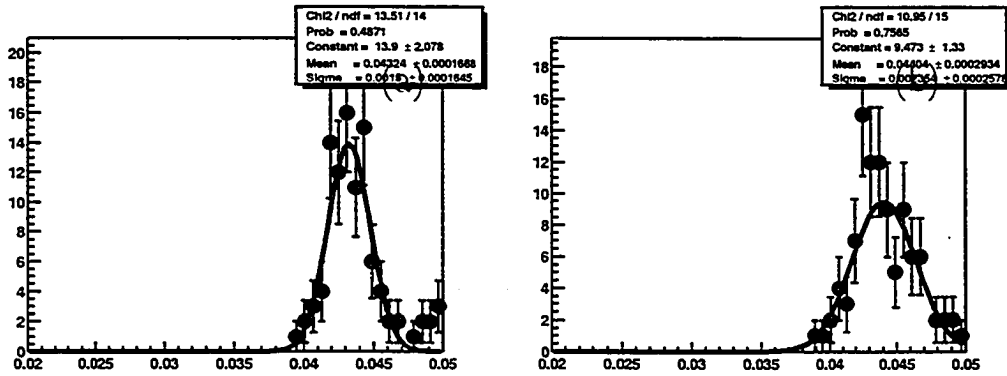
Figure 6.23: Error estimation for $p^* = 0$ extrapolation fit, no penalty function is applied. (a) - distribution of the $p^* = 0$ extrapolation, $B^{\pm}$; (b) - same for B^0 .

Table 6.17: Fit results, no penalty functions are applied.

parameter	floating D/D^* ratio	
	$B^{\pm}$	B^0
a_0^{fit}	1.007 ± 0.020	0.995 ± 0.027
a_1^{fit}	1.001 ± 0.064	1.099 ± 0.066
a_2^{fit}	1.20 ± 0.31	0.80 ± 0.20
a_3^{fit}	1.8 ± 1.0	1.80 ± 0.90
$\chi2/DOF$	$\frac{7.11}{14.0} = 0.508$	$\frac{7.76}{14.0} = 0.554$
Conf. Level	0.890	0.854
p=0 correction, % (relative)	4.32 ± 0.15	4.40 ± 0.24

234

mode	$B \to D^* l\nu$	$B \to Dl\nu$	$B \to D^{**} l\nu$	$B \to D(*)(n)\pi l\nu$	$b \to u$	total
default	5.6020 ± 0.0079	2.0998 ± 0.0048	1.5008 ± 0.0041	1.1951 ± 0.0036	0.233	10.6
$B^{\pm}$	5.64 ± 0.36	2.54 ± 0.66	2.7 ± 1.6	-0.4 ± 1.7	0.233	10.70 ± 0.21
B^0	6.13 ± 0.37	1.67 ± 0.42	2.7 ± 1.3	-0.1 ± 1.5	0.233	10.58 ± 0.29

Table 6.18: Individual channel and total branching fractions, default and fitted, %. No penalty functions are applied. $b \to u$ branching fraction is fixed to 2.24% of the $b \to c$ combined fraction, per latest experimental results.

235

6.1.9 Comparison of the true prompt spectrum in B_{reco} MC sample and default EvtGen spectra

This study is designed to check for any prompt spectrum distortion due to B_{reco} processing. In both cases, Monte-Carlo truth-matched electron spectrum from B-mesons has been extracted. The results of the comparison are shown in Figure 6.24.
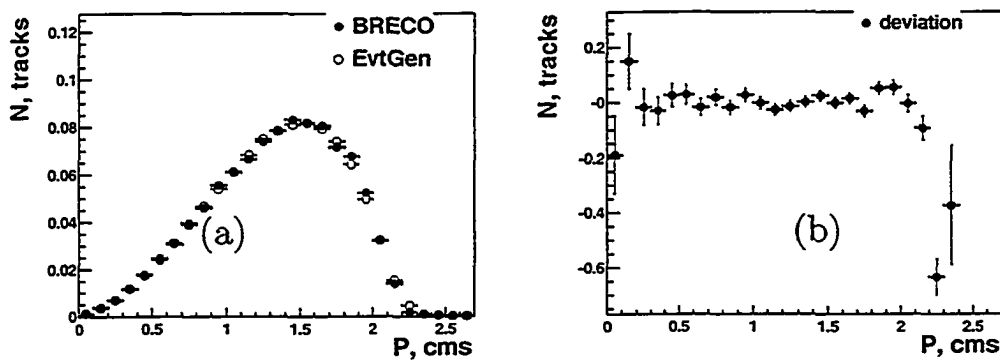
Figure 6.24: Comparison of the true prompt spectrum in B_{reco} MC sample and default EvtGen spectra. (a) - comparison of spectra normalized to unit area, (b) - (B_{reco} -EvtGen)/EvtGen.

No significant discrepancy is observed. This means that B_{reco} efficiency does not significantly depend on the momentum of the prompt electron in the recoil. Therefore, the momentum-independent application of the B_{reco} efficiency bias is justified.

236

Bibliography

[1] J.H.Christenson, J.W.Cronin, V.L.Fitch, and R. Turlay, Phys. Lett. **13**, 138 (1964).

[2] I. I. Y. Bigi et al., *CP violation: Advanced Series on Directions in High Energy Physics*, **Vol 3** p.175, World Scientific, Singapore (1989).

[3] A. D. Sakharov, Zh.E.T.F. Letters, **5** p.32, (1967)

[4] B. Kayser, CP Violation in the K and B Systems, p.6, NSF-PT-96-2, November 1996

[5] B. Kayser, CP Violation and Quantum Mechanics in the B System, FERMILAB-CONF-95-287-T

[6] The *BABAR* Collaboration, *BABAR* Physics Book, SLAC, October 1998

[7] Cornell Electron-positron Storage Ring parameters, accessible through http://www.lns.cornell.edu/public/CESR/info/cesrinfo.html

[8] Jeffrey D. Richmann, Patricia R. Burchat, Leptonic and Semileptonic Decays of Charm and Bottom Hadrons, 1995, UCSB-HEP-95-08, Stanford-HEP-95-01

[9] The Heavy Quark Expansion of QCD, Adam F. Falk, John Hopkins University, October 1996, hep-ph/9610363

[10] Heavy Quark Theory, Gerhard Buchalla, Theory Division, CERN 2002. available as hep/ph/0202092

[11] The *BABAR* Collaboration, *Letter of Intent for the study of CP violation and heavy flavor physics at PEP-II*, SLAC-443, 1994

[12] The *BABAR* Collaboration, The *BABAR* Detector, Nuclear instruments and methods in physics research, section A, 479 (2002) 1-116, 2002

[13] *BABAR* Objectivity databases

http://www.slac.stanford.edu/BFROOT/www/Computing/Online/-Databases/OnlineDatabases.html

[14] ARGUS collaboration, H. Albrecht, *et al.*, Phys. Lett. **B318** (1993) 397.

[15] CLEO collaboration, B.C. Barish, *et al.*, Phys. Rev. Lett. **76** (1996) 1570.

[16] ARGUS collaboration, H. Albrecht, *et al.*, Phys. Lett. **B324** (1994) 249.

[17] CLEO collaboration, M. Artuso, *et al.*, Phys. Lett. **B399** (1997) 321.

[18] Belle collaboration, Measurement of the inclusive semileptonic branching fraction of B-mesons and $|V_{cb}|$. hep/ex0208033, v.1, Aug 2001

[19] T. Brandt *et al.*, Measurement of the Inclusive Lepton Spectrum in B Meson Decays and the Determination of the Semileptonic Branching Ratio and $|V_{cb}|$, BABAR Analysis Document #216 (2001).

[20] U. Langenegger, "Preliminary Measurement of the Semileptonic Branching fractions of charged and neutral B mesons", BABAR Analysis Document #218.

[21] Measurement of $Br(B \to \rho l \nu)$, $|V_{ub}|$, and the Form Factor Slope in $B \to \rho l \nu$ Decay, CLEO Collaboration, July 21, 1998

[22] SVT Overview by Owen Long, accessible through http://www.slac.stanford.edu/BFROOT/www/-Detector/SVT/GeneralInformation/Slides/svt-slides.html

[23] I.I. Bigi, *et al.*, in: B Decays, 2nd edition, S. Stone, ed. (World Scientific 1994).

[24] Weak Annihilation and the End-point Spectrum in Semileptonic B Decays, I.I. Bigi and N.G. Uraltsev, Nucl. Phys. **B423** (1994) 33. (hep-ph/9310285)

[25] U. Langenegger, "Summary of the previous measurements of B-meson Inclusive Semileptonic Branching fractions", accessible through http://www.slac.stanford.edu/ürsl/slbfsx/

[26] D. del Re *et al.*, "Semi-exclusive B reconstruction", BABAR Analysis Document #271.

[27] BRECO AWG, "Exclusive Reconstruction of Hadronic B Decays to Open Charm",

BABAR Analysis Document #150.

[28] J. Blouw *et al.*, "Measurements of Branching Ratios of Charged and Neutral B Mesons into Exclusive Charmonium Final States",

BABAR Analysis Document #113.

[29] U. Langenegger, "Cut-based Electron Identification",

BABAR Analysis Document #90.

[30] CLEO Collaboration, J.E. Duboscq et al., Physical Review Lett. 76 1996
3898.

[31] J.L. Goity and W. Roberts, Physical Review D51 1995 3459.

[32] D. Scora and N. Isgur, Physical Review D52 1995 2783.

[33] B_{reco} Analysis Working Group

[34] T. Brandt, "Likelihood-based Electron Identification",

BABAR Analysis Document #396.

[35] G.C. Fox and S. Wolfram, Phys. Rev. Lett 41 (1978) 1581.

[36] C. Hearty, "Measurement of the Number of $\Upsilon(4S)$ Mesons Produced in Run
1 (B Counting)",

BABAR Analysis Document #134.

[37] T. Brandt, "Studies on Finding Electrons from Conversions and Dalitz De-
cays",

http://www.slac.stanford.edu/t̄brandt/conversion/

[38] BABAR Monte   Carlo   Truth   Matching,   avail-
able   (internally   to   BABAR collaborators   only)   at
http://www.slac.stanford.edu/BFROOT/www/Computing/Offline/Simulation/-
web/mctruth/mctruth_main.html

[39] T. Brandt, "A Closer Look at the Vertexing for Conversions",

http://hep.phy.tu-dresden.de/~tbrandt/conversion/vtxcuts.html

[40] T. Brandt, "A Closer Look at Vertexing Cuts - Dalitz Decays",

http://hep.phy.tu-dresden.de/~tbrandt/conversion/dalitz2

[41] ARGUS collaboration, H. Albrecht, et al., Z. Phys. C 58 (1993) 191.

[42] F. Galeazzi, "Micro smearing/killing for tracks and photons"

http://www.slac.stanford.edu/BFROOT/www/Physics/Tools/BetaTools/MicroKilling.html.

[43] Measurement of the Inclusive Electron Spectrum, Moments and Branching

Fraction for Semileptonic B meson Decays, T. Brandt, 2003

BABAR Analysis Document #636.

[44] Tracking efficiency task force, Babar Analysis Document #324.

[45] Particle Data Group, D.E. Groom, et al., Eur. Phys. J. C15 (2000) 1.

[46] Particle Data Group, K. Hagiwara et al., Phys. Rev. D66, 010001 (2002),

also available from http://pdg.lbl.gov/.

[47] CLEO CONF95-11

[48] Study of Flavor-Tagged Baryon Production in B Decay, CLNS 96/1401,

CLEO 96/7

[49] The LEP Electroweak Working Group, Combined results on b-hadron pro-

duction rates and decay properties, CERN-EP/2001-50 (June 2001)

[50] T.E. Conan et al. [CLEO Collaboration], Phys. Rev. Lett. 80 (1998) 1150.

[51] D. Barate et al. [ALEPH Collaboration], Eur. Phys. J. C 4 (1998) 387.

[52] C. Schwanda [DELPHI Collaboration], DELPHI 2991-105 CONF 404, contributed paper to ICHEP2000

[53] The LEP Electroweak Working Group, Final input parameters for the LEP/SLD heavy flavour analyses, LEPHF 2001-01

[54] The European Physics Journal C, Volume 15, Number 1-4 (2000).

[55] Physical Review D, Volume 66, Number 1-I (2002).

[56] Determination of $|Vub|$ with inclusive semileptonic B decays, BaBar Analysis Document #582, to be submitted to PRL.